Detection of PETN Using Peptide Based Biologically Modified Carbon Nanotubes

by

George D. Kubas

Submitted in Partial Fulfillment of the Requirements

for the Degree of

Doctor of Philosophy

in the

Materials Science & Engineering

Program

YOUNGSTOWN STATE UNIVERSITY

May, 2017

Detection of PETN Using Peptide Based Biologically Modified Carbon Nanotubes

George D. Kubas

I hereby release this dissertation to the public. I understand that dissertation will be made available from the OhioLINK ETD Center and the Maag Library Circulation Desk for public access. I also authorize the University or other individuals to make copies of this thesis as needed for scholarly research.

Signature:

_____
George D. Kubas, Student   Date

Approvals:_____
Dr. Pedro Cortes, Dissertation Advisor   Date

_____
Dr. Diana Fagan, Committee Member   Date

_____
Dr. Tom Oder, Committee Member   Date

_____
Dr. C. Virgil Solomon, Committee Member   Date

_____
Dr. Donald Priour, Committee Member   Date

_____
Dr. Salvatore A. Sanders, Dean of Graduate Studies   Date

Abstract

Explosive detection is an area of great interest in the military, transportation, and safety sectors due to the recent terrorist attacks that have taken place in different parts of the world. Here, detection platforms with high sensitivity and selectivity features are required for the detection of explosives in these senarios. A promising candidate that can fit these specifications is a peptide functionalized carbon nanotube (CNT) due to their unique sensing properties. The present research work has studied the identification of peptides that selectively bind to PETN explosive as well as their incorporation onto CNTs for establishing a nanoscale sensor. This research work has initially concentrated on the use of a phage display technique and enzyme-linked immunosorbent assays in order to screen for those peptides with affinity toward PETNH [a surrogate of the explosive Pentaerythritol tetranitrate (PETN)]. The use of the PETN surrogate in this work allowed the immobilization of the target during the phage screening process, while retaining the chemical profile similar to PETN. The results have suggested that the library here investigated contained peptides selective to PETNH.

Following the panning (screening) procedure, clones were selected and further tested for specificity toward PETNH. The ELISA results from these samples showed that each phage clone has some level of selectivity for binding to PETNH. The peptides from these clones have been sequenced and shown to contain similar amino acid segments among them. These peptides were then used to biologically functionalize single wall carbon nanotubes (SWCNTs) with the purpose of developing a liquid state PETN nanosensor. The results have shown that the peptide-SWCNT complex was able to detect the presence of PETNH.

Also included in this work, is the modeling of the electrical current flow passing through a carbon nanotube field effect transistor (FET) system using density functional tight binding (DFTB) theory via a dftb+ program. The systems investigated included a plain SWCNT, a peptide functionalized SWCNT, and a peptide functionalized SWCNT interacting with PETN. The results have showed that an 8,0 SWCNT FET exhibited an n-type conduction in an oxygen less environment, and that the addition of a peptide or a peptide-PETN interaction did not affect the original n-type conduction profile of the SWCNTs. Furthermore, the results showed that the interaction of PETN with the SWCNT-peptide system displayed an increase in the electrical current of the system suggesting that the explosive sensor resulted in a donation of electrons to the SWCNT conducting channel. The results have shown that the peptide-SWCNT FET operation parameters can be modeled using DFTB theory. This modeling can reduce the experimental work required to identify the functional groups that tailor the selective features of SWCNT based sensors. It is expected that the results presented in this research program can lay out the foundations for developing solid state sensors for explosive materials.

Acknowledgements

Firstly, I would like to thank my advisor, Dr. Cortes, for the guidance in this project. His experience helped me to keep on track through my dissertation and develop the many strategies used to complete the research. Also, he has been instrumental in my academic development starting with my undergraduate degree and research opportunities.

I would also like to thank my committee members for helping me through this arduous process. Dr. Fagan, your help in developing my knowledge in the biological fields was invaluable. Thank you Dr. Solomon for your support on the various electron microscopes throughout the research. Dr. Oder and Dr. Priour, thank you for your help in the solid state and theoretical modeling utilizing Density Functional Theory. Without all of your help, this project could not be completed.

To the graduate students at YSU, thank you for the support and comradery. The agglomeration of different backgrounds and knowledge pools produced new ideas and opportunities that greatly furthered this research.

To my family, thank you for all of your support in not only the pursuit of my doctorate, but also throughout my whole life. My success is a direct reflection of all of the love and time you put into helping me develop into the person I am today. I love you.

Finally, to my wife, Randi. Thank you for the many nights you listened to me complain about failed trials or seemingly insurmountable obstacles. Thank you for showing me how to step away from a problem for a moment, clear my mind, and then tackle it with even more fervor. You always believed in me and supported me no matter what. I love you.

Table of Contents

List of Figures

List of Tables

Chapter 1 . Introduction

1.1 Technological Need

Whether or not they think about it, humans come in contact with sensor technologies every day. In their cars, there are a multitude of sensors that check gas levels, oil quality, and much more. Sensors in their ovens help to keep the temperature steady during cooking. Along with sensors used in everyday life, there are many sensor applications that help keep humans safe. Lab tests can detect early stages of diseases and help to monitor our health. Recently, one of the emerging needs for better sensor technology lies in explosive detection. It seems that every day there is a news story about road side improvised explosive devices harming soldiers or even bombings in otherwise peaceful cities.

On April 15, 2013 two bombs were detonated at the Boston marathon [1]. This bombing killed 3 people and injured over 260. Shown in Figure 1-1 is the aftermath of the first bomb and the subsequent detonation of the second.

Figure 1-1:   2013 Boston marathon bombing [1]

These bombs were created by two inexperienced men and still created a lot of devastation. On November 15, 2015, multiple explosives were detonated in Paris [2]. A total of 130 were left dead and hundreds wounded from the explosions and shooting that took place. On March 22, 2016, a bombing at the Brussels airport and metro station killed 32 people [3]. Finally, on June 28, 2016, a bombing carried out at the Artürk airport in Istanbul killed 41 and injured 230 [4].

With the current increasing concern for national security, the exploration into sensitive and fast explosive detection techniques has garnered considerable interest among governmental, educational, and private institutions [5–9].These initiatives have resulted in different approaches for the detection of explosives [10,11]. However, techniques such as X-ray and sniffing dogs still present various drawbacks such as high time for detection and low portability. Indeed, sniffer dogs require expensive training and sometimes their detection can be inconsistent. To overcome these barriers, much work has been performed to create better methods to detect explosives such as trinitrotoluene (TNT) and 1,3,5-trinitroperhydro-1,3,5-triazine (RDX). A few of the most sensitive sensor techniques exploit the fact that some explosives, such as TNT, are very good electron acceptors [12–14]. For example, some sensors have used a polymer thin film made of a polycarbazole [12]. When brought into contact with TNT vapors, the polymer thin film donates electrons and the films fluorescence intensity decreases. Likewise, other polymers such as tris(phenylene)vinylene (TPV) have been used to interact with RDX and PETN in a similar manner [13].

Another method of TNT detection uses quantum cascade laser photoacoustic spectroscopy (QCL-PAS), which has been reported to sense at the ppb level [15]. One of

the best features of this QCL-PAS method is that it inherently has a very small chance of false positives. The absorption spectrum from the test is a direct function of the chemical composition. Thus, even though a chemical agent may show polymorphism, the spectra will exhibit unique differences.

Indeed, much of the explosive detection work has focused on the detection of TNT and RDX, while research into Pentaerythritol Tetranitrate (PETN), a primary ingredient in Semtex plastic explosives and one of the strongest explosives, has been limitedly investigated due to its low vapor pressure [16]. Some work has been carried out by the Defence and Science Technology Laboratory in the U.K. on the detection of PETN; their research initiatives have resulted in the identification of an antibody specific to the explosive [17]. It has been shown that this antibody can be incorporated into an enzyme immunoassay to develop a detection platform [18,19]. However, it is apparent that there is still a need for more research into alternate sensitive, selective, and portable sensors that can successfully target PETN. A promising candidate to meet these criterion is a PETN specific peptide. It has been shown that peptides selective to volatile organic compounds (VOC) such as benzene, toluene, and xylene can be obtained via a bio-panning of a M13 phage library [20]. The peptides discovered through the biopanning (screening) procedure were used to functionalize a micro-cantilever surface. These sensors were able to discriminate between each organic compound and, in essence, "sense" a single carbon change in the target compound. In addition, these sensors were capable of detecting on the sub-ppm level with relatively rapid detection times. Similarly, work has been performed on identifying peptides selective to TNT [21,22]. Thus, a phage display library technique can be used to find peptides that express selectivity towards chemical constituents similar

to PETN. These peptides can then be incorporated onto an optical-electrical platform to assemble a biosensor. One of the reasons that makes peptides an excellent candidate for being considered as the detection platform of nanosensors is that they are able to be kept in a solid state without the need of storage in a liquid environment [23,24]. An opposite feature to that required by biological selective materials such as antibodies. Certainly, this solid-state storage capability is an important feature for sensor applications.

1.2 Commercialization

Currently, carbon nanotubes are beginning to emerge as commercialized sensors [25–27]. NASA has created sensors based on SWCNT suspensions deposited onto interdigitated electrodes [25]. Some of the areas these sensors have been used include the detection of flammable gasses, quality control, methane detection, monitoring of industrial gases, and emissions of patient's breath. Applied Nanotech Inc., based out of Austin, Texas, has commercialized enzyme coated CNT sensors that target glucose in the liquid and gas phases [26]. These sensitive and selective sensors have been used in blood, urine, and saliva analysis. Nano Engineered Applications, Inc. is another company that focuses on creating solid-state SWCNT sensors targeting airborne gases at the parts per billion level [27]. These sensors are produced in a way that they can monitor different gas levels in real time.

1.3 Overview of Carbon Nanotubes (CNT)

Carbon nanotubes (CNTs) are relatively new nanomaterials that have spurred considerable research in the past few decades. In 1991, Sumio Iijima discovered that

tubular graphite can be formed in direct current arc-discharge evaporation of carbon [28]. This discovery sparked much interest into understanding their growth mechanism. In 1995, at the Center for Nanoscale Science and Technology in Houston, the growth mechanism of direct laser vaporization and metal catalyzed direct laser vaporization techniques were subsequently discovered [29,30]. Later in 1999, the growth model for metal catalyzed CVD was explored and similar results were found [31] . Kinetic modeling of CVD also led to an understanding of the reactions that take place at various locations in the growth chamber [32] . Due to a large amount of variables present in the growth of CNTs, research into different catalysts and support materials, catalyst layer thickness, and agents to keep the growth free of amorphous carbon has led to a more controlled growth process [33–36]. This fundamental understanding has resulted in the growth of vertically aligned CNTs [37], patterned growth of vertically aligned tubes [38], and growth between patterned islands of catalyst to produce very small scale electronic devices [39].

Carbon nanotubes have also attracted much interest in the scientific and applied fields because of their exceptional properties. One attractive property is their mechanical strength. The elastic modulus of CNTs have been measured between 0.41 TPa with a maximum of 4.15 TPa [40–42]. Additionally, CNTs exhibit very good bending properties. They have shown to be very flexible after observing MWCNTs returning to their original position following a bending state with a radius of curvature around 20 nm [43]. Indeed, they have shown an average bending strength of 14 GPa [41]. Due to these outstanding mechanical properties, they are being used on turbine

blades, airplane structures (as integrity monitoring materials), and on sporting goods such as bicycles for enhancing their strength [44].

In addition to their exceptional mechanical properties, CNTs have very interesting and exploitable electrical properties. For instance, depending on the chirality of SWCNTs, a tube may act either as a metal or semiconductor [45]. Also, within the semiconductor regime of the SWCNT, it is possible to adjust whether the tube acts as a p-type or n-type semiconductor [46]. For example, a semiconducting SWCNT inherently behaves as n-type, but once it comes in contact with oxygen it converts into a p-type semiconductor. These electrical properties has led to their use in many nano scale electrical circuits and sensor platforms [47].

1.4 CNT Sensors

The production of a CNT sensor that targets an explosive, such as PETN, would be very valuable in many different application areas. One of the best aspects about these types of sensors is its size. Their small size allows for unparalleled portability that common detection platforms such as X-Ray do not have [10,11]. Thus, these sensors could potentially have the ability to be assembled into electronics on the scale of a hand held device. This means applications where airport employees could use them as real time atmosphere scanners for directly scanning suspicious individuals. Some other applications could reach to the police force where preventative detection could stop terrorists before an act can be committed or to soldiers where monitoring could result in the early detection of improvised explosive devices.

One of the properties of an ideal explosive sensor is the requirement of high sensitivity due to the low vapor pressures that explosives present. Table 1.1 shows the vapor pressures of some explosive materials [48].

Table 1.1 : Vapor pressures for common explosives [48].

Explosive	Vapor Pressure at 25 °C (atm)
TNT	9.7E-09
RDX	6.16E-12
PETN	7.17E-12

Indeed, CNTs have the ability to detect chemicals at very low concentration levels. It has been shown that CNTs inherently exhibit an electrical conductivity change when in contact with varying levels of chemicals such as NO_2, NH_3, and O_2 [49–51]. These CNT based sensors are able to detect as low as the parts per billion level. Other important results from these studies have shown that CNT based sensors outperformed metal oxide detectors in both sensitivity and stability [52,53]. Additionally, CNTs do not have issues with surface stability like that shown in metal oxide sensors.

Another pertinent property of CNT sensors is their ability to target specific explosive structures which reduces the possibility of false positive detections. Here, selectively on CNTs can be incorporated through covalent and noncovalent functionalization routes. It has been shown that Nafion functionalization yields CNTs capable of detecting only the NH_3, in a $NO_2 - NH_3$ mixture [54]. Conversely, functionalization with polyethyleneimine allows the detection of NO_2 but not NH_3. Other research groups have studied the chemical functionalization a step further. They showed that chemical functionalization not only imparts selectivity, but it can also result in the detection of chemicals not inherently

detected by CNTs [55,56] . It has been demonstrated that the use of poly(ethylene glycol) results in a sensor that can detect organic solvents such as chloroform [55]. Wang *et al* [56] proved that the addition of hexafluoroisopropanol substituted polythiophene (HFIP-PT) polymer to the SWCNT sidewalls produced a sensor that targeted dimethyl methylphosphonate (a chemical agent with similar structure and properties to sarin gas). The sensing mechanism is a result of the hydrogen binding between the HFIP and the phosphate esters present in chemical warfare agents, and the resulting charge transfer being detected by the CNT.

Another alluring property of CNT sensors is their recovery capabilities. CNTs sensors present a conductance baseline depending of the construction of the device [50]. Interaction of the analyte with the CNT device results in a change of conductance. Using heat or UV treatment, the CNT sensor can be returned to its original conductance. Depending on the applications, this recovery can occur several times before the recovered baseline is greatly affected. This recovery feature means that the lifetime of a CNT sensor is extended with reductions in the overall cost.

1.5 Molecular Modeling

Theoretical modeling of the interaction between a CNT sensor device and a target analyte elucidates the way in which the sensor can act during detection. Modeling can also help to narrow down operating conditions of the device such as gate voltage and bias voltage. One way to model a CNT-based sensor, is through density functional tight binding (DFTB) theory [57]. The DFTB formalism helps to eliminate many of the complicated integrals present in the density functional theory (DFT) [58]. The main reduction in

difficulty from DFT to DFTB theory comes from disregarding terms that have little effect on the resulting system, and setting some of the integrals to constants that fit values calculated through simpler means. Additionally, the use of the non-equilibrium Green's functions and Poisson equations after the DFTB analysis results in the ability to calculate and model the electrical current passing through the CNT-based sensor [59,60]. This allows for the study of the effect of the analyte-CNT interaction on the electrical properties of the nanotubes.

Using DFTB, many different properties of CNTs have been modeled [61,62]. DFTB has been able to agree with the experimental observations on the electrical nature of CNTs being influenced by their chiral nature [61,62]. It has also been shown that the adsorption of metal particles on the CNT surface could cause a tube previously operating as a semiconductor to act as a metal or conversely (depending on the initial chirality of the undoped CNT) [63]. Finally, DFTB has also been used to show that the chemisorption of a functional group causes a greater change in the electrical properties of CNTs than that displayed by a physisorbed molecule [64,65].

1.6 Experimental Research

The research work here proposed focuses on the selective detection of pentaerythritol trinitrate hemisuccinate (PETNH) [surrogate explosive of pentaerythritol tetranitrate (PETN)] using CNTs. Currently, there has not been a constituent found to selectively bind to or interact with PETN. Hence, an important aspect of this research is the identification of a functional structure selective towards PETNH, and its subsequent covalent attachment onto the CNTs to assemble a robust sensing device. Specifically, the purpose of this

9

research program is to identify and investigate the unique amino acid sequences through a phage display technology approach with exclusive specificity towards PETNH. Here, the identification of the amino acid sequences is assisted by a bio-panning procedure and an enzyme-linked immunosorbent assay (ELISA).

A phage display library consists of a virus expressing peptides, proteins, or antibodies on their surface [66]. In this proposed work, a peptide structure, which consists of short chain amino acids, is considered. This is because peptides have the ability to be used in applications with varying environmental conditions [23]. This feature is critical in explosive detection because sensing environment can range in temperature and humidity in controlled airports to extreme cold or hot temperature conditions in defense operations. Since these libraries consist of phage expressing millions of different peptide sequences, a bio-panning procedure was used to isolate only phage displaying peptides selective to the target PETNH [66]. ELISAs were subsequently used to determine the selectivity of peptide binding [67]. The selected and isolated phage from the biopanning process was then processed and sequenced.

Using the knowledge of the sequence, the peptides were acquired from a third party supplier specialized in the assembly of peptides. Following the acquisition of the peptides, a carbodiimide crosslinker approach was studied as a procedure to attach the peptides to carboxylated CNTs. These target selective peptides functionalized the SWCNTs, and this peptide-CNT complex was then used to test the detection of PETN in the liquid state. Here, similar nitro based compounds were included to study the selectivity of the identified peptides.

Liquid detection was carried out by using an avidin incorporation assay and a biotin tagged peptide, since these two components react and link when they come in contact [68]. Using a detection agent, such as HABA(4'-hydroxyazobenzene-2-carboxylic acid) in avidin, the binding was monitored using a colorimetric change and Beer's law. The schematic of the reaction of the protein with the HABA reagent can be observed in Figure 1-2.
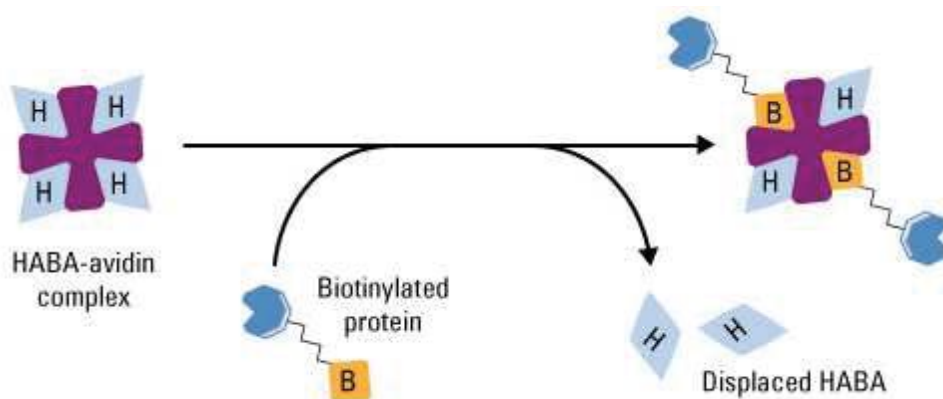
Figure 1-2: HABA/Avidin Biotin Incorporation Assay Schematic [68]. The HABA/Avidin biotinylated peptide complex is then read via visible spectroscopy.

1.7 Modeling Work

This research work also includes the modeling of the interaction between the peptide functionalized SWCNT and PETN. This is performed by employing the use of Density Functional Tight Binding (DFTB) in conjunction with non-equilibrium Green's functions. This model was selected because it is known to correlate well with the experimental results of nanomaterials [58,69–72]. In the DFTB theory, information such as the electron wave functions, base energy, and band gaps can be calculated. This information was then used in Green's functions to calculate values such as the electrical current (at the atomic level

11

and in the tube), the charge density, and conductivity of the tube [59]. Thus, using the DFTB method, it is possible to calculate the change in conductivity when the biologically functionalized SWCNT "detects" the PETN explosive.

Here, a single isolated SWCNT functionalized by a chosen peptide was modeled. Then the model was used to calculate the change in its electrical properties when brought into contact with the PETN. Lastly, the effect of bias and gate voltages on the modeled CNT sensor were also explored.

In summary, the specific objectives for the present research work are:

1. Use of phage display library and biopanning procedures to identify a short chain peptide that specifically binds to Pentaerythritol Trinitrate Hemisuccinate (PETNH).

2. Covalently attach peptide sequences to carboxylated carbon nanotubes through carbodiimide chemistry.

3. Test the liquid state sensing capabilities of the functionalized CNTs towards PETNH.

4. Model the electrical profile of the CNT sensor based on the DFTB theory.

1.8 Organization

The present thesis is organized in five chapters. Chapter 1 presents the need for CNT-based sensor research work. Also, a basic overview of the sensor technology, and the objectives of the work are included. Chapter 2 presents the literature review of CNTs. It describes the physical, electrical, and mechanical properties of CNTs as well as their

synthesis and applications in sensors. This chapter also describes the phage display process and presents an overview of the molecular modeling of CNT systems using Density Functional Theory conjoined with the tight binding formalism, non-equilibrium Green's functions, and Poisson equations. Chapter 3 presents the methods and materials used in this research work. Chapter 4 shows the computer modeling methodology considered in this research. Chapter 5 presents the results and discussion of the experimental and modeling work. It describes the outcome of the phage display library, the covalent binding of the peptide to the CNTs, and the results of the detection of PETN in the liquid state. Also, chapter 5 presents the modeling of the electrical profiles of a bare semiconducting SWCNT, a SWCNT/peptide system, and a SWCNT/peptide system interacting with PETN via DFTB theory. Finally, chapter 6 presents the conclusions of the thesis.

1.9 References

[1] "Boston Marathon bombing of 2013 | terrorist attack, Massachusetts, United States | Britannica.com" [Online]. Available: https://www.britannica.com/event/Boston-Marathon-bombing-of-2013. [Accessed: 07-Sep-2016].

[2] 2015, "Paris attacks: What happened on the night," BBC News.

[3] 2016, "Brussels explosions: What we know about airport and metro attacks," BBC News.

[4] 2016, "Istanbul Ataturk airport attack: 41 dead and more than 230 hurt," BBC News.

[5] Senesac, L., and Thundat, T. G., 2008, "Nanosensors for trace explosive detection," Mater. Today, **11**(3), pp. 28–36.

[6] Hu, Z., Deibert, B. J., and Li, J., 2014, "Luminescent metal–organic frameworks for chemical sensing and explosive detection," Chem. Soc. Rev., **43**(16), pp. 5815–5840.

[7] Bakaltcheva, I. B., Ligler, F. S., Patterson, C. H., and Shriver-Lake, L. C., 1999, "Multi-analyte explosive detection using a fiber optic biosensor," Anal. Chim. Acta, **399**(1–2), pp. 13–20.

[8] Narang, U., Gauger, P. R., and Ligler, F. S., 1997, "A Displacement Flow Immunosensor for Explosive Detection Using Microcapillaries," Anal. Chem., **69**(14), pp. 2779–2785.

[9] Riskin, M., Ben-Amram, Y., Tel-Vered, R., Chegel, V., Almog, J., and Willner, I., 2011, "Molecularly Imprinted Au Nanoparticles Composites on Au Surfaces for the Surface Plasmon Resonance Detection of Pentaerythritol Tetranitrate, Nitroglycerin, and Ethylene Glycol Dinitrate," Anal. Chem., **83**(8), pp. 3082–3088.

[10] Caygill, J. S., Davis, F., and Higson, S. P. J., 2012, "Current trends in explosive detection techniques," Talanta, **88**, pp. 14–29.

[11] Rhykerd, C. L., National Institute of Justice (U.S.)., and National Institute of Standards and Technology (U.S.)., 1999, Guide for the selection of commercial explosives detection systems for law enforcement applications, U.S. Dept. of Justice, Office of Justice Programs, National Institute of Justice, Washington, DC.

[12] Nie, H., Zhao, Y., Zhang, M., Ma, Y., Baumgarten, M., and Müllen, K., 2011, "Detection of TNT explosives with a new fluorescent conjugated polycarbazole polymer," Chem. Commun., **47**(4), pp. 1234–1236.

[13] Gopalakrishnan, D., and Dichtel, W. R., 2013, "Direct Detection of RDX Vapor Using a Conjugated Polymer Network," J. Am. Chem. Soc., **135**(22), pp. 8357–8362.

[14] Xu, B., Wu, X., Li, H., Tong, H., and Wang, L., 2011, "Selective Detection of TNT and Picric Acid by Conjugated Polymer Film Sensors with Donor–Acceptor Architecture," Macromolecules, **44**(13), pp. 5089–5092.

[15] Pushkarsky, M. B., Dunayevskiy, I. G., Prasanna, M., Tsekoun, A. G., Go, R., and Patel, C. K. N., 2006, "High-sensitivity detection of TNT," Proc. Natl. Acad. Sci., **103**(52), pp. 19630–19634.

[16] "PETN [Pentaerythritol tetranitrate]" [Online]. Available: http://www.globalsecurity.org/military/systems/munitions/explosives-nitrate-petn.htm. [Accessed: 07-Sep-2016].

[17] Hesse, A., Biyikal, M., Rurack, K., and Weller, M. G., 2016, "Development of highly sensitive and selective antibodies for the detection of the explosive pentaerythritol tetranitrate (PETN) by bioisosteric replacement," J. Mol. Recognit., **29**(2), pp. 88–94.

[18] Wilson, R., Clavering, C., and Hutchinson, A., 2003, "Electrochemiluminescence Enzyme Immunoassays for TNT and Pentaerythritol Tetranitrate," Anal. Chem., **75**(16), pp. 4244–4249.

[19] Anderson, G. P., Moore, M., Charles, P. T., and Goldman, E. R., 2010, "Bead-Based Fluid Array Detection of Pentaerythritol Tetranitrate: Comparison of Monoclonal vs. Llama Polyclonal Antibodies," Anal. Lett., **43**(18), pp. 2913–2922.

[20] Ju, S., Lee, K.-Y., Min, S.-J., Yoo, Y. K., Hwang, K. S., Kim, S. K., and Yi, H., 2015, "Single-carbon discrimination by selected peptides for individual detection of volatile organic compounds," Sci. Rep., **5**, p. 9196.

[21] Goldman, E. R., Pazirandeh, M. P., Charles, P. T., Balighian, E. D., and Anderson, G. P., 2002, "Selection of phage displayed peptides for the detection of 2,4,6-trinitrotoluene in seawater," Anal. Chim. Acta, **457**(1), pp. 13–19.

[22] Jaworski, J. W., Raorane, D., Huh, J. H., Majumdar, A., and Lee, S.-W., 2008, "Evolutionary Screening of Biomimetic Coatings for Selective Detection of Explosives," Langmuir, **24**(9), pp. 4938–4943.

[23] Lai, M. C., and Topp, E. M., 1999, "Solid-state chemical stability of proteins and peptides," J. Pharm. Sci., **88**(5), pp. 489–500.

[24] Cleland, J. L., Lam, X., Kendrick, B., Yang, J., Yang, T. H., Overcashier, D., Brooks, D., Hsu, C., and Carpenter, J. F., 2001, "A specific molar ratio of stabilizer to protein is required for storage stability of a lyophilized monoclonal antibody," J. Pharm. Sci., **90**(3), pp. 310–321.

[25] Kovo, Y., 2015, "Gas Sensors Based on Coated and Doped Carbon Nanotubes," NASA [Online]. Available: http://www.nasa.gov/ames-partnerships/technology/technology-opportunity-gas-sensors-based-on-coated-and-doped-carbon-nanotubes. [Accessed: 12-Oct-2016].

[26] "Applied Nanotech, Inc. :: Sensors" [Online]. Available: http://www.appliednanotech.net/tech/nanosensors.php. [Accessed: 12-Oct-2016].

[27] "Technology | Nano Engineered Applications" [Online]. Available: http://www.neapplications.com/technology-0. [Accessed: 12-Oct-2016].

[28] Iijima, S., 1991, "Helical microtubules of graphitic carbon," Nature, **354**, pp. 56–58.

[29] Guo, T., Nikolaev, P., Rinzler, A. G., Tomanek, D., Colbert, D. T., and Smalley, R. E., 1995, "Self-Assembly of Tubular Fullerenes," J. Phys. Chem., **99**(27), pp. 10694–10697.

[30] Guo, T., Nikolaev, P., Thess, A., Colbert, D. T., and Smalley, R. E., 1995, "Catalytic growth of single-walled manotubes by laser vaporization," Chem. Phys. Lett., **243**(1–2), pp. 49–54.

[31] Sinnott, S. B., Andrews, R., Qian, D., Rao, A. M., Mao, Z., Dickey, E. C., and Derbyshire, F., 1999, "Model of carbon nanotube growth through chemical vapor deposition," Chem. Phys. Lett., **315**(1–2), pp. 25–30.

[32] Brukh, R., and Mitra, S., 2006, "Mechanism of carbon nanotube growth by CVD," Chem. Phys. Lett., **424**(1–3), pp. 126–132.

[33] Cassell, A. M., Raymakers, J. A., Kong, J., and Dai, H., 1999, "Large Scale CVD Synthesis of Single-Walled Carbon Nanotubes," J. Phys. Chem. B, **103**(31), pp. 6484–6492.

[34] Kong, J., Cassell, A. M., and Dai, H., 1998, "Chemical vapor deposition of methane for single-walled carbon nanotubes," Chem. Phys. Lett., **292**(4–6), pp. 567–574.

[35] Chhowalla, M., Teo, K. B. K., Ducati, C., Rupesinghe, N. L., Amaratunga, G. a. J., Ferrari, A. C., Roy, D., Robertson, J., and Milne, W. I., 2001, "Growth process conditions of vertically aligned carbon nanotubes using plasma enhanced chemical vapor deposition," J. Appl. Phys., **90**(10), pp. 5308–5317.

[36] Hata, K., Futaba, D. N., Mizuno, K., Namai, T., Yumura, M., and Iijima, S., 2004, "Water-Assisted Highly Efficient Synthesis of Impurity-Free Single-Walled Carbon Nanotubes," Science, **306**(5700), pp. 1362–1364.

[37] Zhong, G., Hofmann, S., Yan, F., Telg, H., Warner, J. H., Eder, D., Thomsen, C., Milne, W. I., and Robertson, J., 2009, "Acetylene: A Key Growth Precursor for Single-Walled Carbon Nanotube Forests," J. Phys. Chem. C, **113**(40), pp. 17321–17325.

[38] Fan, S., Chapline, M. G., Franklin, N. R., Tombler, T. W., Cassell, A. M., and Dai, H., 1999, "Self-Oriented Regular Arrays of Carbon Nanotubes and Their Field Emission Properties," Science, **283**(5401), pp. 512–514.

[39] Kong, J., Soh, H. T., Cassell, A. M., Quate, C. F., and Dai, H., 1998, "Synthesis of individual single-walled carbon nanotubes on patterned silicon wafers," Nature, **395**(6705), pp. 878–881.

[40] Treacy, M. M. J., Ebbesen, T. W., and Gibson, J. M., 1996, "Exceptionally high Young's modulus observed for individual carbon nanotubes," Nature, **381**(6584), pp. 678–680.

[41] Wong, E. W., Sheehan, P. E., and Lieber, C. M., 1997, "Nanobeam Mechanics: Elasticity, Strength, and Toughness of Nanorods and Nanotubes," Science, **277**(5334), pp. 1971–1975.

[42] Salvetat, J.-P., Briggs, G. A. D., Bonard, J.-M., Bacsa, R. R., Kulik, A. J., Stöckli, T., Burnham, N. A., and Forró, L., 1999, "Elastic and Shear Moduli of Single-Walled Carbon Nanotube Ropes," Phys. Rev. Lett., **82**(5), pp. 944–947.

[43] Falvo, M. R., Clary, G. J., Taylor, R. M., Chi, V., Brooks, F. P., Washburn, S., and Superfine, R., 1997, "Bending and buckling of carbon nanotubes under large strain," Nature, **389**(6651), pp. 582–584.

[44] Volder, M. F. L. D., Tawfick, S. H., Baughman, R. H., and Hart, A. J., 2013, "Carbon Nanotubes: Present and Future Commercial Applications," Science, **339**(6119), pp. 535–539.

[45] Mintmire, J. W., Dunlap, B. I., and White, C. T., 1992, "Are fullerene tubules metallic?," Phys. Rev. Lett., **68**(5), pp. 631–634.

[46] Derycke, V., Martel, R., Appenzeller, J., and Avouris, P., 2001, "Carbon Nanotube Inter- and Intramolecular Logic Gates," Nano Lett., **1**(9), pp. 453–456.

[47] Bandaru, P. R., 2007, "Electrical Properties and Applications of Carbon Nanotube Structures," J. Nanosci. Nanotechnol., **7**(4–1), pp. 1239–1267.

[48] Ewing, R. G., Waltman, M. J., Atkinson, D. A., Grate, J. W., and Hotchkiss, P. J., 2013, "The vapor pressures of explosives," TrAC Trends Anal. Chem., **42**, pp. 35–48.

[49] Collins, P. G., Bradley, K., Ishigami, M., and Zettl, A., 2000, "Extreme Oxygen Sensitivity of Electronic Properties of Carbon Nanotubes," Science, **287**(5459), pp. 1801–1804.

[50] Li, J., Lu, Y., Ye, Q., Cinke, M., Han, J., and Meyyappan, M., 2003, "Carbon Nanotube Sensors for Gas and Organic Vapor Detection," Nano Lett., **3**(7), pp. 929–933.

[51] Valentini, L., Armentano, I., Kenny, J. M., Cantalini, C., Lozzi, L., and Santucci, S., 2003, "Sensors for sub-ppm NO2 gas detection based on carbon nanotube thin films," Appl. Phys. Lett., **82**(6), pp. 961–963.

[52] Starke, T. K. H., and Coles, G. S. V., 2002, "High sensitivity ozone sensors for environmental monitoring produced using laser ablated nanocrystalline metal oxides," IEEE Sens. J., **2**(1), pp. 14–19.

[53] Cantalini, C., Pelino, M., Sun, H. T., Faccio, M., Santucci, S., Lozzi, L., and Passacantando, M., 1996, "Cross sensitivity and stability of NO2 sensors from WO3 thin film," Sens. Actuators B Chem., **35**(1), pp. 112–118.

[54] Qi, P., Vermesh, O., Grecu, M., Javey, A., Wang, Q., Dai, H., Peng, S., and Cho, K. J., 2003, "Toward Large Arrays of Multiplex Functionalized Carbon Nanotube Sensors for Highly Sensitive and Selective Molecular Detection," Nano Lett., **3**(3), pp. 347–351.

[55] Niu, L., Luo, Y., and Li, Z., 2007, "A highly selective chemical gas sensor based on functionalization of multi-walled carbon nanotubes with poly(ethylene glycol)," Sens. Actuators B Chem., **126**(2), pp. 361–367.

[56] Wang, F., Gu, H., and Swager, T. M., 2008, "Carbon Nanotube/Polythiophene Chemiresistive Sensors for Chemical Warfare Agents," J. Am. Chem. Soc., **130**(16), pp. 5392–5393.

[57] Aradi, B., Hourahine, B., and Frauenheim, T., 2007, "DFTB+, a sparse matrix-based implementation of the DFTB method," J. Phys. Chem. A, **111**(26), pp. 5678–5684.

[58] Slater, J. C., and Koster, G. F., 1954, "Simplified LCAO Method for the Periodic Potential Problem," Phys. Rev., **94**(6), pp. 1498–1524.

[59] Xue, Y., Datta, S., and Ratner, M. A., 2002, "First-principles based matrix Green's function approach to molecular electronic devices: general formalism," Chem. Phys., **281**(2–3), pp. 151–170.

[60] Pecchia, A., Penazzi, G., Salvucci, L., and Carlo, A. D., 2008, "Non-equilibrium Green's functions in density functional tight binding: method and applications," New J. Phys., **10**(6), p. 65022.

[61] Tetik, E., Karadag, F., Karaaslan, M., and Comez, I., 2012, "The Electronic Properties of the Graphene and Carbon Nanotubes: Ab Initio Density Functional Theory Investigation," Int. Sch. Res. Not., **2012**, pp. 416–417.

[62] Salehi, H., and Gharbavi, K., 2012, "Ab Initio Study of Electronic Properties of a Armchair (7,7) Carbon Nanotube," Adv. Mater. Phys. Chem., **2**(3), pp. 159–162.

[63] Louis, C. N., Jayam, S. G., and Raj, A. A., 2010, "Band structure, density of states and superconductivity of adsorbed titanium chains on (8, 8) and (14, 0) carbon nanotubes," Mater. Phys. Mech., **10**, pp. 72–81.

[64] Maiti, A., Hoekstra, J., Andzelm, J., Govind, N., Ricca, A., Svizhenko, A., Mehrez, H., and Anantram, M. P., 2005, "Electronic transport through carbon nanotubes - effect of contacts, topological defects, dopants and chemisorbed impurities," Lawrence Livermore Natl. Lab. Number UCRL-CONF-209763.

[65] Fan, W., and Zhang, R., 2008, "Structural and electronic properties of single-walled carbon nanotubes adsorbed with 1-pyrenebutanoic acid, succinimidyl ester," Sci. China Ser. B Chem., **51**(12), pp. 1203–1210.

[66] Willats, W. G. T., "Phage display: practicalities and prospects," Plant Mol. Biol., **50**(6), pp. 837–854.

[67] Gan, S. D., and Patel, K. R., 2013, "Enzyme Immunoassay and Enzyme-Linked Immunosorbent Assay," J. Invest. Dermatol., **133**(9), pp. 1–3.

[68] "Avidin-Biotin Interaction" [Online]. Available: https://www.thermofisher.com/us/en/home/life-science/protein-biology/protein-biology-learning-center/protein-biology-resource-library/pierce-protein-methods/avidin-biotin-interaction.html. [Accessed: 07-Sep-2016].

[69] Bloch, F., "Über die Quantenmechanik der Elektronen in Kristallgittern," Z. Für Phys., **52**(7–8), pp. 555–600.

[70] Frauenheim, T., Seifert, G., Elsterner, M., Hajnal, Z., Jungnickel, G., Porezag, D., Suhai, S., and Scholz, R., 2000, "A Self-Consistent Charge Density-Functional Based Tight-Binding Method for Predictive Materials Simulations in Physics, Chemistry and Biology," Phys. Status Solidi B, **217**(1), pp. 41–62.

[71] Seifert, G., Eschrig, H., and Bieger, W., 1986, "An approximation variant of LCAO-X-alpha methods," Z. Phys. Chem.-Leipz., **267**(3), pp. 529–539.

[72] Porezag, D., Frauenheim, T., Köhler, T., Seifert, G., and Kaschner, R., 1995, "Construction of tight-binding-like potentials on the basis of density-functional theory: Application to carbon," Phys. Rev. B, **51**(19), pp. 12947–12957.

Chapter 2 . Literature Review

This chapter presents the different methods of carbon nanotube production and their application in the sensor field. This chapter also describes the functionalization of synthesized CNTs to make them selective to specific bio-chem analytes. The research on CNTs has shown that their physical conformation and electrical properties allow them to be used as the core element of chemical sensors. Additionally, the use of phage display libraries to identify chemically specific molecules for developing selective biosensors based on CNTs, is also presented. Finally, the modeling of the electrical properties of CNTs through density function tight-binding (DFTB) theory is described in this chapter.

2.1 Carbon Nanotube Morphology

Carbon nanotubes are allotropic structures of carbon that were initially discovered by Iijima during the d.c. arc-discharge of a carbon electrode [1]. Using high resolution electron microscopy, Iijima was able to image these nano structures as seen in Figure 2-1.
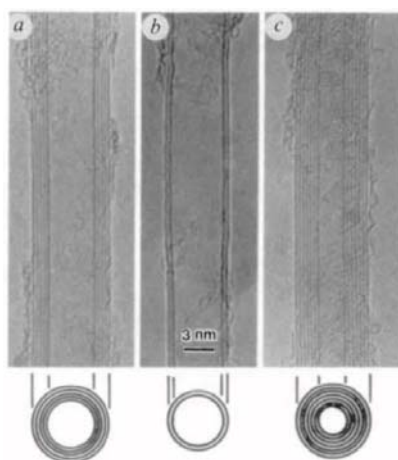
Figure 2-1: High resolution electron images of MWCNTs consisting of 5 (a), 2 (b), and 7 (c) sheets of graphene [1].

From the work performed by Iijima, the spacing between walls in the carbon nanotubes was shown to be about 0.34 nm, a distance similar to the spacing observed between graphene sheets in graphite. The number of sheets observed in the tubes were between 2 and 50, with closed ended tips rather than open. Using CNT images in conjunction with electron diffraction patterns, he conjectured that multi wall carbon nanotube (MWCNT) structures are composed of concentric tubes of graphene rather than a single sheet wrapped continuously around itself. Further work, also carried out by Iijima in the arc-discharge production of CNTs, resulted in the discovery of single walled carbon nanotubes (SWNCTs) [2]. Iijima observed that SWCNTs were constructed of only one rolled sheet of graphene, with diameters smaller than those shown by their MWCNT counterparts. This work formed the basis for the understanding of CNTs.

2.1.1 Nanotube Structure

The atomic structure of CNTs can be described by a chirality vector in the form of equation 2.1 [1–5].

$$\overrightarrow{C_h} = n\overrightarrow{a_1} + m\overrightarrow{a_2} \tag{2-1}$$

This vector describes the way in which a sheet of graphene is wrapped to form a CNT. The $\overrightarrow{a_1}$ and $\overrightarrow{a_2}$ are the lattice vectors and n and m are integers. A schematic representation of the chiral vector is shown in Figure 2-2.
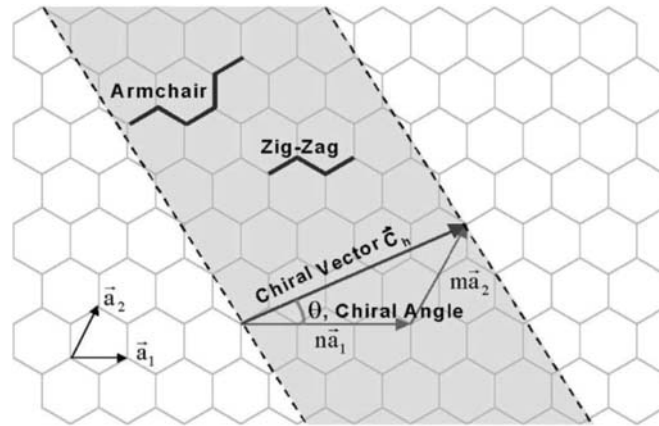
Figure 2-2: Schematic chiral vector schematically imposed on a graphene sheet. This vector determines the conformation of the tube [5].

The combination of the n and m indices describe the conformation of CNTs [6]. In the (n,0) form, a CNT is described by a zigzag structure. In contrast, when n=m, the structure is described as armchair. The third and final chiral structure is described by the (n,m) indice not meeting the specifications of the previously described zigzag and armchair structures. A schematic of these structures is presented in Figure 2-3.
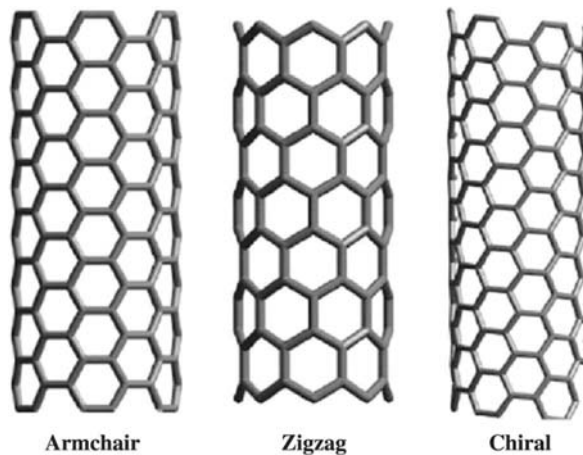
Figure 2-3 : Schematic representation of the Armchair, zigzag, and chiral CNT conformations [6].

2.2 Carbon Nanotube Synthesis

The synthesis of carbon nanotubes can be carried out through different processes such as: arc discharge technology, laser vaporization, chemical vapor deposition (CVD), and plasma enhanced chemical vapor deposition (PECVD) [2,7–9]. The research on these technologies has concentrated on studying the effect of the growth mechanisms of CNTs [7,8].

2.2.1 Arc Discharge Synthesis

In the arc discharge synthesis of CNTs, two electrodes are suspended in a sealed chamber [2]. One electrode is a graphite rod while the other is a carbon rod with iron held at the tip. The chamber is flushed with argon and a carbon source gas (methane was the first carbon source used by Iijima) [2]. Subsequently, a direct current (D.C.) is passed between the electrodes, causing the iron to vaporize and act as a catalyst for the CNT growth (Figure 2-4).
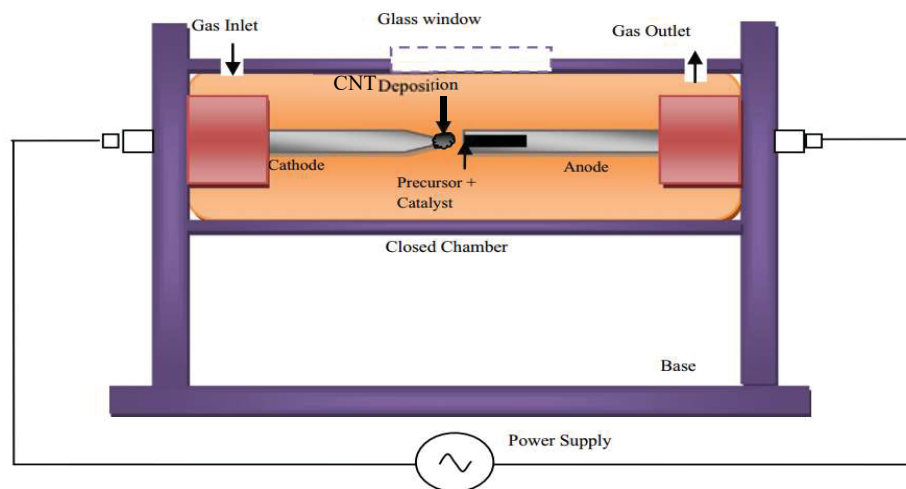
Figure 2-4: Schematic of arc discharge process showing the electrodes, gas flow inlet and outlet, and the deposition area of the CNTs [10].

With the discovery of CNTs in the soot of the arc discharge of graphite, research began to delve into the analysis of the synthesis process and products formed [2,11,12]. Though single wall carbon nanotubes were not observed in the first discovery of CNTs by Iijima in 1991, they were eventually observed via transmission electron microscopy (TEM) in the arc discharge soot [2]. The first micrographs taken of SWCNTs by Iijima are presented in Figure 2-5.
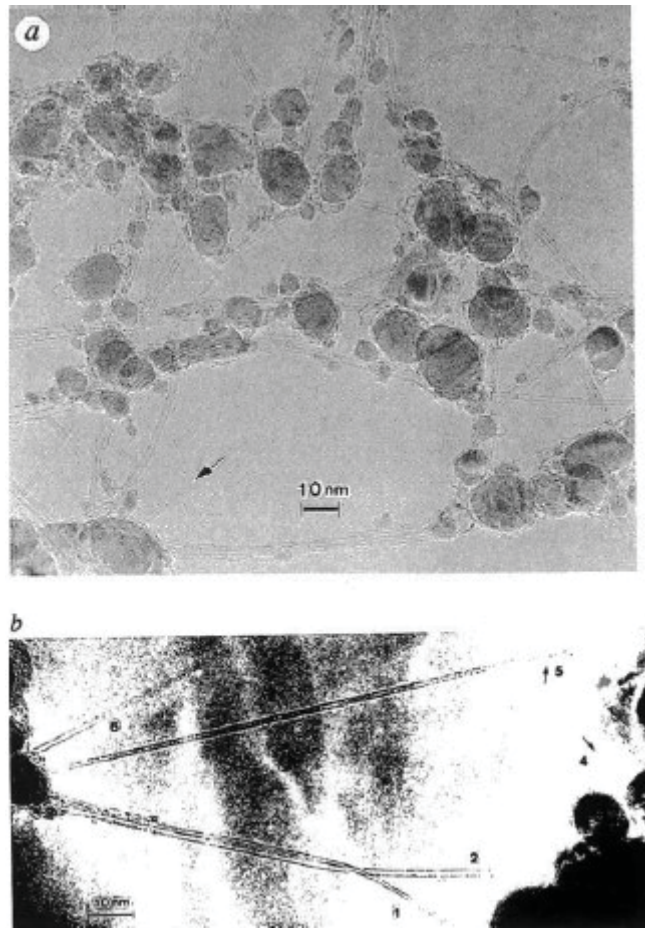
Figure 2-5: TEM micrographs of single wall carbon nanotubes (SWCNTs) entangled with iron nanoparticle catalysts (a), and isolated SWCNTs (b) [2].

Further research performed by Ando and Iijima addressed the effects of growth parameters on the CNTs produced [11]. It was shown that running the arc discharge

experiment under argon lowered the amount of fullerenes (polyhedral graphite particles) produced, but did not affect the amount of CNTs produced. It was also reported that the use of methane resulted in a soot primarily consisting of CNTs with little fullerene content. Finally, it was shown that the introduction of additional hydrogen gas resulted in a cleaner product [12]. This was because the presence of additional hydrogen reduced the amount of carbon smoke in the chamber. This carbon smoke was shown to inhibit the production of CNTs since it deposits onto the electrodes and blocks the growth surface.

2.2.2 Laser Vaporization Synthesis

To study how CNTs grow, laser vaporization growth methods have also been studied [7]. This method allows for better control of the experimental variables than the d.c. arc-discharge technique. In the laser vaporization process, a graphite target is positioned in a tube, placed under vacuum, raised to an elevated temperature, and flushed with argon to remove air. A 532 nm laser is then focused on the target to vaporize the carbon. This vapor is carried by the argon and condensed on a cooled copper rod, forming CNT soot. Samples produced through different operating conditions under the laser vaporization process have been studied using transmission electron microscope (TEM) [7].

One of the first variables studied in the synthesis process of CNTs was the synthesis temperature in the range of 200 ˚C to 1200 ˚C. As the operating temperature decreased, it was shown that the amount of defects in the CNTs increased. No tubes were produced once reaching 200 ˚C. Samples studied in this range, contained no SWCNTs, but rather small spherical carbonaceous structures. This lack of single wall tubes is explained by the fact that once the tube growth is initiated, the single walled tubes anneal almost immediately and close up. This suggests that the multiple walls in a MWCNT must keep the tube end

open during the growth. This has been explained to be due to possible bridges forming between the multiple layers [7]. These bridges would stabilize the open end, which would allow for growth before closing. This mechanism allowed the Smalley research team at Rice University to propose potential reaction pathways for the creation of fullerenes. A schematic figure of the proposed mechanism is shown in Figure 2-6.
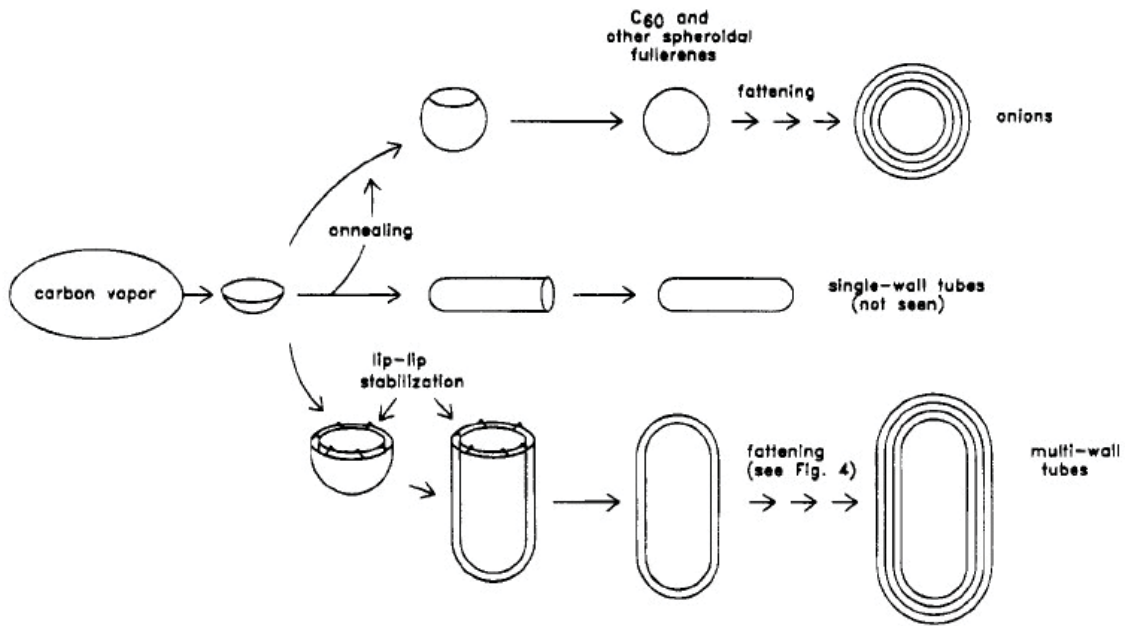
Figure 2-6: Possible CNT growth in laser vaporization, including the immediate closing of the fullerene to form a spherical particle, the production of SWCNTs, and the growth of MWCNTs stabilized by bridges formed between layers [7].

Due to the lack of stability of growing SWCNTs, researchers have investigated the addition of catalysts that could, like the carbon bridges in MWCNTs, support the walls during their growth [13]. Instead of using a pure graphite target, metal-graphite targets have been considered. To create the metal-graphite target, various metals were mixed with

graphite powder, placed into a mold, baked, and then cured. Instead of obtaining MWCNT and spherical single wall particles, the growth of only SWCNTs was observed [13]. Most of the observed SWCNTs showed an alignment feature of bundles held together by Van der Waals forces, with samples containing little amorphous carbon contamination. Results from the growth mechanism study suggested that the metal particle dictates the diameter of the tube. The metal particle also acts as a stabilizer for the growth of SWCNT by keeping the tube end open while allowing carbon vapor to diffuse through and propagate growth.

2.2.3 Chemical Vapor Deposition (CVD)

Although laser vaporization yields a high degree of pure SWCNTs, this technique has limited use for scaling up to large quantities of production. Thus, an alternative synthesis known as chemical vapor deposition (CVD) has been widely studied [8,14–16]. The first step of the CVD process is the preparation of mixture of catalyst and support [15,16]. Supports are typically silica or alumina in either powder or plate form. The support/catalyst sample is loaded into a tube furnace, flushed by an inert gas and brought to elevated reaction temperature. Once the heating area reaches the reaction temperature, a carbon source gas is allowed to flow through the reactor for a predetermined amount of time. This carbon source gas is pyrolyzed in the reaction zone, producing carbon gas [14]. This carbon gas then results in the carbon nanotube growth upon the support/catalyst sample. Finally, inert gas is used to slowly cool the tube down to room temperature.

Studies based on the amount catalyst used during the CVD process has shown that by increasing the catalyst, the average diameter of tubes increases [8]. These results suggest that the size of the CNT diameter is related to the size of catalyst particles used in the process. Thus, a very small catalyst particle will allow the growth of SWCNTs, while

31

increasing the particle size eventually results in MWCNTs [8]. These observations were backed up by reactive empirical bond-order potential calculations. TEM images of CNTs produced from a Fe:C catalyst have shown that catalyst particles are contained within the tip. These results also suggest that CNT growth follows a similar model as that of carbon filaments grown from the metal catalyst (immobilized in the support) [17]. The root and tip growth CNT models are visually represented below in Figure 2-7.
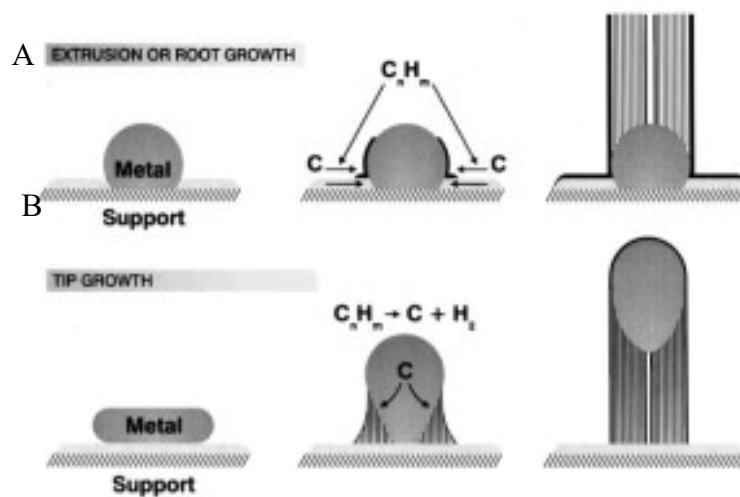
Figure 2-7: Schematic CNT growth model mechanisms: (A) Base growth, where the catalyst is immobilized on the support and the CNT emerges from the top of the catalyst; (B) Tip growth, where the catalyst has little interaction with the support surface and is instead pushed up off of the support surface as the CNT is deposited below [8].

Another study on the growth mechanisms of CNTs carried out by Brukh and Mitra [14], helped to uncover the role of carbon source flow rate, growth time, and catalyst in the CVD process. Tests were carried out at 700 °C while varying the growth times and flow rates. The tests showed that high flow rates, long gas residence times, and long run times

resulted in thicker amorphous carbon layers than those observed by using opposite conditions. These results suggested that CNT growth is limited by the amount of catalyst particle free surface. Without free catalyst, carbon deposits as an amorphous layer, because it is not being consumed by the CNT growth [14]. This data supports the growth model of CNTs shown in Figure 2-7, where carbon gas diffuses into the catalyst until saturation is reached and is then the carbon is deposited on the outer surface of the particle. This carbon deposit limits the carbon source from reaching the metal particle and thus limiting its growth. Complimentary kinetic studies have helped to support these growth conclusions [14].

Additional research has shown that the catalyst and the support play a significant role in the synthesis of CNTs. It has been demonstrated that a support/catalyst mixture with a more porous structure results in purer CNT production [15]. The fact that carbon source gas can more easily be present at metal catalyst sites in an open structure was thought to be an important variable. It was also shown that specific catalysts paired with different supports promote different CNT growth arrangements [15,16]. For example, iron catalyst with alumina support produced unbundled SWCNTs while iron on silica produced entangled SWCNTs.

Further work has investigated the direction and orientation of the CNT growth. As mentioned earlier, once amorphous carbon begins to deposit, the growth of CNTs terminates and only amorphous carbon continues to grow. Thus, a method employing the addition of water was investigated and developed [18]. Ethylene was used as the carbon source, and very small amounts of water were added to the inlet flow. The synthesis resulted in very tall forests of vertically aligned SWCNTs due to the constant removal of

amorphous carbon by the water. A 2.5 mm thick CNT growth layer produced from this process is shown in Figure 2-8. This growth used a water concentration of 175 ppm.
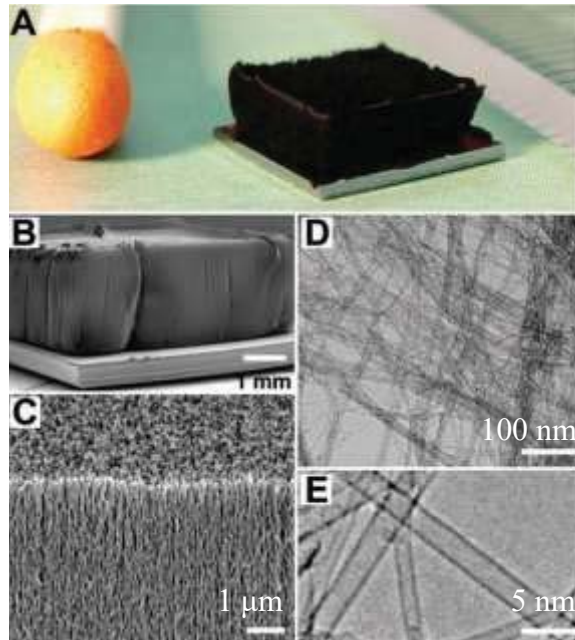
Figure 2-8: Optical and electron microscopy of CNTs: A) Low optical magnification image of SWCNT forest next to a match head as a size reference. B) and C) SEM images confirming vertical alignment. D) and E) TEM images confirming single wall nature [18].

Similar studies have led to CVD conditions that produced vertically aligned SWCNT "forests" without the use of an etchant, such as water [19]. For instance, Kong *et al.* [16] used an iron/alumina layer as catalyst/support, with acetylene as the carbon source. With precise tuning of the acetylene flow ratios to hydrogen, only enough carbon was present to propagate the CNT growth (without the production of amorphous carbon). Modification of the acetylene/hydrogen flow ratio also resulted in changing the type of

CNT produced (SWCNT or MWCNT) with higher ratios of acetylene contributing to the growth of MWCNTs.

Taking a step even further, CVD methods are capable of creating arrays of vertically aligned CNTs. For instance, being able to grow in prescribed formats allows for the creation of electronic devices without the need for special processing of CNT bundles [18,20]. Two methods of patterning have been successful in creating CNT arrays. These methods are lithography and iron evaporation utilizing a masking procedure [18,20]. SEM images of these arrays are shown in Figure 2-9.
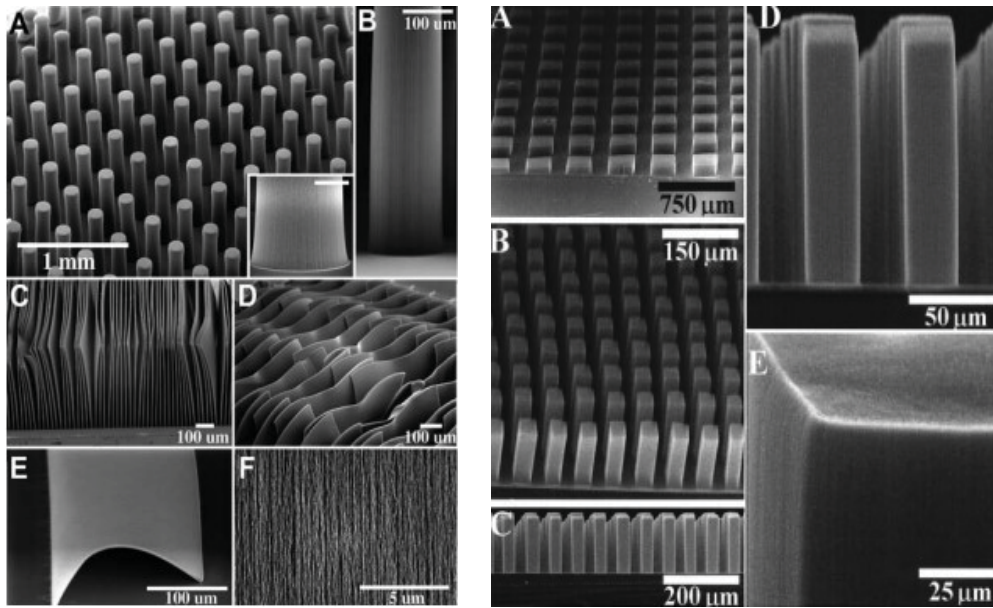
Figure 2-9: SEM pictures of different CNT arrays. Left: CNT forest arrays from lithography patterns: (A-B) cylindrical pillars, (C) sheets of CNT forests in a row, (D) offset sheets, (E) singular collapsed sheet, and (F) verifications of CNT alignment [18]. Right: CNT arrays from evaporation mask technique: (A) Array from 250 μm by 250 μm catalyst pattern, (B) Array from 38 μm by 38 μm catalyst pattern (C-E) different views of the columns shown in (B) [20].

Patterning of catalysts has also led to the production of electrodes that contain only a few, to potentially only one SWCNT strand [21]. This was accomplished using electron beam lithography to pattern islands of catalyst on silicon. The thickness of the deposited islands helps to prohibit vertical growth. Thus, growth of CNTs is only from the sides of the catalyst. In this kind of growth, the SWCNTs create bridges between the islands, a feature that can be seen in Figure 2-10.
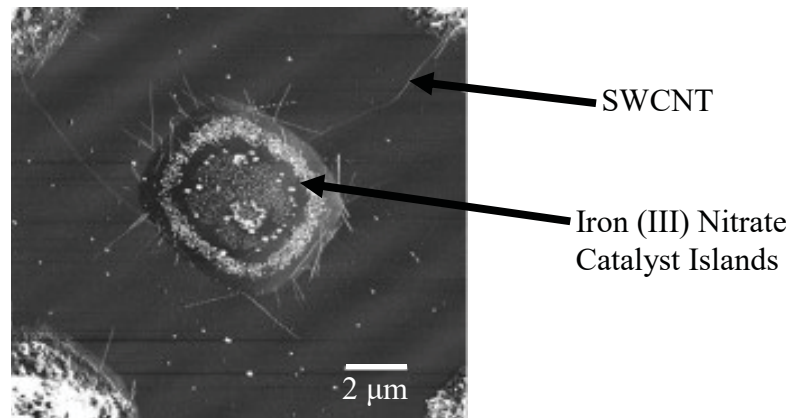
Figure 2-10: Catalyst islands with connecting SWCNTs viewed by tapping mode AFM. Tubes growth is constrained to only the side of the islands [21].

Due to the connection of catalyst islands with CNTs, this research realized the possibility of as grown CNT circuits. One critique of this technique is that Kong *et al.* did not mention the number of islands that have connecting CNTs [21]. As it is evident in Figure 2-10, the process makes sure that CNT growth is in the direction of other islands, but anchoring between islands could still be present, a large drawback if the number of connected islands is low.

2.2.4 Plasma Enhanced Chemical Vapor Deposition (PECVD)

Another CNT production method is the enhancement of CVD through the introduction of plasma [9]. In PECVD, a support with catalyst is loaded into a chamber. The chamber is then placed in a vacuum, and a mixture of nitrogen and hydrogen is allowed to flow into the chamber. The chamber temperature is then raised to 750 °C and the sample is allowed to rest at that temperature for a specified time. Once annealing is complete, ammonia gas, or other etchant, is injected into the chamber. Next, the plasma is started via DC discharge between two electrodes and the carbon source gas is introduced. Finally, when the growth time has been reached, the plasma is turned off and the chamber is allowed to cool to room temperature [9].

Many of the results from PECVD are similar to that of CVD. An overly thick catalyst layer results in no growth unless a significantly longer etchant time is used. Growth from these thick layers of catalyst only grow at the edges. Also, the catalyst particle size dictates the diameter of the CNT, and the growth mechanism follows one of the two aforementioned models (base and tip growth-see Figure 2-7). Unlike CVD where vertical alignment is closely related to the support material and flow rates used, in PECVD, alignment is imposed by the electrical field generated by the plasma.

The CNTs grown through PECVD have been shown to produce multiple walled tubes in nature [9]. This is because growth is not carried out above 900 ˚C. At 900 ˚C, the tubes produced are shown to be increasing in disorder and lacking in alignment. Chhowalla *et al.* [9] conjecture that this is due to high levels of ionization caused by the plasma. Here, high amounts of ion damage may result in the destruction of the aligned motif. Based on this suggestion, it will be difficult to use this technique to produce aligned SWCNT "forests."

In fact, the "forests" produced were not as dense as those produced by CVD. The PECVD alignment is shown in Figure 2-11, where there is a noticeable space between CNTs as compared to the CNT layers grown via CVD (see Figure 2-9). This may be highly unfavorable in certain applications where a denser CNT forest is desirable.
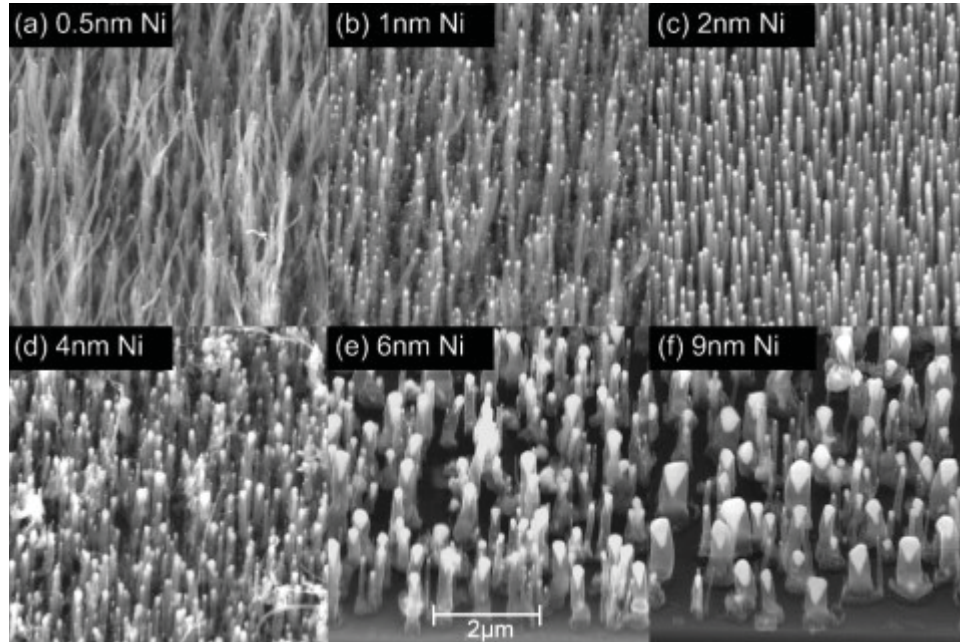
Figure 2-11: CNT forests grown from varying Nickel catalyst layer thicknesses in a PECVD process at -600 V for 15 minutes. Thicker catalyst layers produce thicker columns with less alignment [9].

2.3 Functionalization

Functionalization of carbon nanotubes is described as a modification of a carbon nanotube either chemically or physically [22]. The five types of carbon nanotube functionalization are: 1) defect-group, 2) covalent sidewall, 3) noncovalent exohedral with

surfactants, 4) noncovalent exohedral with polymers, and 5) endohedral. Visualizations of each functionalization type are presented in Figure 2-12.
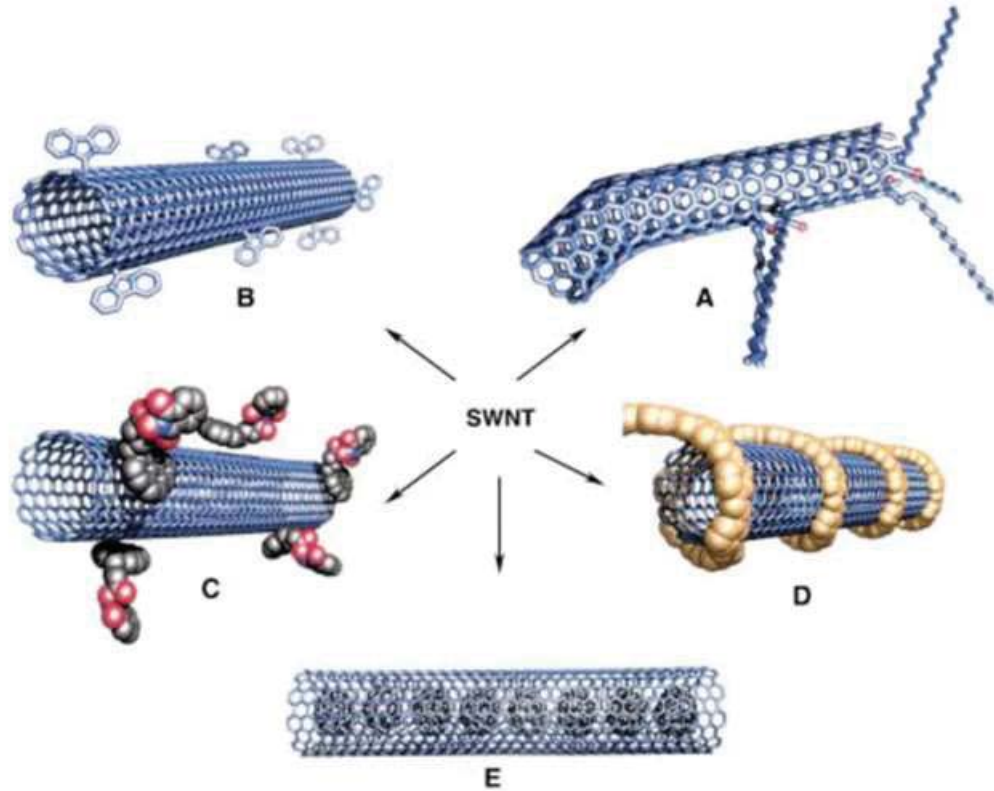
Figure 2-12: Schematic representation of different types of carbon nanotube functionalization: A) defect-group, B) covalent sidewall, C) noncovalent exohedral with surfactants, D) noncovalent exohedral with polymers and E) endohedral [22].

2.3.1 Defect-Group

There are many types of defects that can occur in a carbon nanotube during the purification process [23]. It has been shown that exposure to acids and some organic solvents can cause vacancies and surface topology irregularities [24,25]. For example, nanotube purification using a nitric acid/sulfuric acid mix can create significant openings

in the nanotube walls [24]. High resolution transmission electron microscopy evidence of these openings are presented in Figure 2-13.
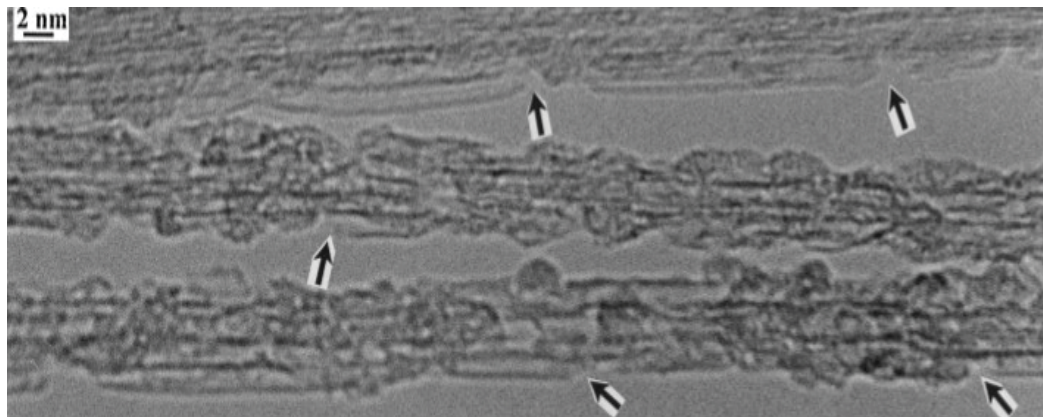
Figure 2-13: High resolution transmission electron microscope image of carbon nanotube wall defects (shown by the arrows) after acid treatment [25].

Similar defects have also been formed by exposure of carbon nanotubes to dimethylformamide (DMF) [25]. Indeed, the presence of these defects will affect the electronic nature of carbon nanotubes. To counteract the presence of defects on CNTs, some recovery and closing of the vacancies can be induced by the addition of an annealing step after purification. Also, the use of a more dilute acid treatment minimizes defect formations.

Another effect of the purification process via acid treatment is the formation of carboxyl groups as physical defects [22,26–28]. This can occur at two different locations. One location is at the edge of the nanotube walls [26]. At these edges, the acid mixture opens the tube wall. The carbon is oxidized and forms carboxyl groups attached to the defect edge. The other location where carboxyl groups can form is at the tube ends [28]. In the same manner as the formation of holes on the tube surface, the acid mixture opens up

the ends of the tubes where oxidation occurs [29]. The mechanism of oxidation is presented in Figure 2-14.
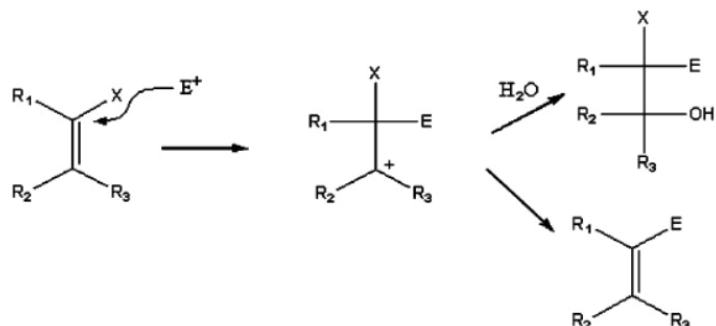
Figure 2-14: Oxidation mechanism of carbon nanotubes through the attack of the double bonds present on the CNT surface to create hydroxyl groups [29].

As shown in Figure 2-14, the electrophile (commonly a nitronium ion) attacks the double bond and breaks it. Next, water reacts with the intermediate to form a hydroxyl group. This hydroxyl is further oxidized to a carboxyl functional group. The first step of this oxidation is the dehydration of the alcohol and formation of an alkene. Next the alkene forms a ketone in which the hydrogen atom is replaced with a hydroxyl group.

2.3.2 Covalent Functionalization

Formation of carboxyl groups on the tubes opens up many different routes for covalent functionalization. One route of functionalization is the reaction of the carboxyl groups on the CNT surface with amine functional groups. This has been demonstrated by the attachment of hemoglobin to carboxylated CNTs via 1-Ethyl-3-(3-dimethylaminopropyl)carbodiimide (EDC) [30]. Tracking the hemoglobin by UV-vis and TEM, it was shown that although hemoglobin passively binds to CNTs, the addition of

EDC significantly increases the binding. The difference between the passive and covalent binding of the hemoglobin to the CNTs is exhibited in Figure 2-15.
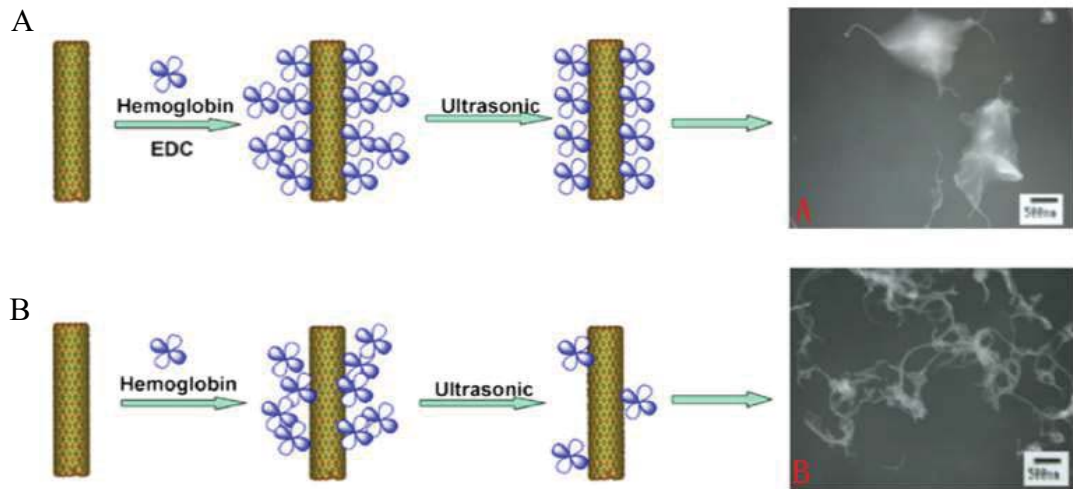
Figure 2-15: Schematic diagram and TEM images of hemoglobin attached onto CNTS with (A) and without (B) the assistance of 1-Ethyl-3-(3-dimethylaminopropyl) carbodiimide (EDC) [30].

As seen in Figure 2-15, the use of EDC causes the hemoglobin to bind in a much higher ratio and in a more ordered fashion than binding without EDC. This is due to the carboxyl groups exhibited on the surface of the oxidized CNTs reacting with the N-terminus valine residue of the hemoglobin. This reaction occurs via the mechanism presented in Figure 2-16.
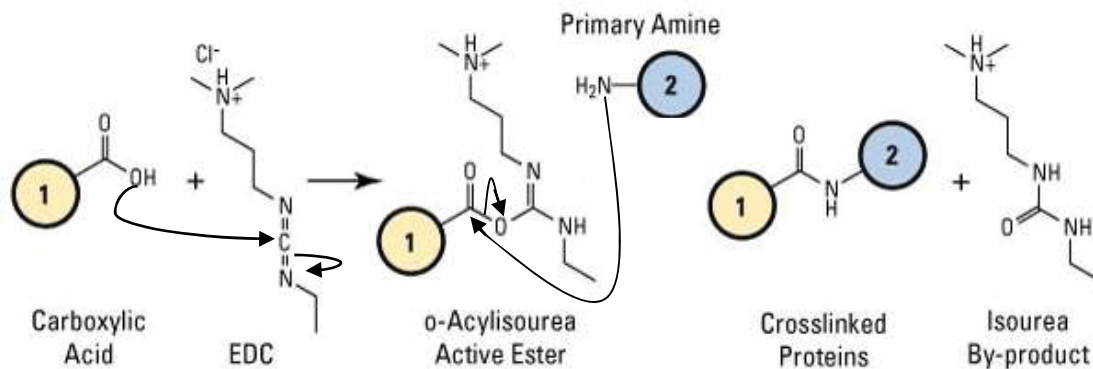
Figure 2-16: Binding mechanism between carboxyl and amine groups by employing EDC [31]. Here, the EDC initially binds to the carboxylic acid forming an active ester. This complex reacts with a primary amine giving up an isourea by-product.

As seen in Figure 2-16, a direct link is formed between the carboxyl and amine groups with EDC as the intermediate reactant. An interesting property exhibited by the hemoglobin functionalized CNTs was that they could electronically sense peroxide [30]. Thus, covalent functionalization of CNTs could have viable applications in the sensor field.

Another option for the functionalization of carbon nanotubes includes fluorination [32–35]. To produce a fluorine sidewall functionalization group, the procedure used is similar to that first discovered as the method to fluorinate graphite [36]. In this procedure, carbon nanotubes are treated with a fluorine/helium mixture at elevated temperatures. This process was found to be reversible by treatment with hydrazine. Further studies on the fluorine functionalized CNTs has resulted in the inclusion of hydrofluoric acid as a catalyst which yields stronger carbon-fluorine bonds and the ability to functionalize at lower temperatures [34]. The ability to add fluorine groups to CNTs has resulted in many different subsequent subreactions to create new types of functionalized CNTs.

The reaction of fluorinated SWCNTs with terminal alkylidene diamines and a pyradine catalyst have also been shown to create amino functionalized CNTs [33]. This type of functionalization allows the SWCNTs to crosslink between tubes making them soluble in water and dilute acids. The fluorine groups also allow the reaction of CNTs with nucleophiles [37,38]. It has been reported that a pretreatment of fluorinated SWCNTs with alkyl magnesium bromide, followed by a reaction with Grignard reagents also produced alkane functionalized SWCNTs [37]. Similarly, the addition of alkanes was achieved by sonicating fluorinated SWCNTs in hexyllithium. This granted the property of solubility in organic solvents. Another research group has sonicated fluorinated SWCNTs in the presence of sodium methoxide [38]. This approach created SWCNTs with side-wall methoxy groups. A schematic diagram showing the different functional groups formed by sub-reaction with fluorine functionalized SWCNTs is presented in Figure 2-17.
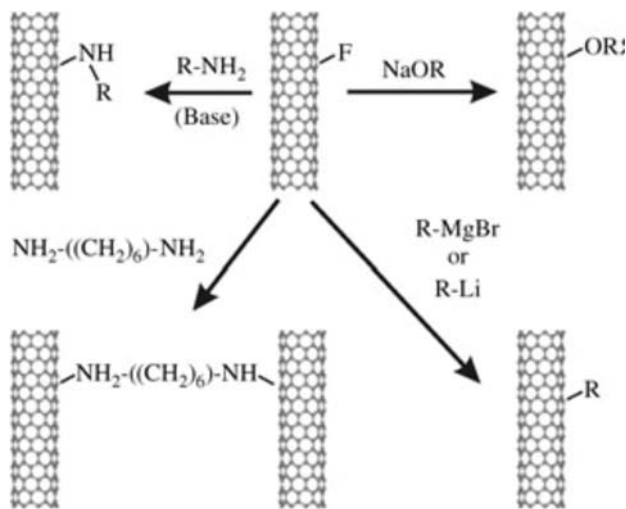
Figure 2-17: Schematic diagram of the formation of possible sidewall functionalization groups by reaction with fluorinated SWCNTs [27].

In addition to oxidation and fluorination, many other routes for functionalization have also been identified [32,39–43]. A general schematic representation of different functionalization pathways is offered in Figure 2-18.
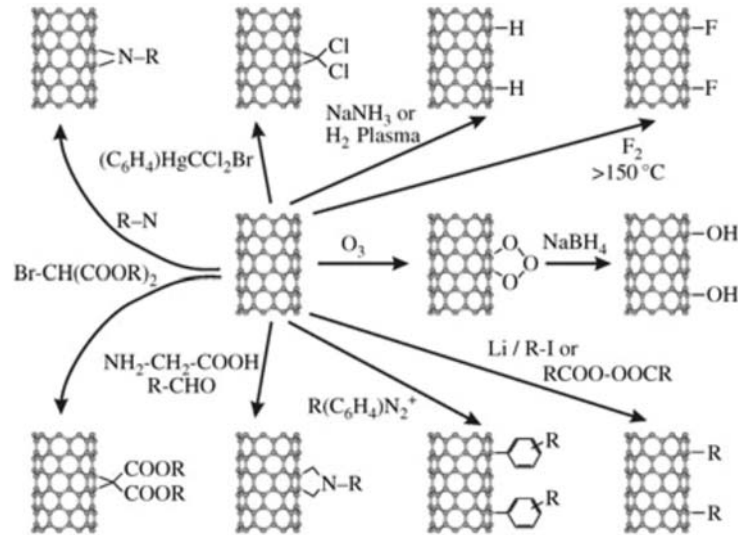
Figure 2-18: Schematic illustration of the different possible covalent sidewall functionalization paths on CNTs [27].

These types of direct modification on the SWCNT surface may prove to be advantageous over other functionalization routes. The attachment of a functional group by reaction of a carboxyl group with an amino group or other direct surface modification routes create a stable and strong bond [27]. Direct functionalization of the SWCNT surface also has a large effect on their electrical properties. The sites of the SWCNT that receive the direct functionalization usually have higher tube curvature, and are therefore more chemically reactive. [32].

2.3.3 Noncovalent

Carbon nanotube functionalization can also be achieved through noncovalent process. The two types of noncovalent functionalization include exohedral and endohedral [22]. Exohedral functionalization is the wrapping of SWCNTs with a polymer or a noncovalent aggregation of a constituent on the exterior surface. Conversely, endohedral functionalization is when molecules of a functional component are contained within the inner cavity of the tube. Exohedral functionalization takes advantage of the propensity of SWNTs to interact with molecules by means of π-π stacking interactions [44–50]. Noncovalent functionalization by π-π interaction has been shown to occur between SWCNTs and aromatic structures [44–46]. Chen *et al.* [44] showed that succinimidyl esters noncovalently attached to the surface of a SWCNT will react with the amine groups present on proteins, such as ferritin and streptavidin, by nucleophilic substitution. Indeed, due to the π-π interaction, the electronic properties of the SWCNT are significantly altered [45]

An example of a polymer that can be used to wrap CNTs is poly(ethylene glycol) (PEG) [47]. Normally a protein called streptavidin will nonspecifically bind to SWCNTs. It was shown that by wrapping SWCNTs in PEG, streptavidin was blocked from binding to the SWCNTs. TEM images showing the differences between the interaction of streptavidin and SWCNTs with and without PEG are shown in Figure 2-19.
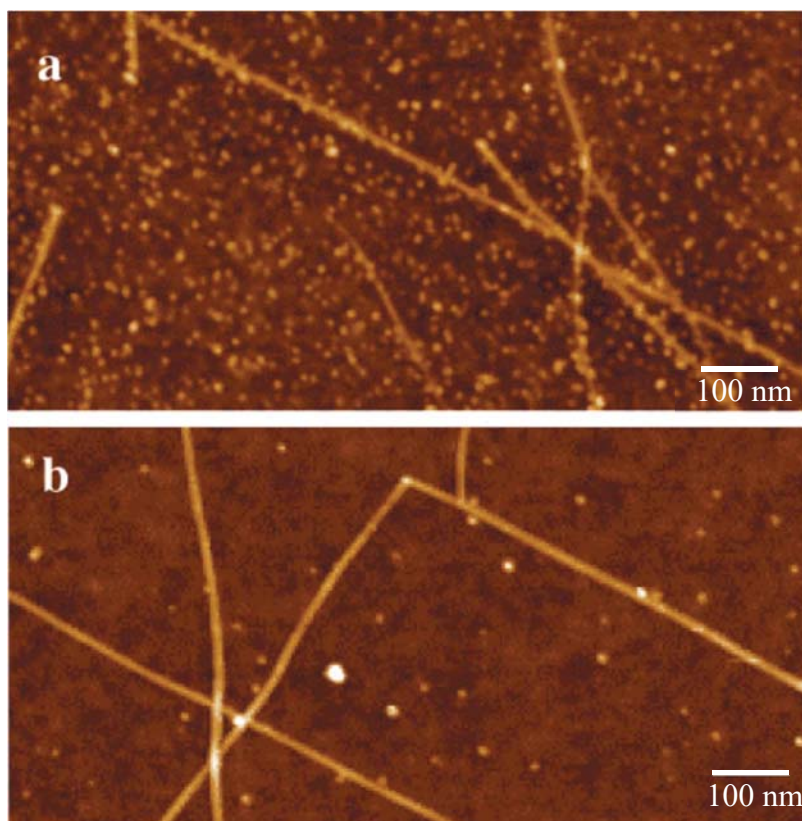
Figure 2-19: AFM pictures of a) As grown SWCNTs with adsorbed streptavidin, and b) PEG wrapped SWCNTs. The picture shows a resistance to streptavidin adsorption due to the blocking provided by the wrapping PEG [47].

As shown in Figure 2-19, polymer wrapping of SWCNTs can be used as a barrier to specific types of molecules. Conversely, Shim *et al.* [47] showed that polymer wrapping can also be used to impart selective binding capabilities.

An additional function of noncovalent polymer wrapping is to preserve the mechanical and electronics characteristics of SWCNTs while still allowing their functionalization [48]. As previously shown, many different covalent binding schemes use oxidative procedures to create vacancies and open segments in the SWCNT surface. This will change the structural and electrical properties of the tubes. Carrillo *et al.* [48] have shown that hydrolyzed-poly(styrene-alt-maleic anhydride) (h-PSMA) can be used to wrap

SWCNTs. An interesting property of h-PSMA is that it contains free carboxyl groups. Thus, by wrapping SWCNTs with h-PSMA, free carboxyl groups can be incorporated noncovalently without introducing defects on the tubes. As described before, this allows for subsequent functionalization with other molecules.

Additional work has also been carried out investigating the many endohedral reactions and functionalization of SWCNTs [51–58]. Han *et al.* [51] showed that gallium nitride nanorods can be produced inside the MWCNTs. Other nanowires such as gold, silver, platinum, palladium, nickel, and nickel oxide have been discovered within the interior of carbon nanotubes after different chemical vapor deposition processes [53,54]. A TEM micrograph of nickel nanowires and other nickel morphologies within CNTs is shown in Figure 2-20.
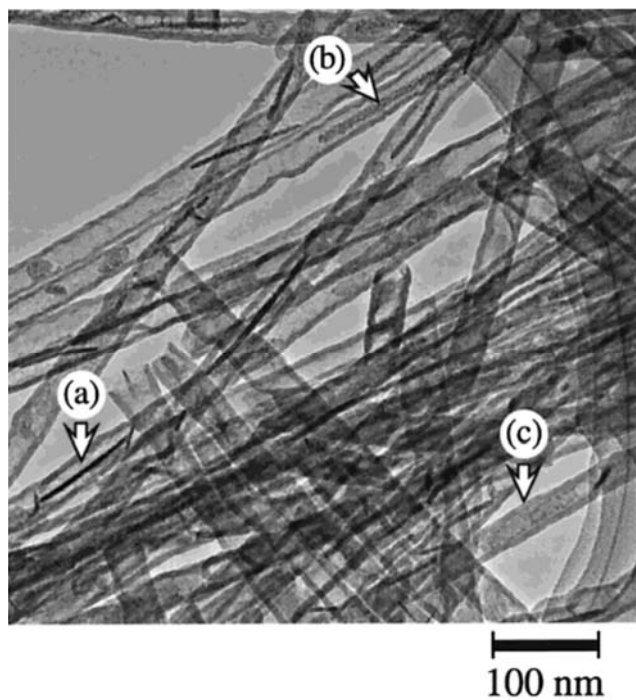
Figure 2-20: TEM micrograph of Nickel nanowires a) and b) and plates c) contained within carbon nanotubes [54].

Carbon fullerenes have also been discovered in carbon nanotube cavities [55,57,58]. The fullerenes are formed after treating the CNTs with acid followed by an annealing process. Also, it has been discovered that salts can form inside tubes when immersed in a molten salt bath [56].

2.3.4 Biological

With the discovery of the presence of surface carboxyl groups on acid treated carbon nanotubes, functionalization with biological agents has been extensively investigated [30,59–63]. One of the most common methods of biological functionalization uses carbodiimide chemistry [59–61]. The carbodiimide approach to biological functionalization of CNTs is either carried out in a one or two-step process [59]. In a one-step process, carboxylated carbon nanotubes are reacted with either N-ethyl-N'-(3-dimethylaminopropyl) carbodiimide hydrochloride (EDAC) or 1-ethyl-3-(3-dimethylaminopropyl) carbodiimide (EDC) and a biological agent such as a protein or peptide in solution. The carbodiimide reacts with the carboxyl groups located on the CNT and forms an unstable intermediate. Next, the intermediate reacts with the amine groups found on the protein or peptide to form an amide linkage. This process is shown in Figure 2-21.
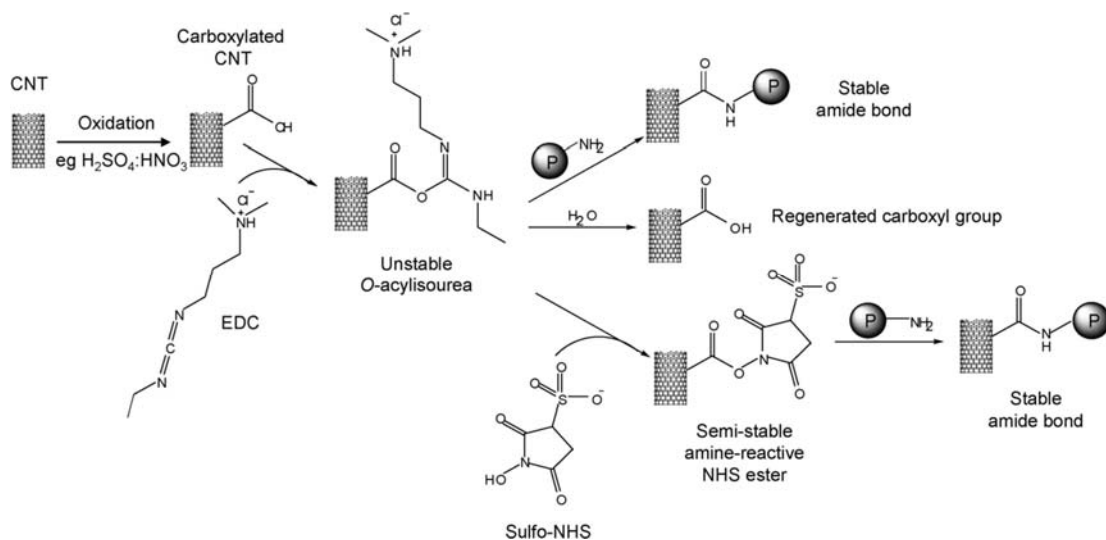
Figure 2-21: Protein functionalization of carboxylated carbon nanotubes through a one and two-step process using EDC [59].

One important aspect to note about the one step process is that the intermediate is very unstable. Because of this, it is common for hydrolysis to occur and reform the carboxyl group. This means that the amount of protein coupled to the CNT is typically low. To combat this issue, a two-step functionalization process has developed [60]. One way to reduce the effect of this instability could be the incorporation of an excess of available amine groups. This would allow the linking reaction to proceed before the O-acylisourea intermediate regenerates the carboxyl functional group.

The two-step process begins identically to the one-step process where the carbodiimide reacts with the carboxyl group and forms the unstable intermediate as shown in Figure 2-21. In lieu of allowing the O-acylisourea intermediate to directly react with the amine groups present on the protein, the two-step process utilizes either NHS (Nhydroxysuccinimide) or Sulfo-(NHS) to form an amine-reactive NHS ester [60]. This NHS ester is much more stable than the O-acylisourea alternative, since it does not easily

hydrolyze. Consequently, the level of protein attachment is significantly increased. Due to the strong amide bond that carodiimide chemistry induces with carboxyl groups, this process has been instituted with many different biological agents. Jiang *et al.* [60] functionalized MWCNTs with Ferritin and bovine serum albumin (BSA) proteins aided by NHS. The TEM micrograph is presented in Figure 2-22
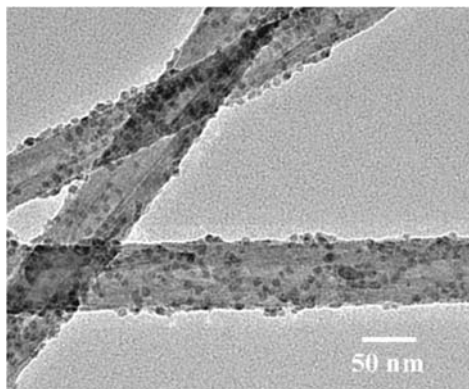
Figure 2-22: TEM image of ferritin functionalized MWCNTs via carbodiimide chemistry. The ferritin protein is the dot like structures covering the surface of the CNT[60].

As shown in Figure 2-22, the use of NHS results in highly efficient binding. In a similar manner, avidin [61] and hemoglobin [30] have also been shown to be attached to CNTs via carbodiimide chemistry. Further studies on hemoglobin functionalized CNTs indicated that they have the ability to detect hydrogen peroxide. These detection capabilities demonstrate that potential biosensor applications exist on functionalized CNTs through the carbodiimide chemistry.

Besides proteins, it has been shown that DNA [62] and antibodies [64] can be coupled to CNTs assisted by EDC. In fact, DNA has been coupled to CNTs by first using

carbodiimide to attach peptide nucleic acid (PNA) to the tubes via the N-terminus amine group. Then, DNA with a sequence complimentary to that of the PNA has been discovered to bind to the PNA functionalized tubes. This has resulted in the ability to tailor DNA functionalized tubes for medical targeting and sensing applications [63].

In addition to biological covalent functionalization, it is also possible to non-covalently attach biological species to CNTs [49,59,65–71]. The first noncovalent immobilization of proteins was carried out by Davis *et al.* in 1998 [66,67]. They showed that the proteins Zn_2Cd_5-metallothionein, cytochrome C, and β-lactamase readily adsorbed in the cavity and on the outer surface of nitric acid purified carbon nanotubes. Studies on non-covalent adsorption on CNTs have shown that some proteins attach in a helical manner [65,67,68]. A schematic representation and electron micrograph of noncovalent attachment are presented in Figure 2-23.
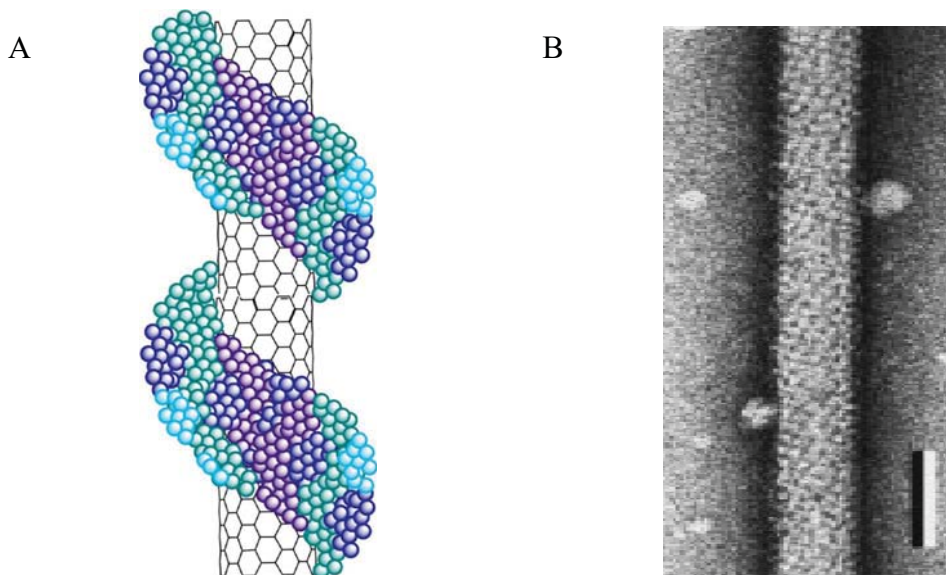
Figure 2-23: Non-covalent attachment of proteins on CNTs. A) Visualization of the helical arrangement of Amyloglucosidase on CNTs [65]; B) SEM image of Streptavidin absorbing in a helical manner onto a CNT (50 nm scale bar) [68].

An additional study on the adsorption of ferritin on CNTs, revealed that non-covalently attached proteins are strongly adhered to the tubes, and that CNTs generally have a strong affinity to protein adsorption [69,70]. Studies on hemoglobin attached to nitrogen doped CNTs, discovered that proteins adsorbed on the doped CNT surface express more bioactivity than those adsorbed onto an undoped CNT [71]. However, most studies have shown that one of the disadvantages of noncovalent immobilization is the bioactivity is significantly reduced after the adsorption [66].

2.4 Electrical Properties

SWCNTs have been shown to exhibit attractive electrical properties [72–75] . For instance, the n and m indices previously described in section 2.1.1 have been shown to determine whether a SWCNT is metallic or semiconducting [72,73,76,77]. In the zigzag structure, the tube will electronically act as a metal when n/3 is an integer. If n/3 is a non-integer, the tube will act as a semiconductor. Likewise, chiral tubes electronically act as a metal when (2n+m)/3 is an integer or act as a semiconductor otherwise. Conversely, armchair tubes are always metallic.

The classification of CNTs as either a metal, semiconductor, or insulator, is based on their band structure. Band structures are described by a valence band, conduction band, band gap, and fermi level [78]. The valence band is comprised of all completely occupied states while the conduction band is comprised of all unfilled electronic states. The band gap lies between the valence and the conduction bands. In this band gap, no electron states can exist, and finally, the fermi level describes the highest occupied state. A schematic

representation of the difference between the band structures of metals, semiconductors, and insulators classification is presented in Figure 2-24.
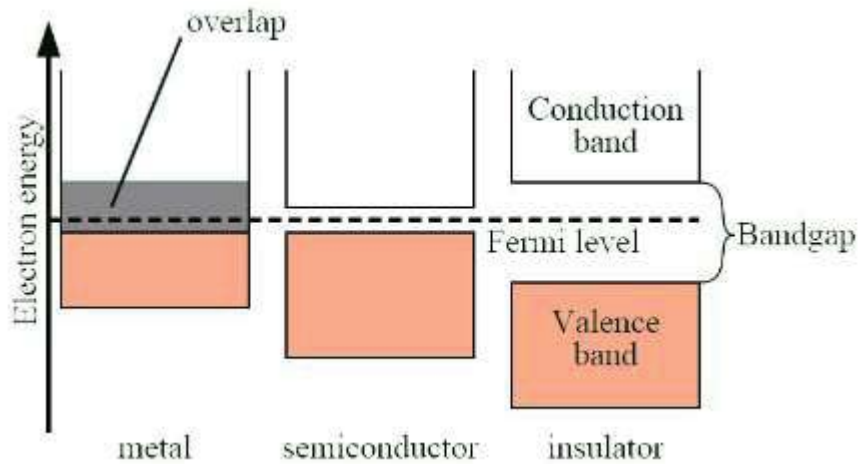
Figure 2-24: Schematic representation of the band gap relation between metals, semiconductors, and insulators [79].

As shown in Figure 2-24, metals contain no band gap which allows for easy transfer of electrons to states contained in the conduction band. Semiconductors are described by a moderate band gap usually below 3 eV [80]. This small band gap allows for electrons to be promoted to the conduction band given sufficient energy. On the other hand, insulators have a much larger band gap above 3 eV that inhibit the transfer of electrons to the conduction band.

2.4.1 Field Effect Transistors (FETs)

A field effect transistor is a device that uses an electric field to control the electrical conductivity of a channel [81]. The two different types of FETs are junction field effect transistors (JFET) and metal oxide semiconductor field effect transistor (MOSFET). SWCNT-FETs act most like MOSFETs; hence, the following section focuses mainly on

this type of FET structure. In a basic MOSFET, the majority of charge carriers are injected at the source, and exit via the drain. Charge carriers can either be electrons or holes. The channel, which is the carbon nanotube, connects the source to the drain. A schematic of a typical MOSFET can be seen in Figure 2-25. In the MOSFET, a gate is placed between the source and drain in a way that the applied electrical field will be perpendicular to the flow in the channel. This electrical field shapes the channel and modulates the amount of electrical current that flows through it.
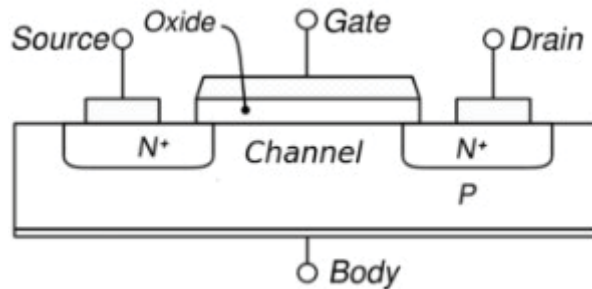
Figure 2-25: Typical MOSFET schematic displaying the orientation of the source, drain, gate, and channel [82].

As seen in Figure 2-25, a thin oxide layer acts as a capacitor that modulates the charge accumulation. One important aspect of MOSFETs is they only require a small amount of current to work, allowing the assembly of small scale devices. Also , they typically amplify signals, which allows for small outputs in magnitude to be monitored [83].

2.4.1 P-Type and N-Type SWCNTs

As described earlier, based on their chirality, SWCNTs can act as semiconductors, with profiles as either p-type or n-type [74,75]. In a p-type semiconductor, the primary charge carriers are holes due to electron vacancies [84]. In contrast, in an n-type semiconductor the main charge carriers are electrons due to an excess of electrons.

SWCNTs exposed to ambient conditions and connected between two contacts have been shown to exhibit p-type properties [75]. This was realized by the fabrication of a field-effect transistor (FET) with a platinum source and platinum drain being connected by one SWCNT [75]. The current-voltage (IV) profile of a SWCNT FET device is shown in Figure 2-26.
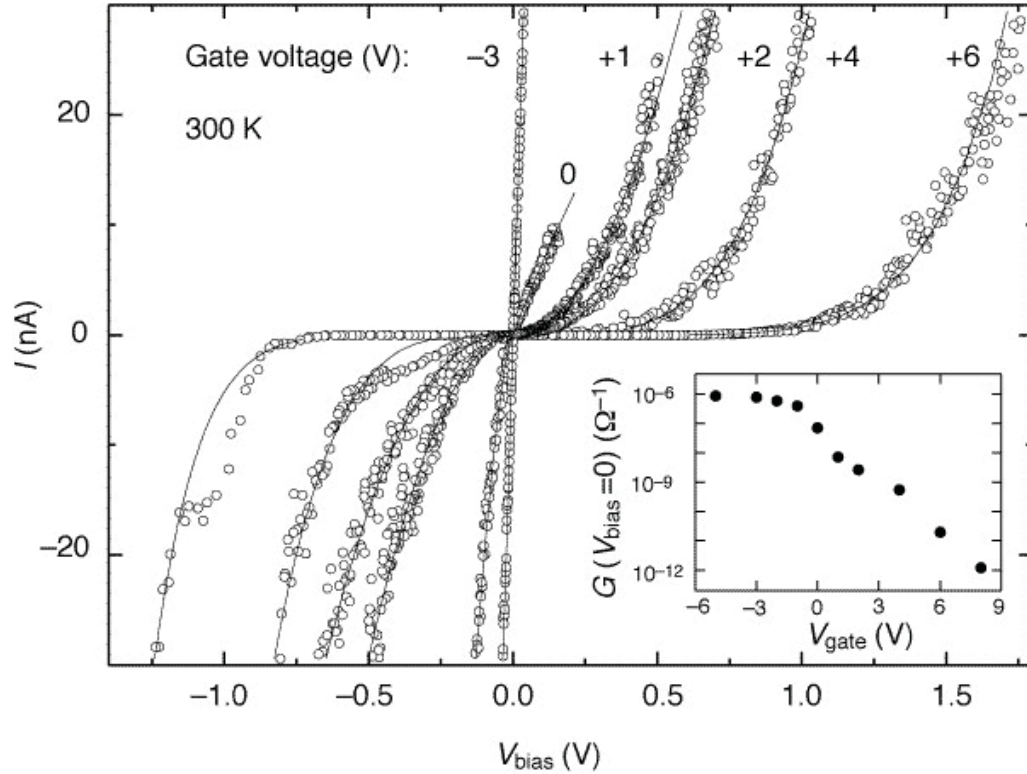
Figure 2-26: Electrical current versus bias voltage behavior of a SWCNT FET as a function of different gate voltages. Inset: Conductance of the device versus gate voltage [75].

Figure 2-26 illustrates the current versus bias voltage characteristics of the device at different gate voltages. Also, the p-type characteristic of the SWCNT is confirmed by the

conductance decreasing as the gate voltage is increased (inset of the figure). This is due to extra electrons being added and depleting the excess of holes in the system.

Further study into the use of SWCNTs as semiconductors revealed that although they exhibit p-type characteristics under ambient air conditions, SWCNTs are inherently n-type [74,85]. This was shown by fabricating a FET with a SWCNT that was annealed and kept away from the presence of oxygen. The switching of semiconductor type is shown in Figure 2-27.
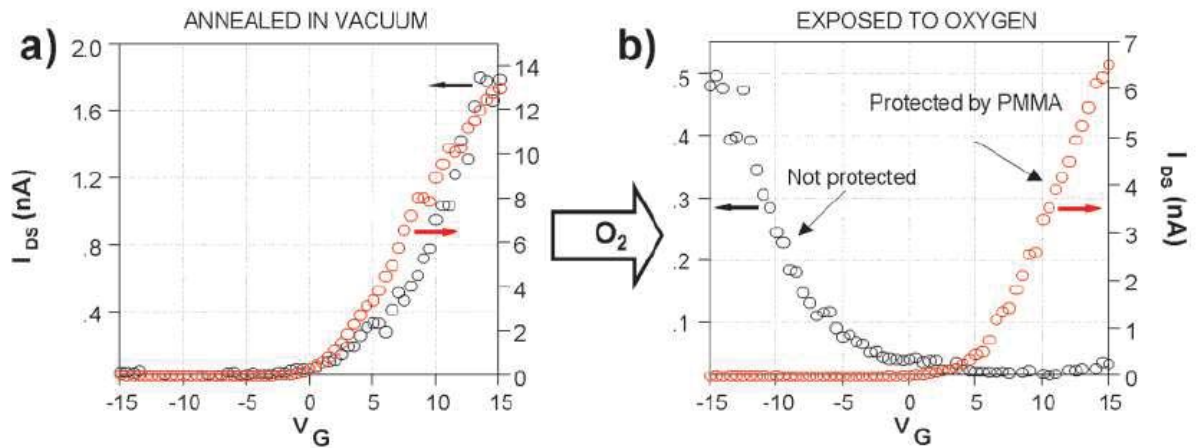
Figure 2-27:   Semiconducting profile of CNTs. A) Annealed unprotected SWCNT showing an n-type characteristic. B) CNTs exposed to oxygen showing the change to p-type [85].

In Figure 2-27, two SWCNT FETs were first annealed and shown to possess n-type characteristics [85]. A subsequent coating on one of the CNTs with Poly(methyl methacrylate) (PMMA) showed that the tube retained the n-type profile following oxygen exposures. In contrast, the uncoated tube showed a change to a p-type semiconducting profile after the exposure of oxygen. To understand how the oxygen interacts with the

SWCNT, doping trials were carried out by Deryck *et al.* [74], and showed that that the oxygen does not actually act as a dopant across the whole tube, but rather affects the band structure at the junction between the metal contacts and the semiconducting SWCNT. Using a Density Functional Theory (DFT) model, it was also suggested that the physical adsorption of oxygen to the SWCNT surface is fairly weak and would result in only a small charge transfer [86]. This implies that physisorption of oxygen onto the tube walls has little impact on the electrical nature of the SWCNT.

In addition to expressing purely p-type or n-type characteristics, it has also been shown that SWCNTs can express ambipolar properties [87,88]. An ambipolar device exhibits both n-type and p-type characteristics under different conditions [89]. This ambipolar effect was first realized after the fabrication of a device with titanium carbide contacts [87]. Here, the titanium contacts were created via optical lithography followed by a heat treatment to form titanium carbide. The ambipolarity of the SWCNT device is presented in Figure 2-28.
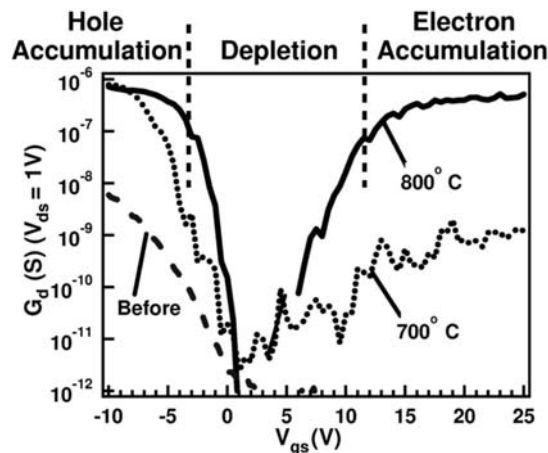
Figure 2-28:   SWCNT device operation showing the conversion of the device from a purely p-type profile to a device expressing ambipolar characteristics induced by annealing at different temperatures [87].

58

From Figure 2-28, it can be seen that the final device indicated by the solid black line presents three clear regimes which include the p-type (hole accumulation), depletion, and n-type regions (electron accumulation). Testing the device using titanium contacts (dashed line), the device expressed a purely p-type operation. Introduction of annealing at 700 °C converted the titanium contacts to titanium carbide [87]. The formation of the titanium carbide contacts resulted in the onset of ambipolar operation (dotted line). The ambipolarity characteristic of the device was elevated further by an annealing procedure carried out at 800 °C (solid line).

2.4.2   SWCNT Field Effect Transistors (FETs)

The first manufactured SWCNT-FETs were assembled based on a silicon back gate setup (see Figure 2-29), where the SWCNT connecting channel is shielded from the back gate by a silica oxide layer [90].
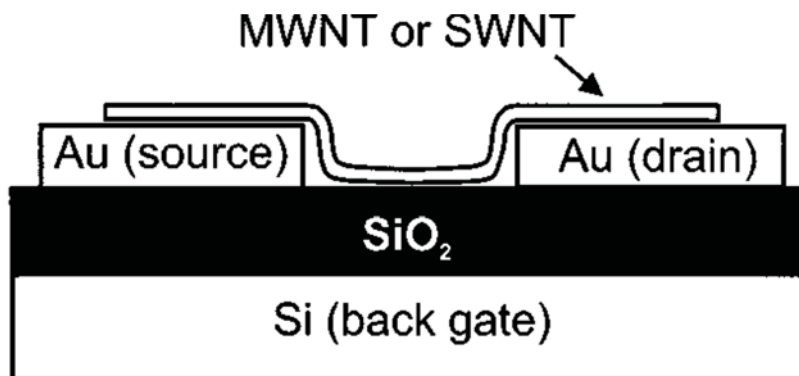
Figure 2-29: Schematic of a back gated Single Wall Carbon Nanotube Field Effect Transistor (SWCNT-FET) Schematic [90].

To fabricate this device, gold electrodes were predefined on the silica layer using electron beam lithography. Then purified SWCNTs were dispersed in solution and dropped over

the electrode area. This dispersion increased the probability of a single isolated SWCNT to bridge the source-drain electrodes in order to act as a channel between the gold contacts instead of a bundle of SWCNTs. This FET geometry is best suited for sensor applications because it exposes the SWCNT to ambient conditions.

To increase the effectiveness of the back gated design, work has been carried out to modify the contacts of the device. It has been shown that the Schottky barrier at the contact/SWCNT interface limits the conductance of the device [91–93]. Hence, palladium has been investigated as a replacement for gold [94]. It has been shown that using palladium contacts, the p-type conductance of the device was greatly increased. Further investigation on the palladium contacts were performed using hydrogen to lower their work function. It was discovered that with this decrease in work function, the hole transport decreased. This meant that the Schottky barrier for hole transport was increased by lowering the contact work function. The use of higher work function metals makes better contacts in SWCNT-FETs.

Additional work has also been performed on the modification of the conducting channel of the SWCNT-FET [95,96]. Snow *et al.* [95] tested the viability of using random CNT networks as the conducting channel in a SWCNT-FET. To form the networks, the growth of SWCNTs was carried out directly on the silica layer and then optical lithography was used to create the titanium contacts. It was shown that using a low enough network density, the device can perform with a decent "ON" state mobility, and with a sufficiently low "OFF" state current. Similar results were found for aligned networks of SWCNTs [96]. Using a Y-cut silica wafer, aligned SWCNTs were able to be obtained via chemical vapor deposition (CVD). Then titanium/gold contacts were fabricated using photolithography

procedures in a way that the orientation of the SWCNTs in the conducting channel was explored. It was found that SWCNTs aligned parallel to the electrical transport acted as a p-type thin film with good hole conduction. Conversely, SWCNTs aligned perpendicular to the conduction pathway provided poor electrical conduction. Thus, orientation of the array seems to be paramount in device configuration. SEM micrographs of the FET device based on CNT networks is shown in Figure 2-30.
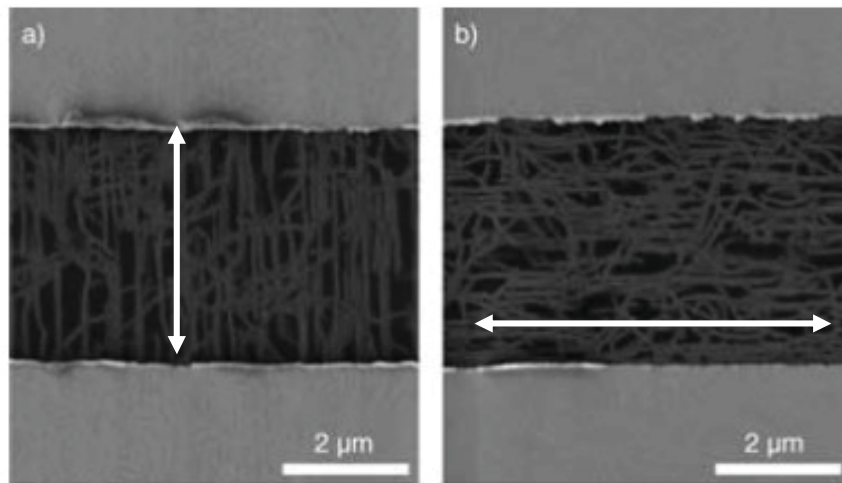
Figure 2-30: SEM micrograph of an aligned SWCNT-FET device based on arrays

A) parallel and B) perpendicular to the conduction path [96].

Further developments on SWCNT-FETs has resulted in the gate being oriented on the top of the CNT [97]. A schematic design of this arrangement is shown in Figure 2-31.
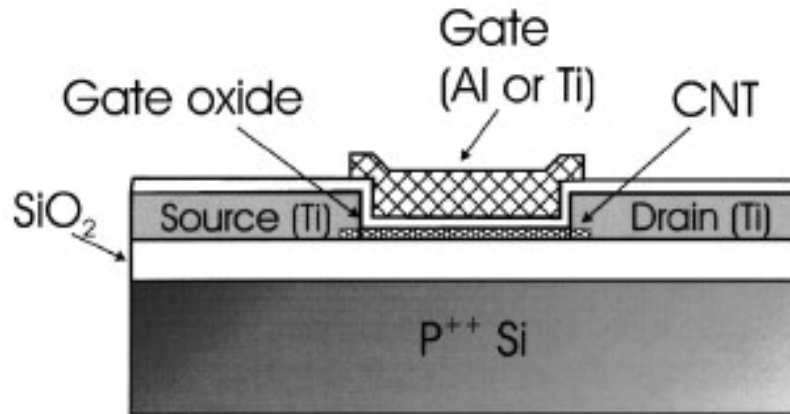
Figure 2-31: Schematic representation of a top gated Single Wall Carbon Nanotube Field Effect Transistor (SWCNT-FET) [98].

The top gated FETs are commonly fabricated by locating a SWCNT on the surface of a ceramic substrate and then depositing metal contacts on both ends of the tube [98]. Then, the device is annealed to reduce resistance at the contacts. Subsequently, a thin dielectric layer is deposited over the whole device after which a metal gate is placed upon the conduction pathway. Due to this fabrication methodology, top gated SWCNT-FETs are much more easily constructed because they do not rely on the randomness of SWCNTs bridging contacts as in the back gated fabrication. Also, top gated SWCNT-FETs have been shown to have more advantages over back gated SWCNT-FETs when applied to ON/OFF applications [98,99]. For instance, since the SWCNT is always exposed to air in the back gated setup, the device can only perform as a p-type FET [98]. In contrast, the top gated FET allows for operations as an n-type FET if the device is annealed before the silica layer is added.

It has also been shown that chemical modification of the source and drain contacts results in a n-type operation [100]. This has been performed by doping palladium contacts

with potassium. Here, the doping reduces the Schottky barrier which allows electrons to become the majority charge carrier. This kind of modified FET device operates with a very high ON/OFF current ratio and suppresses the ambipolar properties that carbon nanotubes can exhibit.

An additional generation of SWCNT-FET devices were created by wrapping the CNT conducting channel by a dielectric and gate layers enclosure [101]. A schematic of this wrap-around gate SWCNT-FET is presented in Figure 2-32.
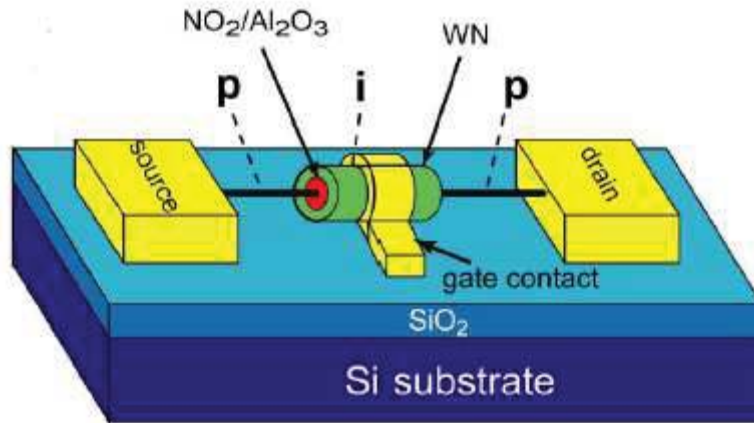
Figure 2-32: Schematic of the wrap around gate Single Wall Carbon Nanotube Field Effect Transistor (SWCNT-FET) [101].

These wrap-around FET devices are initially constructed by surface functionalizing SWCNTs with NO_2 groups [102]. Subsequently, using an atomic layer deposition process, an alumina dielectric layer and tungsten nitride gate layer are consecutively deposited around the tube surface. Finally, the covered SWCNTs are dispersed onto a silicon/silica substrate, followed by the deposition of the metal connections at the ends of the coated CNT [101]. A TEM image of the wrap-around CNT is presented in Figure 2-33.
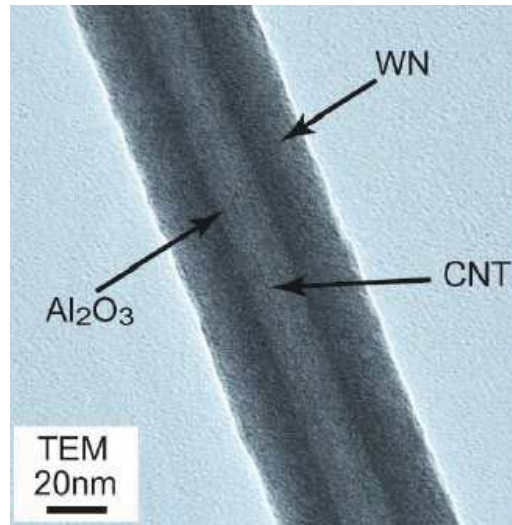
Figure 2-33: TEM image of an alumina (Al_2O_3) and tungsten nitride (WN) layer deposited onto a SWCNT using an atomic layer deposition process [101].

The wrap around gate SWCNT-FETs operate similarly to top gated SWCNT-FETs, but it is believed that higher ON/OFF ratios can be obtained.

An additional SWCNT-FET configuration is based on a suspended set up, which has a superior electrical performance than other FET systems [103–107]. Its fabrication process began with an electron beam resistant material deposited onto the substrate and then an electron beam lithography procedure is followed to pattern the platinum/tungsten contacts and the trench [103,104]. Next, etching is used to form the trench and the deposition was used to create the contacts. Once the base structure of the device is formed, electron beam lithography is again used to pattern the carbon nanotube growth catalyst on the surface of the source and drain contact regions. Finally, a chemical vapor deposition is used to grow SWCNTs across the trench. A schematic of the device is presented in Figure 2-34.
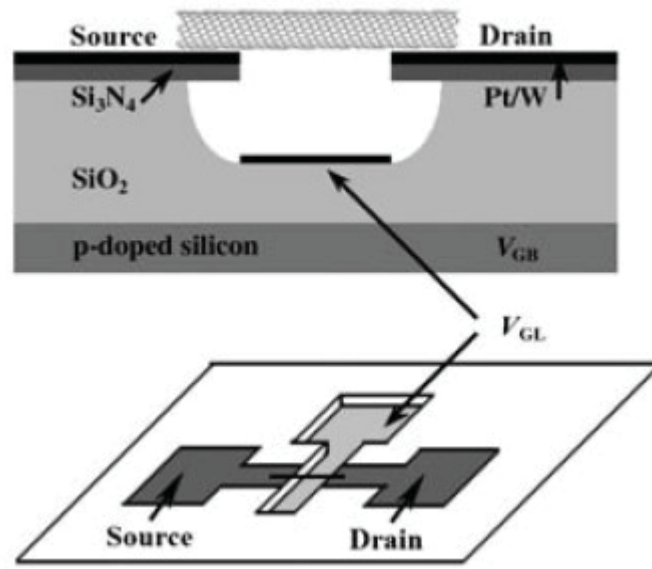
Figure 2-34: Schematic representation of a suspended SWCNT-FET [103].

A study on the interaction between the SWCNT and the oxide gate layer showed that noise is significantly decreased when the SWCNT is suspended rather than in full contact with the oxide [105]. It has also been shown that this configuration allows for ambipolar operation without the need of doping the CNT in a vacuum environment [106]. Likewise, little hysteresis has been observed in suspended SWCNT-FETs [103,106]. An interesting property of this configuration is that it has been shown to be able to be used in detection of gas molecules such as NO_2 [107]. This proves to be a significant advantage over a wrap around SWCNT-FET where the tube surface is covered and cannot interact with ambient conditions. However , one significant drawback of this design, lies in the fact that some gate voltages can cause the SWCNTs to dip into the trench [108]. This can cause the device to easily fail. Thus, this configuration does not represent the best candidate for commercial use.

2.5 Sensors

2.5.1 Chemical Sensors

2.5.1.1   Inherent Sensor Capabilities

In addition to the applications of CNTs into FETs, they have been shown to exhibit change in electrical properties when exposed to O_2, NH_3 and NO_2 [109–111]. In testing the oxygen sensitivity, CNTs were grown by laser ablation and brought to 700 ºC in air to remove the amorphous carbon [109]. CNTs were then dispersed in solution and transferred to electrodes for measurement. The electrodes were then moved to a vacuum chamber, and once in the chamber, the resistance was measured versus time as the chamber was placed under vacuum. As the oxygen contained in the SWCNTs was removed by the vacuum, it was observed that the electrical conductance decreased. This suggests that exposure to oxygen increases the conductance of SWCNTs.

In similar trials, SWCNT dispersions and SWCNT thin films were shown to experience a conductance change when brought in contact with NO_2 and NH_3 gas [110–112]. The electrical output of SWCNTs after being exposed to NO_2 and NH_3 is presented in Figure 2-35.
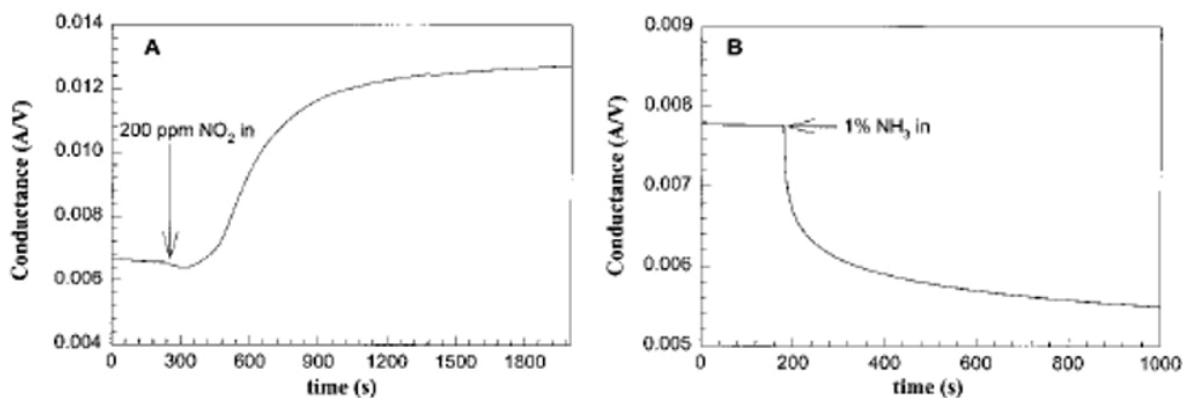
Figure 2-35: Conductance profile of a bulk SWCNT system in contact with A) NO_2

and B) NH_3 [111].

As shown in Figure 2-35, the conductance of the SWCNTs increases when brought

into contact with NO_2 and decreases when "sensing" NH_3. It is interesting to note that the

change in conductance shown in Figure 2-35 is smaller for both cases in comparison to the

electrical profile outcome of an individual SWCNT. This is because the entangled

SWCNTs used by Kong *et al.* [111] contained both metallic and semiconducting tubes, and

some tubes are not exposed to ambient conditions due to the bundled nature of the sensor.

This can cause the signal to be dampened.

An important note for CNT sensors is that once a sample is exposed to an analyte,

the sensor must be recovered. This recovery mechanism employs the use of UV light or

even heating to an elevated temperature while under vacuum [110]. The effect of recovery

on SWCNTs after exposure to NO_2 can be seen in Figure 2-36.
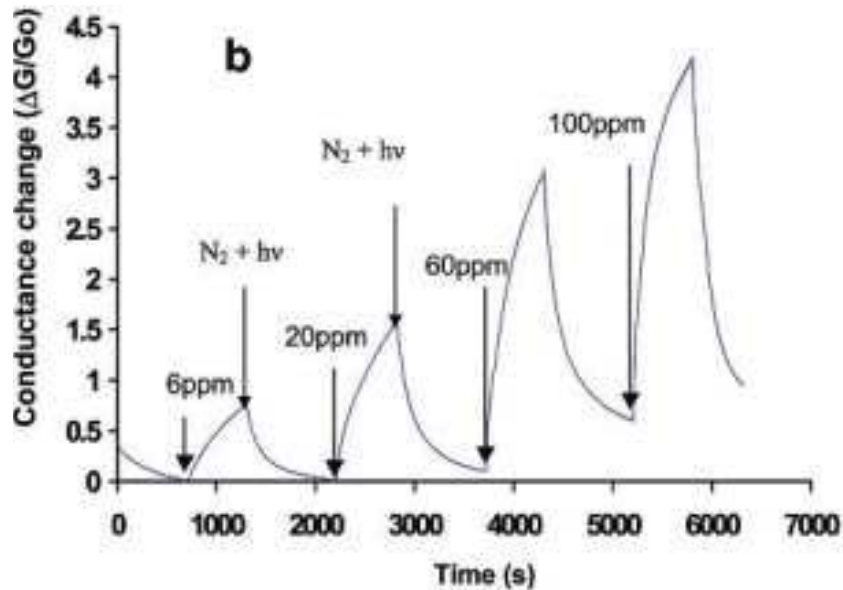
Figure 2-36: **Electrical response of SWCNT sensing at different levels of NO_2 using UV recovery between each test [110].**

As seen in Figure 2-36, this recovery step can be performed many times before the recovered baseline conductance changes dramatically. This shows that although SWCNT sensors can be employed multiple times, there is still a cutoff to the number of times that the sensor can be used.

The NO_2 and NH_3 detection mechanism of SWCNTs has been addressed as a conjunction between modeling and experimental procedures [113–115]. Zhang *et al.* [113] used Poly(methyl methacrylate) (PMMA) to create a barrier between ambient conditions and various sections of the device, and it was shown that when the interface between the SWCNT and the metal contacts were protected from the NO_2, there was a slow response. Conversely, a considerable change in conductance occurred when NO_2 was allowed to be in contact with the whole device. This showed that the interaction between the SWCNT and the metal is a major driving force in the detection of NO_2. Similar work with NH_3

indicated that at room temperature the interaction at the interface is similarly important, but at higher temperatures the adsorption of NH_3, assisted with the presence of oxygen seems to be the primary cause of charge transfer in the device [114].

Theoretical calculations on the interaction between SWCNTs and NO_2 showed that although NO_2 does adsorb on the surface of the SWCNT, the charge transfer associated with this adsorption does not have a considerable effect on the total charge transfer throughout the tube. This result was corroborated by calculations of Robinson *et al.* [115]. However, they showed though, that defects created in SWCNTs during the purification process increased the sensitivity of the sensor. It was revealed that the defects can act as adsorption sites that have a considerable effect on charge transfer.

2.5.1.2   Covalently Functionalized SWCNT Sensors

Since SWCNTs have been shown to have inherent sensing properties, there is considerable potential to increase their sensitivity. To address this issue, chemical functionalization of CNTs has been explored [116]. In a study carried out by Bekyarova *et al.* [116], poly(m-aminobenzene sulfonic acid) (PABS) was covalently attached to SWCNTs, and then incorporated into two electrodes to assemble a sensing device. Without functionalization, the percent resistance change after an exposure of 100 ppm of NH_3 was between 5 and 10 percent depending on the initial electrode resistance. In contrast, the inclusion of the PABS functionalization increased the response to be between 24 and 26 percent. This was attributed to the fact that the interaction between NH_3 and the PABS resulted in less holes for the electrical signal transfer in the tube.

Functionalization of CNTs has also highlighted the feature associated to their inherent sensing properties. Devices employing purely dispersed SWCNTs will have little

selectivity to what is actually being "sensed." Thus, the consideration of various polymers to functionalize SWCNTs has been shown to impart selectivity [117]. Qi *et al.* [117], used catalyst patterning techniques to obtain a CNT electrode which they coated in polyethyleneimine (PEI). Here, the PEI increased the sensitivity of the electrode from ppb to ppt levels of NO_2, whereas it limited the detection of NH_3. It was hypothesized that the PEI enriches the SWCNTs with electrons, creating a stronger binding affinity for NO_2, which is electron withdrawing in nature. In contrast, an electron donating molecule, like NH_3, is blocked from adsorption. Alternatively, the addition of Nafion, in place of PEI, blocks the detection of NO_2, while still allowing the detection of NH_3.

Additional work on the sensing properties of CNTs has been carried out based on the idea that the sensing property is due to mechanical forces rather than chemical reactions [118,119]. Niu *et al.* [118] covalently attached poly(ethylene glycol) (PEG) to carboxylated SWCNTs through a N,N-dicyclohexylcarbodiimide (DCC) mediated reaction. Their work showed that the PEG functionalization imparted unique selectivity towards chloroform. Similarly, SWCNT/hexafluoroiso-propanol in conjunction with polythiophene (HFIP-PT) polymer films were made to selectively target phosphate esters in the detection of chemical warfare agents [119]. Both of these functionalizations resulted in a sensing mechanism primarily resulting from swelling of the polymer coating. This swelling caused the electronic network of CNTs to be disturbed and thus eliciting an electrical response.

2.5.2 Biosensors

The detection of biological molecules is an important activity in many different sectors, such as healthcare and environmental safety, and therefore the development of reliable biosensors is certainly an area of great interest. The implementation of different

bio agents onto CNTs can yield biosensors with unique detection capabilities [120–126]. Bio-sensing agents, such as enzymes, proteins, and antibodies, can be immobilized on the CNT's surface while retaining their biological and electrochemical activity [127,128]. Since these two properties are retained, the functional surface groups of the bio-agents will sensitively react with a target of interest, and will result in a direct electron transfer between the enzyme and the CNT [129,130]. This mechanism will allow an electronic measurement of the interactions, as well as the transfer of electrons between the targeted analyte, and the CNT-biological complex [131]. Mundaca *et al*. [121] developed a biosensor for the detection of andosterone, which is a primary ingredient used in anabolic steroids. They performed the testing by attaching the enzyme 3α-hydroxysteroid dehydrogenase (3α-HSD) to an electrode based on a mixture of MWCNT, n-Octylpyridinium hexafluorophosphate(OPPF6), and oxidized nicotinamide adenine dinucleotide (NAD+). Here, the 3α-HSD interacted with the hydroxyl and carbonyl groups located within the steroid.

Additional work performed by Vicentini *et al.* [122] utilized carbodiimide chemistry to attach Tyrosinase (Tyr) to MWCNTs. Then the Tyr functionalized CNTs were mixed with an ionic liquid and subsequently used to modify a carbon electrode. Using this functionalized biosensor, it was demonstrated that the catechol contained within water samples could be detected for safety measurements. The mechanism of detection involved the transformation of the phenol catechol into o-quinone using the Tyr as the catalyst. The direct electron transfer between the MWCNT and the Tyr caused by the reaction with the catechol was detected by the electrode setup.

Supplementary work has also been performed to create biosensors towards glucose [123–126]. Fatoni *et al.* [123] used a chitosan-bovine serum albumin (chi-BSA) cryogel mixed with MWCNTs, ferrocene, and glucose oxidase. Here, the chi-BSA oxidized the glucose while the MWCNTs were used to detect the resulting electron transfer. Lin *et al.* [124] modified electrodes with MWCNTs and then deposited copper and nickel nanoparticles upon them. The electron transfer due to the oxidation of the glucose by the nickel/copper/MWCNT complex was detected by the system. The electrical output is presented in Figure 2-37 .
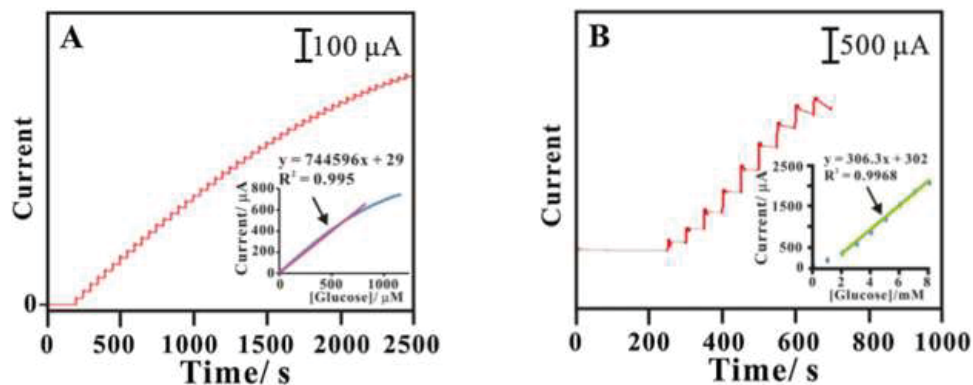
Figure 2-37:   Sequential detection of glucose by a Nickel/Copper/MWCNT system of A) 25 μM–1.15 mM and B) 1-9 mM [124].

Pourasl *et al.* [125] and Palanisamy *et al.* [126] also modified an electrode with graphene oxide in order to electronically sense the oxidation of glucose . Unlike the nickel/copper/MWCNT electrode, it was observed that the current decreases with the detection of glucose.

The previously described biosensors are based on carbon electrodes modified by a CNT/sensing agent mixture. The ability to directly transfer charge between the CNTs and surface functional group has led to the creation of FET biosensors [132–139]. Star *et al.*

[132] created a simple carbon nanotube field effect transistor (CNFET) sensor by functionalizing the carbon nanotube with a poly (ethylene glycol) (PEG)/biotin mixture. A diagram of the setup is displayed in Figure 2-38.
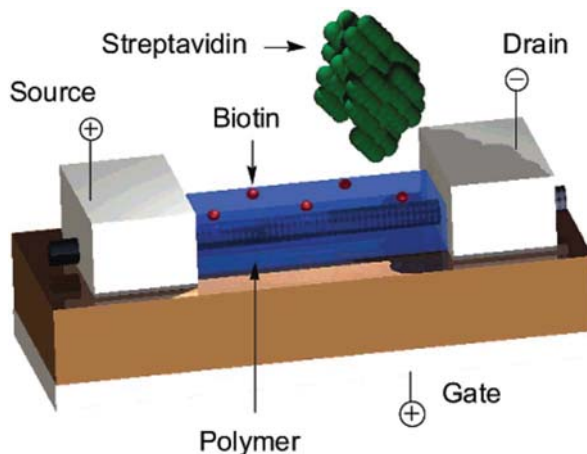
Figure 2-38:   Schematic representation of a CNFET system based on biotin and PEI functionalization for detecting streptavidin [132].

As shown in Figure 2-38, the PEG prevents nonspecific binding of additional proteins while the CNT is used to sense the biotin interaction with streptavidin. This device showed a fast electrical response with a high degree of sensitivity.

Additional studies on CNFET biosensors have focused on using antibodies on the sensor surface [135,139]. Villamizar *et al.* [135] showed that anti-Salmonella adsorbed onto CNTs was able to detect Salmonella Infantis. To introduce selectivity, tween 20 was used to block the binding of other biological agents. Oh *et al.* [139] similarly showed that antibody based CNFETs can be used to detect an Alzheimer's marker (amyloid-beta) in blood. The detection of amyloid-beta at different concentrations is shown in Figure 2-39.
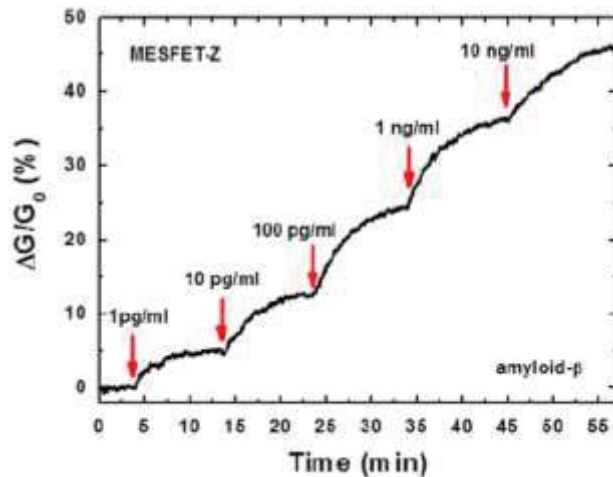
Figure 2-39:   Normalized change in conductance over time profile presenting the detection of amyloid-beta in real time by an antibody based CNFET [139].

As shown in Figure 2-39, detection occurs in minutes and with high degree of sensitivity. Indeed, these properties are highly desirable in many sensor applications. Oh *et al.*'s work [139] also showed that designing the attachment of the antibody on the CNTs can increase the sensitivity of the device. This was realized by comparing a CNFET fabricated by attaching the antibodies to the CNT through a protein linker versus to a CNFET system assembled by directly immobilizing the antibodies through chemical bonds. It was observed that the CNFET utilizing a protein linker was more sensitive than the CNFET employing direct immobilization.

2.6 Phage Display

With the ability of biologically functionalized carbon nanotubes for modulating and detecting the binding of targets, it is imperative to have a technique that will find functional groups with specific selectivity and sensitivity towards desired target analytes. A potential

74

approach for addressing this requirement is the use of a phage display library technology to produce specific functionalized nanotubes. A phage display library consists of bacteriophage which express peptides, proteins, or antibodies on their surface [140–142]. When the library is exposed to a target, those phage with high affinity towards the target will selectively bind to it [143]. Immobilization of the target prior to phage binding allows the non-binding phage to be removed during the biopanning (screening) process, while those phage that bound to the target can be harvested. The DNA, encoded with the peptide information, contained in the phage can then be removed from the harvested phage, purified, and subsequently sequenced to find the amino acids that comprise the protein with selectivity toward the target [144].

It has been shown that peptides selective to volatile organic compounds (VOC) such as benzene, toluene, and xylene can be obtained via a bio-panning of a M13 phage library [145]. The peptides discovered in the biopanning process were used to functionalize a micro-cantilever surface. These sensors were able to discriminate between organic compounds, and in essence, "sense" a single carbon change in the target compound. In addition, these sensors were capable of detecting on the sub-ppm level with relatively rapid detection times. Similarly, work has been performed on identifying peptides selective to TNT [146,147]. Thus, a phage display library technique can be used to find peptides that express selectivity towards chemical constituents. These peptides can then be incorporated onto an optical-electrical substrate to assemble a biosensor. One of the reasons that makes peptides an excellent candidate for being considered as the detection platform of nanosensors is that they are able to be kept in a solid state without the need of their storage in a liquid environment [148,149]. This is a feature which is opposite to that required by

biological selective materials such as antibodies. Certainly, this solid-state storage

capability is an important feature for sensor applications.

2.6.1 M13 Phage

Bacteriophage that can be commonly used in phage display include T7, Lambda, and

filamentous Ff phage [150–152]. For the purpose of this review, the focus will be on the

filamentous phage M13 with surface expressed peptide structures, as it was used in this

research. This type of phage was chosen because its use has been reported in work targeting

TNT [146,147]. Filamentous Ff phage display libraries are commonly used and are easily

modified for a wide range of applications, such as the display of foreign proteins [143].

M13 filamentous Ff phage are comprised of a single, circular DNA molecule surrounded

by a capsid made of five coat proteins: pIII, pVI, pVII, pVIII, and pIX [153]. A graphical

representation of the M13 bacteriophage is presented in Figure 2-40.
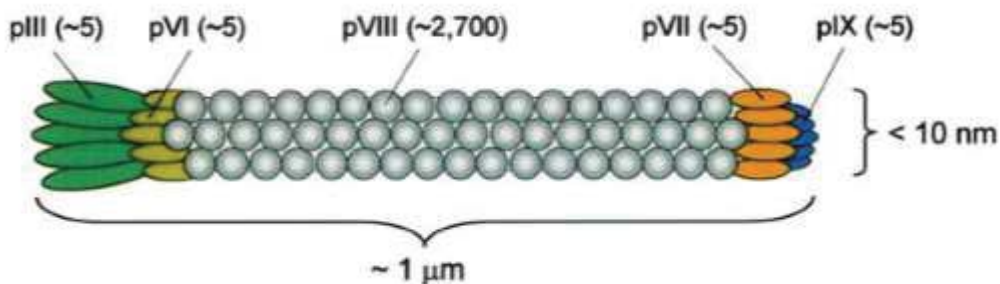
Figure 2-40:   Schematic representation of the basic structure of the M13

bacteriophage [143].

As shown in Figure 2-40, the major coat protein is pVIII with several thousand copies found in the capsid. Conversely, only 5 copies of each of the minor coat proteins are present (pIII, pVI, pVII, pVIII, and pIX).

The pIII coat plays some of the most important roles in the phage infection of bacteria [154]. The structure of pIII is given in Figure 2-41.
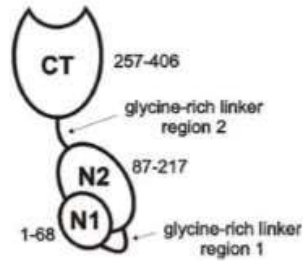
Figure 2-41:   Schematic of pIII coat protein structure [155].

 As shown in Figure 2-41, the two N-terminus domains of pIII are N1 and N2. These two domains are connected by glycine rich linker sequences and intramolecular forces and are responsible for the infectivity of the phage. Figure 2-41 also shows the C-terminus domain (CT) which assists in the termination of an infection and the release of the phage from an infected cell. The binding process of M13 to a host cell is presented in Figure 2-42.
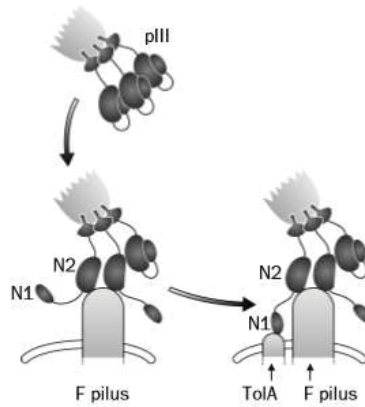
Figure 2-42:   Representation of the M13 filamentous Ff phage infection of a host cell from left-top to right-bottom [155].

As observed in Figure 2-42, the N2 domain interacts with the F pilus of a host bacterium and releases the intramolecular forces, keeping the N1 domain bound to the pilus [156]. Once the N1 is released, it is now free to bind to the Tol A protein of the host [157,158]. Thus, without the pIII coat protein, the phage would not be capable of infecting a host cell [159]. Also, the pIII coat protein can be used to express a peptide on the phage surface [140]. It has become one of the most commonly used expression coat protein used in phage display [154]. Although pIII is commonly used, it is possible for all coat proteins to be expression sites for peptides [160].

2.6.2 Ph. D. Phage Display Library

The Ph. D. phage display library was developed by New England BioLabs [161]. It contains M13 phage expressing peptides on the N-terminal pIII coat. The specific library used for this research work was a Ph. D. -7 library, which expresses 7-mer peptides. In the Ph. D. system, the phage have 5 copies of the peptide expressed (one on each pIII coat).

As long as the peptide is less than 50 residues long, the ability of the phage pII to bind to and infect a host cell is not disturbed [162]. The use of pIII expression produces higher binding affinity peptides towards targeted molecules due to its lower valency than other expression sites, such as the pVIII coat protein [161]. The library contains roughly 10^9 phage unique peptide sequences expressed on phage. This represents almost all of the possible nucleotide combinations available in a 7-mer peptide. To assist in the location of the peptide during sequencing, the peptide is linked to the phage via a Gly-Gly-Gly-Ser sequence. Using this library, peptides selective to enzymes, cell-surface receptors, monoclonal antibodies, semiconductors, ferroelectrics, gadolinium oxide (GdO) particles, and small molecule binders have been discovered [161,163–166]. Thus, it can be seen that the Ph. D. library can be used to find peptides selective for non-biological analytes as well as biological.

2.6.3 Biopanning

Biopanning (or screening) is the procedure that transforms a large and diverse phage library into a small population of phage with affinity to a targeted constituent [142,143,155,167–170]. A graphic of the general procedure of biopanning is shown in Figure 2-43.
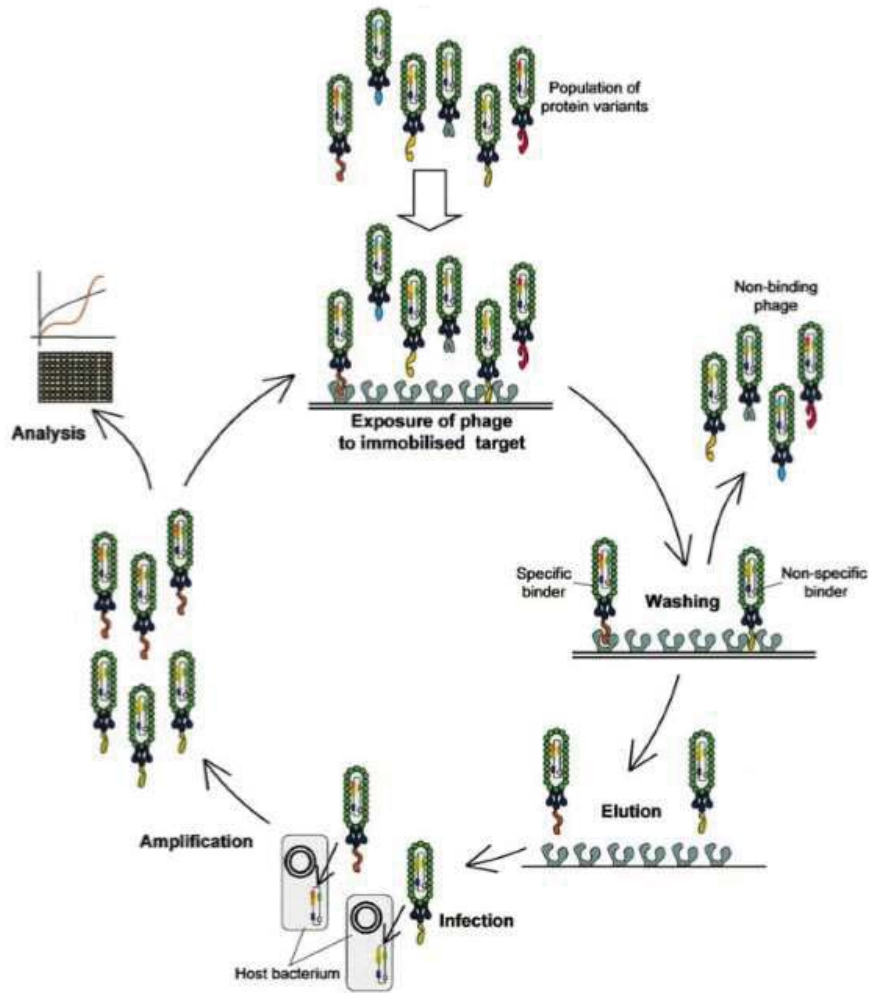
Figure 2-43: Schematic graphic of the general biopanning procedure using a phage display library [143]. Phage are exposed to the immobilized target. Next, the bound phage are eluted and amplified. Finally, phage are either transferred to another round of panning or analyzed.

As presented in Figure 2-43, biopanning begins with the immobilization of the target molecule to a substrate, such as a microwell plate [167]. Subsequently, a blocking buffer is used to reduce the possibility of binding to the substrate surface. Then a library containing millions of phage expressing different peptides, proteins, or antibodies are

brought into contact with the immobilized target. The phage bind to the target in a "lock and key" type mechanism where only phage expressing an agent selective to the target will bind [143]. Next, the well is washed, which removes the phage that do not bind [167,169]. After the washing step, the bound phage are eluted using a low pH buffer [170]. The eluted phage are then usually amplified via infection of a host cell before another round of panning takes place. If the a higher level of specificity is desired, it may be better to directly use the eluted phage without amplification in the next round of panning [169]. Specificity is also generally improved by increasing the number of panning rounds. Once the panning rounds are completed, the eluted phage are amplified and analyzed using techniques such as enzyme-linked immunosorbent assay (ELISA) and sequencing.

2.6.4 Enzyme-linked Immunosorbent Assay (ELISA)

An ELISAs can be used to determine the selectivity of the peptide binding [171]. In the ELISA procedure, the target is attached to a microplate well and the well is subsequently blocked. The amplified isolated phage are then allowed to bind to the target. The wells are washed and antibodies to the phage are added and allowed to bind. These antibodies are covalently labeled with a specific enzyme. A chromogenic solution that is tailored to the enzyme on the antibody results in a color change that indicates the level of binding. This test assists in determining whether or not an isolated phage is actually specific for the target, or if a phage is non-specific due to binding to the microplate well.

2.6.5 Sequencing

One of the major analysis techniques after biopanning is the sequencing process. Sequencing of the DNA contained within the phage results in the identification of the chemical structure of the expressed peptide or protein [172]. The DNA encoding the

peptide is contained in the infected bacterium, the bacteria are lysed and the DNA encoding the peptide is separated from the cells [173]. Once separated, the DNA is purified using a silica spin column and a binding/elution procedure. After purification, the DNA is sequenced. In a basic sequencing process, primers are used to replicate only the specific area of the DNA which contains the peptide information [172]. Subsequently, gel electrophoresis is used to separate the replicated strands by size. The nucleotides are chemically modified to fluoresce different colors under UV light. Thus, nucleotide strands that vary in length will fluoresce with a color corresponding to the nucleotide located at the end of the strand. Each color indicates a unique dideoxy nucleotide at the end of the strand. Using UV light and a color detection system, the colors associated with each nucleotide strand are recorded as they are eluted in order of the length of the nucleotide strand. The order of the nucleotides found at the termini of each strand indicates the nucleotide sequence of the DNA. An example of a sequencing gel can be seen in Figure 2-44.
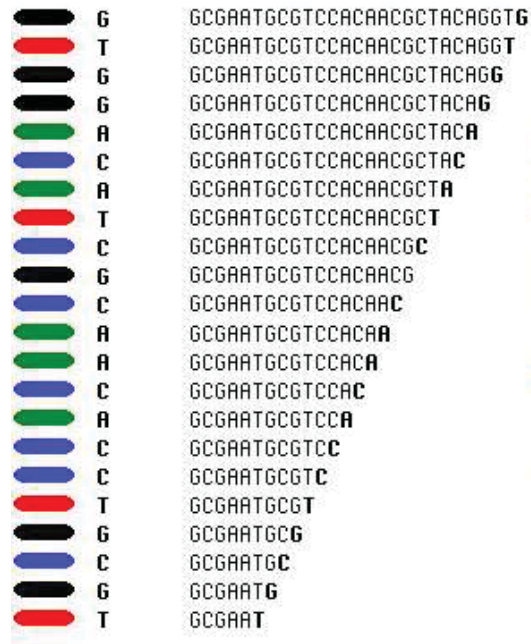
Figure 2-44:   Example of a DNA sequence produced by gel electrophoresis.

Black=G(Guanine), Red=T(Thymine), Green= A(Adenine), Blue=C(Cytosine) [172].

2.7 Modeling

The electronic and physical properties of CNTs are commonly modeled using the density functional tight binding theory (DFTB) in conjunction with the non-equilibrium Green's functions [174–179]. Hence, the following sections show the foundation of density functional theory (DFT) as well as the integration of the tight binding formalism with the non-equilibrium Green's functions. Also, the use of Poisson equations to calculate the electrical current through the system and the types of CNT networks that have been studied via DFTB is presented in the next sections.

2.7.1 Density Functional Theory (DFT)

One of the first formulations of DFT was created in 1964 by Hohenberg and Kohn [180]. DFT calculates properties such as the geometry, electronic characteristics, and

spectroscopic features of a system. This method was an improvement of the Hartree-Fock (HF) approach which was created by Hartree and Fock in 1920 [181]. The HF method uses a Slater determinant to approximate the wavefunction. However, there were two primary caveats with the HF method. The first was that it assumed that electron movement was not affected by other electrons. The other issue is that once the system reached over 20 atoms, the computation time and resource were prohibitive. Hence, DFT was created to counteract these two limitations.

DFT theory assumes that the electron density can be used to find the electronic wavefunction at the ground state [180]. The other basis of the theory rests on the assumption that the minimum of the ground state electron density can be used to determine the energy of the electron. The most recent version of DFT has been formulated by Kohn and Sham [182]. The DFT-KS theory models the system as non-interacting but with the same density as the interacting system. In the Kohn-Sham formulation, the total energy of the non-interacting electrons is given by equation 2.1

$$E[n(r)] = T_s + E_{ext} + E_H + E_{xc} + E_{II} \qquad 2.1$$

where $n(r)$ is the electron density , T_s is the non-interacting kinetic energy, E_{ext} is the external interaction, E_H is the Hartree energy, E_{xc} is the exchange-correlation energy, and E_{II} is the ion-ion interaction energy [183]. A more in depth expression for equation 2.1 is presented in equation 2.2.

$$E[n(r)] = \sum_a f_a \langle \psi_a | (-\frac{1}{2}\nabla^2 + \int V_{ext}(r)n(r)d^3r) | \psi_a \rangle$$

$$+ \int \int' \frac{1}{2}\frac{nn'}{|r - r'|} d^3r'd^3r + E_{xc} + E_{II} \qquad 2.2$$

where f_a is the occupation of the single particle state ψ_a, possessing energy ε_a, and V_{ext} is the energy of interactions between atoms. An important note in this equation is that E_{xc} does not have an exact expression for each electron density. To overcome this, Kohn and Sham assumed that $n(r)$ varies slowly. With this assumption in place, they showed that E_{xc} can be expressed as

$$\boldsymbol{E_{xc} = \int n(r)\epsilon_{xc}\big(n(r)\big)dr} \qquad \text{2.3}$$

where ϵ_{xc} is the exchange and correlation energy per electron at a specific electron gas density [184]. Using equation 2.2 in the single particle form, the single particle Schrodinger equation was solved to produce the expression of the electron density. This form of electron density is given in equation 2.4

$$\boldsymbol{n(r) = \sum_{i=0}^{N} |\psi_i(r)|^2} \qquad \text{2.4}$$

where N is the number of electrons [184]. Since this process is a minimization of the energy, solving for the final electron density and total energy requires an iterative process. In the first iteration, the electron density value is assumed. Subsequently, equations 2.2 and 2.4 are used to find the new value of $n(r)$, which is then used again in equations 2.2 and 2.4. This iterative process is repeated multiple times until the energy is minimized.

2.7.2 Density Functional Tight Binding Theory (DFTB)

Tight binding (TB) theory was first combined with density functional theory (DFT) in 1954 by Slater and Koster [185]. Tight binding theory's initial formulation was described by Bloch in 1928, and it rests on creating a linear combination of the atomic orbitals in a system to form a wave function for every wavenumber (k) [186]. Slater and Koster removed many of the intensive and time consuming calculations in the original DFT

process by first eliminating unimportant terms then keeping the important terms and turning some of them into constants [185]. This resulted in a theoretical model that required much less computational time and power while also retaining some of the accuracy as the full DFT treatment.

The first step in the DFTB method is to create Bloch sums of the atomic orbitals in the system using the Lowdin method [187]. The form of the Bloch sum is presented in equation 2.5

$$\sum (\boldsymbol{R_i}) \boldsymbol{exp}(\boldsymbol{ik} \cdot \boldsymbol{R_i}) \boldsymbol{\phi_n}(\boldsymbol{r} - \boldsymbol{R_i}) \qquad 2.5$$

where R_i is the vector position of the atomic orbital on a given atom, $\phi_n(r - R_i)$ is the atomic orbital, and n is the quantum number of the atomic orbital. This equation is constructed in such a way that it is actually a linear combination of the atomic orbitals that extends over all equivalent atoms in a system. Thus, Bloch sums are created for all of the atoms and corresponding atomic orbitals in a unit cell of a system. Also, equation 2.5 is established in a form that the Bloch sums created for each orbital are orthogonal to each other. This reduces some of the complexity associated with nonorthogonal Bloch sums. Once the Bloch sums are formed, the matrix element of energy between each sum is calculated using equation 2.6.

$$\sum (\boldsymbol{R_j}) \boldsymbol{expik} \cdot (\boldsymbol{R_j} - \boldsymbol{R_i}) \int \boldsymbol{\psi_n^*}(\boldsymbol{r} - \boldsymbol{R_i}) \boldsymbol{H} \boldsymbol{\psi_m}(\boldsymbol{r} - \boldsymbol{R_j}) \boldsymbol{dv} \qquad 2.6$$

where H is the Hamiltonian operator, ψ_n and ψ_m are the orthogonal orbitals created using the Lowdin method, and R_i and R_j are the vector positions of ψ_n and ψ_m respectively.

The integrals present in equation 2.6 are very computationally intensive. Therefore, Slater and Koster replaced some of the integrals with constants. Some important notes

made by Slater and Koster about equation 2.6 were: 1) The three-center integrals are very complicated and do not have a large effect on the system, so they are disregarded. 2) As the interatomic distance grows larger between the atoms, the integral will become substantially smaller. This allowed Slater and Koster to set a minimum distance between an atom and an interacting atom to be considered as a term in the expression. 3) Atoms related by crystal symmetry should have the same interaction integral value. This resulted in the consideration of only the nearest or second nearest neighbors. 4) Only orbitals near the energies that are being targeted need to be considered. Using these simplifications, replacements were presented for the two-center integrals. These are shown in Table 2.1. Indeed, the energy integrals (E) can be used in place of the integrals presented in equation 2.6. These integrals contain two indices to dictate what two orbitals are being considered. For example, the indices abbreviations for the p_x, p_y, and p_z orbitals are x, y, and z respectively while the $d_{z^2}, d_{xy}, d_{xz}, d_{yz}$, and $d_{x^2-y^2}$ are z^2, xy, xz, yz, and $x^2 - y^2$ respectively. Thus, $E_{s,x}$ is the two center integral describing the interaction between the sσ and pσ orbitals.

Table 2.1 : Energy integrals for crystal in terms of the two-center integrals [185].

$E_{s,s}$	$(ss\sigma)$
$E_{s,x}$	$l(sp\sigma)$
$E_{x,x}$	$l^2(pp\sigma) + (1 - l^2)(pp\pi)$
$E_{x,y}$	$lm(pp\sigma) - lm(pp\pi)$
$E_{x,z}$	$ln(pp\sigma) - ln(pp\pi)$
$E_{s,xy}$	$\sqrt{3}lm(sd\sigma)$
E_{s,x^2-y^2}	$\frac{1}{2}\sqrt{3}(l^2 - m^2)(sd\sigma)$
$E_{s,3z^2-r^2}$	$[n^2 - \frac{1}{2}(l^2 + m^2)](sd\sigma)$
$E_{x,xy}$	$\sqrt{3}l^2m(pd\sigma) + m(1 - 2l^2)(pd\pi)$
$E_{x,yz}$	$\sqrt{3}lmn(pd\sigma) - 2lmn(pd\pi)$
$E_{x,zx}$	$\sqrt{3}l^2n(pd\sigma) + n(1 - 2l^2)(pd\pi)$
E_{x,x^2-y^2}	$\frac{1}{2}\sqrt{3}l(l^2 - m^2)(pd\sigma) + l(1 - l^2 + m^2)(pd\pi)$
E_{y,x^2-y^2}	$\frac{1}{2}\sqrt{3}m(l^2 - m^2)(pd\sigma) - m(1 + l^2 - m^2)(pd\pi)$
E_{z,x^2-y^2}	$\frac{1}{2}\sqrt{3}n(l^2 - m^2)(pd\sigma) - n(l^2 - m^2)(pd\pi)$
$E_{x,3z^2-r^2}$	$l\left[n^2 - \frac{1}{2}(l^2 + m^2)\right](pd\sigma) - \sqrt{3}ln^2(pd\pi)$
$E_{y,3z^2-r^2}$	$m\left[n^2 - \frac{1}{2}(l^2 + m^2)\right](pd\sigma) - \sqrt{3}mn^2(pd\pi)$
$E_{z,3z^2-r^2}$	$n\left[n^2 - \frac{1}{2}(l^2 + m^2)\right](pd\sigma) - \sqrt{3}n(l^2 + m^2(pd\pi)$
$E_{xy,xy}$	$3l^2m^2(dd\sigma) + (l^2 + m^2 - 4l^2m^2)(dd\pi) + (n^2 + l^2m^2)(dd\delta)$
$E_{xy,yz}$	$3lm^2n(dd\sigma) + ln(1 - 4m^2)(dd\pi) + ln(m^2 - 1)(dd\delta)$
$E_{xy,zx}$	$3l^2mn(dd\sigma) + mn(1 - 4l^2)(dd\pi) + mn(l^2 - 1)(dd\delta)$
E_{xy,x^2-y^2}	$\frac{3}{2}lm(l^2 - m^2)(dd\sigma) + 2lm(m^2 - l^2)(dd\pi) + \frac{1}{2}lm(l^2 - m^2)(dd\delta)$
E_{yz,x^2-y^2}	$\frac{3}{2}mn(l^2 - m^2)(dd\sigma) - mn[1 + 2(l^2 - m^2)](dd\pi) + mn[1 + \frac{1}{2}(l^2 - m^2)(dd\delta)$
E_{zx,x^2-y^2}	$\frac{3}{2}nl(l^2 - m^2)(dd\sigma) + nl[1 - 2(l^2 - m^2)](dd\pi) - nl[1 - \frac{1}{2}(l^2 - m^2)(dd\delta)$
$E_{xy,3z^2-r^2}$	$\sqrt{3}lm\left[n^2 - \frac{1}{2}(l^2 + m^2)\right](dd\sigma) - 2\sqrt{3}lmn^2(dd\pi) + \frac{1}{2}\sqrt{3}lm(1 + n^2)(dd\delta)$
$E_{yz,3z^2-r^2}$	$\sqrt{3}mn\left[n^2 - \frac{1}{2}(l^2 + m^2)\right](dd\sigma) + \sqrt{3}mn(l^2 + m^2 - n^2)(dd\pi) - \frac{1}{2}\sqrt{3}mn(l^2 + m^2)(dd\delta)$
$E_{zx,3z^2-r^2}$	$\sqrt{3}ln\left[n^2 - \frac{1}{2}(l^2 + m^2)\right](dd\sigma) + \sqrt{3}ln(l^2 + m^2 - n^2)(dd\pi) - \frac{1}{2}\sqrt{3}ln(l^2 + m^2)(dd\delta)$
$E_{x^2-y^2,x^2-y^2}$	$\frac{1}{2}\sqrt{3}(l^2 - m^2)[n^2 - \frac{1}{2}(l^2 + m^2)](dd\sigma) + \sqrt{3}n^2(m^2 - l^2)(dd\pi) + \frac{1}{4}\sqrt{3}(1 + n^2)(l^2$
$E_{x^2-y^2,3z^2-r^2}$	$\left[n^2 - \frac{1}{2}(l^2 + m^2)\right]^2 (dd\sigma) + 3n^2(l^2 + m^2)(dd\pi) + \frac{13}{4}\sqrt{3}(l^2 + m^2)^2(dd\delta)$
$E_{3z^2-r^2,3z^2-r^2}$	$\frac{3}{4}(l^2 - m^2)^2(dd\sigma) + [l^2 + m^2 - (l^2 - m^2)^2](dd\pi) + [n^2 + \frac{1}{4}(l^2 - m^2)^2](dd\delta)$

Using this tight binding formalism, the Kohn-Sham eigenstates, and the addition of a small density fluctuation normalization term ($\delta n(r) = n - n_0$), equation 2.2 becomes equation 2.7 [188].

$$E = \sum \{\Psi_i \,|H^0|\,\Psi_i\} - \frac{1}{2} \int \int \frac{n_0(r')n_0(r)}{|r - r'|} d^3r \, d^3r' + E_{xc}[n_0]$$

$$- \int V_{xc}[n_0] \, n_0(r) \, d^3r + E_N \qquad\qquad 2.7$$

$$+ \frac{1}{2} \int \int (\frac{1}{|r - r'|} + \frac{\delta^2 E_{xc}}{\delta n \, \delta n'}) \delta n \delta n' \, d^3r \, d^3r'$$

Where, E_N is the nuclear repulsion term given in equation 2.8.

$$E_N = \frac{1}{2} \sum \frac{Z_\propto Z_\beta}{|R_\propto - R_\beta|} \qquad\qquad 2.8$$

As in a normal tight binding model, terms were collected into a repulsion term (E_{rep}) and a second order fluctuation term (E^2), as shown in equations 2.9 and 2.10 respectively, in order to produce a simplified energy expression (equation 2.11).

$$E_{rep}[n_0] = -\frac{1}{2} \int \int \frac{n_0(r')n_0(r)}{|r - r'|} d^3r \, d^3r' + E_{xc}[n_0]$$

$$\qquad\qquad 2.9$$

$$- \int V_{xc}[n_0] \, n_0(r) \, d^3r + E_N$$

$$E^2[\delta n, n_0] = \frac{1}{2} \int \int (\frac{1}{|r - r'|} + \frac{\delta^2 E_{xc}}{\delta n \, \delta n'}) \delta n \delta n' \, d^3r \, d^3r' \qquad\qquad 2.10$$

$$E = \sum \{\Psi_i \,|H^0|\,\Psi_i\} + E_{rep}[n_0] + E^2[\delta n, n_0] \qquad 2.11$$

Subsequently, tight binding was used to expand the Kohn-Sham wave functions into localized atomic orbitals. In the construction of these orbitals, the pseudopotential contributions were neglected, an action that was justified by the approximations made in the construction of the orbitals using the localized method [189]. Considering the two-center approximation and neglecting the unnecessary terms, the Hamiltonian matrix elements were shown to be described by equation 2.12 [190].

$$H^0_{\mu v} = \begin{cases} \epsilon^{free\ atom}_{\mu}, & \mu = v \\ \langle \phi_u | \hat{T} + v_{eff}[n^0_\alpha + n^0_\beta] | \phi_v \rangle, & \mu \in \alpha, v \in \beta \end{cases} \qquad 2.12$$

In equation 2.12, v_{eff} is the Kohn-Sham potential, ϕ_u and ϕ_v are the basis functions, and n^0_α and n^0_β are the input densities of the α and β atom indices respectively. The Kohn-Sham potential can be solved by using equation 2.13, while the basis functions and input densities are found by solving the modified Schrodinger equation (see equation 2.14).

$$v_{eff}[n_0] = V_{ext} + \int' \frac{n'_0}{|r - r'|} + V_{xc}[n_0] \qquad 2.13$$

$$\left[\hat{T} + v_{eff}[n^0_\alpha] + \left(\frac{r}{r_0}\right)^2 \right] \phi_v(r) = \epsilon_v \phi_v(r) \qquad 2.14$$

Equation 2.14, was also used to confine the atomic charge densities to model a pseudo atom [185]. This is done because it has been shown to be a better approximation of the atoms in the system being modeled [191]. Frauenheim *et al.* [188] also commented that the use of equation 2.14 to solve for the basis functions and input densities, did not require the calibration of integrals for the optimization of the atomic geometry.

2.7.3 Non-Equilibrium Green's Functions

Non-equilibrium Green's functions (NEGF) are used to model the electron transport of a system at the molecular level [192]. NEGF produces an atomic level description of the electron transport, thus, the channel-contact regions can be modeled, and the tunneling of the Schottky barriers at the contact can be considered [193]. The theory considers an electronic device split up in three sections. The contacts, the molecular conducting channel, and the extended molecule. The ability to model an extended molecule means that surface adsorbed atoms are able to be included. Hence, the NEGF theory in conjunction with DFTB presents itself as an excellent approach to model CNT devices.

The Green's formalism begins with breaking the system into the contact and the device regions [194]. The properties of the contacts are assumed to be that of a bulk material and are considered to be semi-infinite. Also, more than two contacts can be included in the model. The device region is described by the molecular quantum conducting channel connecting the contacts, and are broken into principal layers (PL) which are all the same size and shape. Only the principal layers adjacent to one another can interact. By placing an electric potential between the contacts, charge is forced to be passed through the adjacent PLs in the device region.

In the NEGF theory, the density matrix is computed as follows by equation 2.15

$$\rho = \frac{1}{2\pi i} \int_{-\infty}^{\infty} dE G^{<}(E) \qquad \text{2.15}$$

where $G^{<}$ is the electron-electron correlation matrix. Equation 2.15 can be further expanded into equation 2.16

$$\rho = \int_{-\infty}^{+\infty} dE f_C(E) G^r(E) - \int_{-\infty}^{+\infty} dE f_C(E) G^a(E)$$

$$+ \sum dE \left[f_\alpha(E) - f_c(E) \right] G^r(E) \Gamma_\alpha(E) G^a(E)$$

2.16

where f_C is the Fermi function. The first term in 2.16 is the contribution by the retarded

Green's functions and can be calculated by a complex contour, the second term is the

contribution by the advanced Green's functions and can be completed by taking the adjoint,

and the third term is the contribution by the correlation Green's functions and must be

integrated on a real axis [192]. In the third term, the broadening function can be described

by equation 2.17

$$\Gamma_\alpha(E) = i[\Sigma_\alpha^r(E) - \Sigma_\alpha^{r\dagger}(E)]$$

2.17

where Σ_α are the contact self-energies, which can be computed via equation 2.18

$$\Sigma_\alpha = T_{L(\alpha),\alpha} \, g_{a,a} \, T_{\alpha,L(\alpha)}$$

2.18

where $L(\alpha)$ is the principal layer that interact with the α contact [194]. The $g_{a,a}$ variable

is the surface Green's function of α, and T is the off-diagonal terms described by equation

2.19.

$$T_{L,L+1} = E S_{L,L+1} - H_{L,L+1}$$

2.19

The iterative process of solving the Green's functions of the system begins with the

calculations of the partial surface Green's function of the system cut at L, and interacting

only with the left ($g_{L,L}^R$) and the right ($g_{L,L}^L$) part of the system [194]. This approach is given

by equations 2.20 and 2.21

$$g_{L,L}^R = \left[ES_{L,L} - H_{L,L} - T_{L,L+1}\, g_{L+1,L+1}^R T_{L+1,L}\right]^{-1} \qquad \text{2.20}$$

$$g_{L,L}^L = \left[ES_{L,L} - H_{L,L} - T_{L,L-1}\, g_{L-1,L-1}^L T_{L-1,L}\right]^{-1} \qquad \text{2.21}$$

In both equations (2.20 and 2.21), S represents the overlap matrix while H represents the Hamiltonian matrix of the principal layer L. Solving for $g_{L,L}^R$ begins at the Nth layer and ends at the 1st layer while solving for $g_{L,L}^L$ requires the opposite direction. Finally, the partial Green's functions are used in an iterative process to solve for the Green's functions of each layer starting with layer 1 and finishing at the N layer. These calculations are performed using equations 2.22-2.26

$$G_{1,1} = \left[ES_{1,1} - H_{1,1} - \Sigma_{1,1} - T_{1,2}g_{2,2}^R T_{2,1}\right]^{-1} \qquad \text{2.22}$$

$$G_{L,L} = g_{L,L}^R + g_{L,L}^R T_{L,L-1}G_{L-1,L-1}T_{L-1,L}g_{L,L}^R \qquad \text{2.23}$$

$$G_{L-1,L} = -G_{L-1,L-1}T_{L-1,L}g_{L,L}^R \qquad \text{2.24}$$

$$G_{L,L-1} = -g_{L,L}^R T_{L,L-1}G_{L-1,L-1} \qquad \text{2.25}$$

$$G_{L,L}^{<,\alpha} = G_{L,L(\alpha)}^R \Gamma_\alpha G_{L,L(\alpha)}^{R\dagger} \qquad \text{2.26}$$

Where the layer 1 is described by equation 2.22, layer 2 through N are described by equation 2.23, the off-diagonal blocks by equations 2.24 and 2.25, and the tridiagonal blocks by 2.26. Once a converged solution is reached the charge density can be found by equation 2.15.

2.7.4 Poisson Solutions

A further step in the modeling field is the use of the electron charge density obtained via the DFTB and NEGF models in the Poisson equations to find the electrical current through the molecular conducting channel [193,194]. The first step in the Poisson application is to model the total electron charge density using the neutral atom densities, and the density fluctuations as shown in equation 2.27.

$$n(r) = \sum_i [n_i^0(r) + F_{00}^i(r)\Delta q_i] \qquad 2.27$$

In this equation, $n_i^0(r)$ is the atomic density, $F_{00}^i(r)$ is the s-like radial functions, and Δq_i is the Mulliken charge [194]. The primary Poisson equation for the electrostatic potential is given by equation 2.28

$$\nabla^2 V = 4\pi \sum_i [n_i^0(r) + F_{00}^i(r)\Delta q_i] + \textbf{Boundary conditions} \qquad 2.28$$

where V is the Hartree potential, and the boundary conditions are imposed on the contacts, and the contact/device interface directed by the bulk electrochemical potentials. Equation 2.28 is solved in real space using the partial differential equation 2.29

$$\rho(r) = \sum_{i=x,y,z} c_{ii}(r)\partial_i^2 V(r) + \sum_{i=x,y,z} c_i(r)\partial_i V(r) + c(r)V(r) \qquad 2.29$$

where $c_i(r) = c(r) = 0$ and $c_{ii}(r) = -\frac{1}{4}\pi$ for a two contact system. Using equation 2.29, more constants can be added, and the Dirichlet boundary (fixed boundary) conditions can be used to simulate both planar and cylindrical gates.

Using equation 2.29, an iterative solution to the electrostatic potential is found. This Hartree potential can then be used as an input in equation 2.30 to find the probability of transmission from source to drain or the transmission coefficient ($T(E)$) [193].

$$T(E) = Trace(\Gamma_S G \Gamma_D G^+)$$
2.30

where Γ_S and Γ_D are the broadening functions of the source and drain respectively. Finally, this transmission coefficient in conjunction with the source and drain Fermi functions (f_S and f_S) are used to find the electrical current passing through the system (see equation 2.31)

$$I = \frac{4e}{h} \int T(E)[f_S(E) - f_D(E)]dE$$
2.31

2.7.5 Studies on CNTs using DFT

As previously described, DFT presents itself as a suitable model for carbon nanotubes due to SWCNTs abilities to act as quantum wires. Thanks to this feature, many studies have been performed on them using DFT [174–177]. Louis *et al.* [175] were able to use DFT to confirm that the structure of a SWCNT is linked to its mechanical properties. The calculated band structure of a (14,0) SWCNT showed a small band gap, meaning that it acts like a semiconductor. Conversely, the band gap of a (8,8) SWCNT was zero which points to its metallic nature. These calculated band structures are presented in Figure 2-45.
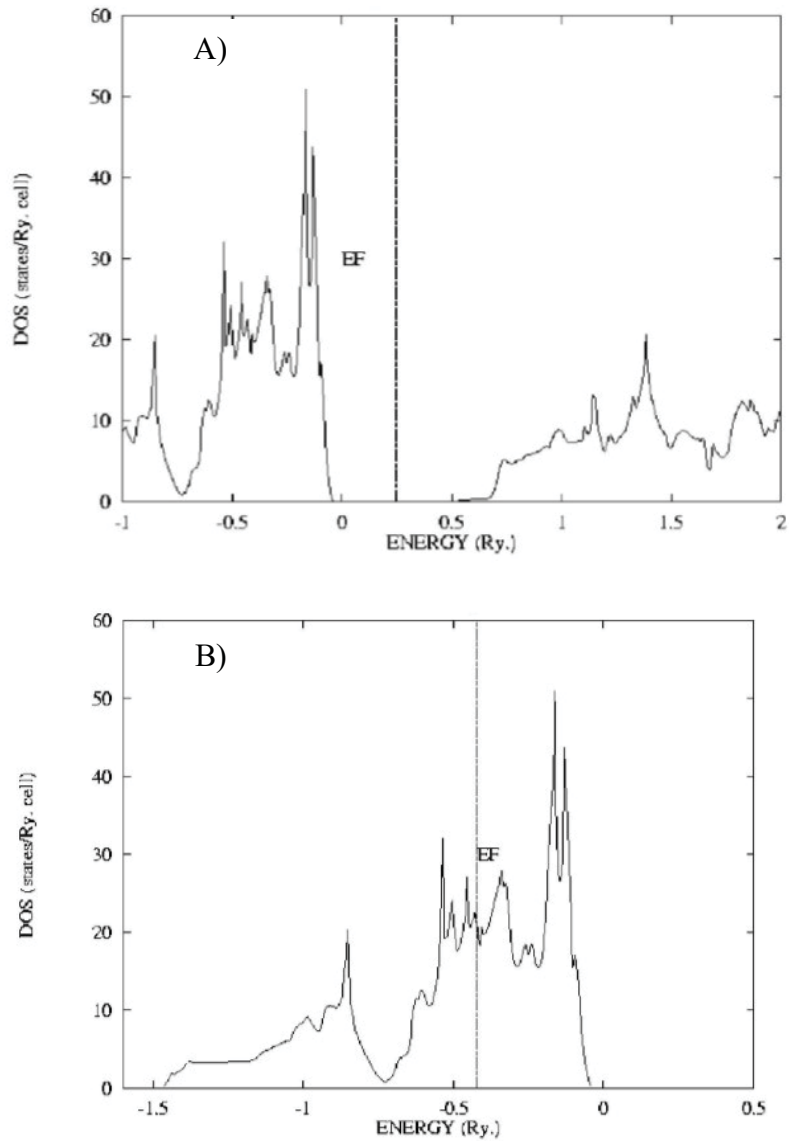
Figure 2-45: Density of states calculated by DFT for A) (14,0) and B) (8,8) SWCNTs with the Fermi level centered in the band gap between the valence and the conduction bands. The band gap in A) signals that a (14,0) SWCNT acts as a semiconductor while a lack of band gap in B) indicates that a (8,8) SWCNT acts as a metal [175].

A study performed by Salehi and Gharbavi resulted in a similar confirmation of the electronic properties being dictated by the SWCNT structure by showing the calculated density of states for a (7,7) structure, which resulted in a zero band gap [176]. Other tube geometries studied include (6,0) , (7,0), (6,2), and (6,3) [177].

DFT has also been used to model the adsorption of titanium onto a SWCNT using the Vienna Ab initio Simulation Package (VASP) [175]. Here, the average electron density near the Fermi level was used instead of the actual Fermi level in order to take van Hove singularities into consideration. The distance between the titanium and the (14,0) zigzag tube was set at 2.14 Å and the distance for the (8,8) nanotube was set at 2.24 Å. Using this setup, it was shown that the titatnium affected the band structure of the tube. The (14,0) SWCNT band structure initially contained a small band gap, but the addition of the titanium reduced this gap to zero. Thus, the (14,0) SWCNT adopted metallic characteristics. Conversly, the electrical properties of the (8,8) SWCNT became like those shown by a semiconductor. Thus, it has been displayed that DFT can model the effect of charge transfer between adsorbed molecules and a CNT.

2.7.6 Studies on CNTs using DFTB

DFTB has been used to investigate the affect of the CNT/contact interaction, defects, and effects of adsorbed molecules on the electical properties of CNTs [178]. Here, three contact materials, gold, platinum, and palladium, were considered. One of the findings was that the bond between platinum and CNT exhibits the highest binding energy of all three contacts. Another finding was that platinum and palladium can form actual covalent bonds with the CNT that can affect their electronic properties. Studying physisorbed and chemisorbed atoms on the CNTs, revealed that while chemisorbed atoms affect the

transmission probability, and therefore their electron conduction properties, physisorbed atoms have no effect on the electronic properties [178]. A study by Fan *et al.* [179] used DFTB to focus on the physisorption of 1-pyrenebutanoic acid, succinimidyl ester (PSE), and showed that the pyrene ring of the PSE ineracts with the CNT through a π-π stacking bond. The various sites of adsorption considered by Fan *et al.* are visualized in Figure 2-46. As seen in Figure 2-46, PSE adsorbs and is locked in place through a π-π stacking. As in the work performed by Maiti *et al.* [178], it was found that this form of binding does not affect the density of states or the electrical transmission properties of the tube [179].
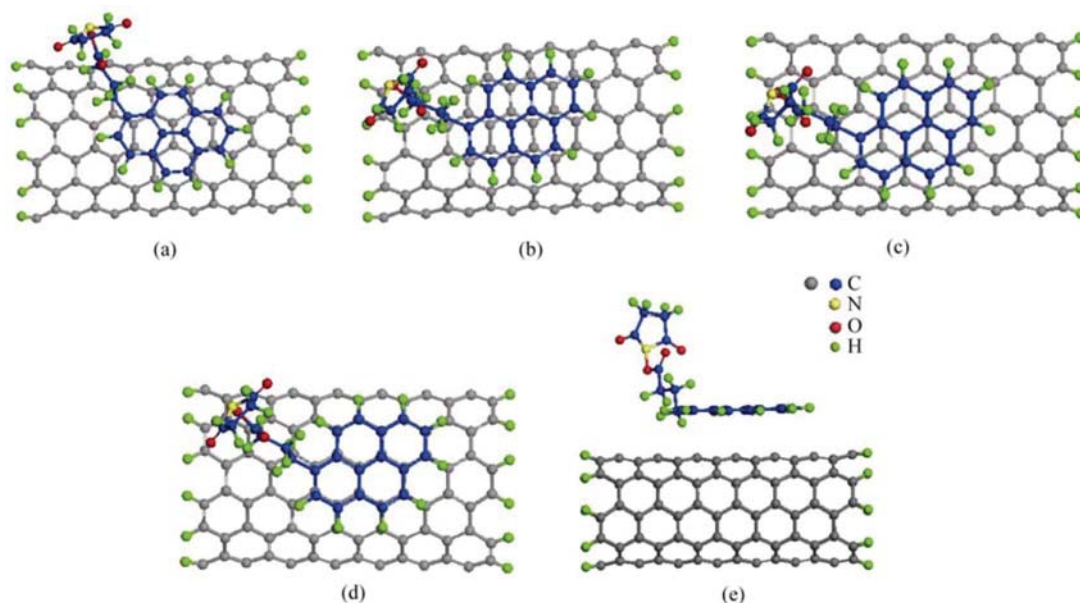
Figure 2-46:   Modeling of the adsorption sites of 1-pyrenebutanoic acid, succinimidyl ester (PSE) on a SWCNT: a) along the tube axis, b) 30° to axis in a bridge orientation, c) 30° to axis in a stack orientation, d) 30° to axis in a hollow orientation, e) side view of PSE in relation to the CNT [179].

2.8 References

[1] Iijima, S., 1991, "Helical Microtubules of Graphitic Carbon," Nature, **354**, pp. 56–58.

[2] Iijima, S., and Ichihashi, T., 1993, "Single-Shell Carbon Nanotubes of 1-Nm Diameter," Nature, **363**(6430), pp. 603–605.

[3] Odom, T. W., Huang, J.-L., Kim, P., and Lieber, C. M., 1998, "Atomic Structure and Electronic Properties of Single-Walled Carbon Nanotubes," Nature, **391**(6662), pp. 62–64.

[4] Belin, T., and Epron, F., 2005, "Characterization Methods of Carbon Nanotubes: A Review," Mater. Sci. Eng. B, **119**(2), pp. 105–118.

[5] Thostenson, E. T., Ren, Z., and Chou, T.-W., 2001, "Advances in the Science and Technology of Carbon Nanotubes and Their Composites: A Review," Compos. Sci. Technol., **61**(13), pp. 1899–1912.

[6] Rafiee, R., and Pourazizi, R., 2014, "Evaluating the Influence of Defects on the Young's Modulus of Carbon Nanotubes Using Stochastic Modeling," Mater. Res., **17**(3), pp. 758–766.

[7] Guo, T., Nikolaev, P., Rinzler, A. G., Tomanek, D., Colbert, D. T., and Smalley, R. E., 1995, "Self-Assembly of Tubular Fullerenes," J. Phys. Chem., **99**(27), pp. 10694–10697.

[8] Sinnott, S. B., Andrews, R., Qian, D., Rao, A. M., Mao, Z., Dickey, E. C., and Derbyshire, F., 1999, "Model of Carbon Nanotube Growth through Chemical Vapor Deposition," Chem. Phys. Lett., **315**(1–2), pp. 25–30.

[9]   Chhowalla, M., Teo, K. B. K., Ducati, C., Rupesinghe, N. L., Amaratunga, G. a. J., Ferrari, A. C., Roy, D., Robertson, J., and Milne, W. I., 2001, "Growth Process Conditions of Vertically Aligned Carbon Nanotubes Using Plasma Enhanced Chemical Vapor Deposition," J. Appl. Phys., **90**(10), pp. 5308–5317.

[10]   Arora, N., and Sharma, N. N., 2014, "Arc Discharge Synthesis of Carbon Nanotubes: Comprehensive Review," Diam. Relat. Mater., **50**, pp. 135–150.

[11]   Ando, Y., and Iijima, S., 1993, "Preparation of Carbon Nanotubes by Arc-Discharge Evaporation," Jpn. J. Appl. Phys., **32**(Part 2, No.1A/B), pp. L107–L109.

[12]   Zhao, X., Ohkohchi, M., Wang, M., Iijima, S., Ichihashi, T., and Ando, Y., 1997, "Preparation of High-Grade Carbon Nanotubes by Hydrogen Arc Discharge," Carbon, **35**(6), pp. 775–781.

[13]   T. Guo, P. N., 1995, "Catalytic Growth of Single-Walled Nanotubes by Laser Vaporization," Chem. Phys. Lett., **243**(1–2), pp. 49–54.

[14]   Brukh, R., and Mitra, S., 2006, "Mechanism of Carbon Nanotube Growth by CVD," Chem. Phys. Lett., **424**(1–3), pp. 126–132.

[15]   Cassell, A. M., Raymakers, J. A., Kong, J., and Dai, H., 1999, "Large Scale CVD Synthesis of Single-Walled Carbon Nanotubes," J. Phys. Chem. B, **103**(31), pp. 6484–6492.

[16]   Kong, J., Cassell, A. M., and Dai, H., 1998, "Chemical Vapor Deposition of Methane for Single-Walled Carbon Nanotubes," Chem. Phys. Lett., **292**(4–6), pp. 567–574.

[17]   Baker, R. T. K., Harris, P. S., Thomas, R. B., and Waite, R. J., 1973, "Formation of Filamentous Carbon from Iron, Cobalt and Chromium Catalyzed Decomposition of Acetylene," J. Catal., **30**(1), pp. 86–95.

[18] Hata, K., Futaba, D. N., Mizuno, K., Namai, T., Yumura, M., and Iijima, S., 2004, "Water-Assisted Highly Efficient Synthesis of Impurity-Free Single-Walled Carbon Nanotubes," Science, **306**(5700), pp. 1362–1364.

[19] Zhong, G., Hofmann, S., Yan, F., Telg, H., Warner, J. H., Eder, D., Thomsen, C., Milne, W. I., and Robertson, J., 2009, "Acetylene: A Key Growth Precursor for Single-Walled Carbon Nanotube Forests," J. Phys. Chem. C, **113**(40), pp. 17321–17325.

[20] Fan, S., Chapline, M. G., Franklin, N. R., Tombler, T. W., Cassell, A. M., and Dai, H., 1999, "Self-Oriented Regular Arrays of Carbon Nanotubes and Their Field Emission Properties," Science, **283**(5401), pp. 512–514.

[21] Kong, J., Soh, H. T., Cassell, A. M., Quate, C. F., and Dai, H., 1998, "Synthesis of Individual Single-Walled Carbon Nanotubes on Patterned Silicon Wafers," Nature, **395**(6705), pp. 878–881.

[22] Hirsch, A., 2002, "Functionalization of Single-Walled Carbon Nanotubes," Angew. Chem. Int. Ed., **41**(11), pp. 1853–1859.

[23] Bellucci, S., 2005, "Carbon Nanotubes: Physics and Applications," Phys. Status Solidi C, **2**(1), pp. 34–47.

[24] Mawhinney, D. B., Naumenko, V., Kuznetsova, A., Yates Jr., J. T., Liu, J., and Smalley, R. E., 2000, "Surface Defect Site Density on Single Walled Carbon Nanotubes by Titration," Chem. Phys. Lett., **324**(1–3), pp. 213–216.

[25] Monthioux, M., Smith, B. W., Burteaux, B., Claye, A., Fischer, J. E., and Luzzi, D. E., 2001, "Sensitivity of Single-Wall Carbon Nanotubes to Chemical Processing: An Electron Microscopy Investigation," Carbon, **39**(8), pp. 1251–1272.

[26] Chen, J., Hamon, M. A., Hu, H., Chen, Y., Rao, A. M., Eklund, P. C., and Haddon, R. C., 1998, "Solution Properties of Single-Walled Carbon Nanotubes," Science, **282**(5386), pp. 95–98.

[27] Balasubramanian, K., and Burghard, M., 2005, "Chemically Functionalized Carbon Nanotubes," Small Weinh. Bergstr. Ger., **1**(2), pp. 180–192.

[28] Hamon, M. A., Hu, H., Bhowmik, P., Niyogi, S., Zhao, B., Itkis, M. E., and Haddon, R. C., 2001, "End-Group and Defect Analysis of Soluble Single-Walled Carbon Nanotubes," Chem. Phys. Lett., **347**(1–3), pp. 8–12.

[29] Zhang, J., Zou, H., Qing, Q., Yang, Y., Li, Q., Liu, Z., Guo, X., and Du, Z., 2003, "Effect of Chemical Oxidation on the Structure of Single-Walled Carbon Nanotubes," J. Phys. Chem. B, **107**(16), pp. 3712–3718.

[30] Zhang, R., Wang, X., and Shiu, K.-K., 2007, "Accelerated Direct Electrochemistry of Hemoglobin Based on Hemoglobin-Carbon Nanotube (Hb-CNT) Assembly," J. Colloid Interface Sci., **316**(2), pp. 517–522.

[31] "Carbodiimide Crosslinker Chemistry" [Online]. Available: https://www.thermofisher.com/us/en/home/life-science/protein-biology/protein-biology-learning-center/protein-biology-resource-library/pierce-protein-methods/carbodiimide-crosslinker-chemistry.html. [Accessed: 07-Sep-2016].

[32] Bahr, J. L., and Tour, J. M., 2002, "Covalent Chemistry of Single-Wall Carbon Nanotubes," J. Mater. Chem., **12**(7), pp. 1952–1958.

[33] Stevens, J. L., Huang, A. Y., Peng, H., Chiang, I. W., Khabashesku, V. N., and Margrave, J. L., 2003, "Sidewall Amino-Functionalization of Single-Walled Carbon Nanotubes through Fluorination and Subsequent Reactions with Terminal Diamines," Nano Lett., **3**(3), pp. 331–336.

[34] Khabashesku, V. N., Billups, W. E., and Margrave, J. L., 2002, "Fluorination of Single-Wall Carbon Nanotubes and Subsequent Derivatization Reactions," Acc. Chem. Res., **35**(12), pp. 1087–1095.

[35] Bettinger, H. F., 2003, "Experimental and Computational Investigations of the Properties of Fluorinated Single-Walled Carbon Nanotubes," ChemPhysChem, **4**(12), pp. 1283–1289.

[36] Lagow, R. J., Badachhape, R. B., Wood, J. L., and Margrave, J. L., 1974, "Some New Synthetic Approaches to Graphite–fluorine Chemistry," J. Chem. Soc. Dalton Trans., **1974**(12), pp. 1268–1273.

[37] Boul, P. J., Liu, J., Mickelson, E. T., Huffman, C. B., Ericson, L. M., Chiang, I. W., Smith, K. A., Colbert, D. T., Hauge, R. H., Margrave, J. L., and Smalley, R. E., 1999, "Reversible Sidewall Functionalization of Buckytubes," Chem. Phys. Lett., **310**(3–4), pp. 367–372.

[38] Mickelson, E. T., Chiang, I. W., Zimmerman, J. L., Boul, P. J., Lozano, J., Liu, J., Smalley, R. E., Hauge, R. H., and Margrave, J. L., 1999, "Solvation of Fluorinated Single-Wall Carbon Nanotubes in Alcohol Solvents," J. Phys. Chem. B, **103**(21), pp. 4318–4322.

[39] García, A., Herrero, M. A., Frein, S., Deschenaux, R., Muñoz, R., Bustero, I., Toma, F., and Prato, M., 2008, "Synthesis of Dendrimer-Carbon Nanotube Conjugates," Phys. Status Solidi A, **205**(6), pp. 1402–1407.

[40] Georgakilas, V., Kordatos, K., Prato, M., Guldi, D. M., Holzinger, M., and Hirsch, A., 2002, "Organic Functionalization of Carbon Nanotubes," J. Am. Chem. Soc., **124**(5), pp. 760–761.

[41] Tagmatarchis, N., Georgakilas, V., Prato, M., and Shinohara, H., 2002, "Sidewall Functionalization of Single-Walled Carbon Nanotubes through Electrophilic Addition," Chem. Commun., (18), pp. 2010–2011.

[42] Umek, P., Seo, J. W., Hernadi, K., Mrzel, A., Pechy, P., Mihailovic, D. D., and Forró, L., 2003, "Addition of Carbon Radicals Generated from Organic Peroxides to Single Wall Carbon Nanotubes," Chem. Mater., **15**(25), pp. 4751–4755.

[43] Lu, X., and Chen, Z., 2005, "Curved Pi-Conjugation, Aromaticity, and the Related Chemistry of Small Fullerenes (< C60) and Single-Walled Carbon Nanotubes," Chem. Rev., **105**(10), pp. 3643–3696.

[44] Chen, R. J., Zhang, Y., Wang, D., and Dai, H., 2001, "Noncovalent Sidewall Functionalization of Single-Walled Carbon Nanotubes for Protein Immobilization," J. Am. Chem. Soc., **123**(16), pp. 3838–3839.

[45] Zhao, J., Lu, J. P., Han, J., and Yang, C.-K., 2003, "Noncovalent Functionalization of Carbon Nanotubes by Aromatic Organic Molecules," Appl. Phys. Lett., **82**(21), pp. 3746–3748.

[46] Zhao, Y.-L., and Stoddart, J. F., 2009, "Noncovalent Functionalization of Single-Walled Carbon Nanotubes," Acc. Chem. Res., **42**(8), pp. 1161–1171.

[47] Shim, M., Shi Kam, N. W., Chen, R. J., Li, Y., and Dai, H., 2002, "Functionalization of Carbon Nanotubes for Biocompatibility and Biomolecular Recognition," Nano Lett., **2**(4), pp. 285–288.

[48] Carrillo, A., Swartz, J. A., Gamba, J. M., Kane, R. S., Chakrapani, N., Wei, B., and Ajayan, P. M., 2003, "Noncovalent Functionalization of Graphite and Carbon Nanotubes with Polymer Multilayers and Gold Nanoparticles," Nano Lett., **3**(10), pp. 1437–1440.

[49] Chen, R. J., Bangsaruntip, S., Drouvalakis, K. A., Kam, N. W. S., Shim, M., Li, Y., Kim, W., Utz, P. J., and Dai, H., 2003, "Noncovalent Functionalization of Carbon Nanotubes for Highly Specific Electronic Biosensors," Proc. Natl. Acad. Sci., **100**(9), pp. 4984–4989.

[50] Chen, J., and Collier, C. P., 2005, "Noncovalent Functionalization of Single-Walled Carbon Nanotubes with Water-Soluble Porphyrins," J. Phys. Chem. B, **109**(16), pp. 7605–7609.

[51] Han, W., Fan, S., Li, Q., and Hu, Y., 1997, "Synthesis of Gallium Nitride Nanorods Through a Carbon Nanotube-Confined Reaction," Science, **277**(5330), pp. 1287–1289.

[52] Dujardin, E., Ebbesen, T. W., Krishnan, A., and Treacy, M. M. J., 1998, "Wetting of Single Shell Carbon Nanotubes," Adv. Mater., **10**(17), pp. 1472–1475.

[53] Govindaraj, A., Satishkumar, B. C., Nath, M., and Rao, C. N. R., 2000, "Metal Nanowires and Intercalated Metal Layers in Single-Walled Carbon Nanotube Bundles," Chem. Mater., **12**(1), pp. 202–205.

[54] Matsui, K., Pradhan, B. K., Kyotani, T., and Tomita, A., 2001, "Formation of Nickel Oxide Nanoribbons in the Cavity of Carbon Nanotubes," J. Phys. Chem. B, **105**(24), pp. 5682–5688.

[55] Smith, B. W., Monthioux, M., and Luzzi, D. E., 1999, "Carbon Nanotube Encapsulated Fullerenes: A Unique Class of Hybrid Materials," Chem. Phys. Lett., **315**(1–2), pp. 31–36.

[56] Wilson, M., and Madden, P. A., 2001, "Growth of Ionic Crystals in Carbon Nanotubes," J. Am. Chem. Soc., **123**(9), pp. 2101–2102.

[57] Smith, B. W., and Luzzi, D. E., 2000, "Formation Mechanism of Fullerene Peapods and Coaxial Tubes: A Path to Large Scale Synthesis," Chem. Phys. Lett., **321**(1–2), pp. 169–174.

[58] Okazaki, T., Suenaga, K., Hirahara, K., Bow, S., Iijima, S., and Shinohara, H., 2001, "Real Time Reaction Dynamics in Carbon Nanotubes," J. Am. Chem. Soc., **123**(39), pp. 9673–9674.

[59] Gao, Y., and Kyratzis, I., 2008, "Covalent Immobilization of Proteins on Carbon Nanotubes Using the Cross-Linker 1-Ethyl-3-(3-Dimethylaminopropyl)carbodiimide—a Critical Assessment," Bioconjug. Chem., **19**(10), pp. 1945–1950.

[60] Jiang, K., Schadler, L. S., Siegel, R. W., Zhang, X., Zhang, H., and Terrones, M., 2004, "Protein Immobilization on Carbon Nanotubes via a Two-Step Process of Diimide-Activated Amidation," J. Mater. Chem., **14**(1), pp. 37–39.

[61] Kim, Y.-S., Cho, J.-H., Ansari, S. G., Kim, H.-I., Dar, M. A., Seo, H.-K., Kim, G.-S., Lee, D.-S., Khang, G., and Shin, H.-S., 2006, "Immobilization of Avidin on the Functionalized Carbon Nanotubes," Synth. Met., **156**(14–15), pp. 938–943.

[62] Williams, K. A., Veenhuizen, P. T. M., de la Torre, B. G., Eritja, R., and Dekker, C., 2002, "Nanotechnology: Carbon Nanotubes with DNA Recognition," Nature, **420**(6917), pp. 761–761.

[63] Singh, K. V., Pandey, R. R., Wang, X., Lake, R., Ozkan, C. S., Wang, K., and Ozkan, M., 2006, "Covalent Functionalization of Single Walled Carbon Nanotubes with Peptide Nucleic Acid: Nanocomponents for Molecular Level Electronics," Carbon, **44**(9), pp. 1730–1739.

[64] Erlanger, B. F., Chen, B.-X., Zhu, M., and Brus, L., 2001, "Binding of an Anti-Fullerene IgG Monoclonal Antibody to Single Wall Carbon Nanotubes," Nano Lett., **1**, pp. 465–467.

[65] Cang-Rong, J. T., and Pastorin, G., 2009, "The Influence of Carbon Nanotubes on Enzyme Activity and Structure: Investigation of Different Immobilization Procedures through Enzyme Kinetics and Circular Dichroism Studies," Nanotechnology, **20**(25), p. 255102.

[66] Davis, J. J., Green, M. L. H., Hill, H. A. O., Leung, Y. C., Sadler, P. J., Sloan, J., Xavier, A. V., and Tsang, S. C., 1998, "The Immobilisation of Proteins in Carbon Nanotubes," Inorganica Chim. Acta, **272**(1–2), pp. 261–266.

[67] Guo, Z., Sadler, P. J., and Tsang, S. C., 1998, "Immobilization and Visualization of DNA and Proteins on Carbon Nanotubes," Adv. Mater., **10**(9), pp. 701–703.

[68] Balavoine, F., Schultz, P., Richard, C., Mallouh, V., Ebbesen, T. W., and Mioskowski, C., 1999, "Helical Crystallization of Proteins on Carbon Nanotubes: A First Step towards the Development of New Biosensors," Angew. Chem. Int. Ed., **38**(13/14), pp. 1912–1915.

[69] Azamian, B. R., Davis, J. J., Coleman, K. S., Bagshaw, C. B., and Green, M. L. H., 2002, "Bioelectrochemical Single-Walled Carbon Nanotubes," J. Am. Chem. Soc., **124**(43), pp. 12664–12665.

[70] Lin, Y., Allard, L. F., and Sun, Y.-P., 2004, "Protein-Affinity of Single-Walled Carbon Nanotubes in Water," J. Phys. Chem. B, **108**(12), pp. 3760–3764.

[71] Jia, N., Wang, L., Liu, L., Zhou, Q., and Jiang, Z., 2005, "Bamboo-like CNx Nanotubes for the Immobilization of Hemoglobin and Its Bioelectrochemistry," Electrochem. Commun., **7**(4), pp. 349–354.

[72] Mintmire, J. W., Dunlap, B. I., and White, C. T., 1992, "Are Fullerene Tubules Metallic?," Phys. Rev. Lett., **68**(5), pp. 631–634.

[73] Hamada, N., Sawada, S., and Oshiyama, A., 1992, "New One-Dimensional Conductors: Graphitic Microtubules," Phys. Rev. Lett., **68**(10), pp. 1579–1581.

[74] Derycke, V., Martel, R., Appenzeller, J., and Avouris, P., 2002, "Controlling Doping and Carrier Injection in Carbon Nanotube Transistors," Appl. Phys. Lett., **80**(15), pp. 2773–2775.

[75] Tans, S. J., Verschueren, A. R. M., and Dekker, C., 1998, "Room-Temperature Transistor Based on a Single Carbon Nanotube," Nature, **393**(6680), pp. 49–52.

[76] Saito, R., Fujita, M., Dresselhaus, G., and Dresselhaus, M. S., 1992, "Electronic Structure of Chiral Graphene Tubules," Appl. Phys. Lett., **60**(18), pp. 2204–2206.

[77] Saito, R., Fujita, M., Dresselhaus, G., and Dresselhaus, M. S., 1992, "Electronic Structure of Graphene Tubules Based on C60," Phys. Rev. B, **46**(3), pp. 1804–1811.

[78] Blakemore, J. S., 1985, *Solid State Physics*, Cambridge University Press.

[79] "Band Gap Measurement - OpenStax CNX" [Online]. Available: http://cnx.org/contents/d1c4c0c9-7bcb-4245-b320-6d6fdb3ade9e@1/Band-Gap-Measurement. [Accessed: 18-May-2016].

[80] Housecroft, C., and Sharpe, A. G., 2012, *Inorganic Chemistry*, Pearson Higher Ed.

[81] Reddy, S. R., 2004, *Electronic Devices and Circuits*, Alpha Science Int'l Ltd.

[82] "Ismail-Beigi Group - - Methods And Materials" [Online]. Available: http://volga.eng.yale.edu/index.php/FlashDrives/MethodsAndMaterials. [Accessed: 19-May-2016].

[83] Baliga, B. J., 2010, *Advanced Power MOSFET Concepts*, Springer Science & Business Media.

[84] Smith, W. F., and Hashemi, J., 2011, *Foundations of Materials Science and Engineering*, McGraw-Hill.

[85] Derycke, V., Martel, R., Appenzeller, J., and Avouris, P., 2001, "Carbon Nanotube Inter- and Intramolecular Logic Gates," Nano Lett., **1**(9), pp. 453–456.

[86] Sorescu, D. C., Jordan, K. D., and Avouris, P., 2001, "Theoretical Study of Oxygen Adsorption on Graphite and the (8,0) Single-Walled Carbon Nanotube," J. Phys. Chem. B, **105**(45), pp. 11227–11232.

[87] Martel, R., Derycke, V., Lavoie, C., Appenzeller, J., Chan, K. K., Tersoff, J., and Avouris, P., 2001, "Ambipolar Electrical Transport in Semiconducting Single-Wall Carbon Nanotubes," Phys. Rev. Lett., **87**(25), p. 256805.

[88] Singh, D. V., Jenkins, K. A., Appenzeller, J., Neumayer, D., Grill, A., and Wong, H. S. P., 2004, "Frequency Response of Top-Gated Carbon Nanotube Field-Effect Transistors," IEEE Trans. Nanotechnol., **3**(3), pp. 383–387.

[89] Pfleiderer, H., and Kusian, W., 1986, "Ambipolar Field-Effect Transistor," Solid-State Electron., **29**(3), pp. 317–319.

[90] Martel, R., Schmidt, T., Shea, H. R., Hertel, T., and Avouris, P., 1998, "Single- and Multi-Wall Carbon Nanotube Field-Effect Transistors," Appl. Phys. Lett., **73**(17), pp. 2447–2449.

[91] Appenzeller, J., Knoch, J., Derycke, V., Martel, R., Wind, S., and Avouris, P., 2002, "Field-Modulated Carrier Transport in Carbon Nanotube Transistors," Phys. Rev. Lett., **89**(12), p. 126801.

[92] Heinze, S., Tersoff, J., Martel, R., Derycke, V., Appenzeller, J., and Avouris, P., 2002, "Carbon Nanotubes as Schottky Barrier Transistors," Phys. Rev. Lett., **89**(10), p. 106801.

[93] Heinze, S., Radosavljević, M., Tersoff, J., and Avouris, P., 2003, "Unexpected Scaling of the Performance of Carbon Nanotube Schottky-Barrier Transistors," Phys. Rev. B, **68**(23), p. 235418.

[94] Javey, A., Guo, J., Wang, Q., Lundstrom, M., and Dai, H., 2003, "Ballistic Carbon Nanotube Field-Effect Transistors," Nature, **424**(6949), pp. 654–657.

[95] Snow, E. S., Novak, J. P., Campbell, P. M., and Park, D., 2003, "Random Networks of Carbon Nanotubes as an Electronic Material," Appl. Phys. Lett., **82**(13), pp. 2145–2147.

[96] Kocabas, C., Hur, S.-H., Gaur, A., Meitl, M. A., Shim, M., and Rogers, J. A., 2005, "Guided Growth of Large-Scale, Horizontally Aligned Arrays of Single-Walled Carbon Nanotubes and Their Use in Thin-Film Transistors," Small, **1**(11), pp. 1110–1116.

[97] Bachtold, A., Hadley, P., Nakanishi, T., and Dekker, C., 2001, "Logic Circuits with Carbon Nanotube Transistors," Science, **294**(5545), pp. 1317–1320.

[98] Wind, S. J., Appenzeller, J., Martel, R., Derycke, V., and Avouris, P., 2002, "Vertical Scaling of Carbon Nanotube Field-Effect Transistors Using Top Gate Electrodes," Appl. Phys. Lett., **80**(20), pp. 3817–3819.

[99] Javey, A., Guo, J., Farmer, D. B., Wang, Q., Wang, D., Gordon, R. G., Lundstrom, M., and Dai, H., 2004, "Carbon Nanotube Field-Effect Transistors with Integrated Ohmic Contacts and High-κ Gate Dielectrics," Nano Lett., **4**(3), pp. 447–450.

[100] Javey, A., Tu, R., Farmer, D. B., Guo, J., Gordon, R. G., and Dai, H., 2005, "High Performance N-Type Carbon Nanotube Field-Effect Transistors with Chemically Doped Contacts," Nano Lett., **5**(2), pp. 345–348.

[101] Chen, Z., Farmer, D., Xu, S., Gordon, R., Avouris, P., and Appenzeller, J., 2008, "Externally Assembled Gate-All-Around Carbon Nanotube Field-Effect Transistor," IEEE Electron Device Lett., **29**(2), pp. 183–185.

[102] Farmer, D. B., and Gordon, R. G., 2006, "Atomic Layer Deposition on Suspended Single-Walled Carbon Nanotubes via Gas-Phase Noncovalent Functionalization," Nano Lett., **6**(4), pp. 699–703.

[103] Cao, J., Wang, Q., Wang, D., and Dai, H., 2005, "Suspended Carbon Nanotube Quantum Wires with Two Gates," Small, **1**(1), pp. 138–141.

[104]   Cao, J., Wang, Q., and Dai, H., 2005, "Electron Transport in Very Clean, as-Grown Suspended Carbon Nanotubes," Nat. Mater., **4**(10), pp. 745–749.

[105]   Lin, Y.-M., Tsang, J. C., Freitag, M., and Avouris, P., 2007, "Impact of Oxide Substrate on Electrical and Optical Properties of Carbon Nanotube Devices," Nanotechnology, **18**(29), p. 295202.

[106]   Sangwan, V. K., Ballarotto, V. W., Fuhrer, M. S., and Williams, E. D., 2008, "Facile Fabrication of Suspended as-Grown Carbon Nanotube Devices," Appl. Phys. Lett., **93**(11), p. 113112.

[107]   Helbling, T., Pohle, R., Durrer, L., Stampfer, C., Roman, C., Jungen, A., Fleischer, M., and Hierold, C., 2008, "Sensing NO2 with Individual Suspended Single-Walled Carbon Nanotubes," Sens. Actuators B Chem., **132**(2), pp. 491–497.

[108]   Tarakanov, Y. A., and Kinaret, J. M., 2007, "A Carbon Nanotube Field Effect Transistor with a Suspended Nanotube Gate," Nano Lett., **7**(8), pp. 2291–2294.

[109]   Collins, P. G., Bradley, K., Ishigami, M., and Zettl, A., 2000, "Extreme Oxygen Sensitivity of Electronic Properties of Carbon Nanotubes," Science, **287**(5459), pp. 1801–1804.

[110]   Li, J., Lu, Y., Ye, Q., Cinke, M., Han, J., and Meyyappan, M., 2003, "Carbon Nanotube Sensors for Gas and Organic Vapor Detection," Nano Lett., **3**(7), pp. 929–933.

[111]   Kong, J., Franklin, N. R., Zhou, C., Chapline, M. G., Peng, S., Cho, K., and Dai, H., 2000, "Nanotube Molecular Wires as Chemical Sensors," Science, **287**(5453), pp. 622–625.

[112]   Valentini, L., Armentano, I., Kenny, J. M., Cantalini, C., Lozzi, L., and Santucci, S., 2003, "Sensors for Sub-Ppm NO2 Gas Detection Based on Carbon Nanotube Thin Films," Appl. Phys. Lett., **82**(6), pp. 961–963.

[113]   Zhang, J., Boyd, A., Tselev, A., Paranjape, M., and Barbara, P., 2006, "Mechanism of NO2 Detection in Carbon Nanotube Field Effect Transistor Chemical Sensors," Appl. Phys. Lett., **88**(12), p. 123112.

[114]   Peng, N., Zhang, Q., Chow, C. L., Tan, O. K., and Marzari, N., 2009, "Sensing Mechanisms for Carbon Nanotube Based NH3 Gas Detection," Nano Lett., **9**(4), pp. 1626–1630.

[115]   Robinson, J. A., Snow, E. S., Bădescu, Ş. C., Reinecke, T. L., and Perkins, F. K., 2006, "Role of Defects in Single-Walled Carbon Nanotube Chemical Sensors," Nano Lett., **6**(8), pp. 1747–1751.

[116]   Bekyarova, E., Davis, M., Burch, T., Itkis, M. E., Zhao, B., Sunshine, S., and Haddon, R. C., 2004, "Chemically Functionalized Single-Walled Carbon Nanotubes as Ammonia Sensors," J. Phys. Chem. B, **108**(51), pp. 19717–19720.

[117]   Qi, P., Vermesh, O., Grecu, M., Javey, A., Wang, Q., Dai, H., Peng, S., and Cho, K. J., 2003, "Toward Large Arrays of Multiplex Functionalized Carbon Nanotube Sensors for Highly Sensitive and Selective Molecular Detection," Nano Lett., **3**(3), pp. 347–351.

[118]   Niu, L., Luo, Y., and Li, Z., 2007, "A Highly Selective Chemical Gas Sensor Based on Functionalization of Multi-Walled Carbon Nanotubes with Poly(ethylene Glycol)," Sens. Actuators B Chem., **126**(2), pp. 361–367.

[119] Wang, F., Gu, H., and Swager, T. M., 2008, "Carbon Nanotube/Polythiophene Chemiresistive Sensors for Chemical Warfare Agents," J. Am. Chem. Soc., **130**(16), pp. 5392–5393.

[120] Yang, N., Chen, X., Ren, T., Zhang, P., and Yang, D., 2015, "Carbon Nanotube Based Biosensors," Sens. Actuators B Chem., **207**, **Part A**, pp. 690–715.

[121] Mundaca, R. A., Moreno-Guzmán, M., Eguílaz, M., Yáñez-Sedeño, P., and Pingarrón, J. M., 2012, "Enzyme Biosensor for Androsterone Based on 3α-Hydroxysteroid Dehydrogenase Immobilized onto a Carbon Nanotubes/ionic liquid/NAD+ Composite Electrode," Talanta, **99**, pp. 697–702.

[122] Vicentini, F. C., Janegitz, B. C., Brett, C. M. A., and Fatibello-Filho, O., 2013, "Tyrosinase Biosensor Based on a Glassy Carbon Electrode Modified with Multi-Walled Carbon Nanotubes and 1-Butyl-3-Methylimidazolium Chloride within a Dihexadecylphosphate Film," Sens. Actuators B Chem., **188**, pp. 1101–1108.

[123] Fatoni, A., Numnuam, A., Kanatharana, P., Limbut, W., Thammakhet, C., and Thavarungkul, P., 2013, "A Highly Stable Oxygen-Independent Glucose Biosensor Based on a Chitosan-Albumin Cryogel Incorporated with Carbon Nanotubes and Ferrocene," Sens. Actuators B Chem., **185**, pp. 725–734.

[124] Lin, K.-C., Lin, Y.-C., and Chen, S.-M., 2013, "A Highly Sensitive Nonenzymatic Glucose Sensor Based on Multi-Walled Carbon Nanotubes Decorated with Nickel and Copper Nanoparticles," Electrochimica Acta, **96**, pp. 164–172.

[125] Pourasl, A. H., Ahmadi, M. T., Rahmani, M., Chin, H. C., Lim, C. S., Ismail, R., and Tan, M. L. P., 2014, "Analytical Modeling of Glucose Biosensors Based on Carbon Nanotubes," Nanoscale Res. Lett., **9**(1), p. 33.

[126]   Palanisamy, S., Cheemalapati, S., and Chen, S.-M., 2014, "Amperometric Glucose Biosensor Based on Glucose Oxidase Dispersed in Multiwalled Carbon Nanotubes/graphene Oxide Hybrid Biocomposite," Mater. Sci. Eng. C, **34**, pp. 207–213.

[127]   Feng, W., and Ji, P., 2011, "Enzymes Immobilized on Carbon Nanotubes," Biotechnol. Adv., **29**(6), pp. 889–895.

[128]   Agüí, L., Yáñez-Sedeño, P., and Pingarrón, J. M., 2008, "Role of Carbon Nanotubes in Electroanalytical Chemistry: A Review," Anal. Chim. Acta, **622**(1–2), pp. 11–47.

[129]   Jose, M. V., Marx, S., Murata, H., Koepsel, R. R., and Russell, A. J., 2012, "Direct Electron Transfer in a Mediator-Free Glucose Oxidase-Based Carbon Nanotube-Coated Biosensor," Carbon, **50**(11), pp. 4010–4020.

[130]   Wooten, M., Karra, S., Zhang, M., and Gorski, W., 2014, "On the Direct Electron Transfer, Sensing, and Enzyme Activity in the Glucose Oxidase/Carbon Nanotubes System," Anal. Chem., **86**(1), pp. 752–757.

[131]   Yang, G., Kang, Z., Ye, X., Wu, T., and Zhu, Q., 2012, "Molecular Simulation of Flavin Adenine Dinucleotide Immobilized on Charged Single-Walled Carbon Nanotubes for Biosensor Applications," Biomaterials, **33**(34), pp. 8757–8770.

[132]   Star, A., Gabriel, J.-C. P., Bradley, K., and Grüner, G., 2003, "Electronic Detection of Specific Protein Binding Using Nanotube FET Devices," Nano Lett., **3**(4), pp. 459–463.

[133] Byon, H. R., and Choi, H. C., 2006, "Network Single-Walled Carbon Nanotube-Field Effect Transistors (SWNT-FETs) with Increased Schottky Contact Area for Highly Sensitive Biosensor Applications," J. Am. Chem. Soc., **128**(7), pp. 2188–2189.

[134] Tang, X., Bansaruntip, S., Nakayama, N., Yenilmez, E., Chang, Y., and Wang, Q., 2006, "Carbon Nanotube DNA Sensor and Sensing Mechanism," Nano Lett., **6**(8), pp. 1632–1636.

[135] Villamizar, R. A., Maroto, A., Rius, F. X., Inza, I., and Figueras, M. J., 2008, "Fast Detection of Salmonella Infantis with Carbon Nanotube Field Effect Transistors," Biosens. Bioelectron., **24**(2), pp. 279–283.

[136] Sharf, T., Kevek, J. W., DeBorde, T., Wardini, J. L., and Minot, E. D., 2012, "Origins of Charge Noise in Carbon Nanotube Field-Effect Transistor Biosensors," Nano Lett., **12**(12), pp. 6380–6384.

[137] Liu, S., and Guo, X., 2012, "Carbon Nanomaterials Field-Effect-Transistor-Based Biosensors," NPG Asia Mater., **4**(8), p. e23.

[138] Maehashi, K., and Matsumoto, K., 2009, "Label-Free Electrical Detection Using Carbon Nanotube-Based Biosensors," Sensors, **9**(7), pp. 5368–5378.

[139] Oh, J., Yoo, G., Chang, Y. W., Kim, H. J., Jose, J., Kim, E., Pyun, J.-C., and Yoo, K.-H., 2013, "A Carbon Nanotube Metal Semiconductor Field Effect Transistor-Based Biosensor for Detection of Amyloid-Beta in Human Serum," Biosens. Bioelectron., **50**, pp. 345–350.

[140] Smith, G. P., 1985, "Filamentous Fusion Phage: Novel Expression Vectors That Display Cloned Antigens on the Virion Surface," Science, **228**(4705), pp. 1315–1317.

[141] Winter, G., Griffiths, A. D., Hawkins, R. E., and Hoogenboom, H. R., 1994, "Making Antibodies by Phage Display Technology," Annu. Rev. Immunol., **12**, pp. 433–455.

[142] Kay, B. K., Winter, J., and McCafferty, J., 1996, *Phage Display of Peptides and Proteins: A Laboratory Manual*, Academic Press.

[143] Willats, W. G. T., "Phage Display: Practicalities and Prospects," Plant Mol. Biol., **50**(6), pp. 837–854.

[144] 't Hoen, P. A. C., Jirka, S. M. G., Ten Broeke, B. R., Schultes, E. A., Aguilera, B., Pang, K. H., Heemskerk, H., Aartsma-Rus, A., van Ommen, G. J., and den Dunnen, J. T., 2012, "Phage Display Screening without Repetitious Selection Rounds," Anal. Biochem., **421**(2), pp. 622–631.

[145] Ju, S., Lee, K.-Y., Min, S.-J., Yoo, Y. K., Hwang, K. S., Kim, S. K., and Yi, H., 2015, "Single-Carbon Discrimination by Selected Peptides for Individual Detection of Volatile Organic Compounds," Sci. Rep., **5**, p. 9196.

[146] Goldman, E. R., Pazirandeh, M. P., Charles, P. T., Balighian, E. D., and Anderson, G. P., 2002, "Selection of Phage Displayed Peptides for the Detection of 2,4,6-Trinitrotoluene in Seawater," Anal. Chim. Acta, **457**(1), pp. 13–19.

[147] Jaworski, J. W., Raorane, D., Huh, J. H., Majumdar, A., and Lee, S.-W., 2008, "Evolutionary Screening of Biomimetic Coatings for Selective Detection of Explosives," Langmuir, **24**(9), pp. 4938–4943.

[148] Lai, M. C., and Topp, E. M., 1999, "Solid-State Chemical Stability of Proteins and Peptides," J. Pharm. Sci., **88**(5), pp. 489–500.

[149]   Cleland, J. L., Lam, X., Kendrick, B., Yang, J., Yang, T. H., Overcashier, D., Brooks, D., Hsu, C., and Carpenter, J. F., 2001, "A Specific Molar Ratio of Stabilizer to Protein Is Required for Storage Stability of a Lyophilized Monoclonal Antibody," J. Pharm. Sci., **90**(3), pp. 310–321.

[150]   Danner, S., and Belasco, J. G., 2001, "T7 Phage Display: A Novel Genetic Selection System for Cloning RNA-Binding Proteins from cDNA Libraries," Proc. Natl. Acad. Sci., **98**(23), pp. 12954–12959.

[151]   Cicchini, C., Ansuini, H., Amicone, L., Alonzi, T., Nicosia, A., Cortese, R., Tripodi, M., and Luzzago, A., 2002, "Searching for DNA–protein Interactions by Lambda Phage Display," J. Mol. Biol., **322**(4), pp. 697–706.

[152]   Kay, B. K., Adey, N. B., Yun-Sheng, H., Manfredi, J. P., Mataragnon, A. H., and Fowlkes, D. M., 1993, "An M13 Phage Library Displaying Random 38-Amino-Acid Peptides as a Source of Novel Sequences with Affinity to Selected Targets," Gene, **128**(1), pp. 59–65.

[153]   Marvin, D., 1998, "Filamentous Phage Structure, Infection and Assembly," Curr. Opin. Struct. Biol., **8**(2), pp. 150–158.

[154]   Clackson, T., and Lowman, H. B., 2004, *Phage Display: A Practical Approach*, OUP Oxford.

[155]   Bratkovič, T., 2009, "Progress in Phage Display: Evolution of the Technique and Its Applications," Cell. Mol. Life Sci., **67**(5), pp. 749–767.

[156]   Deng, L. W., Malik, P., and Perham, R. N., 1999, "Interaction of the Globular Domains of pIII Protein of Filamentous Bacteriophage Fd with the F-Pilus of Escherichia Coli," Virology, **253**(2), pp. 271–277.

[157] Riechmann, L., and Holliger, P., 1997, "The C-Terminal Domain of TolA Is the Coreceptor for Filamentous Phage Infection of E. Coli," Cell, **90**(2), pp. 351–360.

[158] Lubkowski, J., Hennecke, F., Plückthun, A., and Wlodawer, A., 1999, "Filamentous Phage Infection: Crystal Structure of g3p in Complex with Its Coreceptor, the C-Terminal Domain of TolA," Struct. Lond. Engl. 1993, **7**(6), pp. 711–722.

[159] Armstrong, J., N. Perham, R., and Walker, J. E., 1981, "Domain Structure of Bacteriophage Fd Adsorption Protein," FEBS Lett., **135**(1), pp. 167–172.

[160] Sidhu, S. S., 2001, "Engineering M13 for Phage Display," Biomol. Eng., **18**(2), pp. 57–63.

[161] "Ph.D.[TM]-7 Phage Display Peptide Library | NEB" [Online]. Available: https://www.neb.com/products/e8102-phd-7-phage-display-peptide-library#pd-manuals. [Accessed: 11-Aug-2016].

[162] Cwirla, S. E., Peters, E. A., Barrett, R. W., and Dower, W. J., 1990, "Peptides on Phage: A Vast Library of Peptides for Identifying Ligands.," Proc. Natl. Acad. Sci., **87**(16), pp. 6378–6382.

[163] Whaley, S. R., English, D. S., Hu, E. L., Barbara, P. F., and Belcher, A. M., 2000, "Selection of Peptides with Semiconductor Binding Specificity for Directed Nanocrystal Assembly," Nature, **405**(6787), pp. 665–668.

[164] Ahmad, G., Dickerson, M. B., Cai, Y., Jones, S. E., Ernst, E. M., Vernon, J. P., Haluska, M. S., Fang, Y., Wang, J., Subramanyam, G., Naik, R. R., and Sandhage, K. H., 2008, "Rapid Bioenabled Formation of Ferroelectric BaTiO3 at Room Temperature from an Aqueous Salt Solution at near Neutral pH," J. Am. Chem. Soc., **130**(1), pp. 4–5.

[165] Schwemmer, T., Baumgartner, J., Faivre, D., and Börner, H. G., 2012, "Peptide-Mediated Nanoengineering of Inorganic Particle Surfaces: A General Route toward Surface Functionalization via Peptide Adhesion Domains," J. Am. Chem. Soc., **134**(4), pp. 2385–2391.

[166] Rodi, D. J., Janes, R. W., Sanganee, H. J., Holton, R. A., Wallace, B. A., and Makowski, L., 1999, "Screening of a Library of Phage-Displayed Peptides Identifies Human Bcl-2 as a Taxol-Binding protein1," J. Mol. Biol., **285**(1), pp. 197–203.

[167] Hoess, R. H., 1993, "Phage Display of Peptides and Protein Domains," Curr. Opin. Struct. Biol., **3**(4), pp. 572–579.

[168] Hoogenboom, H. R., 1997, "Selecting Phage AntibodiesDesigning and Optimizing Library Selection Strategies for Generating High-Affinity Antibodies," Trends Biotechnol., **15**(2), pp. 62–70.

[169] Hoogenboom, H. R., de Bruïne, A. P., Hufton, S. E., Hoet, R. M., Arends, J.-W., and Roovers, R. C., 1998, "Antibody Phage Display Technology and Its Applications," Immunotechnology, **4**(1), pp. 1–20.

[170] Smith, G. P., and Petrenko, V. A., 1997, "Phage Display," Chem. Rev., **97**(2), pp. 391–410.

[171] Gan, S. D., and Patel, K. R., 2013, "Enzyme Immunoassay and Enzyme-Linked Immunosorbent Assay," J. Invest. Dermatol., **133**(9), pp. 1–3.

[172] "How Do We Sequence DNA?" [Online]. Available: https://seqcore.brcf.med.umich.edu/sites/default/files/html/educ/dnapr/sequencing.html. [Accessed: 11-Aug-2016].

[173] "DNA Purification" [Online]. Available:https://www.promega.com/resources/product-guides-and-selectors/protocols-and-applications-guide/dna-purification/. [Accessed: 11-Aug-2016].

[174] Kuganathan, N., 2010, "Electronic Properties of Graphite and Single Walled Carbon Nanotubes-A DFT Study," Internet J. Nanotechnol., **3**.

[175] Louis, C. N., Jayam, S. G., and Raj, A. A., 2010, "Band Structure, Density of States and Superconductivity of Adsorbed Titanium Chains on (8, 8) and (14, 0) Carbon Nanotubes," Mater. Phys. Mech., **10**, pp. 72–81.

[176] Salehi, H., and Gharbavi, K., 2012, "Ab Initio Study of Electronic Properties of a Armchair (7,7) Carbon Nanotube," Adv. Mater. Phys. Chem., **2**(3), pp. 159–162.

[177] Tetik, E., Karadag, F., Karaaslan, M., and Comez, I., 2012, "The Electronic Properties of the Graphene and Carbon Nanotubes: Ab Initio Density Functional Theory Investigation," Int. Sch. Res. Not., **2012**, pp. 416–417.

[178] Maiti, A., Hoekstra, J., Andzelm, J., Govind, N., Ricca, A., Svizhenko, A., Mehrez, H., and Anantram, M. P., 2005, "Electronic Transport through Carbon Nanotubes - Effect of Contacts, Topological Defects, Dopants and Chemisorbed Impurities," Lawrence Livermore Natl. Lab. Number UCRL-CONF-209763.

[179] Fan, W., and Zhang, R., 2008, "Structural and Electronic Properties of Single-Walled Carbon Nanotubes Adsorbed with 1-Pyrenebutanoic Acid, Succinimidyl Ester," Sci. China Ser. B Chem., **51**(12), pp. 1203–1210.

[180] Hohenberg, P., and Kohn, W., 1964, "Inhomogeneous Electron Gas," Phys. Rev., **136**(3B), pp. B864–B871.

[181] Szabo, A., and Ostlund, N. S., 1989, *Modern Quantum Chemistry: Introduction to Advanced Electronic Structure Theory*, Courier Corporation.

[182] Kohn, W., and Sham, L. J., 1965, "Quantum Density Oscillations in an Inhomogeneous Electron Gas," Phys. Rev., **137**(6A), pp. A1697–A1705.

[183] Koskinen, P., and Mäkinen, V., 2009, "Density-Functional Tight-Binding for Beginners," Comput. Mater. Sci., **47**(1), pp. 237–253.

[184] Kohn, W., and Sham, L. J., 1965, "Self-Consistent Equations Including Exchange and Correlation Effects," Phys. Rev., **140**(4A), pp. A1133–A1138.

[185] Slater, J. C., and Koster, G. F., 1954, "Simplified LCAO Method for the Periodic Potential Problem," Phys. Rev., **94**(6), pp. 1498–1524.

[186] Bloch, F., "Über die Quantenmechanik der Elektronen in Kristallgittern," Z. Für Phys., **52**(7–8), pp. 555–600.

[187] Löwdin, P.-O., 1950, "On the Non-Orthogonality Problem Connected with the Use of Atomic Wave Functions in the Theory of Molecules and Crystals," J. Chem. Phys., **18**(3), pp. 365–375.

[188] Frauenheim, T., Seifert, G., Elsterner, M., Hajnal, Z., Jungnickel, G., Porezag, D., Suhai, S., and Scholz, R., 2000, "A Self-Consistent Charge Density-Functional Based Tight-Binding Method for Predictive Materials Simulations in Physics, Chemistry and Biology," Phys. Status Solidi B, **217**(1), pp. 41–62.

[189] Seifert, G., Eschrig, H., and Bieger, W., 1986, "An Approximation Variant of LCAO-X-Alpha Methods," Z. Phys. Chem.-Leipz., **267**(3), pp. 529–539.

[190] Porezag, D., Frauenheim, T., Köhler, T., Seifert, G., and Kaschner, R., 1995, "Construction of Tight-Binding-like Potentials on the Basis of Density-Functional Theory: Application to Carbon," Phys. Rev. B, **51**(19), pp. 12947–12957.

[191] Eschrig, H., 1989, *Optimized LCAO Method: And the Electronic Structure of Extended Systems*, Springer, Berlin ; New York.

[192] Xue, Y., Datta, S., and Ratner, M. A., 2002, "First-Principles Based Matrix Green's Function Approach to Molecular Electronic Devices: General Formalism," Chem. Phys., **281**(2–3), pp. 151–170.

[193] Kordrostami, Z., and Hossein, M., 2010, "Fundamental Physical Aspects of Carbon Nanotube Transistors," *Carbon Nanotubes*, J. Mauricio, ed., InTech.

[194] Pecchia, A., Penazzi, G., Salvucci, L., and Carlo, A. D., 2008, "Non-Equilibrium Green's Functions in Density Functional Tight Binding: Method and Applications," New J. Phys., **10**(6), p. 65022.

Chapter 3 . Experimental Methodology

This chapter presents the methods utilized to identify peptides targeting PETNH using a phage display technology. Enzyme-linked immunosorbent assays and biopanning methods for selecting peptides tailored with affinity towards PETNH are also here presented. Included in this chapter are the methods for sequencing the phage containing the peptide genetic information and the data analysis using Gene Studio. The methodology incorporating peptides onto CNTs to create functionalized nanotubes for sensing applications is also here described. Finally, protocols for the biotinylation of peptides, testing of peptide selectivity to PETNH, and testing of the PETNH in liquid state using a peptide/SWCNT system are also presented.

3.1 Enzyme-Linked Immunosorbent Assay

The specificity that a phage shows towards an analyte may be determined by the ELISA technique. The initial requirement of this technique is the immobilization of a target molecule onto the wells of a microtiter plate [1].Typically, the targets that are immobilized on the plate for the ELISA technique are biomolecules such as peptides, proteins, or antibodies because they will passively absorb to well surfaces. However, in this project the immobilization of PETN was rather unique since it was not a biomolecule. Additionally, PETN is a relatively small molecule with only NO_2 groups in its terminal sites (see Figure 3-1 A).
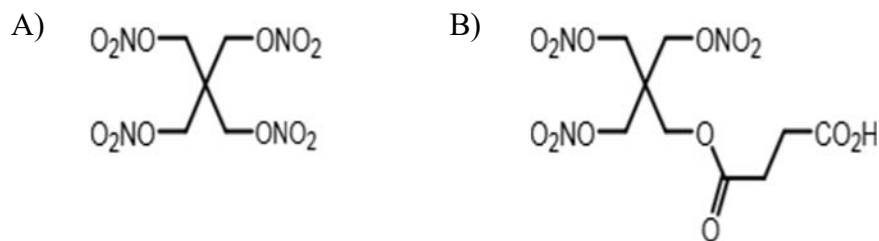
Figure 3-1: Schematic representation of the chemical structures investigated in this work. A) PETN and B) PETNH (surrogate)

Since PETN was not a biomolecule, passive absorption into the microwells was not a viable option. Therefore, pentaerythritol trinitratehemisuccinate (PETNH), which contains a carboxyl (COOH) group was used instead as a surrogate of PETN (see Figure 3-1 B) [2]. The presence of a COOH group in the structure allows for covalent attachment of the surrogate to amine functionalized microtiter plates using carbodiimide chemistry [3]. The use of surrogates for immobilization purposes has been previously used in phage display for binding 2,4,6-trinitrobenzene (TNB) to bovine serum albumin (BSA), as well as in the discovery of antibodies for targeting anthrax [4,5]. The use of surrogates is a widely known procedure for investigating the detection of explosives, deadly pathogens, chemical weapons, and bioterrorist agents [6–9]. This is due to their similar size and chemical nature as their original counterpart as wells as their safer profile and easiness of chemical modification, binding, and acquisition. Hesse *et al.* [10] have used PETNH as a surrogate of PETN when developing antibodies that were specific for PETN. The PETN surrogate used in this work was purchased from SynChem Inc. (Elk Grove Village, US).

Immobilization of PETNH on PureCoat Amine Surface microwell plates (Purchased from Becton Dickinson Biosciences) was carried out using a 1-Ethyl-3-(3

dimethylaminopropyl) carbodiimide (EDC) crosslinker approach [3]. This immobilization was performed in wells labeled test, negative control and blank. Simultaneously, positive control wells were coated with $2x10^{11}$ pfu/ml of M13KE Ph. D.-7 phage library (from New England BioLabs) in a 50 mM sodium carbonate buffer, pH 9.6. Additionally, pre-absorption wells were coated with a dry milk buffer made of 5% dry skim milk in TBS. The pre-absorption wells were used as a prescreening process in order to remove the phage that bind to the wells or to dry milk block, while simultaneously retaining those phage that can have selectivity to the explosive. Subsequently, all the wells were incubated for an hour at room temperature, and once the incubation was completed, all wells were washed with phosphate-buffered saline (PBS) solution six times and blocked with dry milk buffer. After an one hour incubation with the block, the pre-absorption wells were aspirated to remove excess block and then coated with of Ph.D.-7 phage library. An additional incubation step was performed for 45 minutes at room temperature to allow for the removal of the nonspecific phage (binding to block) in the pre-absorption wells while all of the remaining wells were aspirated and incubated with 20 µl of 5 % non-fat dry milk (NFDM) block.

Thereafter, all the blocked wells were aspirated, and the phage from the pre-adsorption wells were added to both the test and negative control wells. TBS was added to the positive control and blank wells, whilst M13KE (phage without displayed peptide), $2x10^{11}$ pfu/ml, was added to the negative control wells. Following incubation for 2 hours at room temperature, all wells were washed six times with PBS. To all wells, horseradish peroxidase (HRP) conjugated anti-M13 monoclonal antibody in 0.1 % Casein /(tris-buffered saline) TBS buffer was added, and the wells were then incubated overnight

at 4°C. The HRP/Anti-M13 solution was aspirated and all wells were washed six times with PBS, followed by the addition of 100 µl tetramethylbenzidine (TMB) substrate. After blue color in the positive well was visible, the reaction was stopped in all wells by the addition of 50 µl of 2N sulfuric acid. The absorbance of each well was then read at 450 nm. Table 1 details the ELISA procedure performed on each well. A visual schematic of the ELISA procedure in the test wells can also be seen in Figure 3-2.

Table 3.1 : ELISA summary for the M13 Library used in this work

Order of the addition to the wells						
Name	Target	Block	Phage	Antibody	Substrate	Stop
Test	PENTH	Dry Milk	M13 from Pre. Abs.	Anti-M13	TMB	H_2SO_4
Blank	PETNH	Dry Milk	x	Anti-M13	TMB	H_2SO_4
Positive	M13 Library	Dry Milk	x	Anti-M13	TMB	H_2SO_4
Negative control	x	Dry Milk	M13 from Pre. Abs.	Anti-M13	TMB	H_2SO_4
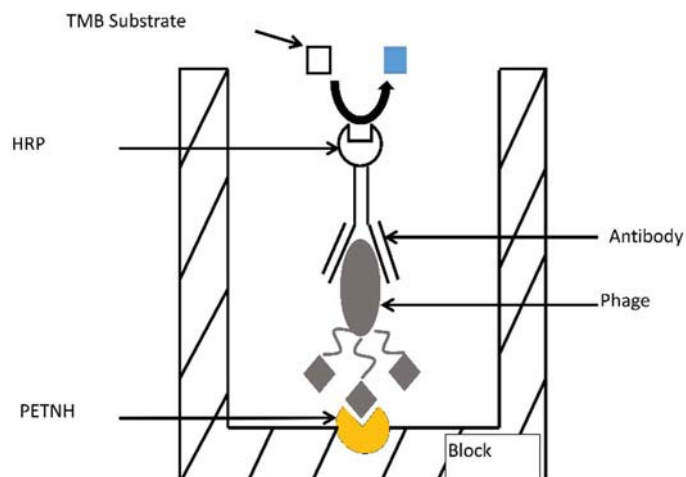
Figure 3-2: Schematic of the binding process in the test wells for the ELISA. The PETNH is immobilized, the free surface of the wells is blocked, then phage with specificity to the PETNH interacts and binds to the PETNH. Antibodies specific for M13 phage and labeled with horseradish peroxidase (HRP) are added and allowed to bind to the phage. Finally, TMB substrate is incorporated, which interacts with HRP to form a blue color for visible detection.

3.2 Biopanning

After determining if the M13KE Ph. D.-7 library contained phage selective to PETNH via ELISA, a biopanning protocol was subsequently performed. Biopanning is a procedure that is used for isolating highly selective phage towards the analyte of interest. Here, the biopanning consisted of immobilizing the analyte (in this case PETNH) into six different wells, using an EDC chemistry described in the ELISA section [3] (see section 3.1). Additionally, pre-adsorption wells were included by adding milk block in two separate wells. All the wells were then allowed to incubate overnight at 4 ºC. After 24

hours, the six wells containing the target were aspirated and washed six times with PBS. Of the initial six wells containing the immobilized analyte, dry milk buffer was added to the first four, while bovine serum albumin (BSA) buffer was added to the remaining two wells. The first two wells with the dry milk buffer were used for the panning round 1, while the two containing the BSA block were used for the panning round 2 wells, and the last two wells with the dry milk block for the panning round 3 wells. The pre-absorption wells were also aspirated, washed, and then the M13Ph.D.-7 library was added and allowed to incubate for 2 hours on a plate rocker at room temperature. The purpose of incorporating the pre-adsorption wells was to remove the majority of the phage that bound nonspecifically to the wells or to the block.

After incubation, the dry milk buffer was removed from the panning round 1 wells, then these wells were washed, and the unbound phage from the pre-adsorption wells was added. The wells were incubated for 2 hours at room temperature. Subsequently, the unbound phage from the panning round 1 wells were removed, the wells were washed, and the bound phage in panning round 1 wells were eluted via incubation with a solution consisting of 500 mM KCl and 10 mM HCl, pH2, and rocked at room temperature for 5 minutes. Simultaneously, the excess of BSA from the panning round 2 wells was removed and the wells were washed. The eluates from panning round 1 wells were neutralized with 25 μl of 20M Tris-HCL (pH 8) and 10 μL of each eluate was stored for further titering, while the rest was transferred to the wells blocked with BSA. Again, the wells from panning 2 were incubated for 2 hours on a rocker, followed by elution and neutralization of the eluate as described in the steps of the previous panning round. Amplification of the

phage between panning rounds was not performed, as previous data has shown that nonspecific phage titers increase with amplification between panning rounds.

On the other hand, the eluates from panning round 2 were transferred to the panning round 3 wells, and incubation was carried out for the completion of the third round of panning. The eluate from the third panning was neutralized, and then stored in 50% sterile glycerol at -20 °C. The general schematic for the biopanning procedure is shown in Figure 3-3.
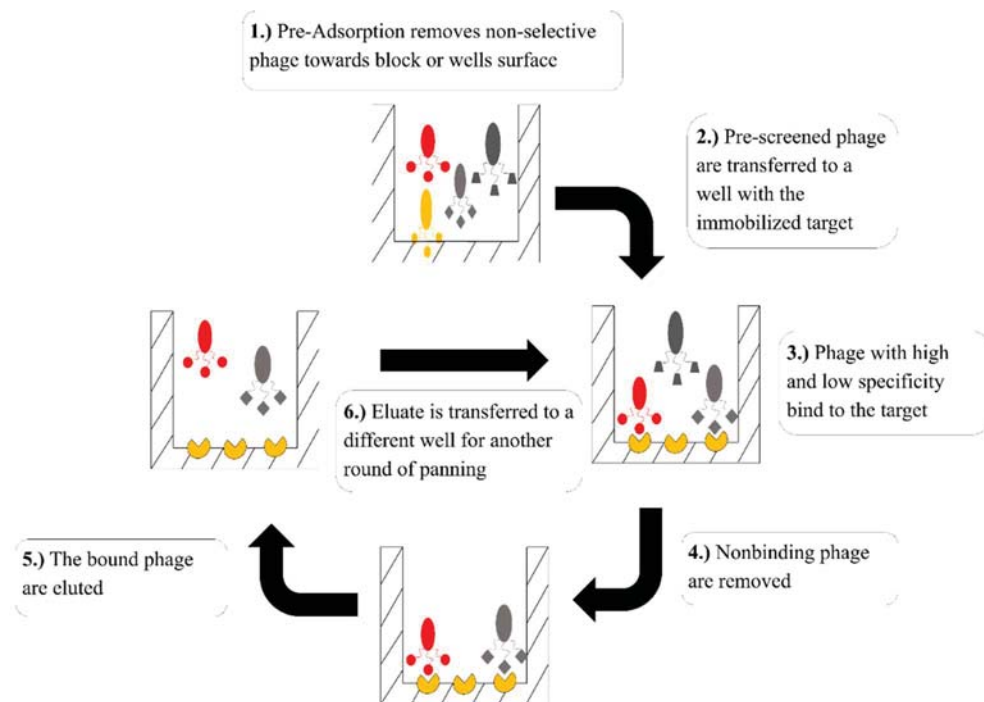
Figure 3-3: Schematic of the biopanning process. The biopanning scheme begins with the preadsorption of the M13 library to an initial block (non-fat dry milk) for removal of non-specific phage. The non-bound phage from this block (1) are transferred to wells with immobilized target. Phage with affinity to the analyte, bind to the target with varying levels of specificity while the phage that did not bind to the target are removed in subsequent steps (3 and 4). Finally, the phage bound to the target are eluted and used for the next round of selection (5 and 6).

3.3 Titering Stage

Following the panning procedure, the eluates were titered. Titers were performed on the different eluates from the various panning rounds. The purpose of the tittering process was to quantify the concentration of the phage in solution. The titer protocol here used, was adapted from a phage display library instruction manual provided by New England BioLabs [11]. Initially, *E. coli* was grown for 12 hours (overnight) before the titer procedure. This was carried out by inoculating *E. coli* ER2738 into 20 ml LB (lysogeny broth) containing 20 µl of 12.5 mg/ml tetracycline. Twelve hours later, a pre setup for the titer was also carried out by melting top agar in a microwave and dispensing 3 ml into sterile culture tubes. To each of these tubes, 40 µl of 2% X-gal (5-bromo-4-chloro-3-indolyl-β-D-galactopyranoside) and 40 µl of 2% IPTG (Isopropyl β-D-1-thiogalactopyranoside) were added, and the tubes were maintained at 45 °C until use.

Following the preparation of the agar, three 1:100 serial dilutions of the phage in PBS were prepared. Here, the dilutions were 10^2, 10^4, and 10^6. To prevent contamination, fresh aerosol resistant tips were used for each dilution. Once the serial dilutions were completed, 200 µl of the prepared ER2738 culture was placed into sterile microfuge tubes, one for each phage dilution. Subsequently, 10 µl of each phage dilutions were added to each microfuge tube containing the 12 hour ER2738 culture so the infection of the *E. coli* could take place. As soon as the phage dilution was added, the tube was vortexed quickly and incubated for 1-5 minutes at room temperature. It is important to note that the incubation should not exceed 5 minutes. Here, the infection of the *E. coli* is carried out with the purpose of transferring the genetic information encoded within the peptide sequence to the *E. coli*.

After the incubation was completed, the infected E. coli in the microfuge tubes were transferred to the culture tubes containing the top agar, 40 μl 2% X-gal, and 40 μl 2% IPTG. This mixture was then vortexed briefly (5 seconds) and immediately poured onto pre-warmed LB tetracycline plates (LB tetracycline plates were pre-warmed at 37 °C at least one hour before use). The liquid was then quickly spread evenly by titling the plate. Once evenly distributed, the plate was allowed to cool for 5 minutes. After this, the plates were inverted and incubated overnight at 37°C. Following 12 hours of incubation, plaques formed on the plate. These plaques were counted and then converted to plaque forming units (pfu) per ml. This conversion is performed by multiplying the number of plaques by the dilution factor.

3.4 Amplification and Polyethylene Glycol (PEG) Purification

Amplification is a technique that uses host bacteria cells to multiply the number of phage in solution, and it was used to increase the number of specific phage for the ELISAs and the sequencing process. In this work, amplified plaques were synthesized from the samples obtained from the third round of panning. This final round of panning yielded the phage with the highest specificity towards the analyte (PETNH). The lab protocol for amplification and PEG purification was again adopted from the New England BioLabs manual [11]. A basic amplification schematic is shown in Figure 3-4.
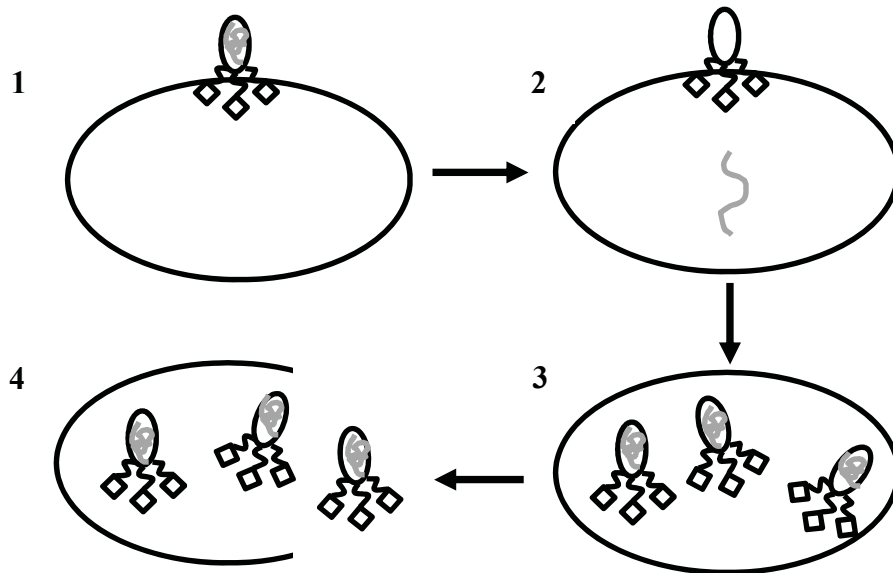
Figure 3-4: Basic amplification schematic showing attachment of the phage to the *E. coli* (step 1), infection of the *E. coli* via insertion of the genetic material (step 2), replication of the phage (step 3), and lysing and release of the phage (step 4).

Preparation for this protocol began by swirling ER2738 into a LB-tetracycline broth made with 20 ml of LB broth and 20 μl of tetracycline and incubating for 12 hours. Following the incubation step, the culture was diluted 1:100 in 20 ml of LB-tetracycline. This dilution was then dispensed into culture tubes, one tube for each plaque to be amplified. Subsequently, a sterile glass pipette was used to stab and extract the blue plaques from the tittering plate and transfer it into the culture tubes. The plaques were then incubated in the tubes for 4.5-5 hours at 37 °C.

Once the incubation was completed, the cultures were transferred to microfuge tubes and centrifuged at 16,000 x *g* for 30 seconds. This formed a pellet of phage infected bacteria in the bottom that was discarded while the supernatant was transferred to a new microfuge tube. The supernatant was then spun again at 16,000 x *g* for 30 seconds. From

the second centrifugation, only the top 80 % was removed. This top 80 % (16 ml) constituted the amplified phage stock. To allow for long term storage (up to several years) 500 μl of the amplified phage was diluted 1:1 in sterile glycerol. Simultaneously, the remaining 15.5 ml of amplified stock was saved for a subsequent PEG purification step.

PEG purification is a biological procedure that is performed with the purpose of removing contaminants in the system. Here, 4 ml of a 2.5 M NaCl/20 % PEG-8000 (w/v) solution was added to the 15.5 ml of amplified stock in order to precipitate the phage. The precipitation was carried out for about 12 hours at 4 ºC, but it can also be performed for 1 hour on ice if needed. After the precipitation stage, the precipitated phage were pelleted by centrifugation at 12,000 x g at 4 °C for 15 min. The supernatant was then removed and the pellet was resuspended in 1 ml of tris-buffered saline (TBS). The resuspended pellet was then transferred to an Eppendorf tube where 200 μl of a 2.5 M NaCl/20 % PEG-8000 (w/v) solution was subsequently added. Incubation of this mixture was carried out for 60 minutes on ice. After incubation, the solution was spun on a benchtop centrifuge at 16,000 x g for 10 minutes and the supernatant then removed. If the pellet broke up before all supernatant was removed, the tube was spun again and the remaining supernatant was removed. The pellet was finally resuspended in 400 μl of 50:50 TBS/glycerol. To ascertain the concentration of phage in solution after the amplification and the PEG purification steps, titers were performed, as previously described (see section 3.3).

3.5 Sequencing

Sequencing determines the nucleic acid composition of the peptide expressed by the phage. It was performed on each of the PEG purified plaques. The preparation of phage for

sequencing was performed using the Wizard® *Plus* SV Minipreps DNA Purification System [12]. The sequencing reactions used primers 96 gIII and 28 gIII, purchased from New England BioLabs.

3.5.1 Replicate Form (RF) M13 Isolation

In order to sequence the peptides displayed by the phage, the replicate form (RF) of the M13 DNA was here isolated. Initially, a culture of ER2738 in 2 ml of LB was prepared [12]. Twelve hours later, 50 ml of terrific broth was inoculated with 500 μl of the ER2738 culture for each PEG purified phage clone. Then 50 μl of each PEG purified phage was added to each ER2738 bacteria culture so the *E. coli* infection could take place. This step proceeded for 5-6 hours at 37 ºC under shaking. In the infection process, the phage infect the *E. coli* with their genetic material which contains the information describing the peptide sequence which the phage expresses. Once the infection was completed, the solutions were centrifuged for 10 minutes at 10,000 x *g*. The supernatants were removed and the pellet was frozen for 12 hours at -20 ºC.

After storage at -20 ºC, the frozen pellets were vortexed in 250 μl of cell resuspension solution [50mM Tris-HCL (pH 7.5), 10mM EDTA and 100μg/ml RNase A]. Once the pellets were well suspended, 250 μl of cell lysis solution [250 μl; 0.2M NaOH and 1% sodium dodecyl sulfate (SDS)] was added to each tube, which was subsequently inverted 4 times to mix. Then 10 μl of alkaline protease solution (isolated from the bacterium Bacillus licheniformis [13]) was added to each tube, and they were mixed again 4 times by inversion followed by an incubation step for 5 minutes at room temperature. After incubation, 350 μl of a neutralization solution (350 μl of a mixture based on 4.09M guanidine hydrochloride, 0.759M potassium acetate, 2.12M glacial acetic acid) was added

to each tube, which was again mixed by inversion 4 times. This process results in lysis the cells containing the DNA encoded with the peptide information.

The next step was to isolate the RF phage DNA from the rest of the material in the lysed cells. This was carried out using silica based spin columns provided in the Wizard® *Plus* SV Minipreps DNA Purification System. Those columns were inserted into a collection tube and then the supernatant from each lysing step was transferred to them. The system was then centrifuged at 14,000 x g for 1 minute at room temperature and the flow passed through them was discarded. At this point, the DNA was bound to the columns.

The next step was to wash the DNA by adding 750 µl of a wash solution [20 ml mixture of 162.8mM potassium acetate, 22.6mM Tris-HCl (pH 7.5), and 0.109mM Ethylenediaminetetraacetic acid (EDTA, pH 8.0) diluted with 35ml of 95% ethanol] to the column and centrifuging again for 1 minute. This step was repeated again using 250 µl of the wash solutions, and centrifuged until no wash solution was present. After the washing steps, the spin columns were transferred to a new sterile microcentrifuge tube. Once in the new tube, 100 µl of nuclease free water was added and the tube was spun at 14,000 xg for 1 minute at room temperature. This process removed the DNA from the column and transferred it to solution. The obtained solution was then stored at -20 ºC.

3.5.2 Gel Electrophoresis

Gel electrophoresis is used to help determine the molecular weight of DNA. To perform the gel electrophoresis protocol on the isolated DNA, agarose (1%) in Tris-phosphate EDTA buffer (TPE) [0.08M with 0.002M EDTA] was heated to 50°C. Then hot agar was poured into the mold and a comb was clamped at the top of the mold to form wells. The gel was allowed to set at room temperature for about 45 minutes and then the well forming

bar was removed. Next, TPE was added to the tank to bring the level of liquid to 1 mm above the gel. In the first well, the DNA ladder was added (lane 1 of Figure 3-5). The isolated DNA samples were then mixed with loading buffer/dye (EZ-vision ® 3 dye) in 5:1 volume ratio, and subsequently injected into the individual wells. The gel was run for 2 hours at 60 V and the DNA bands were viewed using UV light. A schematic for the gel electrophoresis experimental setup is shown in Figure 3-5.
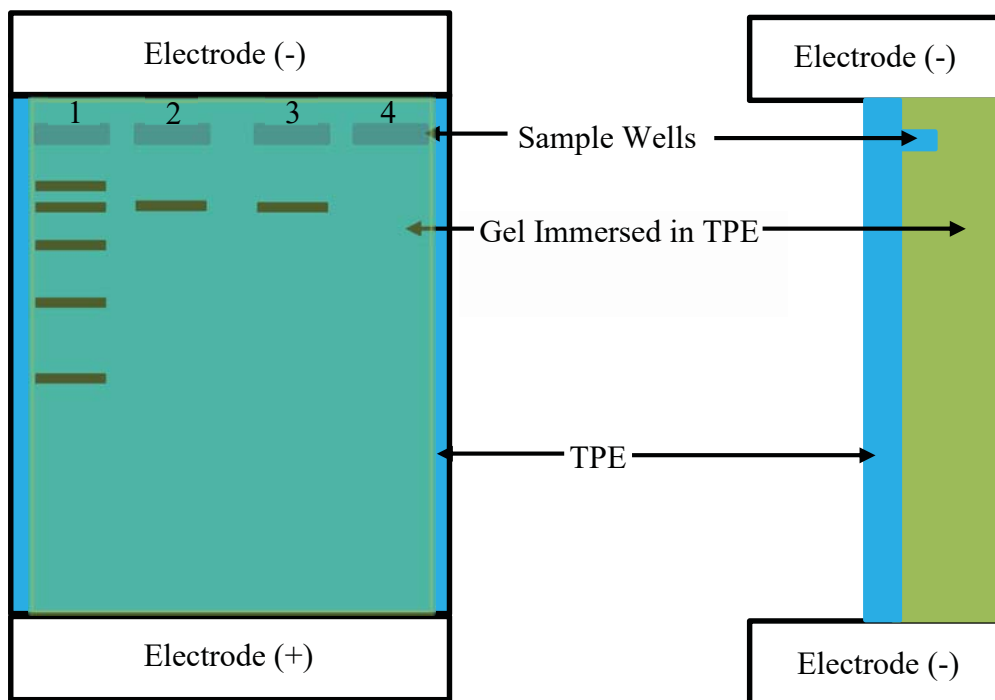
Figure 3-5: Top (A) and side (B) schematic views of the basic gel electrophoresis setup showing the placement of the electrodes, sample wells, and gel (green) immersed in TPE (blue)

3.5.3 DNA Sequencing

The DNA sequencing was performed at the Molecular Biology Analytical Core Laboratory at Youngstown State University, using the GenomeLab™ Dye Terminator Cycle Sequencing (DTCS) with the Quick Start kit. Initially, a NanoDrop spectrophotometer from Thermo Scientific was used to analyze the concentration of DNA in solution. Using those results, 260 ng of DNA from each amplified/purified phage was brought up to 10 µl using sterile water. Here, 2 solutions per DNA sample were prepared for each sequencing primer used (28 gIII and 96 gIII). Next, 2 µl of 1pmol/ µl of primer 96 gIII was added to one tube, while the same amount of primer 28 gIII was added to the other. Primers are used as a starting point for the DNA replication where one primer is considered the forward primer and the other is considered the reverse primer. The two primers replicate the DNA in opposite directions and the produced DNA copies are read and compared to create a consensus. Subsequently, 8.0µl of DTCS Quick Start Master Mix was added to both tubes and mixed thoroughly. Following the addition and mixing of the primers, the tubes were placed in a thermal cycling machine for 30 cycles where each cycle consisted of 20 seconds at 96°C, 20 seconds at 50 °C, and 4 minutes at 60°C. Once the thermal cycles were completed, 5µl of stop solution (Sodium Acetate 2µl of 1.2 mM, pH 5.2, 2 µl of 40 mM $Na_2 - EDTA$, pH 8.0, and 1 µl of 4 mg/ml of glycogen) was added to each tube and mixed thoroughly. Once mixed, the sequencing reactions were removed and added to 60 µl of 95 % cold ethanol in water, mixed, and subsequently centrifuged at 16,000 x g for 15 minutes at 4 °C. After centrifugation, the supernatants were removed and stored. Then the pellets were washed 2 times with 70 % ethanol in water and centrifuged at 16,000 x g and 4 °C for 2 minutes to reform the pellet. The supernatants from each wash were stored by

adding them to the previously stored supernatant before the wash. After the second wash step, the collected supernatants were transferred to new microcentrifuge tubes and vacuum dried for 10 minutes using the CentriVapDNA. Once dried, the pellets formed from the CentriVapDNA were suspended in 40 µL of sample loading solution (GenomeLab™ Dye Terminator). These solutions were then added to the sequencer (Beckman Coulter CEQ™ 2000XL DNA Analysis System) for their analysis. The output of the results were presented in a DNA Sequence Chromatogram (SCF) format. To analyze the SCF format results, a program called Gene Studio was here used. The Beckman Coulter CEQ™ 2000XL DNA Analysis System is shown in Figure 3-6.

Figure 3-6: The Beckman Coulter CEQ™ 2000XL DNA Analysis System used for the sequencing of purified DNA from the isolated phage in the biopanning process.

3.5.1 Gene Studio

The files associated to the DNA reading initiated by the 96 gIII and 28 gIII primers were analyzed in the Gene Studio software. It is important to analyze only the files associated with one peptide at a time in order to avoid poor alignment of the sequences. The program then aligned the sequences to each other and then output a contig file that results from the consensus of the alignment. This consensus is then used to find the inserted peptide nucleotide sequence by finding the flanking Kpn 1 and Eag 1 sites which are the markers for the beginning and end of the inserted phage DNA. An example of the performed analysis using the Gene Studio program is presented in Figure 3-7.
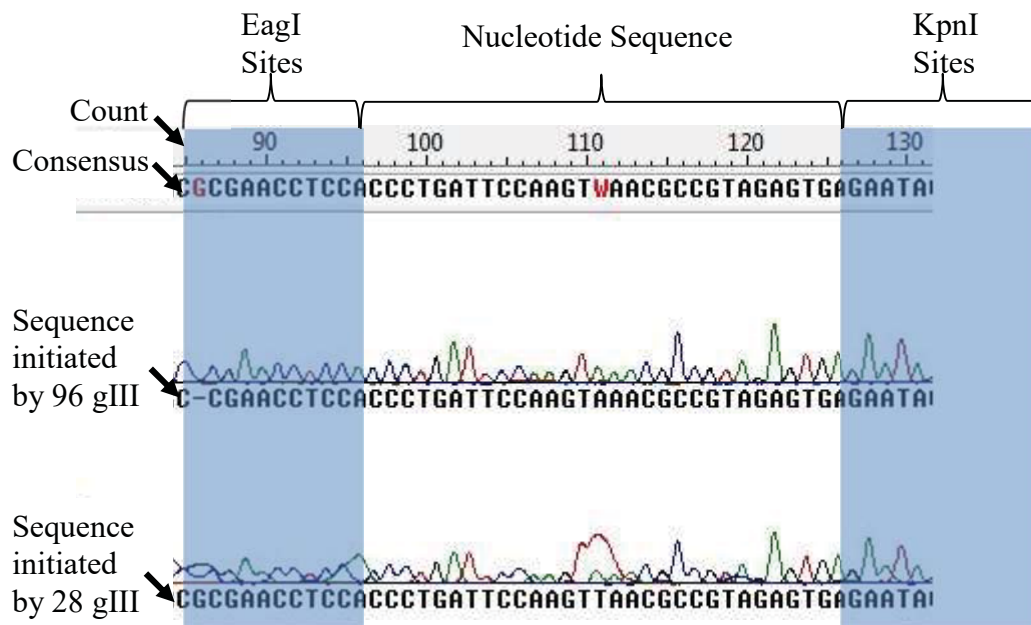
Figure 3-7: Alignment of the nucleic acid sequences initiated by the 96 gIII and 28 gIII primers using the Gene Studio software with the consensus, KpnI sites, and EagI sites labeled.

As shown in Figure 3-7, the nucleotide sequence readings as initiated by the 96 gIII and 28 gIII primers are imported into Gene Studio. The program then aligns the two sequences to create a consensus of the two sequences. Once aligned, the nucleotide sequence of the analyzed DNA can be found between the EagI and KpnI sites. This is because once the DNA is copied by initiation via the primers, it is inserted into the M13 genome for reading at this location between the EagI and KpnI sites. Insertion of DNA into a specific location of the genome allows the user to pinpoint the location of the analyzed DNA sequence and isolate it as it can be seen in Figure 3-7 between count 89 and 120.

Using this technique, sequences of 30 nucleotides in length were obtained. This is expected, as the phage library used in this research contains phage expressing 7-mer peptides with 3 glycines as the linker sequence where each mer is comprised of three nucleotides. Using the ExPASy web translation tool, the nucleotide sequences were translated into peptide sequences. The reading frame elected was that which contained the 3 glycine residue marker.

3.6 Peptide Biotinylation

Biotinylation of peptides was used in this research to track the binding of the peptides to SWCNTs. This method utilized carbodiimide chemistry to attach the biotin to the peptides (see section 2.3.4) [14]. Initially, a fresh solution of 100 mg/ml 1-Ethyl-3-(3-dimethylaminopropyl) (EDC) in 0.1 M N-morpholinothene sulfonic acid (MES) was prepared. Subsequently, 25 μl biotin-PEG4-hydrazide (50 mM) and 1000 μl of an identified peptide solution (0.5 mg/ml) was mixed in a microcentrifuge tube. After a

141

thorough mixing step, 1.25 µl of the 100 mg/ml EDC solution was added, mixed, and allowed to rock overnight (12 hours).

Subsequently, the biotinylated peptide was separated from the other components using Pierce™ Graphite Spin Columns [15]. For the separation process the spin columns were initially prepared. Here, the caps were removed from the columns, and the columns were placed into collection tubes. Two columns were prepared for each biotinylated peptide solution due to saturation limits. To each collection tube, 100 µl of 1M NH_4OH was added and the tube was centrifuged at 2000 x g for 1 minute. The initial flow passing through the tubes was discarded and the step was repeated. The graphite in the column was activated by the addition of 100 µl of acetonitrile. The column was then centrifuged at 2000 x g for 1 minute, and the flow-through was discarded. To complete the column preparation, 100 µl of 1% trifluoroacetic acid (TFA) was added to each column, the columns were centrifuged at 2000 x g for 1 minute, and the flow-through was discarded. This last step was repeated one more time.

Following the column preparation, the unpurified biotinylated peptide sample which contains biotinylated peptide and free biotin was diluted 1:1 in 2.5 % trifluoroacetic acid (TFA). The diluted biotinylated peptide sample (500 ul) was injected into the top of the column, which was placed in a fresh collection tube. The biotinylated peptide was then allowed to bind to the graphite for 10 minutes with periodic vortexing for a few seconds. When the reaction time was complete, the column was centrifuged at 1000 x g for 3 minutes. Subsequently, another 500 µl of the diluted biotinylated peptide sample was again injected, mixed, and centrifuged. Once the binding was complete, the column was washed with 200 µl of 1.0 % TFA, followed by centrifugation at 2000 x g for 1 minute. This

washing procedure was repeated once. After washing, the sample was eluted by placing the column in a new collection tube, and adding 100 µl of 0.1 % formic acid in 50:50 acetonitrile/water, and centrifuging at 2000 x g for 1 minute. This step was repeated 3 more times, thus forming 800 µl of biotinylated peptide (400 µl from each tube). The sample was gently dried in a vacuum evaporator and resuspended in MES buffer for storage and testing.

3.7 Biotin Incorporation Assay

A biotin incorporation assay was used to determine the concentration of the biotinylated substance in solution. This procedure was used to determine how much peptide was effectively biotinylated. Initially, the spectrophotometer was blanked using 1 ml of deionized water at 500 nm. After the blanking was complete, the absorbance of 900 µl of a 4'-hydroxyazobenzene-2-carboxylic acid (HABA)/avidin solution was measured. Here, 5 ml of a HABA/avidin solution was prepared by mixing 150 µl of 2.42 mg/ml HABA in water, 250 µl of 10 mg/ml avidin in water, and 4.6 ml of 1 x phosphate buffered saline (PBS) solution. After measuring the absorbance of the HABA/avidin complex, 100 µl of 0.1 M MES was added, and the solution was mixed thoroughly. The absorbance of the newly mixed solution was measured at 500 nm. It is important to note that the absorbance was recorded only when it was steady for 5 minutes. This measurement acted as a blank where the absorbance change due to the addition of MES was shown to not be caused by a HABA/biotin interaction, but was instead caused by the dilution effect.

To measure the absorbance change due to the biotin content, the cuvette was washed, 900 µl of the HABA/avidin solution was added, and the absorbance was measured. The

biotinylated peptide solution was then added (100ul) and mixed thoroughly. The absorbance of this solution was taken and recorded when the absorbance was steady. If the new absorbance value of the mixed solution was less than 0.15, the test had to be repeated with a diluted biotinylated sample. It is important to note that this procedure can be used with any biotinylated constituent. A schematic of the process is shown in Figure 3-8.
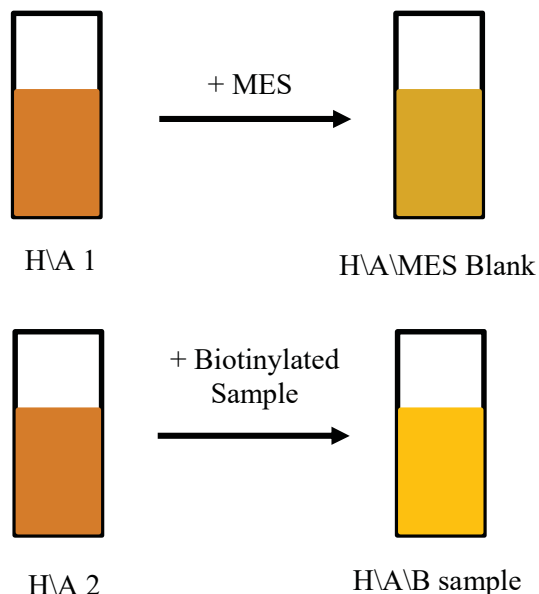
Figure 3-8: Basic biotin incorporation assay schematic showing the different solutions whose absorbances were measured at 500 nm and how the relative colors are changed with the addition of different samples. H\A is the absorbance of the HABA/avidin complex, and H\A\MES Blank is the absorbance of the HABA/avidin/MES blanking mixture, and H\A\B sample is the absorbance of the HABA/avidin/biotinylated sample mixture.

To calculate the concentration of biotinylated peptide, the Beer Lambert Law (Beer's Law) was employed. Beer's law is presented in equation 3.1.

$$\Delta A_{500} = Cb\varepsilon_{\lambda}$$

<div align="right">3.1</div>

In equation 3.1, ΔA_{500} is the change in the absorbance of the sample at 500 nm wavelength, ε is the extinction coefficient of the wavelength (34,000 M^{-1} cm^{-1} for HABA/avidin solutions), b is the cell path (1.0 cm for the cuvette), and C is the concentration of the sample (mol/L). To calculate the change in absorbance (ΔA_{500}) for the sample including dilution effects, equation 3.2 was employed.

ΔA_{500} = ((H\A 2) - (H\A\B sample))- ((H\A 1) - (H\A\MES Blank))

<div align="right">3.2</div>

In equation 3.2, H\A is the absorbance of the HABA/avidin complex, H\A\MES Blank is the absorbance of the HABA/avidin/MES blanking mixture, and H\A\B sample is the absorbance of the HABA/avidin/biotinylated sample mixture. Thus, by using equations 3.1 and 3.2 , the concentrations of the biotinylated solutions were calculated.

3.8 Competitive Peptide ELISA

Peptide ELISA is a procedure that is used to determine the selectivity of a peptide to an analyte. In this work, the PETN selectivity of the identified phage in the biopanning process was performed using PureCoat Amine Surface microwell plates (purchased from Becton Dickinson Biosciences). In this protocol, test wells, streptavidin blank wells and competition wells were coated with 100ul of a 10μg/ml of PETNH solution containing 10x molar excess amount of EDC. All conditions were tested in triplicate. PETNH, TNT, Nitrobenzene, Sodium Nitrate, and Pentaerythritol were tested to investigate the selectivity of the peptides to PETNH. A positive control well was also included, and coated with 100μl

of 2×10^{11} pfu/ml phage in Na_2CO_3. Additionally, blocking buffer (5 % nonfat dry milk in PBS) was added to wells that did not receive the PETNH and were labeled as negative wells. All wells were incubated for 2 hours at room temperature.

The wells were aspirated and washed once with PBS wash buffer. Blocking buffer (200 ul) was added to each well and incubated again for an hour at room temperature. During the incubation, competition solutions were prepared consisting of 10 µg/mL of biotinylated peptide and 1 µg/mL of competition substance. Each competition solution was mixed thoroughly and incubated for 45 minutes at room temperature. Here, incubation of the blocking buffer ended simultaneously with the incubation of the competition solutions. At the completion of the incubation step, the blocking buffer in each well was aspirated and all wells were washed 3 times with wash buffer. To the test wells and negative wells, 100 µl of 10 µg/mL biotinylated peptide was added. The blank and positive control wells received the PBS solution. To each set of competition wells 100 µl of the corresponding competition mixture was added. For instance, to the TNT competition wells a 100 µL pre-reacted solution of 10 µg/mL biotinylated peptide and 1 µg/mL TNT in PBS was added. Subsequently, all wells were incubated for 2 hours at room temperature.

After the incubation period, the wells were aspirated and washed 6 times with PBS. A 1:5000 dilution of HRP/anti-M13 monoclonal antibody peroxidase conjugate was added to the positive control well. Simultaneously, 100 µl of a 1:10,000 dilution of HRP-Streptavidin (SA) in sample buffer was added to all remaining wells and incubated for 2 hours at room temperature. The wells were washed three times with wash buffer and 100 µl of TMB substrate solution was added to every well. After blue color in the positive well was visible, the reaction in all wells was stopped by the addition of 50 µl of 2N sulfuric

acid. The absorbance of each well was then read at 450 nm, and the degree of selectivity was then evaluated. Table 3.2 details the competitive peptide ELISA procedure performed on each well.

Table 3.2 : Competitive Peptide ELISA summary for the peptides discovered in the biopanning process.

Order of the addition to the wells ———————————————————————→						
Name	Target	Block	Peptide	HPR Labeled Constituent	Substrate	Stop
Test	PENTH	Dry Milk	Biotinylated Peptide	Streptavidin	TMB	H_2SO_4
Competition	PETNH	Dry Milk	Biotinylated Peptide + Competition Substance	Streptavidin	TMB	H_2SO_4
SA Blank	PETNH	Dry Milk	x	Streptavidin	TMB	H_2SO_4
Positive	M13 Library	Dry Milk	x	Anti-M13	TMB	H_2SO_4
Negative control	x	Dry Milk	Biotinylated Peptide	Streptavidin	TMB	H_2SO_4

3.9 Bio-functionalization of SWCNTs with Peptide

Attaching peptides to SWCNTs followed a similar approach to the protocol used on the biotinylate peptides (see section 3.6). Initially, a fresh 100 mg/ml solution of EDC in MES and 1 ml of a 10 mg/ml solution of surface carboxylated single wall carbon nanotubes from NanoLabs was prepared. Then two different vials for each peptide to be attached to the SWCNTs were prepared. In one vial, 1 ml of a biotinylated peptide solution was placed, and in the other vial 1 ml of peptide solution (non-biotinylated) was incorporated. Here the

biotinylated peptide was run in parallel to the non-biotinylated peptide in order to calculate the amount of peptide that is actually attached to the SWCNTs under the same conditions. To each of these vials, 2 µl of the 100 mg/ml EDC solution was added and mixed. After thoroughly mixing each vial, 100 µl of the carboxylated SWCNT solution was added, the vials were vortexed, and then allowed to rock for 10 minutes. This step was repeated 4 more times to result in the total addition of 500 µl of carboxylated SWCNT solution. This successive addition of reactants resulted in the amine groups present in the peptides being always in excess and available for attachment. After the last addition of the carboxylated SWCNT solution, the vials were rocked for 12 hours at room temperature on a test tube rocker.

After rocking for 12 hours, the reaction solutions were centrifuged for 10 minutes at 3,000 rpm and 25 °C to pellet the bio-functionalized SWCNTs. The supernatants were removed and the supernatant from the vial containing the biotinylated peptide was kept. This supernatant contained the unbound biotinylated peptide. To ensure that all unbound peptides were removed, the pellets in each vial were washed. This was carried out by suspending the pellet in 1 ml of the 0.1 M MES solution, centrifuging at 3,000 rpm and 25 °C for 10 minutes, and removing the supernatant. This wash was performed 2 times and the wash removed from the vial was stored each time. After the washes, the functionalized SWCNT pellets were suspended in 1 ml of 0.1 M MES buffer and stored at 4 °C until use.

To calculate the amount of peptides that bound to carbon nanotubes, a biotin incorporation assay protocol was here performed on the biotinylated peptide/SWCNT complex. Indeed, due to carbon nanotubes being a black solid, the absorbance change cannot be correctly measured. Thus, a mass balance approach was implemented. Instead

of measuring the change in absorbance due to solutions comprised of biotinylated peptides connected to SWCNTs, the wash that was kept during removal of non-attached biotinylated peptide was instead used in the assay. Thus, by subtracting the biotinylated peptide from the wash after the SWCNT attachment from the amount of biotinylated peptide before the SWCNT attachment, the amount of biotinylated peptide attached to the SWCNT was calculated via visible spectroscopy using Beer's Law (see section 3.7 and equations 3.1 and 3.2).

3.10   Detection Test of Biotinylated PETNH in Liquid State

To perform a liquid state detection test, a mass balance approach was taken by tracking the explosive via biotin. By using the free carboxyl group present in the PETN surrogate (PETNH), hydrazide-PEG4-biotin was attached to PETNH (see Figure 3-9 A). This was carried out by first mixing 26 µl of a 50 mM biotin hydrazide solution with 1 ml of 0.5 mg/ml PETNH in water. Then 3 µl of freshly made 100 mg/ml EDC was added. The reaction was then allowed to rock for 12 hours.

Subsequently, the biotinylated PETNH was separated from the free biotin by adding 10 mg of carboxylated SWCNTs to the reaction mixture, vortexing, and then rocking overnight (12 hours) (see Figure 3-9 B) . Here, the free carboxyl groups on the CNTs acted as trap for the free biotin. In order to remove the SWCNTs with trapped biotin, the mixture was centrifuged at 3,000 rpm for 10 minutes at 25 °C. Then, the supernatant (biotinylated and unbiotinylated PETNH) was removed and analyzed via biotin incorporation assay for its quantification (see section 3.7).

The detection of the biotinylated PETNH began by first ultrasonicating 1 ml of 5 mg/ml peptide functionalized SWCNTs for 5 minutes at room temperature. This helped to break up the SWCNT bundles held together by Van der Waals forces and disperse them in the solution. Then 325 µl of biotinylated PETNH was added, and the mixture was vortexed for 20 seconds and allowed to rock for 2 hours at room temperature. The reaction products can be seen in Figure 3-9 C. After the reaction period was completed, the solution was vortexed at 3,000 rpm for 10 minutes. Then the supernatant was removed and kept. The pellet was then washed 2 times with 0.1 M MES to remove any biotinylated PETNH that could be trapped by the SWCNT network and not by peptide/PETNH interaction. This washing procedure consisted of suspending the pellet in 0.1 M MES, followed by a centrifugation at 3,000 rpm for 10 minutes, and the removal and storage of the supernatant. Here, the stored wash was analyzed using the biotin incorporation assay and Beer's Law protocols described earlier to find the concentration of biotinylated PETNH in the wash. Thus, the amount left attached to the carbon nanotubes was calculated through mass balance by subtracting the amount of biotinylated PETNH after the interaction with the bio-functionalized SWCNTs (detection test) from the amount of biotinylated PETNH originally used in the test. A schematic of the whole detection test of the biotinylated PETNH in the liquid state can be seen in Figure 3-9.
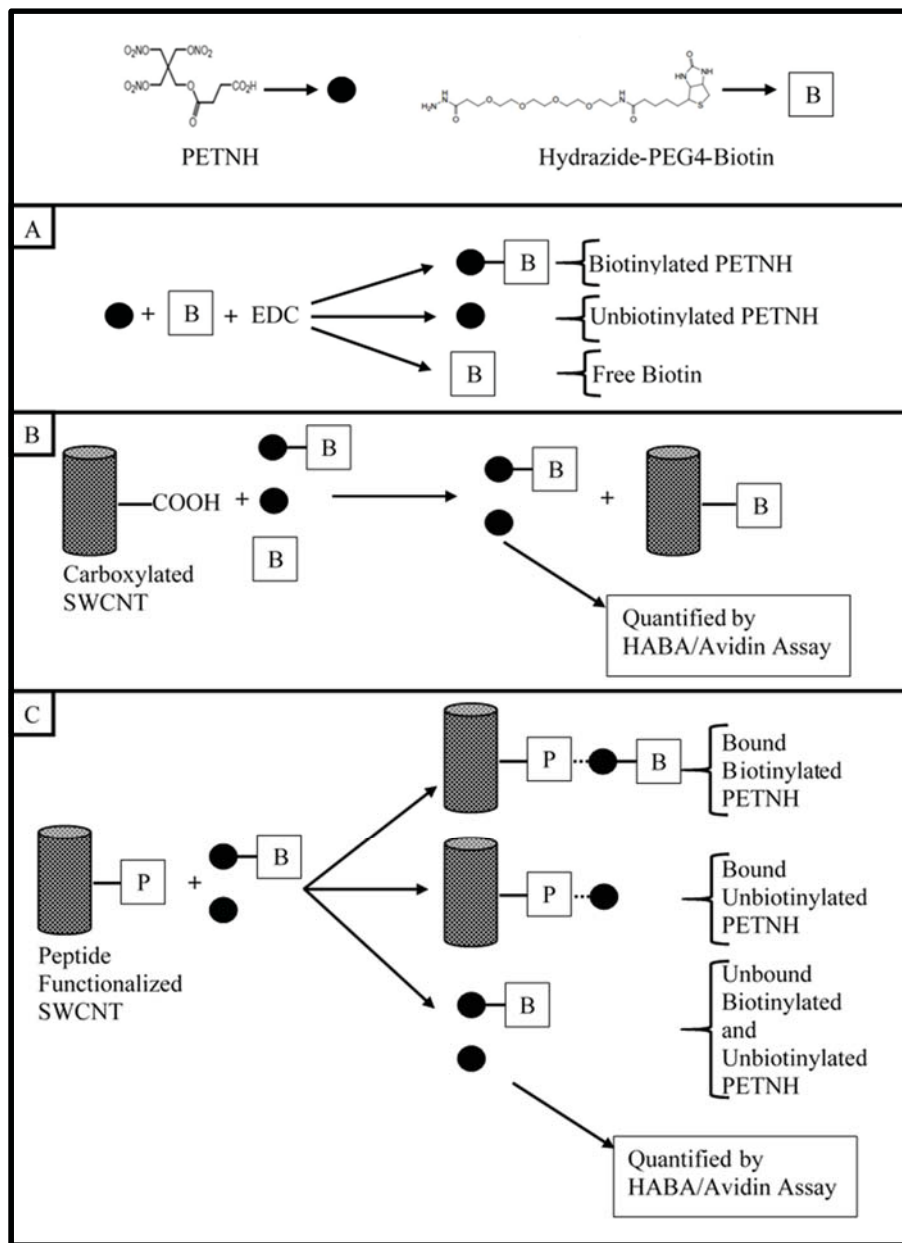
Figure 3-9: Basic schematic for the detection test of biotinylated PETNH in the liquid state showing the biotinylation of PETNH (A), and purification and quantification of biotinylated PETNH (B). Also, shown is the binding of biotinylated peptide to SWCNTS and quantification of unbound biotinylated peptide (C).

3.11 References

[1] "Overview of ELISA" [Online]. Available: http://www.piercenet.com/method/overview-elisa. [Accessed: 06-Dec-2016].

[2] Blackburn, G. M., Beadham, I. G., Adams, H., Hutchinson, A. P., and Nicklin, S., 2000, "Synthesis of Haptens and Their Protein Conjugates for Immunological Determination of Nitrate Esters and Nitramines," J. Chem. Soc., Perkin Trans. 1, (2), pp. 225–230.

[3] "Carbodiimide Crosslinker Chemistry" [Online]. Available: https://www.thermofisher.com/us/en/home/life-science/protein-biology/protein-biology-learning-center/protein-biology-resource-library/pierce-protein-methods/carbodiimide-crosslinker-chemistry.html. [Accessed: 07-Sep-2016].

[4] Goldman, E. R., Pazirandeh, M. P., Charles, P. T., Balighian, E. D., and Anderson, G. P., 2002, "Selection of Phage Displayed Peptides for the Detection of 2,4,6-Trinitrotoluene in Seawater," Anal. Chim. Acta, **457**(1), pp. 13–19.

[5] Zhou, B., Wirsching, P., and Janda, K. D., 2002, "Human Antibodies against Spores of the Genus Bacillus: A Model Study for Detection of and Protection against Anthrax and the Bioterrorist Threat," Proc. Natl. Acad. Sci., **99**(8), pp. 5241–5246.

[6] Ding, J., Xie, K., Liu, E., Zhang, Y., Hsia, Y., and Luo, Z., 1999, "Study of Surrogates for SW846 Method 8330," J. Chromatogr. Sci., **37**(3), pp. 65–70.

[7] Rusu, A. D., Moleavin, I. A., Hurduc, N., Hamel, M., and Rocha, L., 2014, "Fluorescent Polymeric Aggregates for Selective Response to Sarin Surrogates," Chem. Commun., **50**(69), pp. 9965–9968.

[8]   Bennett, R. A., Behrens, E., Zinn, A., Duncheon, C., and Lamkin, T. J., 2014, "Mustard Gas Surrogate, 2-Chloroethyl Ethylsulfide (2-CEES), Induces Centrosome Amplification and Aneuploidy in Human and Mouse Cells : 2-CEES Induces Centrosome Amplification and Chromosome Instability," Cell Biol. Toxicol., **30**(4), pp. 195–205.

[9]   Cortes, P., Deng, S., and Smith, G. B., 2009, "The Adsorption Properties of Bacillus Atrophaeus Spores on Single-Wall Carbon Nanotubes," J. Sens., **2009**, p. e131628.

[10]   Hesse, A., Biyikal, M., Rurack, K., and Weller, M. G., 2016, "Development of Highly Sensitive and Selective Antibodies for the Detection of the Explosive Pentaerythritol Tetranitrate (PETN) by Bioisosteric Replacement," J. Mol. Recognit., **29**(2), pp. 88–94.

[11]   "Ph.D.^{TM}-7 Phage Display Peptide Library | NEB" [Online]. Available: https://www.neb.com/products/e8102-phd-7-phage-display-peptide-library#pd-manuals. [Accessed: 11-Aug-2016].

[12]   "Wizard® Plus SV Minipreps DNA Purification System Protocol" [Online]. Available: https://www.promega.com/resources/protocols/technical-bulletins/0/wizard-plus-sv-minipreps-dna-purification-system-protocol/. [Accessed: 06-Dec-2016].

[13]   "Purification of the Proteolytic Enzyme from Bacillus Subtilis." [Online]. Available: https://www.docphin.com/research/article-detail/15198036/PubMedID-13182800/Purification-of-the-proteolytic-enzyme-from-Bacillus-subtilis. [Accessed: 21-Mar-2017].

[14] "EZ-Link Hydrazide-PEG4-Biotin - Thermo Fisher Scientific" [Online]. Available: https://www.thermofisher.com/order/catalog/product/21360. [Accessed: 08-Dec-2016].

[15] "Pierce Graphite Spin Columns - Thermo Fisher Scientific" [Online]. Available: https://www.thermofisher.com/order/catalog/product/88302. [Accessed: 08-Dec-2016].

Chapter 4 . Modeling

In this work, the electrical current flow passing through a carbon nanotube field effect transistor was modeled using the dftb+ program developed by the Bremen Center of Computational Materials Science in Germany on a Linux based operating system. To create the geometry files containing the xyz coordinates of various atoms, Avogadro molecular modeling software was here implemented, and for rapid viewing of the molecular structure, Jmol software was instituted. Finally, an analysis of the effect of varying the gate and bias voltages on the CNT system is also here presented.

4.1 Computer and Modeling Set-Up

The Avogadro, Jmol, and Fortran compilers were initially installed using a package installer native to Debian and coupled to a DFTB program which was downloaded from www.dftb-plus and installed on the computer [1–3]. Here, the DFTB+ program was run in a linux based operating system. The dftb+ version used included the Non-equilibrium Green's Function (NEGF) add-on. The downloaded zip file contained the precompiled dftb+negf binary, examples, tutorials, and files to compile a new binary. For this work, the precompiled binary was used and run from a local folder instead of using the global bin.

Once the main programs were in place, essential files and folders were put into a work folder. Also, Slater Koster files (skf) were downloaded from the www.dftb.org webpage for each interacting atom considered in the system. For example, a carbon nanotube was comprised on only carbon, so modeling it only required the C-C skf file. To model the carbon nanotube/ peptide system, the files needed included the C-C, C-H, H-C,

C-N, N-C, H-H, O-H, H-O, C-O, O-C, O-O, O-N, N-O, N-N, N-H, and H-N interactions.

These files are shown in Figure 4-1.
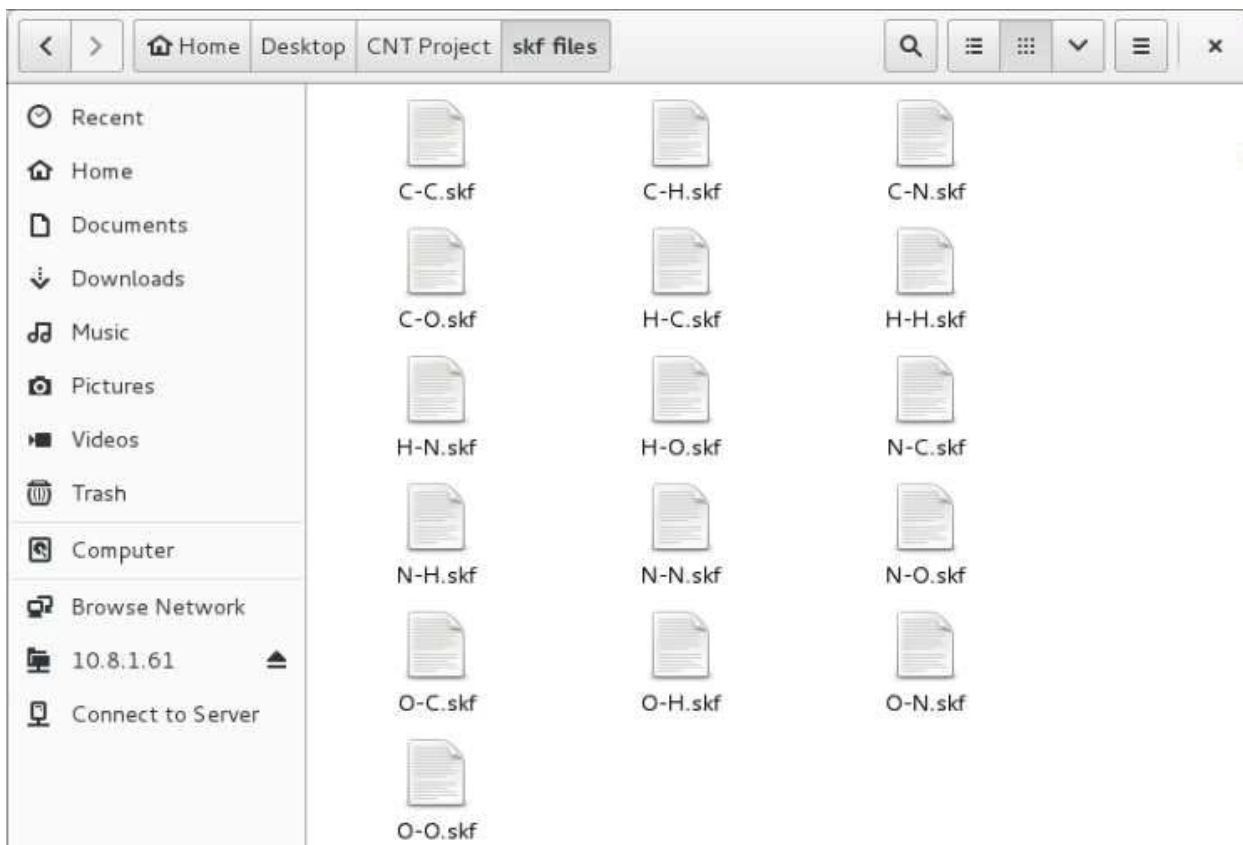
Figure 4-1: Image of the Slater Koster files used for all of the molecule-molecule interactions present in the carbon nanotube/peptide system used in this work.

It is important to note that these files were placed in the same location as the compiled dftb+ binary. Indeed, when the program calls for the skf files to be read, they must be in the same path. To complete the initial computer setup, GS (ground state), and contacts folders were created in the same location as the dftb+ binary and the skf files. These folders were left empty since they were later filled by running the code.

4.2 Geometry Creation

One of the first (user) generated files used in the code was the geometry (gen) file. To create the basic model of a carbon nanotube, a website called TubeGen Online was used [4]. The chirality of the tube was set to (8,0) since this chirality signifies a semiconducting tube. The carbon-carbon bond length was set at the equilibrium distance of 1.4210 Å. The length of the tube was set to 26 cells aligned in the z direction where each cell was comprised of 32 atoms of carbon. These parameters generated the xyz coordinates of carbon atoms that comprise a 110.03 Å long SWCNT oriented in the z direction. An example of the input and output of the TubeGen Online is presented in Figure 4-2.
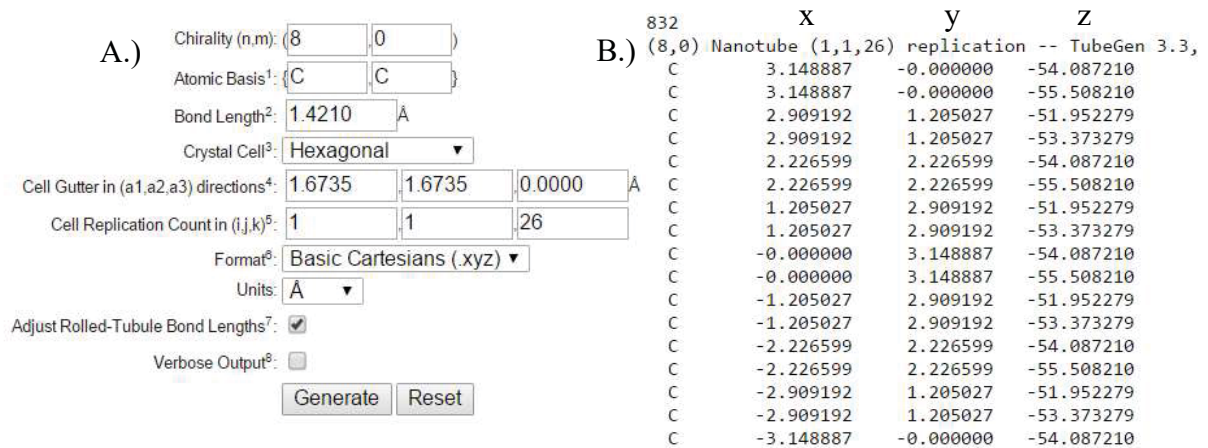
Figure 4-2: (A) Example of the inputs for the TubeGen program including chirality, bond length, and unit cell replication count by direction. (B) Output for the TubeGen Online generator showing the xyz coordinates of each carbon atom and total number of atoms in the system (832).

To visualize the SWCNT described by the xyz coordinates shown in Figure 4-2 B, a CNT.xyz file was created. Then Jmol was used to read the coordinates and display the resulting structure as shown in Figure 4-3.
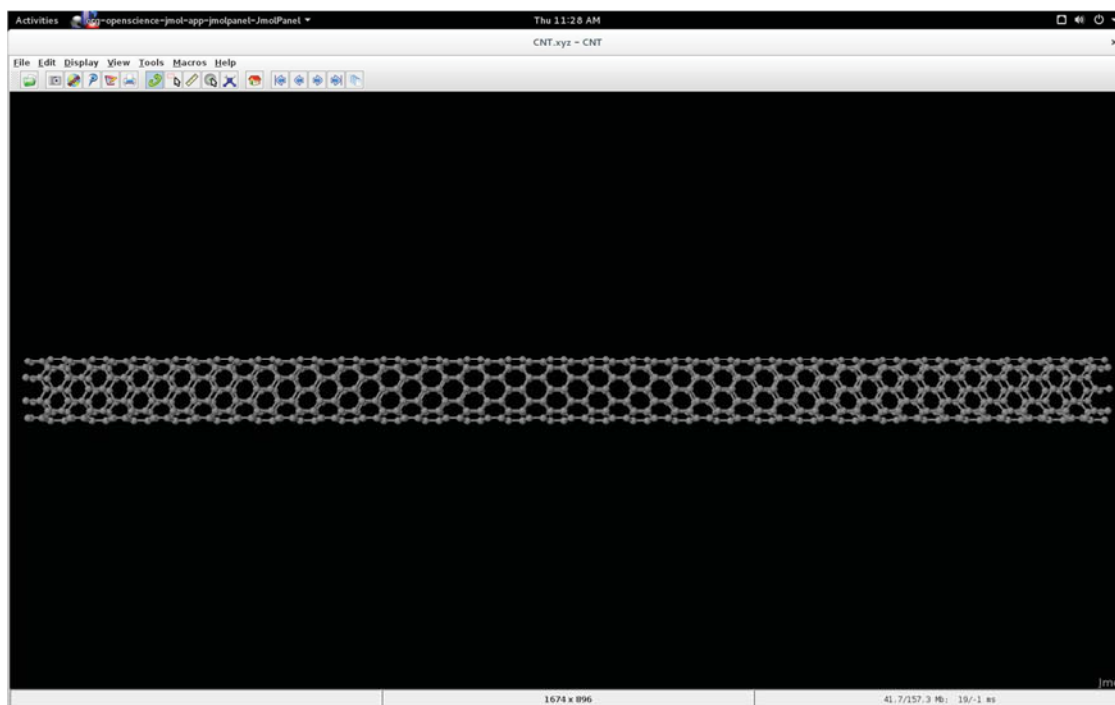
Figure 4-3: 3-Dimensional visualization of a (8,0) SWCNT in Jmol.

The creation of a SWCNT/peptide and SWCNT/Peptide/PETN systems required the use of a molecular modeling program such as Avogadro. This was carried out by initially importing the .xyz file into the Avogadro software. Once the SWCNT was visualized in the monitor, the peptide was added to the program using the peptide insertion window as presented in Figure 4-4.
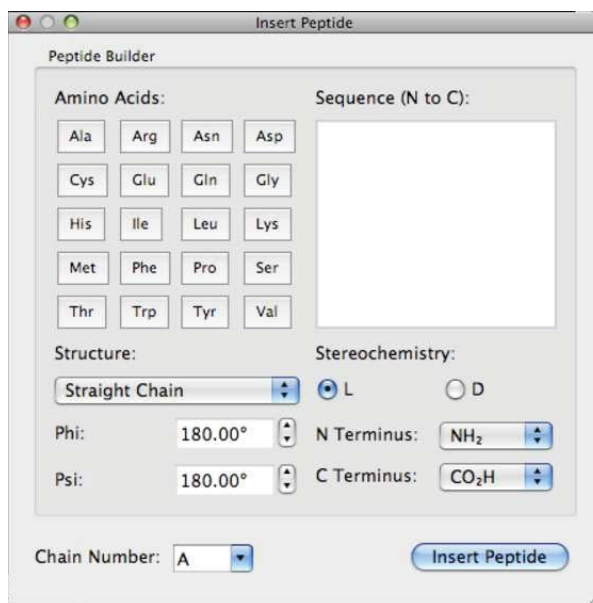
Figure 4-4: Peptide generation window used to include the peptide in the SWCNT. This option has the ability to include different amino acids, N terminus, and C terminus settings.

In this work, the modeling was performed based on one of the peptides discovered in the biopanning process and was labeled as peptide 1. Using the known sequence of peptide 1 (Thr-Leu-Trp-Thr-Asp-Thr-Ser), the structure was added into the peptide generation window and was connected to the SWCNT. Here, a covalently linked carboxyl group was first generated at the midpoint of the SWCNT. Then, the nitrogen of the peptides N-terminus was attached to the carbon of the carboxyl group. The linking of the N-terminus of the peptide to the CNTs was based on the fact that this is the actual chemical link that forms between the peptide and the SWCNTs when using the carbodiimide chemistry [5]. It is also important to note that during the modeling, hydrogens were removed from the amine group with the addition of the bond between the N-terminus and the carboxyl group in order to mimic the real chemical bond formed.

Since the peptide was attached through a user based approach (manually), the bond lengths and orientation of the peptide might not be correct. Thus, the final step in the generation of the SWCNT/peptide system was to the find the conformation that results in the lowest or minimum steric energy. Before energy minimization could be carried out, the first 64 carbon atoms and the last 64 carbon atoms in the system were set to be excluded from the minimization since these were used as the source and drain contacts of the system. These contacts were excluded because energy minimization flays out the ends of the tube and makes different sections of the contacts to have different diameters. Indeed, this out of plane opening of the tube ends does not allow the DFTB+ program to run since dftb splits each contact up into 2 sections that must be mirrors of each other. Once the contacts were pinned, the built in energy minimization algorithm (MMFF94) was implemented since it is optimized for peptides. The energy minimized SWCNT/peptide structure is presented in Figure 4-5.
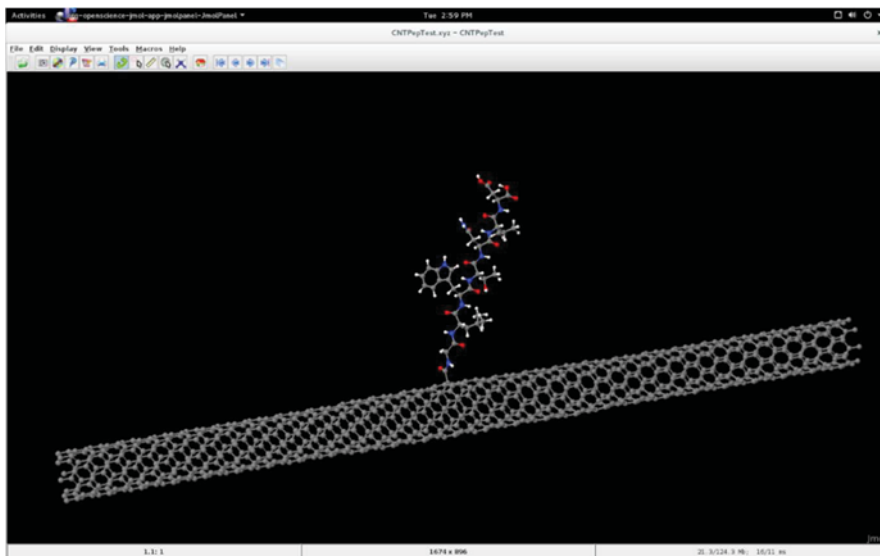
Figure 4-5: Visualization of the SWCNT/Peptide structure in Avogadro molecular modeling software following an energy minimization

Following the assembly process of the SWCNT and the peptide, the interaction of PETN explosive was incorporated within the system. To complete this, the PETN structure was included into the Avogadro workspace using a manual molecule addition. In this work, only one perturbation of the peptide/explosive interaction site was considered. The location on the peptide for the interaction with the explosive was the leucine-tryptophan segment, since Khan *et al.* [6,7] have shown that the leucine-tryptophan are the segments of a peptide that interact with TNT and nitro based explosives. Khan *et al.* have associated these peptide segments to the PETN reductase system, which is a flavoprotein that has shown to degrade most explosives. Khan *et al.* also have observed that there is an additional electron density between the nitro groups of TNT and the tryptophan group that is the result of a conformational change of the tryptophan to alleviate the steric hindrances and to accept the nitro group. Additionally, they have shown that the indole side chain of the tryptophan located within the PETN reductase active site reduces the nitro groups through a nitroreductase mechanism. Thus, the PETN was located near the leucine-tryptophan segment that allowed for the interaction with the indole side chain of the peptide and the nitro group of the PETN. Finally, the conformation energy was minimized in Avogadro (again isolating the contacts) such that the interaction of the peptide and PETN was considered to be at an equilibrium distance.

4.3 Gen File Creation

Once the SWCNT structure was generated, the xyz file was manually converted to a gen file. In the gen files, the SWCNT is broken up into source, device, and drain regions. Additionally, the source and drain layers were further broken up into 2 principle layers

which contained the same number of atoms and were structural mirrors of each other. A schematic of the divided SWCNT is shown in Figure 4-6.

| S_{PL1} | S_{PL2} | Device (CNT) | D_{PL1} | D_{PL2} |

Figure 4-6: Schematic division of the SWCNT structure into source principle layer 1 (S$_{PL1}$), source principle layer 2 (S$_{PL2}$), device, drain principle layer 1 (D$_{PL1}$), and drain principle layer 2 (D$_{PL2}$).

More specifically, each source and drain principle layer was set to be the size of 1 cell or 32 atoms as previously described. Thus, the device region was 22 cells long. Once properly divided, a new file was created with a .gen extension. In this new file, the regions were ordered as *device,* S_{PL2} , S_{PL1}, D_{PL1}, S_{PL2}. A sample of a partial gen file is presented in Figure 4-7.


```
                                      CNT.gen
  Open  ▼    ⏏                                                        Save   ≡    ×
                    ~/Desktop/CNT Project/CNT-Peptide files/26 unit long (copy)
    832  C
C                     x              y              z
1       1         3.148887         0          -45.547485
2       1         3.148887         0          -46.968485
3       1         2.909192      1.205027       -43.412554
4       1         2.909192      1.205027       -44.833554
5       1         2.226599      2.226599       -45.547485
6       1         2.226599      2.226599       -46.968485
7       1         1.205027      2.909192       -43.412554
8       1         1.205027      2.909192       -44.833554
9       1         0            3.148887        -45.547485
10      1         0            3.148887        -46.968485
11      1        -1.205027      2.909192       -43.412554
12      1        -1.205027      2.909192       -44.833554
13      1        -2.226599      2.226599       -45.547485
14      1        -2.226599      2.226599       -46.968485
15      1        -2.909192      1.205027       -43.412554
16      1        -2.909192      1.205027       -44.833554
17      1        -3.148887         0          -45.547485
18      1        -3.148887         0          -46.968485
19      1        -2.909192     -1.205027       -43.412554
20      1        -2.909192     -1.205027       -44.833554
```

Figure 4-7: Sample of the information contained in a gen file including the total number of atoms in the system, the types of atoms, and the coordinates of the atoms.

As seen in Figure 4-7, the first row is the number of atoms in the system and the C represents that the system is treated as a cluster. The second row describes the types of atoms in the system. For a bare SWCNT, only carbon (C) atoms are present, but when the SWCNT/peptide system is modeled, nitrogen(N), oxygen (O), and hydrogen (H) are also present. The following rows contain information on the type of atom and its location. Column 1 represents the atom number which acts as a count for the program. Column 2 represents the type of atom relative to the order of atoms called out in row 2. Thus, column 2 would be 1 for carbon, 2 for nitrogen, 3 for oxygen, and 4 for hydrogen. Finally, columns 3, 4, and 5 are the x, y, and z Cartesian coordinates of the atoms in angstroms respectively.

4.4 Contact File Sample Code

Once the gen file was constructed, the next step was to create the dftb+ code file for the contacts. The name of the file was set to dftb_in.hsd.source and dftb_in.hsd.drain for the source and drain respectively. For the sample code, the SWCNT/ peptide system was here considered. The first two blocks of the code (established by the curly brackets) for the source were as follows.

```
Geometry = GenFormat {
            <<< 'CNTPepTest.gen'
            }
```

```
Transport {
Geometry {
Device {
 AtomRange = 1 815
 }
Contact {
 Id = "source"
AtomRange = 816 879
ShiftAccuracy = 1e-4
}
Contact {
Id = "drain"
AtomRange = 880 943
ShiftAccuracy = 1e-4
}
}
Task = ContactHamiltonian{
ContactId = "source"
}
}
```

Where this first block caused the SWCNT geometry to be loaded from a gen file. The
second block of code defined the atom ranges for the device, source, and drain regions
present in the gen file. The ShiftAccuracy code was used to relax the stringency of the
program when checking if the principle layers in the contact are identical. Using a high of
level of accuracy resulted in failure of the program. The "Task = ContactHamiltonian"
required the program to perform the calculations on the contact. For the previous sample
code, the source section is called out in the ContactId section, but the drain can be used
instead for its respective calculations.

The next section of code focuses on the Driver and Hamiltonian settings and is
described as follows.

```
Driver = {}

Hamiltonian = DFTB {
SCC = Yes
MaxSCCIteractions=1000
SCCTolerance = 1e-7
MaxAngularMomentum = {
C = "p"
N = "p"
O = "p"
H = "s"
}
```

The Driver section concentrates on the dynamics calculations where the atoms are free to move and be acted upon external forces such as current. Since the atoms in the modeled system here investigated were fixed, the driver settings were left blank. In the Hamiltonian section, the DFTB theory was initialized. The SCC code turned on the self-consistent charge setting. The MaxSCCIterations sets the maximum number of iterations that were carried out if the defined SCCTolerance was not reached. The MaxAngularMomentum setting defined the farthest electron shell that was considered in the calculations. For carbon, nitrogen, and oxygen the farthest orbital was set as p and for hydrogen it was set to s.

The next code section was associated to the assignment of electrons to energy states according to a fermi distribution at electron temperature T.

```
Filling = Fermi {
Temperature [Kelvin] = 0
}

SlaterKosterFiles = {
C-C = "C-C.skf"
O-C = "O-C.skf"
C-O = "C-O.skf"
N-C = "N-C.skf"
N-H = "N-H.skf"
C-N = "C-N.skf"
H-N = "H-N.skf"
C-H = "C-H.skf"
H-C = "H-C.skf"
H-O = "H-O.skf"
O-H = "O-H.skf"
N-N = "N-N.skf"
O-O = "O-O.skf"
N-O = "N-O.skf"
O-N = "O-N.skf"
H-H = "H-H.skf"

}

KpointsAndWeights = SupercellFolding{
25 0 0
0 1 0
0 0 1
0.0 0.0 0.0
}


Eigensolver = DivideAndConquer{}

}
```

Here, the SlaterKosterFiles syntax called out all files for the atomic interactions present in

the system. As described earlier, the bare SWCNT only contained a file for carbon-carbon

interactions, but for the peptide system 15 more interactions files were included. Next, the

values for KpointsAndWeights were selected in a way that they represented an ideal one

dimensional nanowire since a single wall carbon nanotube is best described under such

conditions. Finally, the Eigensolver setting defined what type of solver was used to diagonalize the Hamiltonian. In this case, the selected solver was DivideAndConquer for the contacts since although it applied the most memory intensive solver, the contact calculations were still performed in less than a minute.

4.5 Device File Sample Code

The device sample code described in this section refers to the SWCNT with a peptide covalently attached at the midpoint of the tube. The file for the device section was named dftb_in.hsd.device. In the following sample code, the geometry section required the gen file which contained the information of the peptide-SWCNT system. The transport section was here used to define the device, source, and drain layers.

```
Geometry = GenFormat {
<<< 'CNTPepTest.gen'
}


Transport {
Geometry {
Device {
AtomRange = 1 815
}
Contact {
Id = "source"
AtomRange = 816 879
ShiftAccuracy = 1e-4
}
Contact {
Id = "drain"
AtomRange = 880 943
ShiftAccuracy = 1e-4
}
}
```

```
Task = UploadContacts {
FirstLayerAtoms= 1
FermiLevel[eV]= SetForAll{-3.848849}
ContactPotentials {
source[eV]=0.0
drain[eV]=1.25
}
EnergyRange[eV]= -6 -1
EnergyStep[eV]=0.020
WriteTunneling=Yes
}
}
```

The difference in this code in contrast to that shown in the contact file sample section (see section 4.4), occurs within the upload contacts section. Here, the FermiLevel option sets the Fermi level of the contacts. This Fermi level was found by running the code presented in the Contact File Sample Code section (see section 4.4). In this work, although different calculations were run for the source and drain, the Fermi levels were found to be equal. This was expected since the contacts are comprised of the same atoms in the same configuration. Thus, the SetForAll option was used, and it fixed the source and drain contacts at the same Fermi level.

Continuing with the device file sample code, the ContactPotentials section defined the source and drain voltage bias placed across the tube. These values were studied as variable parameters in this research. The EnergyRange variable defined the range over which the transmission function and the local density of states were calculated (set to contain the Fermi level), and the EnergyStep indirectly set the number of sample points in the energy range by setting the variation in energy between each calculated point.

The next section contains the driver and Hamiltonian settings. Most of the sections are the same as presented in the contacts file sample section (see section 4.4). Indeed, due

to the higher complexity of the device section, the SCC (self-consistent charge) tolerance

was lowered to 1e-4 which was the highest accuracy value that allowed convergence of the

program. Also, a mixer was implemented in order to combine charges from previous

iterations for preventing non-converging oscillating calculations and lowering the

computation time. Here, MaxAngularMomentum defined the highest orbital for each

element that was included in the calculations. For example, since carbon was set as p, both

s and p orbitals were considered.

```
Driver = {}

Hamiltonian = DFTB {
SCC = Yes
MaxSCCIterations = 10000
SCCTolerance = 1e-4
Mixer=Broyden{MixingParameter=0.02}
MaxAngularMomentum = {
C = "p"
N = "p"
O = "p"
H = "s"
}
```

The next section of the code describes the electron assignment to the energy levels,

which called out the appropriate Slater Koster files, and defined the settings for the Poisson

solver used to solve the NEGFs. In this code, the PoissonBox defined the dimensions of

the box in three dimensions. The MinimalGrid set the mesh size created within the Poisson

box. Here, the initiation of the BuildBulkPotential was used to make the program solve for

the electrostatic potential of the system using Dirichlet boundary conditions. The

SavePotential was implemented to save the calculated potential to an output file. The

Verbosity was set to a value between 0 and 100. A higher number outputs more real time

information about the calculations as they are carried out. A higher verbosity was used

during this work to monitor the convergence. The AtomDensityTolerance defined the cutoff where the imposed Mulliken charges vanish. The PoissonAccuracy was used to indicate when Poisson convergence occurred, and the BoundaryRegion was set to circle instead of the default global because it was the most appropriate parameter for a 1D nanowire.

```
Filling = Fermi {
Temperature [Kelvin] = 0
}

SlaterKosterFiles = {
C-C = "C-C.skf"
O-C = "O-C.skf"
C-O = "C-O.skf"
N-C = "N-C.skf"
N-H = "N-H.skf"
C-N = "C-N.skf"
H-N = "H-N.skf"
C-H = "C-H.skf"
H-C = "H-C.skf"
H-O = "H-O.skf"
O-H = "O-H.skf"
N-N = "N-N.skf"
O-O = "O-O.skf"
N-O = "N-O.skf"
O-N = "O-N.skf"
H-H = "H-H.skf"
}
```

```
Electrostatics = Poisson {
Poissonbox[Angstrom]= 30.0 30.0 30.0
MinimalGrid [Angstrom] = 0.4 0.4 0.4
BuildBulkPotential = Yes
SavePotential = Yes
verbosity=91
AtomDensityTolerance = 1e-5
PoissonAccuracy = 1e-6
BoundaryRegion = Circle{}
```

The last section of code constructed a physical gate in the system and imposed settings for the NEGF solver. The first block of code in this section is related to the gate. The GateLength_l sets the size of the gate in the transport direction (z), the GateLength_t sets the length of the gate in the x direction, and the GateDistances sets the distance of the gate from the device region in the positive y direction. As an important note, since the gate was constructed by the program in the positive y direction, the peptide was attached on the SWCNT facing the –y direction to avoid interaction between the peptide and the physical gate. The GatePotential defined the potential applied to the gate and was investigated as a variable in this work. The second block of the code defined the Eigen solver. The Delta parameter is a small positive number used in the Green's function formalism. The ContourPoints set the number of points calculated along the integration of Green's function, where the number of points had a large effect on the computation time. The LowestEnergy defined the value at which the integrations of the Green's functions began, and the EnclosedPoles set the number of poles considered in the contour. The value of this setting is usually between 3 and 5.

```
Gate=Planar{
GateLength_l[Angstrom]=12.0
GateLength_t[Angstrom]=30.0
GateDistance[Angstrom]=7
GatePotential[eV]=-0.15
}
}

Eigensolver = GreensFunction {
FirstLayerAtoms= 1
Delta [eV] = 1e-5
ContourPoints = 30 40
LowestEnergy [eV] = -60.0
EnclosedPoles = 4
}
}
```

4.6 Running the dftb+ Program

The first step in running the dftb+ program was to run calculations on the source and drain sections. In order to carry this out, the dftb_in.hsd.source file was renamed to dftb_in.hsd. When the dftb+ code is run, it searches for this file name. Once the name of the source file was changed, the dftb+ program was run in the local folder using the ./dftb+NEGF command. Here, the contact calculations took place in under a minute after which an output file named detailed.out that contained information from the calculation of the source was created. The primary value used from this calculation was the Fermi level which was used in the device's UploadContacts section. Once the Fermi level information was transferred to the device file, the dftb_in.hsd extension was renamed to dftb_in.hsd.source and the dftb_in.hsd.drain file was renamed to dftb_in.hsd. Again the dftb+ program was run, and the Fermi level was placed into the device file. To complete the contact calculations, the dftb_in.hsd file was renamed to dftb_in.hsd.drain. As previously described, three systems were considered in this work (bare SWCNT, SWCNT/peptide, and SWCNT/peptide/PETN). It is important to note that contact calculations had to be re-run before the device calculations for each SWCNT system were carried out. However, the contact calculations were not re-run when the gate or bias voltages where adjusted.

Once contact calculations were completed, the device file was processed using the dftb+ software. In a similar manner to the contacts, the dftb_in.hsd.device extension was renamed to dftb_in.hsd. Since the calculation for the device is much more time intense, the *ulimit –s unlimited* command was used to open up more memory before the program was initialized using the ./dftb+NEGF command. Due to the complexity of the calculations,

these iterations took much longer than that of the contacts. Simulations on bare SWCNTs took anywhere between 1 hour and 8 hours. Conversely, calculations of the SWCNT/peptide and SWCNT/peptide/PETN systems took between 2 days to 1 week to converge. Once convergence was reached, a new detailed.out file was created. In this file, the last line contained the electrical current passing though the tube at a set bias and a set gate voltage. For the purpose of this work, the bias and gate voltages where the main variables studied in the three aforementioned SWCNTs systems. Finally, graphs of electrical current versus bias voltage at a specified gate voltage and current versus gate voltage at a set bias voltage were here generated. A schematic of the flow for a dftb+ run is presented in Figure 4-8.
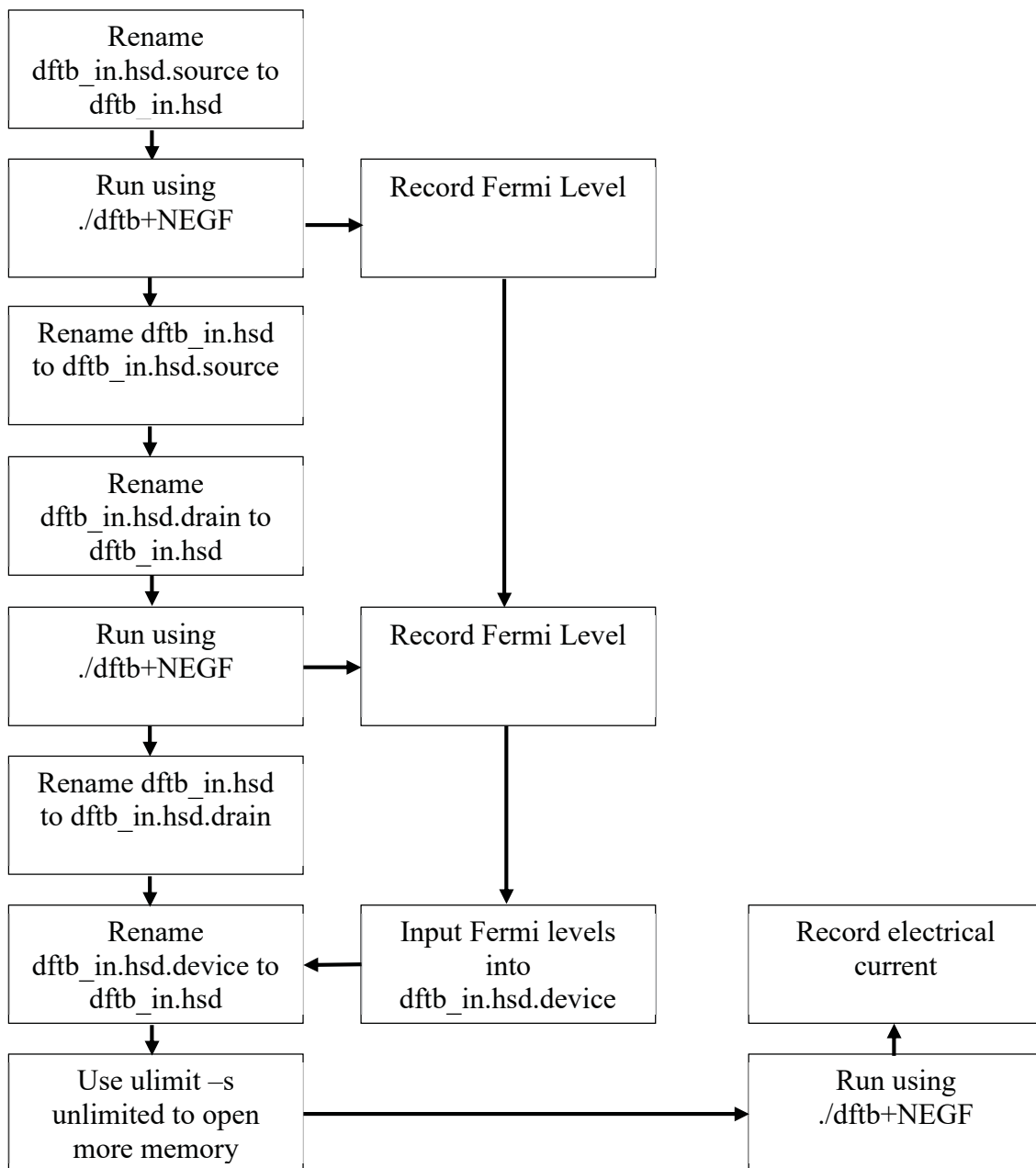
Figure 4-8: Schematic flow of the steps taken to run the dftb+ program to produce the electrical current.

4.7 References

[1] "Avogadro - Free Cross-Platform Molecule Editor" [Online]. Available: http://avogadro.cc/wiki/Main_Page. [Accessed: 13-Dec-2016].

[2] "Jmol: An Open-Source Java Viewer for Chemical Structures in 3D" [Online]. Available: http://jmol.sourceforge.net/. [Accessed: 13-Dec-2016].

[3] "About DFTB+" [Online]. Available: http://www.dftb-plus.info/about-dftb/. [Accessed: 13-Dec-2016].

[4] "TubeGen Online - v3.4" [Online]. Available: http://turin.nss.udel.edu/research/tubegenonline.html. [Accessed: 15-Aug-2016].

[5] "Carbodiimide Crosslinker Chemistry" [Online]. Available: https://www.thermofisher.com/us/en/home/life-science/protein-biology/protein-biology-learning-center/protein-biology-resource-library/pierce-protein-methods/carbodiimide-crosslinker-chemistry.html. [Accessed: 07-Sep-2016].

[6] Khan, H., Harris, R. J., Barna, T., Craig, D. H., Bruce, N. C., Munro, A. W., Moody, P. C. E., and Scrutton, N. S., 2002, "Kinetic and Structural Basis of Reactivity of Pentaerythritol Tetranitrate Reductase with NADPH, 2-Cyclohexenone, Nitroesters, and Nitroaromatic Explosives," J. Biol. Chem., **277**(24), pp. 21906–21912.

[7] Khan, H., Barna, T., Harris, R. J., Bruce, N. C., Barsukov, I., Munro, A. W., Moody, P. C. E., and Scrutton, N. S., 2004, "Atomic Resolution Structures and Solution Behavior of Enzyme-Substrate Complexes of Enterobacter Cloacae PB2 Pentaerythritol Tetranitrate Reductase Multiple Conformational States and Implications for the Mechanism of Nitroaromatic Explosive Degradation," J. Biol. Chem., **279**(29), pp. 30563–30572.

Chapter 5 . Results and Discussion

The following chapter presents the results obtained in the investigation of selective peptides toward PETNH as well as the detection capabilities of a peptide/SWCNT system towards PETNH. Also included in this chapter are the results from the molecular modeling of a SWCNT/peptide system. Here, a phage display protocol was used to identify the selected peptides. Once the peptides were identified via sequencing, they were used to functionalize the surface of carboxylated SWCNTs to create a sensor platform. These sensors were then tested in a liquid state and the peptides were further tested for selectivity. Finally, the conditions of a SWCNT Field Emission Transistor (FET) platform were modeled using a DFTB method to simulate the solid state sensing of PETN.

5.1 ELISA testing of the M13KE Ph.D.-7 Library

The ELISA performed on the target PETNH using the M13 Ph.D.-7 phage library was performed in order to ascertain if there were phage in the aforementioned library with affinity and specificity towards the investigated target. Here two different methods of PETN immobilization were studied. The first approach consisted of a passive absorption of PETN onto polystyrene microwells. In this methodology, PETN was allowed to passively absorb to the wells. Then, 1 % bovine serum albumin (BSA) and TWEEN-20 in phosphate-buffered saline (PBS) was used as the blocking buffer. Following the addition of the block, an M13 phage library was allowed to bind to the passively absorbed PETN. After the phage, antibodies were added to the wells and were used to bind to the phage to determine the amount of phage attached to the immobilized PETNH. These antibodies were tagged with an enzyme that causes a color change in the presence of 3,3',5,5'-

Tetramethylbenzidine (TMB). This color change was monitored using the absorption of visible light, and a higher absorbance in the wells indicated a higher level of phage binding on the wells. The results of this test are presented in Figure 5-1.
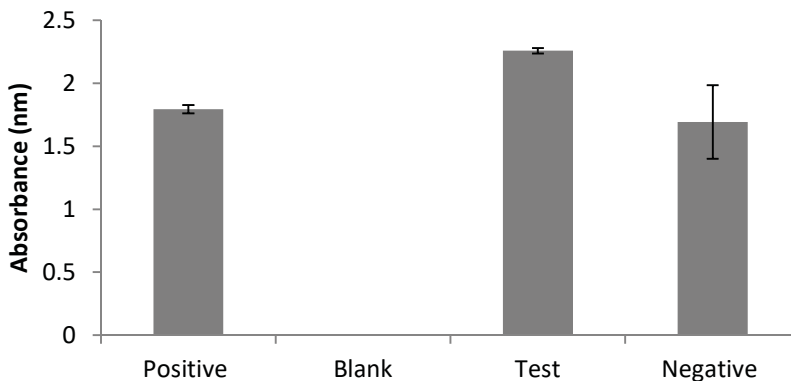
Figure 5-1: ELISA results employing a passive absorption technique of PETN on polystyrene wells for immobilization purposes.

As shown inFigure 5-1, the high absorbance in the negative control wells and the little differentiation between the test and negative wells suggests a high level of nonspecific binding by the peptides. This implies that the phage bound with the same degree of affinity to both the PETN and the blocked wells. To rule out experimental error, this test was performed a second time and similar results were obtained.

A second trial was performed with the removal of the TWEEN-20 solution. The results are shown in Figure 5-2.
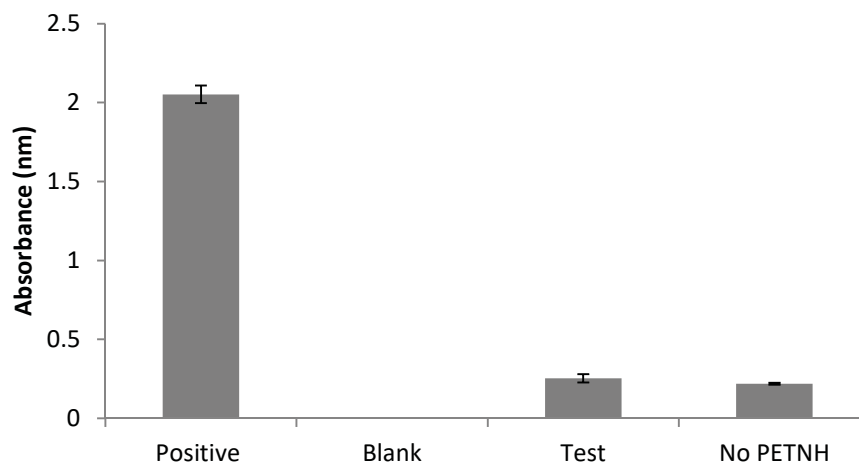
Figure 5-2: ELISA results obtained in the absence of TWEEN-20 and employing passive absorption of PETN on polystyrene wells for immobilization purposes.

As evident in Figure 5-2, the test and negative control wells exhibited noticeably lower levels. However, the results of this test still show no difference between the test and negative wells. Therefore, the passive absorption of PETN was not a viable immobilization technique in this research program.

Hence, a second immobilization approach was studied. Here, pentaerythritol trinitrate hemisuccinate (PETNH), a surrogate of PETN was immobilized on the microwells. This surrogate of PETN replaces one of the NO_3 groups with a COOH group, which allowed for its covalent immobilization on amine based microwells using the reaction between its carboxyl functional group and the amine functional groups in the wells via the 1-Ethyl-3-(3 dimethylaminopropyl) carbodiimide (EDC) reaction (see section 3.1). This technique was investigated by mixing 5 times more molar excess of EDC with a PETNH solution, and then added to the amine surface functionalized ELISA wells in order to immobilize the PETNH. The results of this test are presented in Figure 5-3.
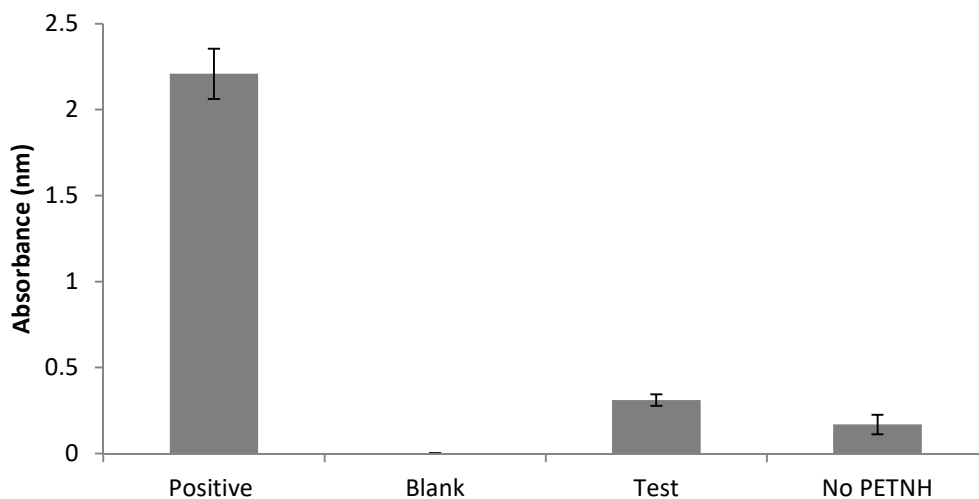
Figure 5-3: ELISA results with immobilization via covalent attachment of a PETN surrogate containing a free carboxyl group onto amine surface functionalized wells.

As it can be seen in Figure 5-3, there is a small difference between the test and negative control wells. Indeed, by performing a standardized t-test, it was found that their difference was not statistically significant. Therefore, a further optimization in the process was investigated.

The optimization consisted of studying the effect of the amount of PETNH added to each well along with an excess of EDC. The levels of PETNH studied were: 1 μg, 2 μg, and 3 μg per well. For each of these values, 5 and 10 times EDC molar excess was included as part of the testing. The results of this study are presented in Figure 5-4.
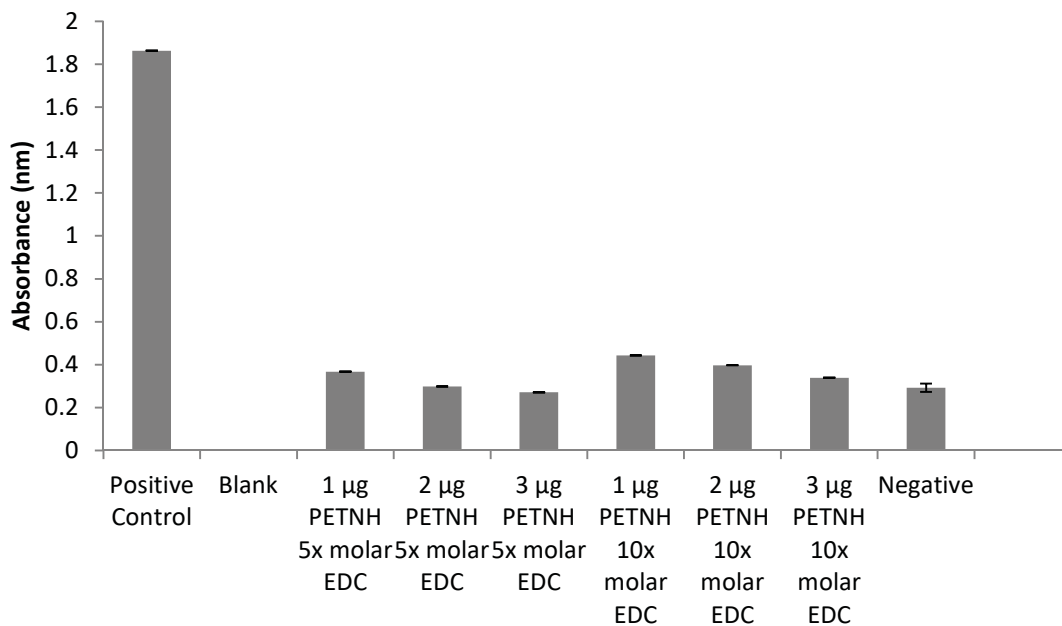
Figure 5-4: ELISA results studying the effect of varying the amounts of immobilized PETNH surrogate and EDC concentrations.

As shown in Figure 5-4, as the amount of immobilized target at each EDC molar excess was increased, the absorbance decreased. This suggests that the amount of PETNH bound on the microwells decreased by increasing its concentration. This is most likely as a result of either a decrease in non-specific binding or steric hindrance issues. Conditions that seem to be associated to the overcrowding of the immobilized target on the wells. The figure also shows that by using 10 times more molar excess of EDC than PETNH, a higher absorbance, and therefore a higher amount of bound phage was observed. Based on these results, the remaining immobilizations used 1 μg of PETNH and 10 times more molar excess of EDC. From Figure 5-4 it was also observed that the negative control wells still showed a high level of nonspecific binding, suggesting that the peptides attached equally to both the PETNH and to the well.

In order to decrease the level of nonspecific binding, the type of block buffer used was investigated. Several trials were studied with different blocks (1% BSA block, 1% casein block, and a block made from 5 % non-fat dry milk (NFDM) dissolved in PBS). The results of the ELISA employing the dry milk block buffer are shown in Figure 5-5. Here, the 5% NFDM block buffer results are the only ones presented since these displayed the highest absorbance difference between the test and negative samples. This difference between the absorbance in the test and negative wells seems to be associated with a higher degree of specificity of the phage to the PETNH over the blocked wells. The figure shows that the test wells (those containing PETNH) displayed an absorbance 5.5 times larger than the wells without PETNH. Using a standardized t-test, it was observed that the differences in absorbance were statistically significant. Based on these results, the identification of selective peptides towards PETNH were carried out on wells blocked with non-fat dry milk (NFDM).
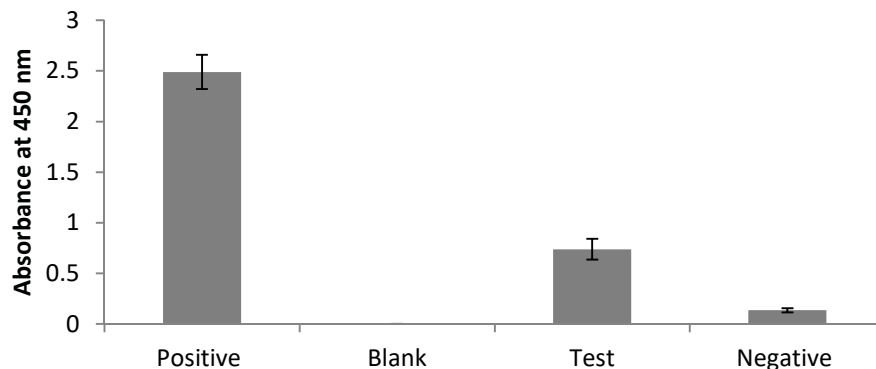
Figure 5-5: ELISA results based on 1 μg of immobilized PETNH, 10 times molar excess EDC, and 5 % non-fat dry milk block buffer.

By comparing the test versus the negative results from Figure 5-5, it is observed that the negative control samples (no PETNH analyte) displayed a low level of absorbance which suggests that although some degree of nonspecific binding was still present in the phage

studied, most of the phage seems to have been bound to the PETNH. Indeed, the limited level of nonspecificity shown in the negative wells could not be totally eliminated with any of the blocks here investigated. It is believed that the amine surface coating of the wells used for attaching the PETNH caused the phage to nonspecifically bind to the blocked wells.

5.2 Biopanning using the M13KE Ph. D.-7 Library

After determining the ability of the M13KE library to bind to the immobilized surrogate, a biopanning (screening) procedure was performed against the PETNH immobilized target. The biopanning consisted of first immobilizing the PETNH into amine functionalized wells and subsequently blocking the wells via NFDM. Then, the M13 phage library was added to the wells and the phage with affinity to the PETNH bound to it (Here, the phage that did not bind to the PETNH were removed from the wells). Next, the bound phage were eluted, and two more rounds were carried out with the purpose of increasing the selectivity of the phage. After each round, a small amount of the selective phage were used in a titer to determine the concentration of phage in solution (pfu/ml - plaque forming units/milliliter). Briefly, a titer consists of infecting *E. coli* with serial dilutions of a phage sample followed by the growth of the infected *E. coli* on an agar plate for its counting. This count is directly related to the concentration of phage in the solution used to infect the *E. coli*. The results of the biopanning process showed that the difference in phage concentration between the first round of panning (2.2×10^7 pfu/ml) and the third (50 pfu/ml), was six orders of magnitude. This indicates that the majority of the non-specific phage were removed by the third round of panning. From the titer performed on the third

round of panning sample, five plaques were removed (extracted) from the plate using a glass pipette and transferred to separate microcentrifuge tubes.

Following the removal and isolation of the plaques from the third round titer plate, the amplification and PEG purification stages were performed on the isolated plaques. The amplification consisted of infecting the *E. coli* by the phage followed by an incubation period where the *E. coli* is allowed to grow more phage. In contrast, the PEG purification (removal of contaminants) consists of utilizing a PEG solution to precipitate the phage and form a pellet which is later reconstituted in a non-contaminated solution. Indeed, the PEG purification not only purifies the target, but also concentrates the phage. Hence, both procedures (amplification and PEG purification) were used to obtain a concentration of phage in solution above $2x10^{11}$pfu/ml (the minimum concentration required by the ELISA protocol technique). The results from the amplification and PEG purification are shown respectively in Table 5.1 and Table 5.2.

Table 5.1 : Amplification of the five plaques harvested from the third round of biopanning (tntc = too numerous to count).

	Dilution	Plaque Colonies	Concentration(pfu/ml)
Plaque 1 Eluate Amplified	1.00×10^4	tntc	NA
	1.00×10^6	2292	1.15×10^{11}
	1.00×10^8	29	1.45×10^{11}
Plaque 2 Eluate Amplified	1.00×10^4	tntc	NA
	1.00×10^6	1752	8.76×10^{10}
	1.00×10^8	11	5.50×10^{10}
Plaque 3 Eluate Amplified	1.00×10^4	tntc	NA
	1.00×10^6	1420	7.10×10^{10}
	1.00×10^8	19	9.50×10^{10}
Plaque 4 Eluate Amplified	1.00×10^4	tntc	NA
	1.00×10^6	1984	9.92×10^{10}
	1.00×10^8	17	8.50×10^{10}
Plaque 5 Eluate Amplified	1.00×10^4	tntc	NA
	1.00×10^6	1980	9.90×10^{10}
	1.00×10^8	24	1.20×10^{11}

Table 5.2 : PEG purification of the five plaques harvested from the third round of biopanning (tntc=too numerous to count).

	Dilution	Plaque Colonies	Concentration(pfu/ml)
Plaque 1 Eluate PEG Purified	1.00×10^6	tntc	NA
	1.00×10^8	tntc	NA
	1.00×10^{10}	142	7.10×10^{13}
Plaque 2 Eluate PEG Purified	1.00×10^6	tntc	NA
	1.00×10^8	996	4.98×10^{12}
	1.00×10^{10}	6	3.00×10^{12}
Plaque 3 Eluate PEG Purified	1.00×10^6	tntc	NA
	1.00×10^8	396	1.98×10^{12}
	1.00×10^{10}	9	4.50×10^{12}
Plaque 4 Eluate PEG Purified	1.00×10^6	tntc	NA
	1.00×10^8	1100	5.50×10^{12}
	1.00×10^{10}	19	9.50×10^{12}
Plaque 5 Eluate PEG Purified	1.00×10^6	tntc	NA
	1.00×10^8	1068	5.34×10^{12}
	1.00×10^{10}	6	3.00×10^{12}

From Table 5.1 and Table 5.2, it is evident that some dilutions resulted in a number of plaques too numerous to count. Hence, these samples did not allow the quantification of pfu/ml concentration. For dilutions where the number of plaques was accessible to count, the calculation of the number of plaque forming units per milliliter (pfu/ml) was obtained by using equation 5.1.

$$\text{Concentration} \left(\frac{\text{pfu}}{\text{ml}}\right) = \frac{\text{Plaque Colony Count}}{\text{Volume of sample used to infect bacteria (ml)}} * \text{Sample Dilution Factor} \qquad 5.1$$

In equation 5.1, the volume of diluted sample used to infect the bacteria was 20 µl for all trials. From the results shown in Table 5.1, the representative concentration of phage in solution was selected from those samples that contained above 100 colonies since samples containing too few number of colonies were not an accurate representation of the amplified phage. For instance, from the amplified plaque 3 (see Table 5.1), the 1420 colonies was the more representative concentration of the sample. Thus, the solution concentration of the amplified plaque 3 was 7.10×10^{10} pfu/ml (see Table 5.1). As shown in Table 5.2, all plaque forming units present in each isolated plaque solution were further increased by two orders of magnitude following the PEG purification process.

Subsequently, the ELISA technique was performed on each amplified and PEG purified sample in order to corroborate the selectivity of each isolated phage. The ELISA procedure was similar to that used on the full phage library (see section 3.1). Here, a concentration of 2×10^{11} pfu/ml of each isolate phage was tested. In the ELISA testing,

two trials were run for each plaque, and the samples were tested in triplicate wells (n=3). The results of these ELISAs can be seen in Figure 5-6.
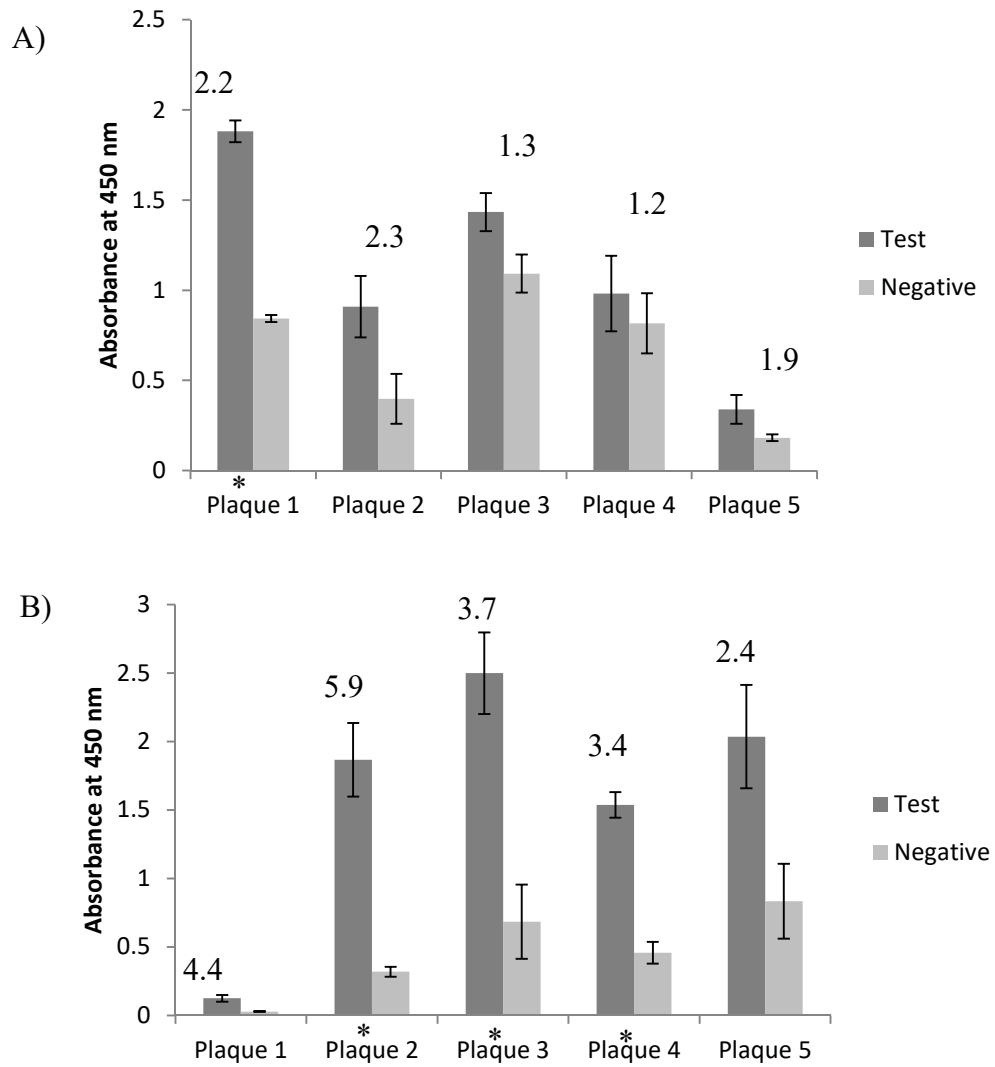
Figure 5-6: Comparison of the absorbance of the test wells to the negative control wells for trial 1 (A) and trial 2 (B). The number above each plaque column corresponds to the ratio of absorbance of the tests to the negative control wells. The presence of an asterisk (*) above the plaque indicates that the mean difference is significant (P≤0.05) via a T-test.

From Figure 5-6, it can be seen that the selected phages show a marked affinity towards PETNH, as well as a different degree of affinity among them, when compared to the relative intensity of those wells with no PETNH (negative). Indeed, the phage that appear to have shown a statistical difference ($P \leq 0.05$) between the test and negative control were plaque 1 from Figure 5-6 A and plaques 2,3, and 4 from Figure 5-6 B. Figure 5-6 A displays that the clones from plaque 1 showed a significant binding to wells containing PETNH ($P \leq 0.05$), when compared to wells without PETNH. On trial 2, the plaque 1 wells did not pass the t-test parameters, however they were close with a P value of 0.057. Also, in trial 2 (Figure 5-6 B), clones from plaques 2, 3, and 4 showed statistically higher binding when comparing to the absorbance of the test wells against the negative control wells. Thus, based on these results, the phage from plaques 1-4 were processed using the DNA purification kits and further sequenced.

5.3 Sequencing of the Plaques Isolated During Biopanning

The DNA purification of the selected plaques was performed using the Wizard® Plus SV Minipreps DNA Purification System. To determine the size and integrity of the purified DNA, gel electrophoresis was performed. Briefly, in gel electrophoresis a current is run through a gel containing a DNA ladder in one well and DNA samples to test in the other wells. Depending on the charge and size of the DNA, the molecules move different distances in the lanes. The distance the DNA moves can then be visualized using UV light since the DNA is dyed. The DNA ladder is a solution that contains known lengths of DNA that create a scale to compare to other samples, which allows for the the size of analyzed DNA to be read. The gel here used was composed of 1% agarose in Tris-phosphate buffer

(0.08M EDTA with 0.002M TPE), and the results of the electrophoresis can be seen in Figure 5-7.
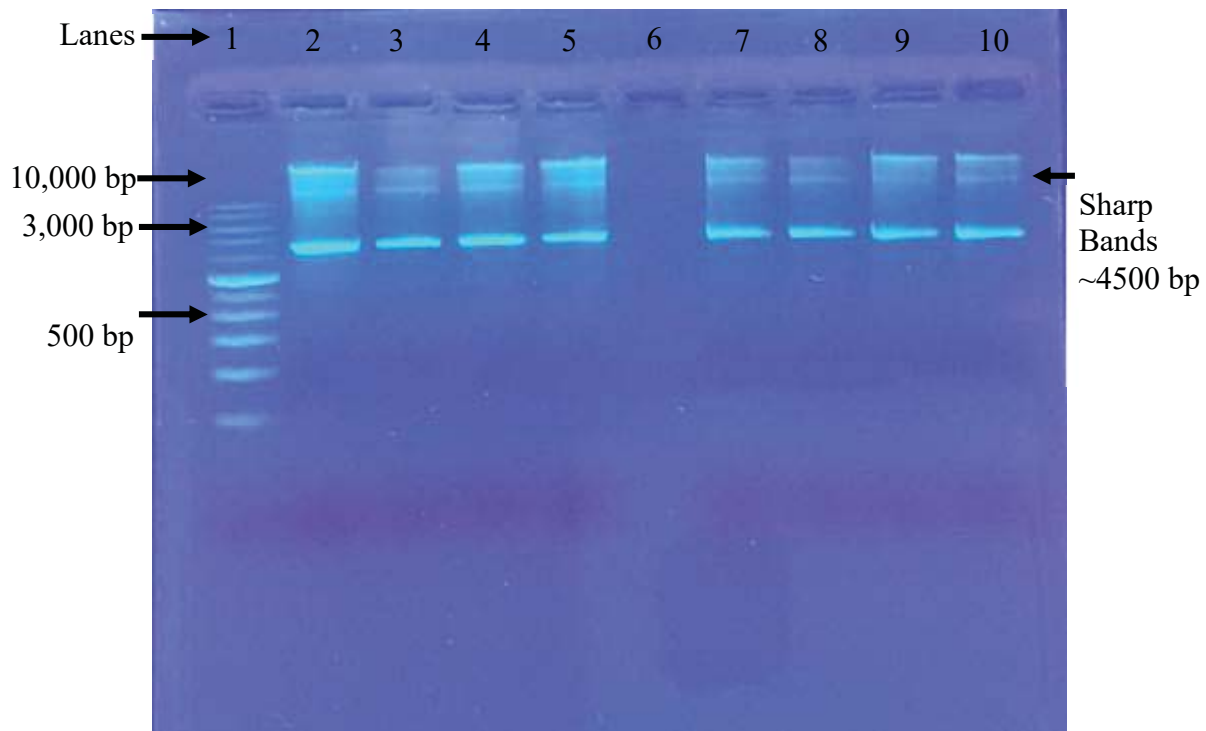
Figure 5-7: Gel electrophoresis of clones 1,2,3, and 4. Lane 1 is the 10,000 bp (base pairs) ladder. Lanes 7, 8, 9, and 10 are clones from the isolated phage 1, 2, 3, and 4 respectively.

As it can be seen from the sharpness of the bands present in lanes 7 through 10 in Figure 5-7, the DNA integrity is considered good [1]. Also, the clones were read at approximately 4,500 bp in length.

To determine the purity and concentration of the purified DNA in solution, a NanoDrop UV-Vis Spectrophotometer was employed. The results of the NanoDrop experiment are shown in Table 5.3.

Table 5.3 : NanoDrop results of the purified phage clones 1,2,3, and 4.

DNA Sample	A_{260}	A_{280}	A_{260}/A_{280}	Concentration (ng/µl)
1	1.744	0.994	1.754527	87.2
2	1.522	0.83	1.833735	76.1
3	4.126	2.216	1.861913	206.3
4	1.979	1.079	1.834106	99

To determine the purity of DNA from a NanoDrop experiment, the ratio A_{260}/A_{280} (ratio of the absorbance of the sample at 260 nm to the absorbance of the sample at 280 nm) was used. It is generally accepted that pure DNA has a A_{260}/A_{280} ratio of about 1.8 [2]. As shown in Table 5.3, all 4 DNA samples extracted and purified from their respective plaques can be considered pure.

Once the purity, integrity, and concentration of phage DNA was determined, each clone was sequenced using a Beckman CEQ2000 DNA Sequencer. This resulted in the nucleotide sequence which contains the phage DNA insert. Indeed, only a small section of the total clone sequence contains the information of the peptide. Using the gene studio software, the sequences read in the 5` and 3` directions were imported. These 5' and 3' directions are associated to the forward and reverse readings of the DNA sequences that were initialized respectively by the 96 gIII and 28 gIII primers. Here, the program lined up the sequences and then outputs a contig file that is the result from the consensus of the alignment. This consensus was then used to find the inserted peptide nucleotide sequence by finding the flanking Kpn 1 and Eag 1 sites, which are the markers for the beginning and end of the inserted phage DNA. Using this technique, sequences of 30 nucleotides in length were obtained. This was expected, since the phage library used contained phage expressing 7-mer peptides with 3 glycines as the linker sequence. Using the ExPASy web translation

tool, the nucleotide sequences were then translated into peptide sequences. The results of the sequencing and subsequent translation can be seen in Table 5.4.

Table 5.4 : Sequencing results for peptide 1-4. Similarities in the peptide sequences are bolded while the three glycine residue linker sequences are underlined. The bolded 30 letter long code (in the peptide sequence column) is the nucleotide sequence, and the identified amino acid sequences are based on the single letter code (*i.e.* T=Threonine, etc.).

Peptide	Nucleotide Sequence	Peptide Sequence
1	**actttgtggacggatacttcgggtggaggt**	T **L** W **T** D T S <u>G G G</u>
2	**ggtttgtggacgaatgttgatggtggaggt**	G **L** W **T** N V D <u>G G G</u>
3	**ggtttgagtacgtttgatgtgggtggaggt**	G L S T F D V <u>G G G</u>
4	**acggcgtttacttggaatcagggtggaggt**	T A F **T** **W** N Q <u>G G G</u>

In each nucleotide sequence, three nucleotides correspond to one amino acid (*i.e.* the nucleotide sequence **act** of peptide 1 corresponds to T in the peptide sequence). Using the knowledge of the different reading frames and the linker sequence, which is three glycine residues as stated in the phage display manual, the correct reading frame for each nucleotide sequence can be determined [3]. Thus, the correct peptide sequence is the first seven amino acids that have a three glycine long terminus as indicated in Table 5.4 (ie TLWTDTS for peptide 1). In this study, it is known that only the first seven amino acids are the peptide sequence, as the library used was comprised of phage expressing seven mer peptides. Using this fact, it can be seen that each peptide was successfully sequenced. It is also shown in Table 5.4, that although none of the peptides present the same sequence, they

display some similarities. For instance, peptide 1 and 2 both contain a leucine-tryptophan-threonine (LWT) segment, while peptide 4 also has a threonine connected to a tryptophan (TW). This is highlighted with the bold letters in Table 5.4. This could suggest that this similar segment (LWT) is the component that interacts with the PETNH explosive. Based on these results, a possible interaction mechanism between the LWT peptide segment and the PETNH could be addressed through the contact of the leucine-tryptophan segments of the peptides and the surrogate explosive. Khan *et al*. [4,5] have shown that the leucine-tryptophan segments of a peptide interact with TNT and explosives. Khan *et al.* have associated these peptide segments to the PETN reductase system, which is a flavoprotein that has been shown to degrade most explosives. Khan *et al.* also observed that there is an additional electron density between the nitro groups of TNT and the tryptophan that is the result of multiple conformations of the tryptophan. Additionally, they showed that the indole side chain of the conservative tryptophan located within the PETN reductase active site reduces the nitro groups through a nitroreductase mechanism. In the present work, peptides 1 and 2, express the same leucine-tryptophan segments, which could be assumed as the active site that interacts with the PETNH. In contrast, peptide 3 displays a more unique sequence (although it also shares a threonine-phenylalanine (TF) segment with peptide 4). This suggests that the presence of PETNH can be potentially corroborated with different amino acid sequences. Thus, peptides 1 through 4 were purchased from NeoBioLabs for subsequent selectivity testing and for their attachment onto CNTs in order to create a nanosensor. The attachment of peptides to CNTs is shown in the following section using a peptide derived from bee venom as the platform for the CNT/peptide attachment optimization

5.4 Bombolitin II Biotinylation Optimization

In parallel to the biopanning of the M13KE phage library against the immobilized surrogate PETNH, an additional peptide by the name of Bombolitin II (BII) was here investigated. Bombolitin II is a hydrophobic 17-mer peptide with a molecular weight of 1805.11 g/mol that derives from bee venom [6]. The sequence for BII is SKITDILAKLGKVLAHV via single letter code. Heller *et al.* [7] have shown that SWCNTs with physically absorbed BII experience a near-infrared photoluminescence shift when interacting with nitroaromatics such as TNT. Due to its affinity to explosives, BII was also purchased from NeoBioLabs and used to create a covalently functionalized SWCNT. To perform this, the N-terminus amine group of the peptide was reacted with the carboxyl group of the SWCNTs using the 1-Ethyl-3-(3-dimethylaminopropyl) (EDC) reactant (see section 2.3.4 and 3.1) [8]. This route allowed for the covalent anchoring of the peptide onto the CNT in order to form a selective nanosensor.

To track the amount of peptide bound to the SWCNTs, the peptides were first biotinylated by connecting the amine group present on the hydrazide-PEG4-Biotin to the C-terminus (end of the peptide containing a free carboxyl group) of the peptides. The presence of biotin on a tagged molecule elicited an absorbance change in a HABA/Avidin assay which was related to the concentration of the substance in solution via the Beer-Lambert Law (Beer's Law) [9]. Beer's law is presented in equation 5.2 where ΔA_{500} is the change in absorbance at 500 nm, C is the concentration, b is the cell path (1 cm for a cuvette), and ε_λ is the extinction coefficient (34,000 $M^{-1}cm^{-1}$ for the HABA/Avidin complex).

$$\Delta A_{500} = Cb\varepsilon_\lambda \qquad\qquad 5.2$$

To study the biotinylation of BII, two different trails were run based on the volume of hydrazide-PEG4-Biotin used. The conditions for each of these trials can be seen in Table 5.5. The EDC solution concentration was 100 mg/ml, the concentration of biotin hydrazide was 50 mM, and the concentration of BII was 0.5 mg/ml.

Table 5.5 : Trial descriptions for studying the optimization of biotin on the BII peptide.

Trial	Peptide Volume (µl)	EDC Volume (µl)	Hydrazide-PEG4-Biotin Volume (µl)
1	500	1.25	25
2	500	1.25	2.5

As seen in Table 5.5, the peptide and EDC solution volumes were kept constant. The peptide solution volume was kept constant in order to act as the control, and the EDC volume was kept constant since the molar excess of EDC had previously been optimized in the ELISA optimizations (see section 5.1). The Hydrazide-PEG4-Biotin was in excess for both trials so that the probability of an available Hydrazide-PEG4-Biotin molecule being near to a peptide for creating a link with the BII was high. Due to this condition, there was unreacted (free) biotin in the reacted biotin-BII sample. Hence, to correctly quantify the level of biotinylated peptide, the reaction solutions had to be purified.

Here, the reaction solutions from each trial were purified via Pierce C18 spin columns. In these columns, the peptide was bound to the carbon followed by an elution and

a purification process (see section 3.6). The results of trials 1 and 2 for the biotinylation of BII purified by the C18 spin columns is presented in Table 5.6.

Table 5.6 : Results of the biotinylated BII following a purification process using C-18 spin columns.

Trial	Biotinylated BII after Purification (mmol)	Percent of BII Biotinylated
1	8.53×10^{-5}	61.59
2	6.65×10^{-5}	48.00

As it is seen in Table 5.6, it seems that the excess biotin was removed through the C-18 spin columns, since the percent of biotinylated BII was not above 100 percent in either trial. Also, using an excess of 25 µl hydrazide-PEG4-biotin resulted in a larger level of attachment than using 2.5 µl. This is most likely due to more biotin being available to bind to the unstable O-acylisourea intermediate formed from the reaction between EDC and the peptide carboxyl group (see section 2.3.4). Based on the results here presented, this technique was used on the sequenced peptides identified from the M13 phage library. The results are shown in the following section.

5.5 Attachment of Sequenced Peptides to SWCNTs

Once the peptides discovered through the biopanning were sequenced, the next step of the research was their biotinylation as a tagging technique for their further attachment to SWCNTs. This was carried out by following the approach described in the previous section. Here, the biotinylation was performed on the four identified peptides in the

biopanning procedure (see Table 5.4). The results of two peptide biotinylation trials purified by graphite spin columns on the four identified peptides are presented in Table 5.7.

Table 5.7 : Extent of biotinylation for peptides 1 through 4 via biotin incorporation assay and Beer's law.

Peptide-Trial	Peptide Biotinylated (mmol)	Percent of Peptide Biotinylated
1-1	3.88×10^{-4}	63.83
1-2	4.29×10^{-4}	70.63
2-1	6.79×10^{-4}	54.58
2-2	6.97×10^{-4}	56.00
3-1	4.76×10^{-4}	70.27
3-2	4.95×10^{-4}	73.07
4-1	2.35×10^{-4}	40.77
4-2	2.35×10^{-4}	40.70

From the results presented in Table 5.7, it can be observed that each peptide was biotinylated. It can also be seen that 100 percent biotinylation was not obtained. This was expected due to the unstable reaction intermediate formed during the reaction between the free carboxyl groups and the EDC. This unstable reaction intermediate increases the possibility of peptides linking to each other through the reaction of their free carboxyl groups and amine groups. Additionally, it is believed that some mass losses were present during the experimental purification in the graphite spin columns. It can also be seen in Table 5.7, that the peptides had different levels of biotinylation. Peptide 1 and 3 were biotinylated to the greatest extent. This can be explained by the presence of an aspartic amino acid in both peptides. The aspartic acid segment contains a free carboxyl side group that can react with the N-terminus amine group from the peptide. Thus, peptides 1 and 3 exhibit a side chain carboxyl group in addition to the C-terminus carboxyl group. Peptide

4 does not contain this carboxyl side group and thus it is biotinylated to a smaller extent. Peptide 2 biotinylation levels are smaller than 1 and 3 but larger than 4. This could be associated to the presence of both a carboxyl side group and an amine side group in peptide 4. The additional carboxyl group in peptide 4 would suggest that the biotinylation percent would be higher, but due to the presence of an additional side chain amine group, there is an increased opportunity for the crosslinking between peptides. This crosslinking would reduce the carboxyl sites available for biotinylation.

Once the peptides were shown to be effectively biotinylated, the next step was to connect them to the SWCNTs. In parallel to the functionalization of SWCNTS with the biotinylated peptide, the same amount of unbiotinylated peptide was used to functionalize another set of SWCNT solutions. Here, it is expected that the unbiotinylated peptide-CNT would be the actual explosive sensor. However, the incorporation of the biotinylated peptide was performed in this work with the purpose of quantifying, monitoring, and corroborating its attachment to the SWCNTs.

During the peptide SWCNT binding procedure, it was found that the amount of bound peptide could not be directly measured. Indeed, the presence of SWCNTs in solution resulted in an absorbance too high to be measured. Thus, the peptide binding was calculated through a mass balance procedure. The mass balance process consisted of reacting a known amount of biotinylated peptide with the carboxylated SWCNTs. Then, the functionalized SWCNTs were pelleted by centrifugation and the supernatant was removed. This supernatant contained the unattached biotinylated peptide that was quantified by a HABA/Avidin assay. Thus, by knowing how much biotinylated peptide was in the supernatants, and how much was originally added, the amount of biotinylated peptide

attached to the SWCNTs was calculated. It was also observed that the washed peptide (supernatants) contained some suspended functionalized SWCNTs which seemed to affect their absorbance readings and the total mass balance. Thus, 0.02 micron anopore membrane syringe filters were used to remove the suspended functionalized SWCNTs in the aliquots removed after the binding (supernatants). The results of the SWCNTs functionalized with peptides 1 through 4 and BII are shown in Table 5.8.

Table 5.8 : Amount of peptides attached to SWCNTS following the EDC chemistry.

Peptide	Peptide Bound to SWCNT (mmol)
1	3.84×10^{-4}
2	5.62×10^{-4}
3	3.71×10^{-4}
4	1.19×10^{-4}
BII	6.77×10^{-5}

As seen in Table 5.8, peptide 2 bound to the SWCNTs to the highest degree. Again this can be described by the existence of additional amine functional groups in peptide 2 when compared to BII or peptide 1 and 3. Here, BII and peptide 1 and 3 only have one available amine group at the N-terminus available for linking to the carboxyl groups of the SWCNTs. Conversely, peptide 2 has two available amine groups, one at the N-terminus and the other as a side group. In contrast, peptide 4 was found to be an outlier since although it has 3 available amine groups, it showed the lowest amount bound to the nanotubes. This could be attributed to the concentration of peptide 4 in solution. As seen in Table 5.7, peptide 4 was biotinylated to a much lower extent. Thus, peptide 4 solution was considerably less biotinylated peptide rich than peptide solutions 1,2, and 3.

An electron microscopy analysis of the carboxylated SWCNTs and the peptide functionalized SWCNTs was also performed. The samples were examined in the field emission scanning electron microscope (FESEM) in the STEM mode. Micrographs from each sample can be seen in Figure 5-8.
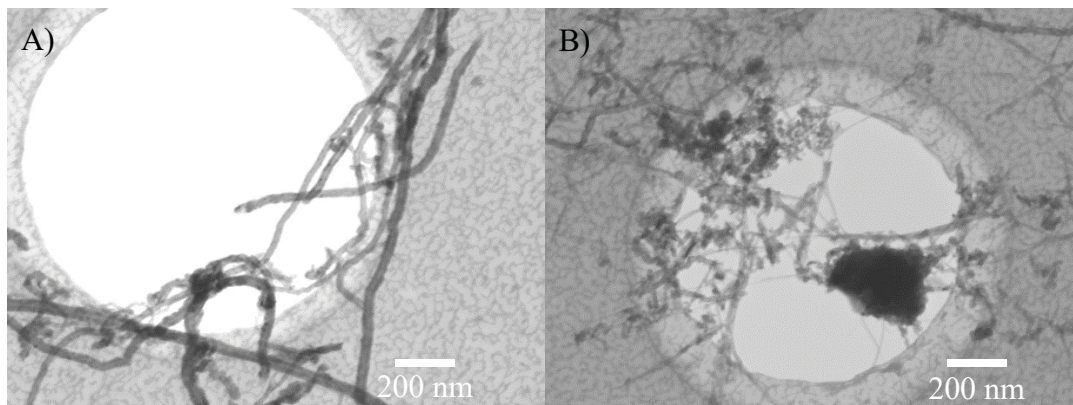

Figure 5-8: STEM micrographs of the carboxylated SWCNTs (A) and SWCNTs with covalently attached peptide 2 (B).

As seen in Figure 5-8, the SWCNTs in Figure 5-8 (A) seem to have a much more defined surface edge than those in Figure 5-8 (B). Due to the only difference in sample preparation being the presence of the peptide, the extra material that appears on the surface of the SWCNTs present in Figure 5-8 B is most likely due to the peptide functionalization.

5.6 PETN Liquid State Detection

Following the attachment of each peptide to the sidewalls of the SWCNTs, the basis of a liquid state detection platform to test the ability of the peptide-SWCNT system to bind to PETN was investigated. In this test, PETNH was biotinylated with hydrazide-PEG4-biotin in order to track its interaction with the bio-functionalized SWCNTs. Here, the biotinylated PETNH was initially purified by placing them in contact with a solution based

on suspended carboxylated SWCNTs which acted as a filter. The carboxyl groups present on the SWCNTs reacted with the EDC and biotin trapping the unreacted biotin. This process resulted in a purified biotinylated PETNH that was subsequently quantified via mass balance through a HABA/Avidin assay. Different masses of carboxylated SWCNTs were tested as filters. The results can be seen in Figure 5-9.
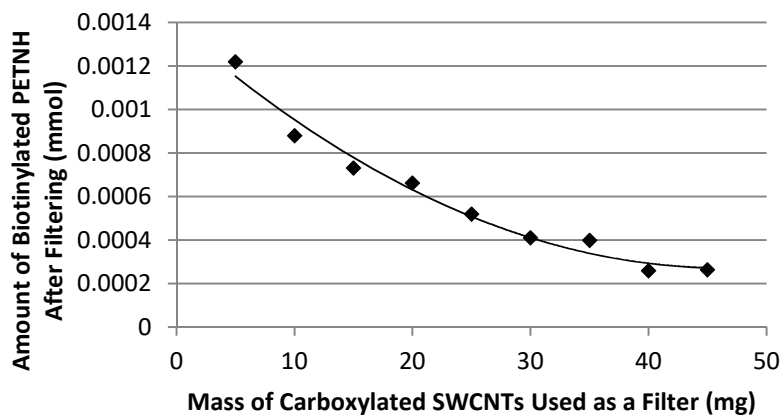

Figure 5-9: Results of the removal of excess of biotin (free) using different amounts of carboxylated SWCNTs which acted as a filter.

As seen in Figure 5-9, as the mass of the carboxylated SWCNT filter is increased, the amount of excess biotin removed increased. Also, it is observed that once 40 mg of CNT filter was used, the graph begins to level out. This suggests that the majority of excess of biotin is removed when using 40 mg of carboxylated SWCNTs acting as a filter.

Following the purification and quantification of the biotinylated PETNH, it was then added to the peptide functionalized SWCNT solutions. The solutions were then rocked for 2 hours, and the supernatant was subsequently removed and filtered. The biotinylated PETNH content in the wash (unbound) was quantified, and through a mass balance of the biotinylated PETNH before and after the exposure to the functionalized SWCNTs, the amount bound to the SWCNTs was determined.

The liquid state detection tests were carried out by adding 325 μl of biotinylated PETNH to 5 mg of peptide functionalized SWCNTs. This was also carried out on the SWCNTs functionalized with biotinylated peptide to test if the presence of biotin had any effect on the explosive binding. It is important to note that in each trial, the 325 μl biotinylated PETNH samples added to the SWCNTs were from the same solution. This removed any error that could arise from different PETNH concentrations. Additionally, 325 μl of biotinylated PETNH was added to 5 mg of carboxylated SWCNTs to act as a control. The amount of biotinylated PETNH detected by each peptide/SWCNT system is presented in Table 5.9.

Table 5.9 : Results of the liquid state detection test on the four identified peptides from the M13 phage library and the BII. The labeling B indicates that the SWCNT sensor was functionalized with a biotinylated peptide.

Trial	Functional Detection Group	Biotinylated PETNH Detected (mmol)	Percent of Initial Biotinylated PETNH Detected
1	COOH	1.52×10^{-4}	38.36
	BII	1.39×10^{-4}	34.78
	1	9.06×10^{-5}	22.84
	1B	8.37×10^{-5}	21.09
	2	2.26×10^{-4}	56.82
	2B	2.49×10^{-4}	62.52
	3	2.42×10^{-4}	60.75
	3B	2.30×10^{-4}	57.75
	4	2.58×10^{-4}	64.67
	4B	2.75×10^{-4}	68.97
2	COOH	8.32×10^{-5}	28.25
	BII	1.39×10^{-4}	33.50
	1	1.58×10^{-4}	53.83
	1B	1.68×10^{-4}	57.15
	2	1.56×10^{-4}	52.83
	2B	1.30×10^{-4}	44.20
	3	1.82×10^{-4}	61.80
	3B	1.15×10^{-4}	39.21
	4	1.38×10^{-4}	46.85
	4B	1.02×10^{-4}	34.56

As seen in Table 5.9, the biotinylated PETNH seems to have bound to the carboxylated SWCNTs, probably due to a physical entrapment of the biotinylated explosive in the SWCNT network. Indeed, carbon nanotubes can form tangled bundles that trap biomolecules [10]. This entangled network of carbon nanotubes can be seen in Figure 5-10.
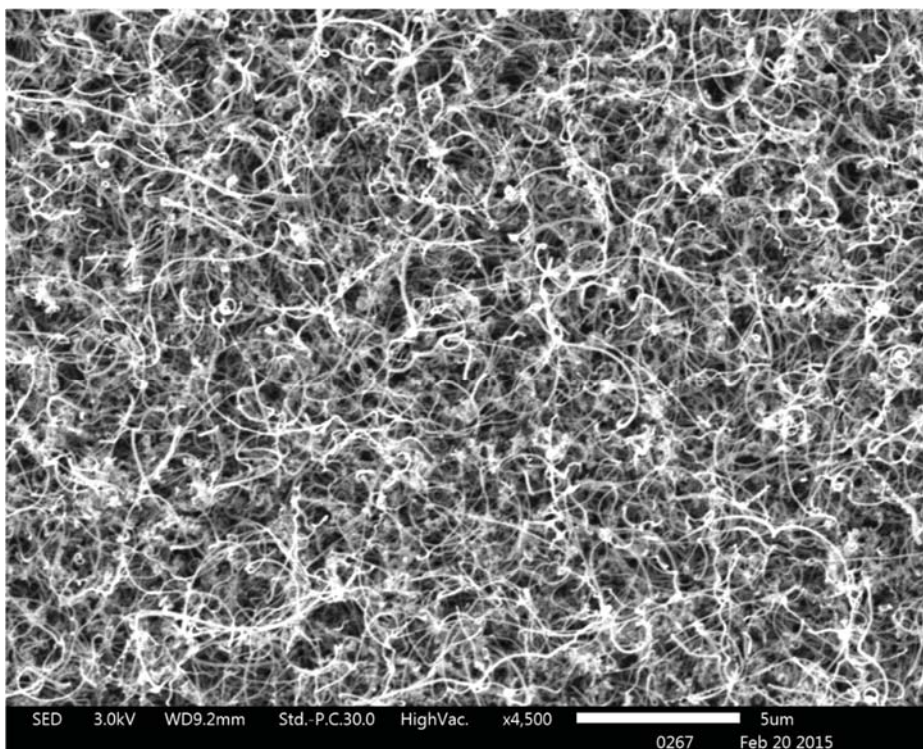

Figure 5-10: SEM micrograph of carboxyated carbon nanotubes. The micrograph shows the entangled state that CNTs can present.

As seen in Figure 5-10, these networks can become very tangled, creating regions that can accept and trap foreign compounds.

The results in Table 5.9 also show that SWCNTs functionalized by BII do not retain more explosive than the carboxyl control. Indeed, BII has been identified as a selective peptide for nitroaromatics as originally tested by Heller *et al.* [7] rather than for detecting

functional structures on general explosives. Conversely, the presence of peptides 1 through 4 shows a high degree of biotinylated explosive surrogate binding (around 60 % of binding). Here, it can be observed that peptide 2 showed the highest degree of binding toward the PETNH. These results appear to be supported by the work carried out by Khan *et al*. [4,5] where it has been stated that the existence of a leucine-tryptophan segment in the peptide may play a key role in modulating binding.

From the results shown in Table 5.9, it is apparent that the detection of PETNH by peptide 1 in trial 1 seemed to be an outlier. One reason that can support this outcome was the lack of ultrasonication of the peptide/SWCNT complex before the addition of the biotinylated PETNH. The addition of ultrasonication seems to increase the available detecting functional groups in the peptide/SWCNT system. This ultrasonication step was implemented in the second trial using peptide 1, as well as both trials for all the other peptides. It is interesting to note from Table 5.9, that the presence of biotin in the peptide/SWCNT complex does not hinder the binding of the peptide to PETNH. This suggests that the biotin does not interfere with the PETNH interaction area of the peptide. Due to the consistency of all other trials, trial 2 of the biotinylated peptide 3 attached to SWCNT (39.21 %) was also considered as an outlier since it did show a decrease in binding when compared to its unbiotinylated (counterpart) peptide 3 system in trial 2 (61.80 %).

5.7 Competitive Peptide ELISA

In order to corroborate the selectivity of the identified peptides to PETN, a peptide ELISA was employed. Due to the selective consistency of peptide 2 towards PETNH in both the phage ELISAs and in the the SWCNT/peptide liquid state test, it was decided to

use this peptide for the competitive peptide ELISA test. The initial testing of this section consisted of corroborating if the 5 % NFDM in PBS block used in the phage ELISA was also an appropriate blocking agent for the selective peptide testing. Thus, five different blocks were tested: 5 % NFDM in PBS, 1 % casein in PBS, 1 % BSA in PBS, 1 % yeast extract in PBST, and 5 % fetal calf serum in PBS. These blocks were added in wells not containing PETNH to determine which block reduces the peptide binding in negative control wells the most. The results of the blocking buffer tests can be seen in Figure 5-11.
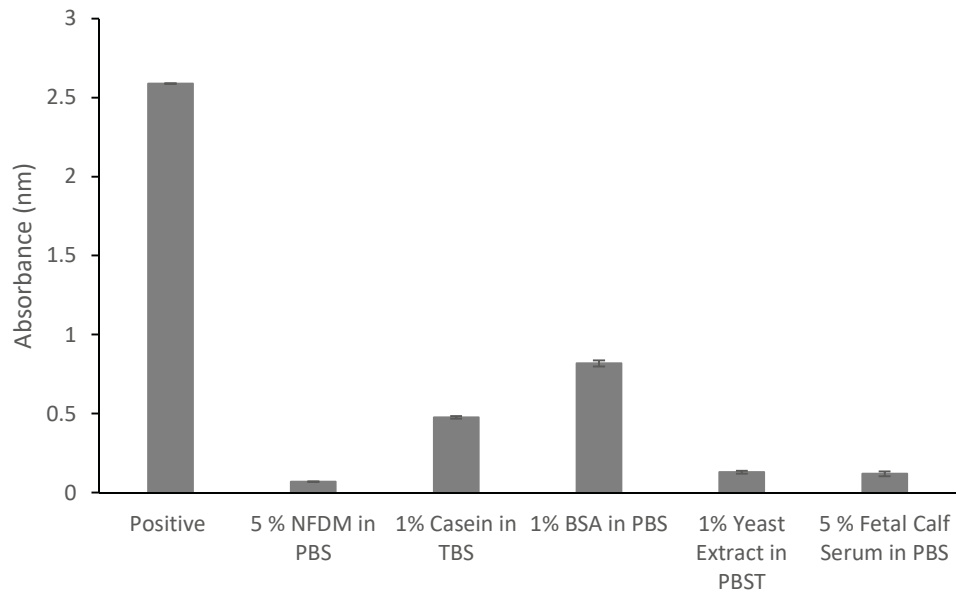

Figure 5-11: Testing the effectiveness of each block in wells not containing immobilized PETNH.

As seen in Figure 5-11, the wells containing 5 % NFDM in PBS exhibited the lowest absorbance and thus the lowest level of non-selective binding. It can also be seen that the 1 % yeast extract in PBST, and the 5 % fetal calf serum in PBS also seem to have yielded a low degree of absorbance. Based on these results, the 5 % NFDM in PBS was also used as the blocking agent in the selective peptide ELISA tests.

After determining the optimal blocking buffer for the peptide ELISA testing, the selectivity of peptide 2 towards PETNH and additional competitive analytes was tested. In the competitive peptide ELISA testing, the PETNH was initially immobilized in the amine functionalized wells via the carbodiimide chemistry followed by a blocking of the wells with 5 % NFDM buffer. In this testing, non-competition and competition wells were included in the protocol. In the non-competition wells, the biotinylated peptide 2 was added, whereas in the competition wells, a pre-mixture of peptide 2 and the competition substance was added. The competition substance considered in this work were PETNH, TNT, Nitrobenzene, Sodium Nitrate, and Pentaerythritol (initial structure transformed into PETN during the synthesis). These substances were investigated due to the fact that they contain nitro groups as well as similar chemical structures to PETN.

After incubation of the wells, they were aspirated, and streptavidin labeled horseradish peroxidase (HRP) was added with the purpose of binding to any peptide that had bound to the immobilized PETNH. Finally, the addition of TMB initiated a color change due to its interaction with the HRP and the absorbance was read by visible light where a higher visible absorbance of a well meant a superior binding (and therefore selectivity) of the peptide to the immobilized PETNH. Indeed, if a tested substance competes with the peptide-PETNH binding, a lower absorbance would be observed in the corresponding competition well. The results of this competitive peptide ELISA testing are presented in Figure 5-12.
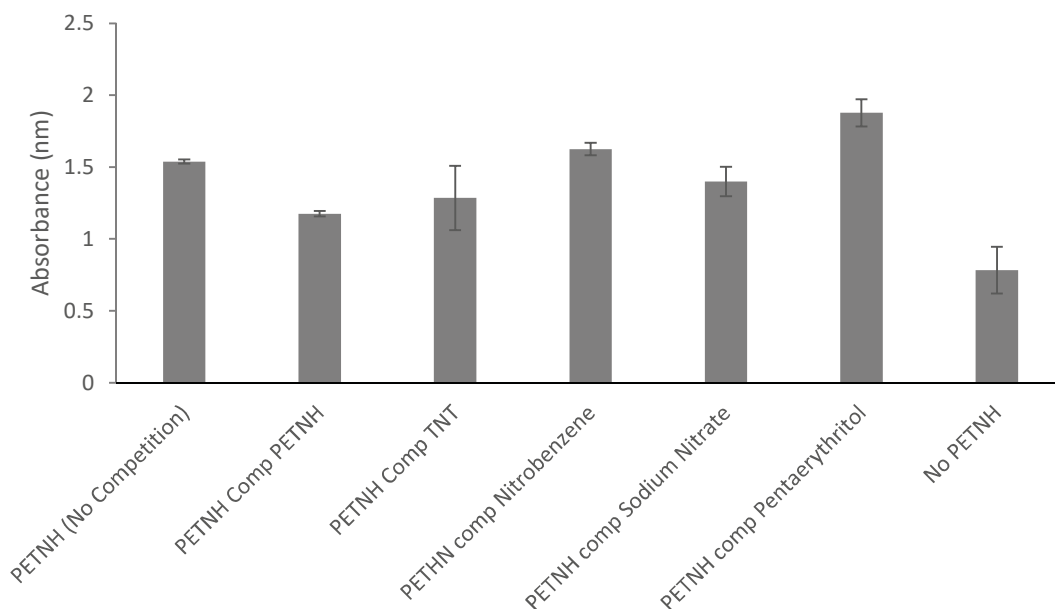
Figure 5-12: Selectivity testing of peptide 2 to PETNH and additional compounds with similar structures to PETN. The graph shows lack of competition from competing substances other than PETNH.

As seen in Figure 5-12, competition of the peptide 2 with PETNH results in a lower absorbance than the testing of the pure PETNH-peptide without competition. This is because a competition of the PETNH with peptide 2 already used the interaction sites of the peptide which results in lower interactions with the immobilized PETNH in the wells. Indeed, this was expected because the peptide was tailored to PETNH. Testing TNT as a competitor also showed an average decrease in binding, suggesting that peptide 2 could also be a TNT binder. However, it is observed that its standard deviation overlaps with the level of binding in the non-competition PETNH. Looking at the level of binding in the nitrobenzene wells, it is observed that the nitrobenzene did not compete with the PETNH-peptide binding since the absorbance of the nitrobenzene wells was similar to that observed in the non-competition PETNH wells. It is worth noting that nitrobenzene has a very similar

structure to TNT, so although TNT competition requires further experimental trials to determine if peptide 2 really binds to it, the lack of binding to nitrobenzene could suggest that peptide 2 may also not bind to TNT. Also shown in Figure 5-12, are the absorbance of the Sodium Nitrate and Pentaerythritol competition wells. The absorbance showed in these wells were similar or higher than the non-competition wells suggesting that they do not compete with peptide 2 binding to PETNH. These results seem to indicate that peptide 2 has a relative selectivity towards PETNH.

5.8 Modeling

In this work, the electrical properties of a plain SWCNT FET were modeled using the density functional tight binding (DFTB) theory. In this study, a plain SWCNT was modeled as part of a FET system and variables such as the dimensions of the FET and gate voltages were investigated. Once optimized, a modeled peptide was attached to the SWCNT, and the electrical properties of a peptide functionalized SWCNT FET were studied. Finally, using DFTB the change in electrical properties of the SWCNT FET interacting with PETN were modeled.

5.8.1 Modeling of the Electrical Properties of a Plain SWCNT

Before DFTB could be implemented, the geometry files for a semi conducting SWCNT were generated. This was carried out using the TubeGen Online - Version 3.4 software in conjunction with Jmol molecular modeling software. The generated 8,0 SWCNT can be seen in Figure 5-13, where the 8,0 is related to the integers m,n of the SWCNT's chiral vector, representing a zig-zag conformation (see section 2.1.1). Here, an

8,0 SWCNT conformation was used since it represents a semiconducting nanotube (an electrical feature most commonly used in SWCNT-FET sensors) [11–13].
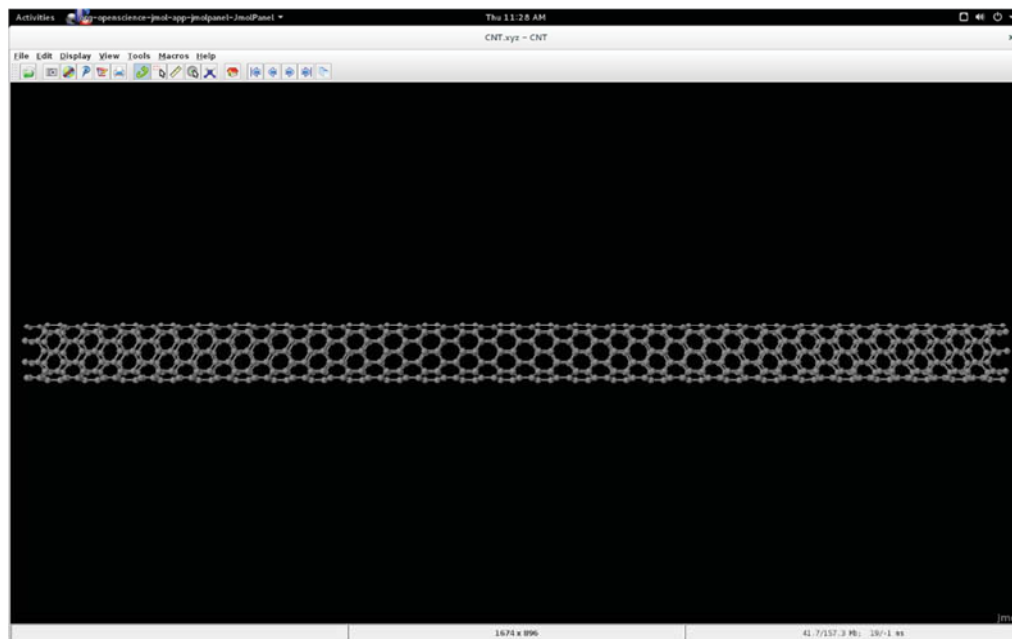

Figure 5-13: Visualization of a 8,0 SWCNT using the Jmol molecular modeling program.

As seen in Figure 5-13, the SWCNT generated had two open ends. The diameter of the generated tube was 0.63 nm and the length was 11.03 nm. Using this generated tube, the xyz positions were used to create a geometry file that was then imported into the dftb+ program.

After corroborating the geometry of the system, the density of states for the generated 8,0 SWCNT was calculated to confirm the semiconducting nature that should be inherent in a zigzag CNT structure. The density of states for the 8,0 SWCNT is shown in Figure 5-14.
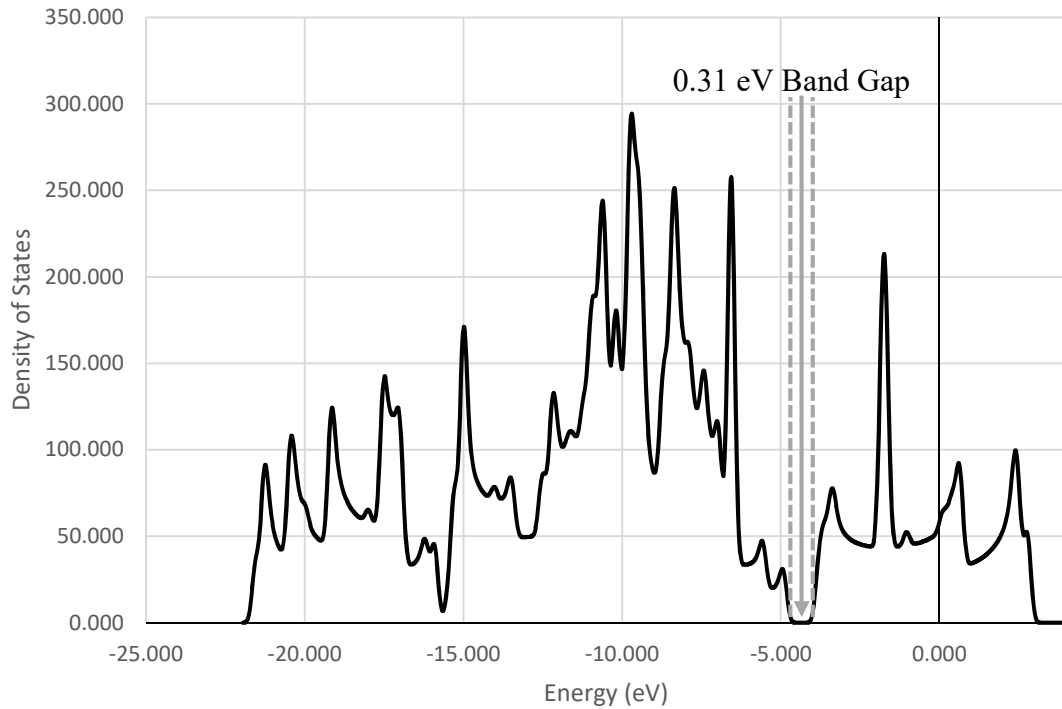
Figure 5-14: Density of States for an 8,0 SWCNT showing a 0.31 eV band gap.

As shown in Figure 5-14, the calculated density of states using dftb+ exhibits a 0.31 eV band gap. This band gap was obtained by subtracting the energy of the conduction band (-4.21 eV) edge from the energy of the valence band edge (-4.52 eV). Band edges are shown by the dashed lines in Figure 5-14. Experimental work of Peng *et al.* [14] showed that a 8,0 SWCNT semiconducting tube implemented in a FET setup had a measured band gap of 0.5 eV. Comparison of these values shows that the dftb+ representation is a close approximation of a real experimental setup.

Once the geometry and band gaps were verified, the dftb+ program was implemented to study the effect of changing the gate dimensions at a bias voltage of 0.1 V. The gate length parallel to the SWCNT was varied between 1.2 nm and 5.0 nm and both planar and circular gates were studied. The planar gate setup modeled the FET with the

dielectric layer laying on top of the CNT, while in the circular gate modeled the dielectric layer as a continuous layer around the CNT. The results of the different gate lengths and gate type are shown in Figure 5-15.
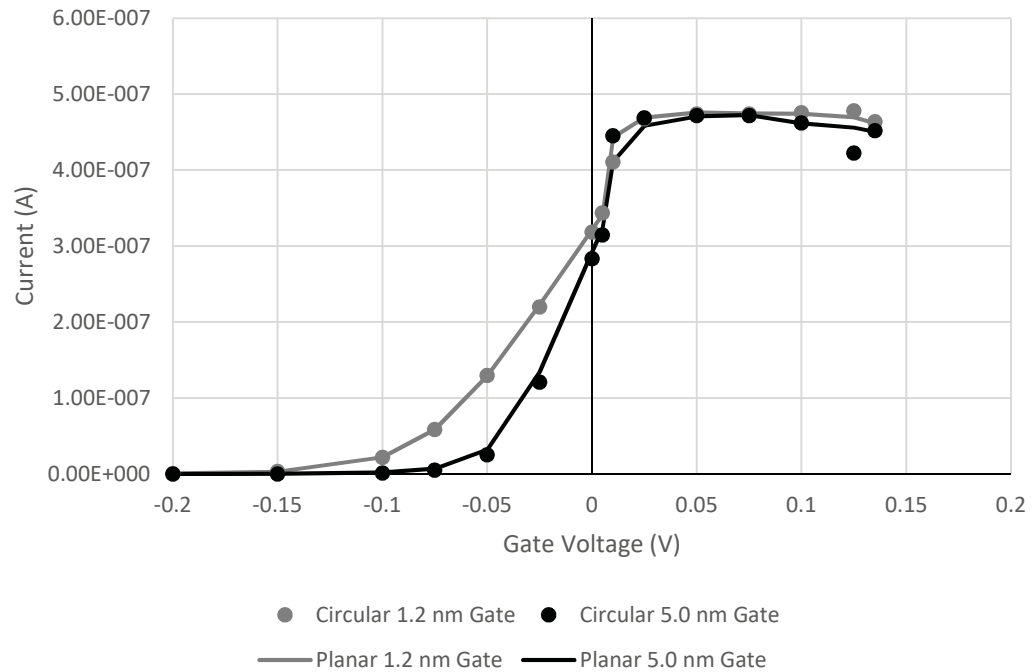

Figure 5-15: Model of the electrical current versus gate voltage using circular and planar gates. The graph shows the electrical response of a plain SWCNT featuring an n-type behavior.

As shown in Figure 5-15, the increase in current with an increase in gate voltage suggested that a 8,0 SWCNT acts like a n-type semiconductor. This is because in an n-type semiconductor, as the gate voltage increases, the conducting channel is widened, allowing for higher conduction [15]. This was expected since although semiconducting CNTs are p-type under ambient conditions, they are actually n-type inherently in the absence of oxygen [16–18]. Here, the absorbed oxygen results in a charge transfer from CNTs to the absorbed

oxygen resulting in a p-type doping. Indeed, the SWCNT modeled was undoped and did not contain any oxygen.

Another observation from Figure 5-15 was that the difference between circular and planar gates was insignificant. Under lack of atmospheric conditions this would be expected because the operation is virtually the same. Only under atmospheric conditions where the wrapping around the dielectric would keep oxygen from absorbing onto the CNT should the different gate geometries make a difference. Based on these results, planar gates were implemented throughout the rest of the modeling study. Indeed, a planar gate allowed for the surface of the CNT to be exposed, whereas in the circular gate the CNT is completely enclosed by the dielectric gate. Circular gates are used for *on/off* FET applications [19], but since this research work focused on the detection of PETN through the interaction of a peptide on the surface of a SWCNT, a circular gate would block this interaction from happening.

Comparison of the simulated electrical current versus gate voltage graph (see Figure 5-15) to literature data shows a similar n-type trend as shown in Figure 5-16. As it is observed in Figure 5-16, both SWCNT FETs act as n-type semiconductors when are not in the presence of oxygen. One primary difference between Figure 5-15 (modeled data) and Figure 5-16 (literature data) lies in the order of magnitude of the electrical current in Derycke *et al.*'s study [16].
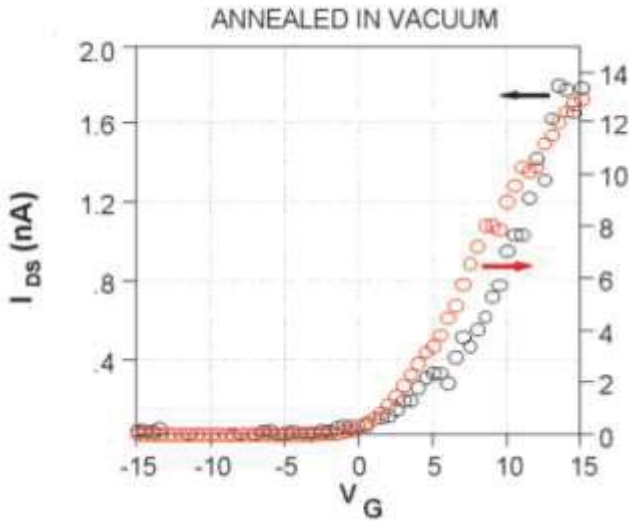
Figure 5-16: Current versus gate voltage for two individual semiconducting

SWCNTs in the absence of oxygen [16].

When compared to this research work using the DFTB theory, it was observed that the electrical current here obtained was in the 10^{-7} amphere order of magnitude, while Derycke et al.'s results exhibited currents in the 10^{-9} amphere range. This could be due to a few reasons. The SWCNTs used in this research work had a diameter of 0.63 nm while those in Derycke et al.'s study were 1.4 nm in diameter. This suggests that the chirality of the observed SWCNTs were not 8,0 in Derycke et al.'s study. In fact, their work never stated the chirality of the studied tubes. Also, the conducting channel in this research program was only 11.03 nm long while those used in the experimental study were much longer tubes spanning in a width of 250 nm between contacts. A longer SWCNT would mean a higher baseline resistance and thus a lower electrical current.

Electrical currents in the order of magnitude of 10^{-7} ampheres are better corroborated by the work performed by Bushmaker et al. [20]. In this study, 8,0 SWCNT FETs were experimentally tested and modeled using DFT. A plot of their electrical current versus gate voltage is shown in Figure 5-17.
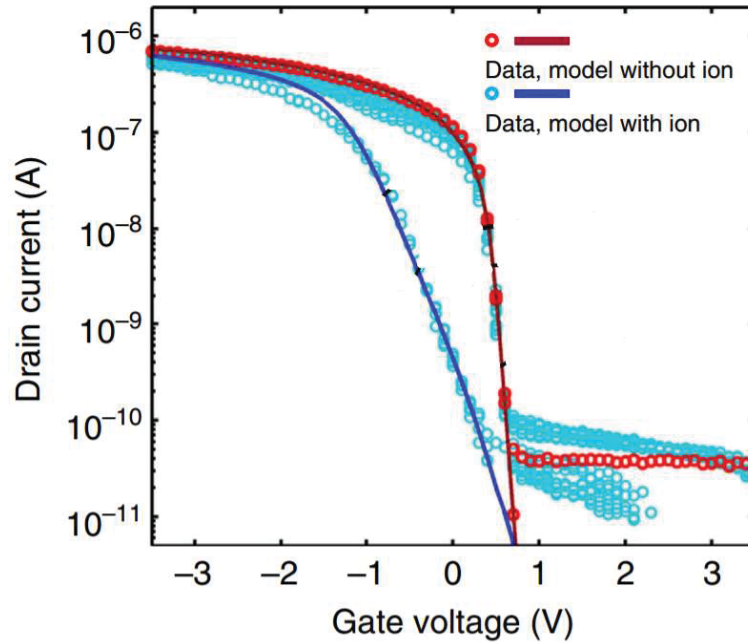
211

Figure 5-17: Electrical current versus gate voltage for a plain SWCNT (red circles) and CNTs exposed to ionized gas (cyan circles). Included in the plot is the modeled data using DFT (solid red and cyan lines respectively) [20].

In Figure 5-17, the main set of data to consider is the red circles that represent the experimental data of a 8,0 SWCNT under 0.1 V bias voltage in ambient conditions. Indeed, these conditions are comparable to those modeled in the present research work except that the tests run by Bushmaker *et al.* [20] were in ambient conditions. Since the tests and models were run in air, their FET acts as p-type. However, their electrical current is in the order of 10^{-7} ampheres, which seems to corroborate the model presented in this research program.

Following the electrical current versus gate voltage study, an electrical current versus bias voltage investigation was performed at -0.15 V, -0.2 V, and -0.3 V gate potentials. A planar gate with length 5.0 nm was also here used based on results shown in

Figure 5-15**,** where it is observed that this gate length produced a smoother n-type curve. Also, the 5.0 nm gate length resulted in a better convergence of the iterations at each data point. The results of the electrical current versus bias voltage study are presented in Figure 5-18.
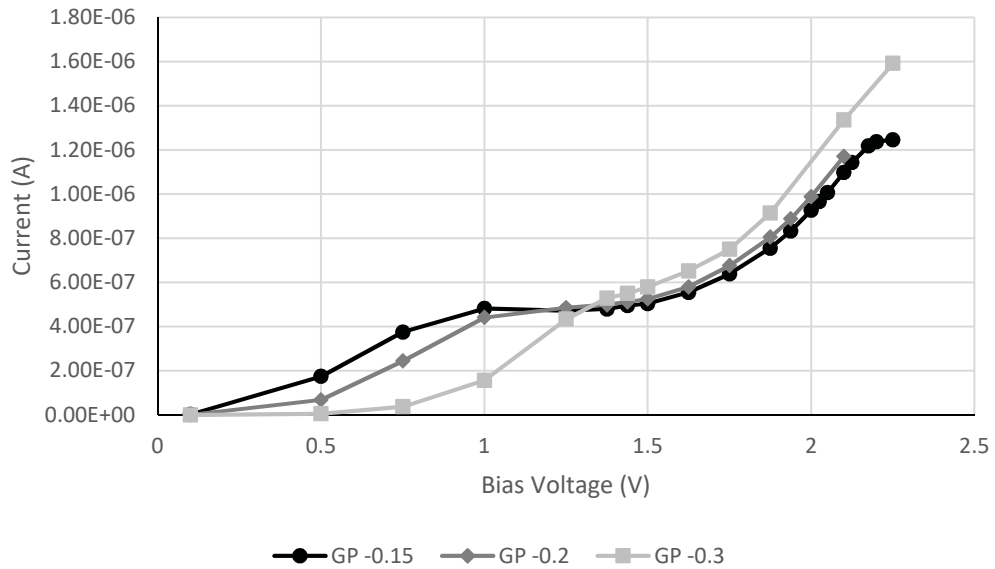

Figure 5-18: Electrical current versus bias voltage for a plain SWCNT at -0.15 V, -0.2 V, and -0.3 V gate potentials (GP).

As seen in Figure 5-18, at low bias voltages, a gate voltage of -0.15 V results in the highest current through the CNTs conducting channel. This is again expected in an n-type operation [16], since as the gate voltage becomes more positive, the channel for conduction becomes larger. When comparing gate potential of -0.15 to -0.2 V the electrical current does not vary significantly at higher bias voltages. In contrast, a gate potential of -0.3 V produces the highest current at larger bias voltages. This is believed to be due to convergence issues. Indeed, at a gate potential of -0.3 V, the model was not converging well. Due to this issue, some of the accuracies were relaxed to allow for convergence.

Considering these results, a gate potential of -0.15 V was used to study the peptide/SWCNT and peptide/SWCNT/PETN systems.

5.8.1 Modeling of the Electrical Properties of SWCNT/Peptide and SWCNT/Peptide interacting with PETN systems

Once the modeling of the plain SWCNT was investigated, the electrical properties of a peptide functionalized SWCNT and the change in electrical properties induced by its interactions with PETN were modeled. In this research work, peptide 1 was attached to the middle of the SWCNT to create the SWCNT/peptide system. In contrast to experimental work where peptide 2 was selected for investigating selectivity towards PETNH, the peptide 1 was here selected because it contained the most similar peptide segment to the protein interaction site shown in Khan *et al.* work (Leucine-Tryptophan-Threonine) [4,5]. To study the interaction of the peptide with PETN and its resulting electrical properties output, the PETN was oriented at an equilibrium distance from the indole side chain present in peptide 1. This location was selected because the work by Khan *et al.* showed a possible interaction between nitro groups of the explosive and the indole group of the peptide [4,5]. The SWCNT/peptide modeled complex is shown in Figure 5-19, whereas the SWCNT/peptide/PETN system is shown in Figure 5-20.
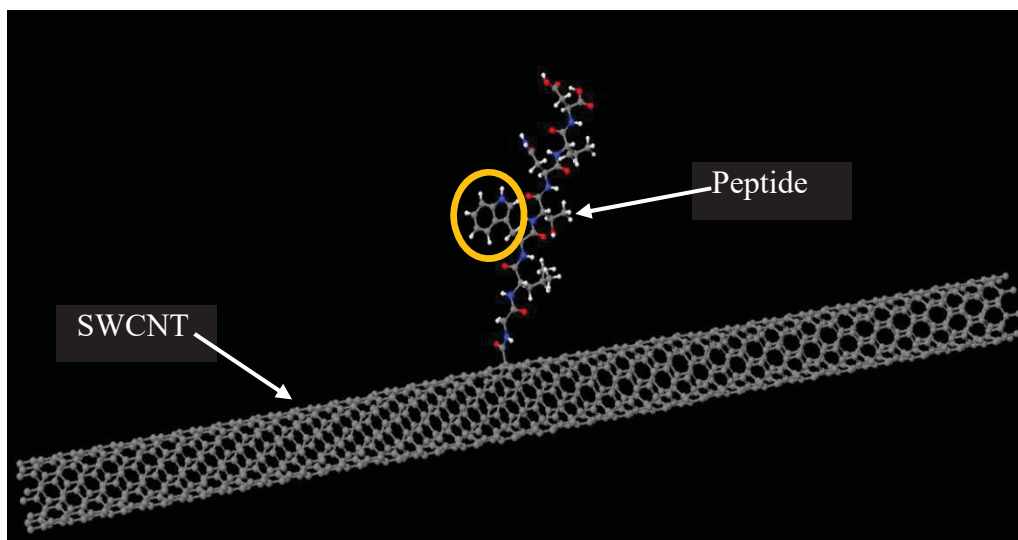
Figure 5-19: Schematic of the SWCNT with covalently bound peptide 1 at the center of the tube. The indole side chain is highlighted by the orange circle.
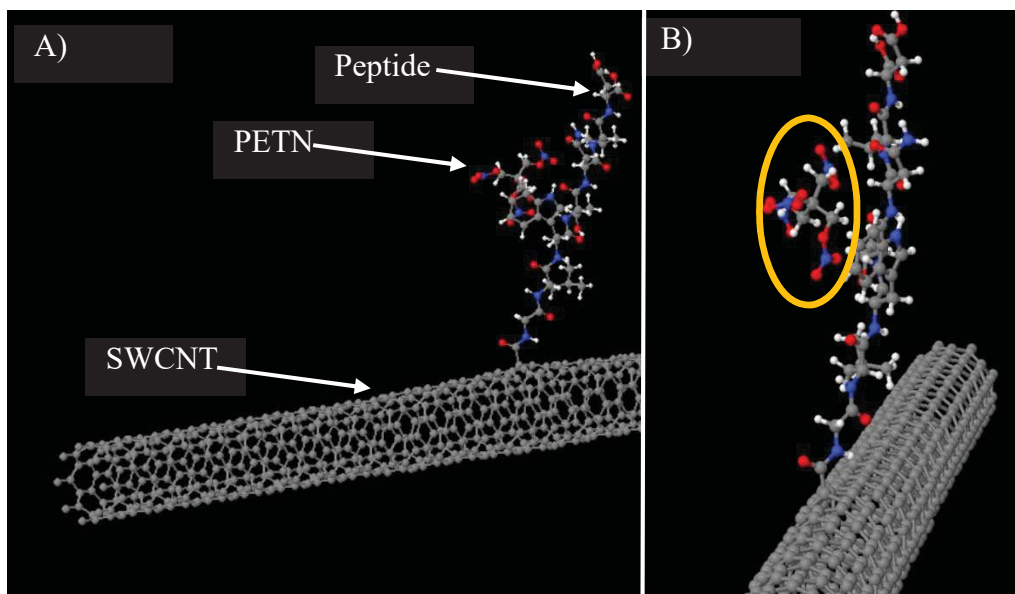

Figure 5-20: Schematic of SWCNT covalently bound to peptide 1 at the center of the tube and PETN (orange circle) located near the indole side chain at equilibrium distance. A) Low magnification, B) High magnification

Operation parameters for the modeling of these two systems were obtained from the initial SWCNT modeling which were a planar device and a gate length of 5.0 nm. For the electrical current versus gate voltage studies, the bias voltage was set at 0.1 V. The results of the electrical current versus gate voltage are shown in Figure 5-21.
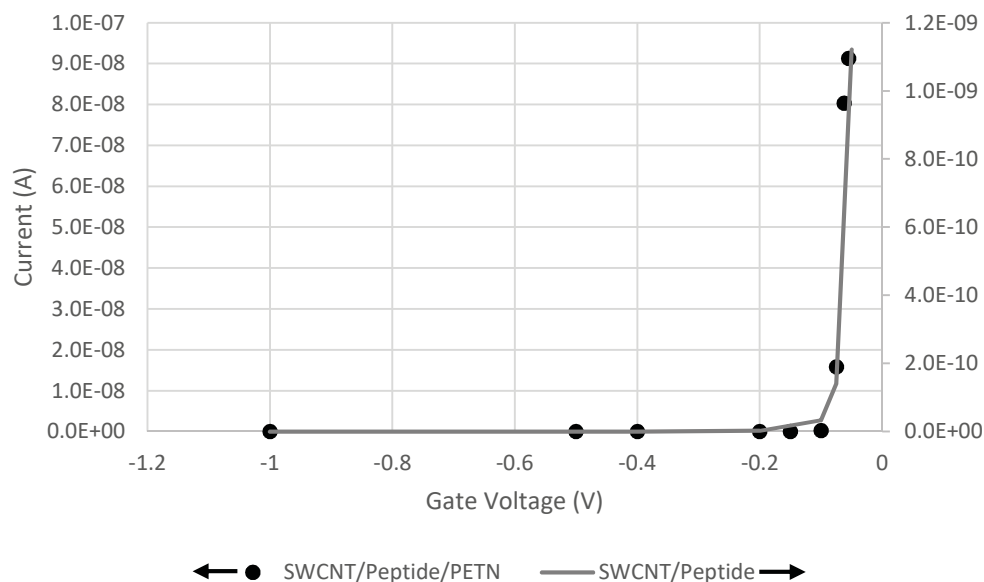

Figure 5-21: Electrical current versus gate voltage results for a SWCNT/Peptide and a SWCNT/Peptide/PETN system. The arrows next to each data set indicates the corresponding reading axis.

As shown in Figure 5-21, the addition of peptide 1 covalently attached to the SWCNT sidewall resulted in a two order of magnitude decrease in the electrical current when compared to Figure 5-15 (plain SWCNT). This phenomenon has been corroborated by Chen *et al.* [21]. In the work performed by Chen *et al.*, SWCNTs experienced a decrease in conductance when functionalized with proteins such as streptavidin and staphylococcal protein A. This is most likely due to either a charge transfer between the protein and the SWCNT, or a gating effect induced by the protein. One interesting feature to observe in Figure 5-21 is that at a gate potential of -0.05 V, the added PETN interaction increased the

electrical current almost two orders of magnitude. This suggests that at this gate potential, the PETN and peptide interaction results in a donation of electrons to the SWCNT channel. The larger difference in electrical current is seen at higher gate voltages because this is considered the *on* regime for a FET [15]. In the *off* regimes, almost no electrical current is present. In this *on* regime is where the largest differences in conductance due to the PETN interaction will occur. These results (at a gate potential of -0.05 V and bias voltage of 0.1 V) advocate for experimental trials of a 8,0 SWCNT FET for detection testing of PETN.

For the electrical current versus bias voltage studies, the gate voltage was set to -0.15 V, and again the SWCNT/Peptide and SWCNT/Peptide/PETN systems were investigated. The results of the electrical current versus bias voltage studies are shown in Figure 5-22. As it was observed in the electrical current vs. gate voltage study (see Figure 5-21), the addition of a covalently attached peptide on the SWCNTs also resulted in a decrease of the electrical current vs bais voltage profile when compared to the plain SWCNT (see Figure 5-22 and Figure 5-18). Also, it can be seen that at a bias voltage of 1.1 V the interaction of peptide 1 with the PETN increased the electrical current by one order of magnitude which again suggests that the PETN-peptide interaction results in a donation of electrons to the SWCNT channel.
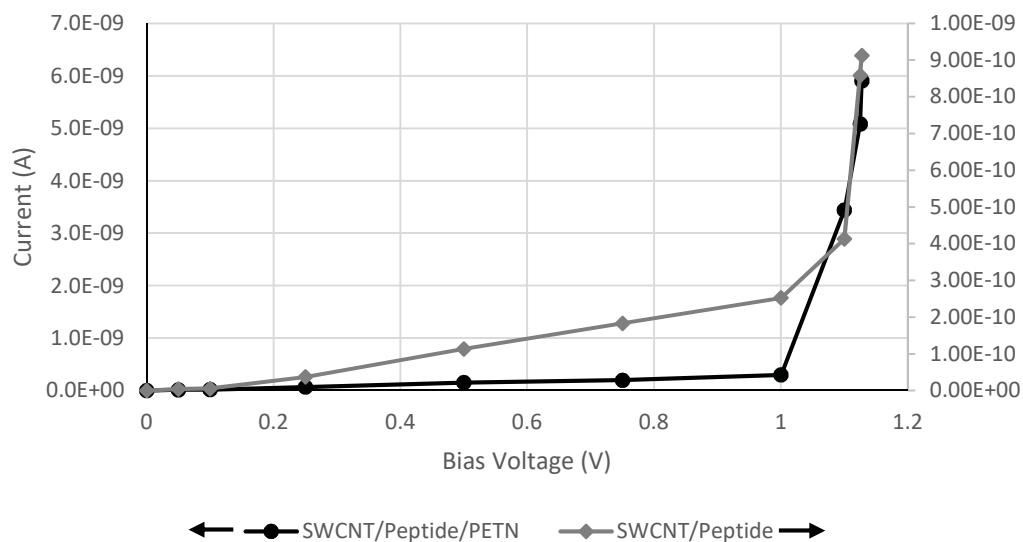
Figure 5-22: Electrical current versus bias voltage of a SWCNT/Peptide and SWCNT/Peptide/PETN system. The arrows next to each data set indicates the corresponding reading axis.

The modeling work in this research program has shown that the DFTB theory in conjunction with non-equilibrium Green's functions can model changes in the electrical properties of a peptide functionalized SWCNT FET caused by the interaction of PETN with the system. In some conditions, this interaction will induce an increase up to two orders of magnitude in the electrical current of the system. Future modeling work should focus on the analysis of the other peptides identified via the phage display experimental work here performed (see Table 5.4). It is possible that the best peptide for detection applications could be predicted using the presented modeling work. Additionally, the location of the peptide on the SWCNT and the peptide/PETN interaction should be further studied. Optimization of these locations could assist to theorize the detection mechanism involved in biologically functionalized carbon nanotube based sensors.

5.9 References

[1] "Methods to Check RNA Integrity" [Online]. Available: https://www.thermofisher.com/us/en/home/references/ambion-tech-support/rna-isolation/tech-notes/is-your-rna-intact.html. [Accessed: 29-Mar-2017].

[2] "Measure Proteins with NanoDrop Products" [Online]. Available: http://www.nanodrop.com/protein.aspx. [Accessed: 24-Jan-2017].

[3] 2016, "Ph.D. Phage Diplay Libraries."

[4] Khan, H., Harris, R. J., Barna, T., Craig, D. H., Bruce, N. C., Munro, A. W., Moody, P. C. E., and Scrutton, N. S., 2002, "Kinetic and Structural Basis of Reactivity of Pentaerythritol Tetranitrate Reductase with NADPH, 2-Cyclohexenone, Nitroesters, and Nitroaromatic Explosives," J. Biol. Chem., **277**(24), pp. 21906–21912.

[5] Khan, H., Barna, T., Harris, R. J., Bruce, N. C., Barsukov, I., Munro, A. W., Moody, P. C. E., and Scrutton, N. S., 2004, "Atomic Resolution Structures and Solution Behavior of Enzyme-Substrate Complexes of Enterobacter Cloacae PB2 Pentaerythritol Tetranitrate Reductase Multiple Conformational States and Implications for the Mechanism of Nitroaromatic Explosive Degradation," J. Biol. Chem., **279**(29), pp. 30563–30572.

[6] Argiolas, A., and Pisano, J. J., 1985, "Bombolitins, a New Class of Mast Cell Degranulating Peptides from the Venom of the Bumblebee Megabombus Pennsylvanicus," J. Biol. Chem., **260**(3), pp. 1437–1444.

[7]   Heller, D. A., Pratt, G. W., Zhang, J., Nair, N., Hansborough, A. J., Boghossian, A. A., Reuel, N. F., Barone, P. W., and Strano, M. S., 2011, "Peptide Secondary Structure Modulates Single-Walled Carbon Nanotube Fluorescence as a Chaperone Sensor for Nitroaromatics," Proc. Natl. Acad. Sci., **108**(21), pp. 8544–8549.

[8]   "Carbodiimide Crosslinker Chemistry" [Online]. Available: https://www.thermofisher.com/us/en/home/life-science/protein-biology/protein-biology-learning-center/protein-biology-resource-library/pierce-protein-methods/carbodiimide-crosslinker-chemistry.html. [Accessed: 07-Sep-2016].

[9]   "Avidin-Biotin Interaction" [Online]. Available: https://www.thermofisher.com/us/en/home/life-science/protein-biology/protein-biology-learning-center/protein-biology-resource-library/pierce-protein-methods/avidin-biotin-interaction.html. [Accessed: 07-Sep-2016].

[10]   Li, H., Gui, X., Zhang, L., Wang, S., Ji, C., Wei, J., Wang, K., Zhu, H., Wu, D., and Cao, A., 2010, "Carbon Nanotube Sponge Filters for Trapping Nanoparticles and Dye Molecules from Water," Chem. Commun., **46**(42), pp. 7966–7968.

[11]   Collins, P. G., Bradley, K., Ishigami, M., and Zettl, A., 2000, "Extreme Oxygen Sensitivity of Electronic Properties of Carbon Nanotubes," Science, **287**(5459), pp. 1801–1804.

[12]   Li, J., Lu, Y., Ye, Q., Cinke, M., Han, J., and Meyyappan, M., 2003, "Carbon Nanotube Sensors for Gas and Organic Vapor Detection," Nano Lett., **3**(7), pp. 929–933.

[13] Kong, J., Franklin, N. R., Zhou, C., Chapline, M. G., Peng, S., Cho, K., and Dai, H., 2000, "Nanotube Molecular Wires as Chemical Sensors," Science, **287**(5453), pp. 622–625.

[14] Peng, S., O'Keeffe, J., Wei, C., Cho, K., Kong, J., Chen, R., Franklin, N., and Dai, H., 2001, "Carbon Nanotube Chemical and Mechanical Sensors," *Proceedings of the 3rd International Workshop on Structural Health Monitoring*, pp. 1–8.

[15] Baliga, B. J., 2010, *Advanced Power MOSFET Concepts*, Springer Science & Business Media.

[16] Derycke, V., Martel, R., Appenzeller, J., and Avouris, P., 2001, "Carbon Nanotube Inter- and Intramolecular Logic Gates," Nano Lett., **1**(9), pp. 453–456.

[17] Derycke, V., Martel, R., Appenzeller, J., and Avouris, P., 2002, "Controlling Doping and Carrier Injection in Carbon Nanotube Transistors," Appl. Phys. Lett., **80**(15), pp. 2773–2775.

[18] Kang, D., Park, N., Ko, J., Bae, E., and Park, W., 2005, "Oxygen-Induced P-Type Doping of a Long Individual Single-Walled Carbon Nanotube," Nanotechnology, **16**(8), p. 1048.

[19] Chen, Z., Farmer, D., Xu, S., Gordon, R., Avouris, P., and Appenzeller, J., 2008, "Externally Assembled Gate-All-Around Carbon Nanotube Field-Effect Transistor," IEEE Electron Device Lett., **29**(2), pp. 183–185.

[20] Bushmaker, A. W., Oklejas, V., Walker, D., Hopkins, A. R., Chen, J., and Cronin, S. B., 2016, "Single-Ion Adsorption and Switching in Carbon Nanotubes," Nat. Commun., **7**, p. 10475.

[21] Chen, R. J., Bangsaruntip, S., Drouvalakis, K. A., Kam, N. W. S., Shim, M., Li, Y., Kim, W., Utz, P. J., and Dai, H., 2003, "Noncovalent Functionalization of Carbon Nanotubes for Highly Specific Electronic Biosensors," Proc. Natl. Acad. Sci., **100**(9), pp. 4984–4989.

Chapter 6 Conclusion

The present research work has identified and investigated the amino-acid sequences that display a selective affinity towards a pentaerythritol tetranitrate (PETN) explosive surrogate using a phage display library approach. PETNH (pentaerythritol trinitrate hemisuccinate) has been used as the PETN surrogate, due to the presence of a carboxyl group in its structure, which allows its immobilization onto amine coated wells via an EDC [1-Ethyl-3-(3 dimethylaminopropyl) carbodiimide] chemistry in an ELISA identification testing. Although phage display is a commonly used technology for identification of peptides towards specific bioanalytes, this research program addresses a new way to immobilize explosive surrogates onto microwells and presents for the first time peptides that show affinity towards PETNH. Also, an identified peptide from the phage display library technique here investigated has been used to functionalize a single wall carbon nanotube (SWCNT), and the peptide-CNT system has been tested for a liquid state detection of PETNH. Finally, the SWCNT/peptide complex has been modeled in a field effect transistor (FET) sensor configuration using density functional tight binding (DFTB) theory in order to identify the configuration and electrical properties of solid state nanosensors.

In this work, it has been shown that a covalent immobilization of a PETN surrogate (PETNH) via attachment of the surrogate's carboxyl group onto amine functionalized wells resulted in a high degree of binding in the test wells. Further optimization on the PETN-amino functionalized wells was obtained by using blocking buffer based on 5 % non-fat dry milk dissolved in PBS. Here, the optimal amount of immobilized PETNH in the test wells was obtained by using 1 μg of the surrogate explosive with 10 times molar excess of

EDC. ELISAs performed under the optimized conditions showed that the Ph.D.-7 library contained phage with specificity towards PETNH.

After optimizing the ELISA procedure and confirming the presence of specific phage in the library, a biopanning procedure against immobilized PETNH was carried out to further identify selective phage towards PETNH. It was shown via titers that after three biopanning rounds, there was an eleven-fold order of magnitude decrease in phage concentration. This confirmed that only phage with a relative level of selectivity made it through the panning process. From the titer of the third panning round, four plaques were removed, amplified, and PEG purified. Using the PEG purified product of each of the isolated phage, ELISAs were performed to determine the relative levels of selectivity for each phage.

The isolated plaques were then sequenced to determine the composition of the peptide expressed on the phage surface. It was observed through gel electrophoresis that the purified DNA possessed good integrity. Also, a NanoDrop UV-Vis Spectrophotometer test on each sample showed that the DNA sample was sufficiently pure. It was also shown that each sample produced a unique peptide sequence. Observations of the selected peptide's sequences showed that they displayed similar segments to those observed in PETN reductase which is a protein known to interact with explosives such as TNT. Following the sequencing of the identified peptides, these were attached to carboxylated SWCNTs. Here, the peptides were tagged with hydrazide-PEG4-biotin in order to quantify and corroborate their coupling to the nanotubes. Also, using biotin as a tracking approach, the detection capabilities of the peptide functionalized SWCNTs towards PETNH in the

liquid state was performed. It was observed that the peptides investigated were able to detect about 1.6 x 10^{-4} mmol of PETNH.

The selectivity of one of the identified peptides was further investigated by testing it against TNT, Nitrobenzene, Sodium Nitrate, and Pentaerythritol. The initial results showed that neither TNT, nitrobenzene, sodium nitrate, nor Pentaerythritol compete with the PETNH binding of the selected peptide.

The solid state detection capabilities of a SWCNT/ peptide system were also here simulated using DFTB theory. In this work, an 8,0 SWCNT with a diameter of 0.63 nm and a length of 11.03 nm was modeled in a FET configuration. The electrical properties were simulated, and the electrical current versus gate voltage curves showed that the SWCNT acted like a n-type semiconductor. This was expected due to the lack of physisorbed oxygen in the SWCNT. In the conducting state, the system current was on the 10^{-7} Amps order of magnitude.

When a simulated peptide was covalently attached to the SWCNT side wall, the model showed that the device still acted as a n-type semiconductor, but the electrical current in the conducting state decreased by two orders of magnitude. The peptide-SWCNT system was also modeled in the presence of PETN. It was here observed that although the system also maintained its n-type character, the interaction with the PETN resulted in an increase in the elctrical current of the SWCNT/peptide complex. It was also observed that at a gate voltage of -0.05 V and a bias voltage of -0.1 V, the SWCNT/peptide PETN interaction system showed an increase of the electrical current change by almost two orders of magnitude (from 10^{-9} to 10^{-7} Amps). This suggested that the interaction of PETN with a peptide functionalized SWCNT results in a net donation of electrons to the conducting

channel. Likewise, comparison of the electrical current versus bias voltage for the SWCNT/peptide and the SWCNT/peptide/PETN system showed that at -0.15 V gate voltage and 1.1 V bias voltage, the SWCNT/peptide PETN interaction system exhibited a one order of magnitude increase in the electrical current. The results of these simulations can therefore provide possible operation parameters for real solid state FET detection system consisting of a peptide functionalized SWCNT conducting channel.

In summary, this research program has shown that a phage display technology can be used to find peptides that selectively bind to explosive compounds (such as PETN). These peptides can then be used in conjunction with SWCNTs to create a sensing platform capable of detecting explosives in liquid state and potentially in solid state. Indeed, the theoretical modeling results suggest that these SWCNT/peptide systems can be utilized in a FET setup to detect PETN in the solid state. It is expected that the present research work will lay the foundations for finding peptides selective to explosives as well as the operating electrical parameters to be used on CNT-FET sensors.